

AD A 073 763

LEVEL

AD-E000318
NRL Report 8311
EOTPO Report No. 46

12

The Fundamentals of Thermal Imaging Systems

Edited By

FRED ROSELL AND GEORGE HARVEY

13010484
0003413

May 10, 1979

DIC
RECEIVED
SEP 13 1979
C

LM



ELECTRO-OPTICAL TECHNOLOGY PROGRAM OFFICE
NAVAL RESEARCH LABORATORY
Washington, D.C.

REPRODUCED FROM
BEST AVAILABLE COPY

Approved for public release; distribution unlimited.

79 08 30 006

FILE COPY

Reviewed and Approved by

Dr. John M. MacCallum

SECURITY CLASSIFICATION OF THIS PAGE (When Data Entered)

REPORT DOCUMENTATION PAGE		READ INSTRUCTIONS BEFORE COMPLETING FORM
1. REPORT NUMBER NRL Report 8311 EOTPO Report No. 46	2. GOVT ACCESSION NO.	3. RECIPIENT'S CATALOG NUMBER
4. TITLE (and Subtitle) THE FUNDAMENTALS OF THERMAL IMAGING SYSTEMS		5. TYPE OF REPORT & PERIOD COVERED Interim report on a continuing NRL Problem.
		6. PERFORMING ORG. REPORT NUMBER
7. AUTHOR(s) John B. Goodell, George L. Harvey, Walter R. Lawson, James A. Ratches, Robert E. Roberts, Fred A. Rosell, Robert L. Sendall, and David L. Shumaker		8. CONTRACT OR GRANT NUMBER(s) NRL Problem N01-29
9. PERFORMING ORGANIZATION NAME AND ADDRESS Naval Research Laboratory Washington, D.C. 20375		10. PROGRAM ELEMENT, PROJECT, TASK AREA & WORK UNIT NUMBERS
11. CONTROLLING OFFICE NAME AND ADDRESS Naval Research Laboratory Washington, D.C. 20375		12. REPORT DATE May 10, 1979
		13. NUMBER OF PAGES 259
14. MONITORING AGENCY NAME & ADDRESS (if different from Controlling Office)		15. SECURITY CLASS. (of this report) Unclassified
		15a. DECLASSIFICATION/DOWNGRADING SCHEDULE
16. DISTRIBUTION STATEMENT (of this Report) Approved for public release; distribution unlimited.		
17. DISTRIBUTION STATEMENT (of the abstract entered in Block 20, if different from Report)		
18. SUPPLEMENTARY NOTES		
19. KEY WORDS (Continue on reverse side if necessary and identify by block number) Imaging systems FLIR Television systems Atmospheric transmission		
20. ABSTRACT (Continue on reverse side if necessary and identify by block number) The purpose of this book is to provide the reader with a document which brings together under one cover an overview of radiometric and photometric concepts involved in thermal imaging systems. Governing equations are derived from simple fundamental concepts. Also, models used for the visual discrimination i.e., detection, recognition, or identification, of real scene objects are discussed. It is hoped that the text will be useful to FLIR designers, evaluators, and thermal imaging system modelers, as well as those whose sole interest is a grasp of the concepts involved in thermal imaging.		

PREFACE

This document was supported by the Joint Technical Coordinating Group for Thermal Imaging Systems and the NAVMAT Electro-Optical Technology Program Office. The document is meant to be of tutorial and reference value to program managers and scientists who are familiar with thermal imaging techniques and systems but need detailed information relating systems modeling procedures to visual displays and thermal imaging system performance.

The authors would like to acknowledge the helpful comments of members of the Joint Technical Coordinating Group as well as others who have made suggestions and inputs including Lucian Biberman, Stephen Campana, Edward Hooper, William Lawson, John MacCallum, George Mavko, Paul Moser, James Ratches and John Walsh. A special note of gratitude is expressed for Mrs. Dora Wilbanks of the Technical Information Division for struggling with the many revisions of this document.

Accession For	
NTIS GRA&I	<input checked="checked" type="checkbox"/>
DDC TAB	<input type="checkbox"/>
Unannounced	<input type="checkbox"/>
Justification	<input type="checkbox"/>
By _____	
Institution/ _____	
Date of Accession _____	
Date of Review _____	
A	

CONTENTS

Preface	iii
Chapter I — INTRODUCTION.....	1
Chapter II — CHARACTERIZATION OF THE THERMAL SCENE.....	7
Chapter III — ATMOSPHERIC EFFECTS ON INFRARED SYSTEMS	21
Chapter IV — VIDEO, DISPLAY AND PERCEIVED-IMAGE SIGNAL-TO-NOISE RATIOS	49
Chapter V — LABORATORY PERFORMANCE MODEL	85
Chapter VI — STATIC FIELD PERFORMANCE MODELS	97
Chapter VII — THERMAL-IMAGING SYSTEM (TIS) DYNAMIC FIELD PERFORMANCE	111
Appendix A — NOMENCLATURE, UNITS, AND SYMBOLS	143
Appendix B — SYMBOLS.....	149
Appendix C — THE NIGHT VISION LABORATORY STATIC PERFORMANCE MODEL BASED ON THE MATCHED FILTER CONCEPT.....	159
Appendix D — STATIC PERFORMANCE MODEL BASED ON THE PERFECT SYNCHRONOUS INTEGRATOR MODEL	181
Appendix E — THE COLTMAN AND ANDERSON EXPERIMENT	205
Appendix F — BASIC SNR AND DETECTIVITY RELATIONS.....	209
Appendix G — EFFECTS OF IMAGE SAMPLING.....	215
Appendix H — PSYCHOPHYSICAL EXPERIMENTATION.....	223
Appendix I — OBSERVER RESOLUTION REQUIREMENTS	237
INDEX	253

Chapter I

INTRODUCTION

G. L. Harvey
F. A. Rosell

A. OBJECTIVE

The purpose of this book is to provide an overview of radiometric and photometric concepts involved in thermal imaging systems. Governing equations are derived from simple fundamental concepts. Also, models used for the visual discrimination, *i.e.*, detection, recognition, or identification, of real scene objects are discussed.

It is hoped that the material in the text will be useful to forward-looking infrared radar (FLIR) designers, evaluators, and thermal imaging system modelers, as well as those whose sole interest is a grasp of the concepts involved in thermal imaging.

B. OVERVIEW OF THE CHAPTERS

This chapter contains an overview of the content and significance of the following chapters. The report is structured so that the appendixes present the basic definitions and mathematical tools which are used in the preceding discussion. The nature of the target signature is considered first. Then its modification by the atmosphere, its processing by the FLIR system, the interpretation of the displayed information by a human observer, and the use of these systems in a dynamic environment in which the problems of search and limited time for the completion of assigned tasks must be considered.

1. Characterization of the Thermal Scene (Chapter II)

The scene, because of variations in either temperature or emissivity, is the source of most of the radiation sensed by thermal imaging systems sensitive in the 3 to 5 or 8 to 14 micrometer spectral bands. Most of the scene objects obtain their energy from the Sun, and even man-made objects such as trucks appear very much like trucks on thermal imaging system displays when heated by external sources. However, the thermal images of trucks may appear radically different when heated by their own internal sources such as engines or comfort heaters. The detailed calculations of thermal scene object-to-background contrast are very complex and beyond the scope of this report. However, the results of a number of such calculations are discussed. In particular, it is shown that thermal object-to-background signatures are strongly dependent upon cloud cover, the insolation, and the aspect angles between the viewer, the scene object, and the Sun and sky. A ship on the open sea, for example, can reverse in contrast a number of times when viewed from a low flying aircraft as the aircraft approaches from a long distance and then overflies the ship. The background may be the horizon sky, low-emissivity water viewed at a shallow angle, high-emissivity water viewed directly downward, or

even mirrored sky. The ship's temperature may also be greater than the ambient air or water temperature in the daytime and smaller at night.

In system design and analysis, it has been common practice to assume an equivalent scene object and background of unit emissivity. The temperature of the scene object is averaged over the object's area and, similarly, the temperature of the background is averaged over a patch equal to the scene object's area. The only information used is a single numerical value for the object-to-background temperature differential and the object's dimensions. Thus all temperature gradients within the object and background are ignored. In the case of a hot spot on the scene object, ignoring large temperature gradients may lead to pessimistic detection ranges and optimistic recognition ranges. Similarly background gradients may constitute clutter with noise-like properties. In addition, temperature differentials are sometimes averaged over a 24-hour or some other fairly long time period. While, as a practical matter, it is often necessary to make gross simplifying assumptions for the purpose of comparing competing systems of the same type, it will become clear in Chapter II that the use of some assumptions can lead to enormous errors when computing the probabilities of visually discriminating displayed thermal scene objects in a dynamically changing environment.

Though existing computer models can be used to obtain quite detailed thermal signatures with detail within the objects and backgrounds, most of the thermal imaging models now used are not now capable of using the amount of detail which could be provided. However, it is important that gross changes in signature due to changes in insolation, viewing aspect, cloud cover, and the like be considered as a minimum.

2. Atmospheric Effects on Infrared Systems (Chapter III)

The atmosphere is characterized by transmitting windows whose spectral location restricts the choice of detector and optical materials. IR imaging systems can be severely degraded by high humidity or by poor visibility. The 3-5 μm window is generally superior in transmittance on clear humid days while hazy dry days favor the 8-12 μm band. In Chapter III, the reader is provided with an easy to use (but accurate) procedure for evaluating atmospheric transmission. Computer-based tables give transmittances with respect to a 10°C blackbody over the 3-5 and 8-12 μm windows. From temperature, relative humidity or dew point, and visual range measurement, the user reads molecular and continuum transmittances corresponding to a selected range directly from the tables. This value of transmittance is then multiplied by the value of the aerosol transmittance calculated by using the results of visibility measurements to obtain the composite atmospheric transmittance.

The chapter begins with a brief discussion of the main absorbing gases and continues with a more detailed exposition of aerosol scattering and the difficulty it causes because of its extreme variability. The chapter continues with the definition of atmospheric transmittance, the concept of visual range, and the temperature and pressure effects on molecular band absorption. This discussion is followed by a description of the LOWTRAN 3B computer program for computing atmospheric transmittance as developed by the Air Force Geophysics Laboratory in Cambridge, Mass.

Detailed expositions of meteorological variables such as seasonal variations of pressure and temperature and the relative merits of different atmospheric models have been purposely

avoided in this chapter. Also detailed discussion of molecular band absorption which is contained in the voluminous references cited are not included. However, the computer algorithms which produced the data in the tables provided have exploited all available current knowledge.

3. Video, Display, and Perceived-Image Signal-to-Noise Ratios (Chapter IV)

This chapter is devoted to the basic concepts and derivations of fundamental mathematical relations used to describe and analyze thermal imaging systems when the input test patterns are standardized and quantitatively describable objects such as rectangles and periodic bar patterns. The concept of the image signal-to-noise ratio obtainable from a sensor is developed along with other sensor related quantities such as the detector detectivity, the video Signal-to-Noise Ratio (SNR_v) and the noise-equivalent temperature difference $NE\Delta T$. SNR_v is of primary interest when the output of the sensor feeds a machine such as a video tracker or a scene object cueing or pattern recognition device. The SNR_D is the image signal-to-noise ratio available to an observer when the displayed image is limited only by finite sensor apertures or internally generated sensor or sensor generated noises and not by parameters of the observer's eye. When all pertinent observer eye parameters are included, the SNR_D becomes the perceived SNR or SNR_p . In many cases of practical interest, the SNR_D and SNR_p are equal. As may be surmised, the SNR_D and SNR_p are directly related to the observer's ability to discern a displayed test pattern and do take into account the ability of the observer to spatially and temporally integrate an image.

The video SNR_v and the $NE\Delta T$ are generally related to the SNR_D and SNR_p , but the relationship is not necessarily linear or direct. A sensor with a lower SNR_v and a larger $NE\Delta T$ may in fact produce a superior SNR_D . The reason for this apparent anomaly is that the SNR_v and $NE\Delta T$ include the video bandwidth as part of their definition, and this bandwidth is comparatively immaterial to the observer. When discerning images, the observer himself becomes, in effect, the limiting overall system bandwidth.

Two models are developed for the SNR_D , a periodic model used when the input image is a sine or square wave bar pattern and an aperiodic model used when the test images are rectangles. These two models are made necessary because the effects of system apertures or optical transfer functions on image detectability are distinctly different for the two types of images and not primarily because of observer effects (although some observer differences exist). In Chapter IV, a number of thermal imaging sensor configurations are discussed along with the modulation transfer functions* of various sensor elements including the lens, the detectors, the multiplexers, and displays. The effects of the image sampling process in the cross-scan direction are also considered in Appendix G, along with the criteria for eliminating spurious responses (aliasing) while maintaining a flat-field-display-luminance distribution. More detailed derivations at basic equations used in Chapter IV are presented in Appendixes C through G.

4. Laboratory Performance Model (Chapter V)

In Chapter IV, the primary effort was to quantitatively determine the display SNR_D obtainable from the sensor when the input test images are rectangles or periodic bar patterns. If the observer's SNR requirements are known, then the probability that an observer will discern an image under a given set of operating conditions should be analytically predictable. The

*The modulation transfer function is the modulus of the optical transfer function which describes the effects of sensor apertures.

ability to perform such prediction is of considerable aid in designing and evaluating sensory systems.

Over the past decade, many psychophysical experiments have been performed to determine the image SNR required by an observer, and a representative sample of the more pertinent experimental results is discussed in Chapter V and Appendix H. It is found that the SNR_D required to detect rectangles is approximately a constant for images which are not too large in two directions simultaneously and that the eye can spatially integrate surprisingly well over long thin rectangles. The eye's ability to integrate over the length of a bar in a bar pattern is more limited, but the threshold value of SNR_D required to discern the presence of a pattern appears to fall off at the higher spatial frequencies. The observer's SNR requirements are usually specified in terms of a threshold value (50% probability of discerning the test image) and as a function of the probability of detection. Approximately twice the SNR_D is required to discern an image at the near 100% level than at the 50% level.

The two primary measures of the laboratory performance of thermal imaging systems are the minimum resolvable temperature difference (MRT) and the minimum detectable temperature (MDT). In the MRT case, the input test image is defined to be a four-bar pattern with the length of each bar being seven times its width. The MRT represents the smallest temperature difference between the bars which permits the observer to resolve all of bars at the 50% probability level. The MRT of the sensor is plotted as a function of the bar pattern's spatial frequency. In the MDT case, the test image is defined to be a square. The MDT represents the smallest temperature between the square and its background which can be discerned by the observer at the 50% probability of detection level. Both the MRT and MDT are analytically predictable if the image SNR obtainable from the sensor is known, since the observer thresholds have been determined with fair-to-good accuracy at least for the cases in which the image SNR is system rather than observer eye noise limited.

It has been shown experimentally that the ability to discern a displayed test image can be limited by fluctuation noise generated in the eye's primary photoconversion process. In Appendix H it is shown that the retinal fluctuation noise terms can be added to the system noise terms to create a perceived signal-to-noise ratio expression but that the necessary psychophysical experiments have not been performed to obtain the necessary eye parameters. The SNR_p expression must also, of course, include the effects of the eye's apertures.

5. Static Field Performance Models (Chapter VI)

The analytical models of Chapters IV and V can be used to predict the incremental temperature difference required to detect either aperiodic or periodic images of known geometry. However, there are continuing efforts to correlate threshold resolution as measured or predicted with the ability to discriminate visually (detect, recognize, identify, etc.) real scene objects. In this chapter, we review the historical approaches which have been used, starting with the well-known Johnson criteria wherein real scene objects are replaced by bar patterns of equivalent contrast and of spatial frequencies which are a function of the level of visual discrimination desired. The higher the level of visual discrimination wanted, the higher the spatial frequency.

In the early 1970's, Rosell and Willson attempted to quantify further the Johnson criteria, using SNR and improved resolution considerations. The notion was to use Johnson's criteria directly to establish the bar pattern spatial frequency and to attempt to correlate probability of

recognition and identification with bar pattern SNR. While the agreement appeared good for isolated targets on a uniform background, the agreement became poorer for cluttered scenes. As a next step, the Night Vision and Electro-Optics Laboratory at Ft. Belvoir, Va. hypothesized that the threshold bar pattern spatial frequency required at the 50% level of recognition or identification could be selected on the basis of the Johnson criteria but that higher levels of probability required a higher sensor threshold resolution (as opposed to a higher image SNR alone). In concurrent experiments by O'Neill at the Naval Air Development Center at Warminster, Pa. and Rosell and Willson, it was shown that the threshold spatial frequency response required at the 50% probability level is not a constant but instead, it increases as the imagery tends toward the noise limited as opposed to the aperture or MTF limited condition. On the other hand, while it appears that the Johnson criteria cannot be used to select the bar pattern spatial frequency at the 50% probability level, the NVL approach as formulated by Johnson and Lawson to determine higher and lower probability levels appears to be superior to the SNR_D approach based on parallel experiments on human face identification by Rosell and Willson.

By a further analysis of the O'Neill data, it is hypothesized that ability to discern real images may be strongly related to the video signal-to-noise ratio (defined with respect to a reference video bandwidth). A method of taking the video SNR into account is proposed in Chapter VI, and the method appears to have promise but it has not been verified experimentally. The general result of the O'Neill data analysis is that for video SNR above about 3-4, the threshold resolution required at the 50% level of visual discrimination is a constant but increases rapidly as the video SNR decreases below 3. It should be observed that O'Neill's experiments were conducted with images of 100% contrast and whether the technique suggested will work or not for images of lower contrast has not been explored. The details of these various experimental results are discussed in Appendix I.

The original levels of visual discrimination proposed by Johnson were: detection, orientation, recognition, and identification. The orientation criterion has seen little use, and it is proposed that it be dropped. However, it is proposed to increase the number of levels overall primarily because the gap between simple detection and classical recognition is felt to be too large. In the specific case of detection, an object may be considered to be more than simply detected even though the sensor's threshold resolution is only sufficient to permit simple detection in the classical Johnson sense. A rapidly moving blob on a road, for instance, is probably a vehicle. Thus auxiliary cues may lead to a higher level of visual discrimination than resolution alone would tend to indicate. It is also observed that the number of resolvable lines required to discriminate a real scene object is often a function of the viewing aspect angle.

Chapter VI concludes with a discussion of methods of performing range analysis as traditionally performed and also, by including some of the newer concepts discussed above. In performing static field range predictions, atmospheric and sightline instability effects are included.

6. Thermal-Imaging (TIS) Dynamic Field Performance (Chapter VII)

The previous chapters have been directed toward the detection of a target when the observer has an unlimited amount of time. In Chapter VII the element of time is introduced into the task of physical acquisition, visual acquisition, and extraction of the required information. All of the probabilities involved in acquiring and detecting a target are discussed using a typical scenario for a FLIR system.

HARVEY AND ROSELL

In Section VIIC the mechanics of visual search are described, the meaning of a "glimpse" is discussed, and some typical values of visual search time are given.

The following sections discuss the probability of visual direction under a variety of conditions, such as changing SNR, high SNR environment, and an increasingly detectable object.

Finally, Section VIIF shows how system parameters may cause the probability of detection and identification for a high-resolution system to be lower than the probabilities of a lower resolution system.

Chapter II

CHARACTERIZATION OF THE THERMAL SCENE

F. A. Rosell

A. INTRODUCTION

Like the visible scene, the thermal scene has infinite variety, and the detailed description of all but a limited number of specialized cases would be prohibitively costly. Elaborate computer models have been developed to describe various scenes in some detail, but experimental verifications of the models are few. However, those experimental results which exist show the same trends as the analytical models predict. The detailed calculations of thermal scene object-to-background thermal contrasts, which are based on rather conventional heat transfer considerations, are beyond the scope of this report but a number of the results of calculations which have been made will be discussed in the chapter (Ref. 2-1).

The scene, owing either to variations in temperature or emissivity, is the source of most of the radiation sensed by the thermal imaging sensor. Most of the scene receives its energy from the Sun, and the thermal scene displayed appears very like the visual scene although the contrasts between scene objects can be radically different. Man-made objects, when heated by internal sources, can produce a very unnatural appearance.

It is not uncommon to assume that a scene object such as a ship or a tank always has a certain incremental temperature above background. This assumption can lead to considerable error even when for example, a tank has been exercised for a considerable period. The terrain, for example, generally heats and cools much more rapidly than objects of large thermal mass such as tanks and therefore both positive (hotter) and negative (colder) contrasts between the object and its background can exist. It may also be erroneously assumed that a thermal imaging sensor is always the sensor of choice for night applications and that night and day performances will be approximately equal. While this may sometimes be true, it is found that thermal scene signatures will generally be smaller at night and during other periods of low insolation (Sun heating).

In this chapter, a number of typical scene objects and their backgrounds will be discussed in order to provide some physical insight to the general problem of characterizing the thermal scene. The cases discussed are specific to the particular environment involved and are not meant to be generally applicable. For more specific information, the reader is referred to References 2-2 through 2-4.

B. GENERAL SCENE CHARACTERISTICS

FLIR sensors detect radiation of wavelengths in the 3-5 or 8-14 micrometer atmospheric windows and derive their images from variations in the radiation received. These variations can be due either to variations in the emittance of the scene or to variations in the radiation

F. A. ROSELL

reflected from the scene. The radiation reflected from the scene can come from a variety of natural sources such as clouds, sky, and background, but is usually less than that associated with a target at ambient temperature. The primary scene signal results from variations in emittance and may be due to variations in temperature or emissivity. That is, the scene is the source generating most of the radiation itself due to its inherent temperature.

The background radiation is that associated with the average scene temperature and emissivity. Since FLIR systems currently employ ac coupling between the detectors and their amplifiers, the signal is due to variations about the average. One primary source of noise is that due to the conversion of scene photons to electrons by the detectors.

Most objects in a scene obtain their energy (heat) from the Sun. Heat absorbed during the day is lost at night. The process depends upon the atmospheric conditions, the degree of overcast, and the general air temperature. When humidity is high, the sky is cloud covered, and the air temperature is near constant, the scene tends not to vary much from day to night. Everything stabilizes at air temperature as though the whole system were in a blackbody cavity. Objects with low emissivity tend to take on the temperature of the air with a lag determined by the thermal mass of the object and its thermal conductivity. Materials that conduct poorly are apt to have surface temperatures which determine their radiation characteristics and which vary greatly. Objects with high emissivity are more likely to have their temperatures strongly influenced by the physical characteristics of the scene objects and the radiation characteristics of the sky and atmosphere than those of low emissivity.

The effect of a strong wind is to reduce substantially the temperature excursions within a scene. In effect, the thermal signature is partially "blown away." During and after a rainstorm, the scene tends to become isothermal. Also, an extended period of overcast will reduce the amplitude of cyclic scene temperature variations. The reductions in temperature differences can substantially degrade the appearance of the natural scene at long range, because the scene thermal signature is further reduced by the atmosphere. However, the detection of hot man-made objects could be enhanced by the washout of the background. It is also generally true that periods of poor atmospheric transmittance and periods of low insolation tend to go together.

C. BACKGROUNDS

The radiation characteristics of a complicated scene can take on infinite variety, and detailed analysis of any but a small number of representative typical cases has been prohibitively costly in the past. In the future, wider use should be made of computer-generated thermal scene object/background signatures provided that such efforts are paralleled with experimental programs to validate the models. In the following some examples of computer-generated thermal signatures are discussed. The results have not been verified experimentally, but the results appear to be reasonable and are in general agreement with existing data.

Trees and bushes may be significantly warmer than grassy ground. In Fig. 2-1, a computer-generated thermal signature is shown for five different background materials, as a function of time of day from 6 a.m. to 8 p.m. The conditions are given in Table 2-1. It is also seen that sand heats more slowly and cools more slowly than the other backgrounds. The relative thermal contrast, which is defined to be the differential radiance between grass and the other materials, is shown in Fig. 2-2. Observe that in this case, the sand is of negative contrast

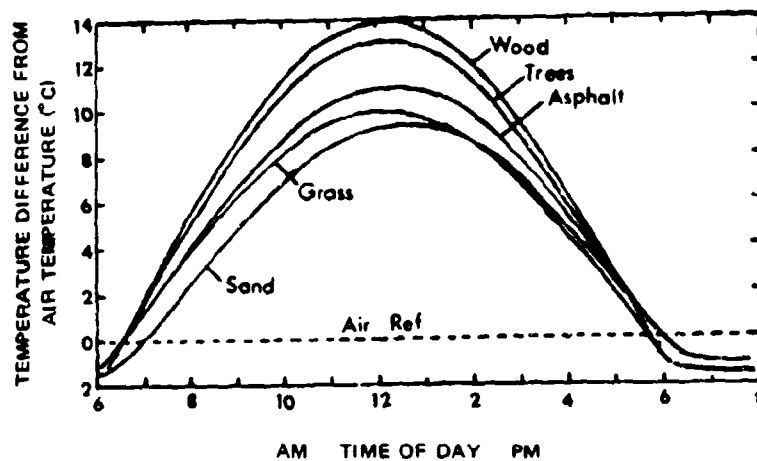


Fig. 2-1 — Temperature difference between various background materials and air as a function of the time of day

Table 2-1 Conditions for the Calculations of Temperature Difference Shown in Fig. 2-1

Ambient Temperature	298 K	Cloud Cover	0.6
Pressure	1013 mbar	Latitude	20°N
Declination	0 deg	Wind Velocity	12 mph
Visible Range	20 km	Range	4 km
Mixing Ratio	16		

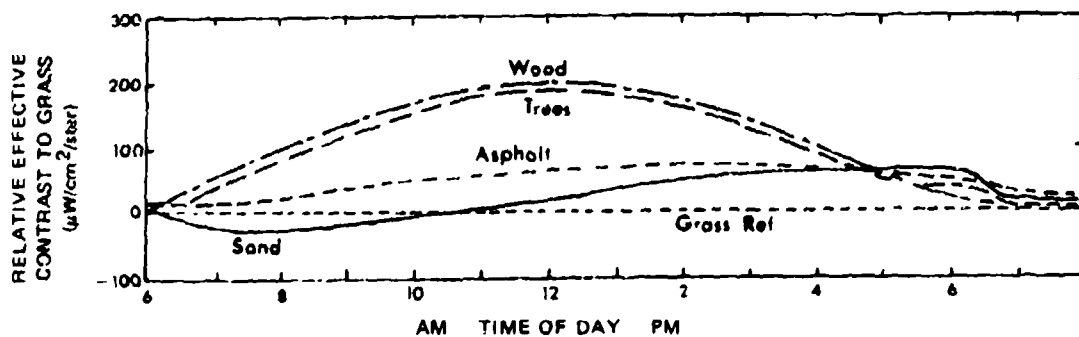


Fig. 2-2 — Effective radiant contrast between various background materials and grass as a function of the time of day

during the early morning hours and of positive contrast in the afternoon. Both the scene temperature and the thermal contrast of the scene are seen to be strongly time dependent.

At night, trees mirrored in water appear even warmer. Three reasons for this effect have been postulated: 1) the undersides of leaves may stay warmer than the top surfaces due to the fact that they cool by radiation to a warm ground rather than than a cold sky; 2) the net emissivity of the leaves' undersides may be higher due to dew; and 3) the sensor viewing the undersides of leaves off the water sees a cavity effect inasmuch as the water adds radiation and the reflection from the underside of a leaf sees another leaf, etc. so as to cause a blackbody effect while the top of the leaf reflects the sky.

Usually, a calm sea under a sky appears cold at shallow viewing angles due to its high reflectivity and low emissivity as can be inferred from Fig. 2-3. At steeper viewing angles, the emissivity is greater and the water appears warmer. A sky overcast with low-altitude clouds can make the water appear warmer. In Fig. 2-4, we show the angular reflectance properties of water vs wavelength, which in turn shows that the angular reflection properties of Fig. 2-3 apply throughout the infrared regions of interest.

The disturbed sea surface is difficult to describe in a closed mathematical expression. In first order analysis it is common to use the sine wave and sawtooth approximations shown in

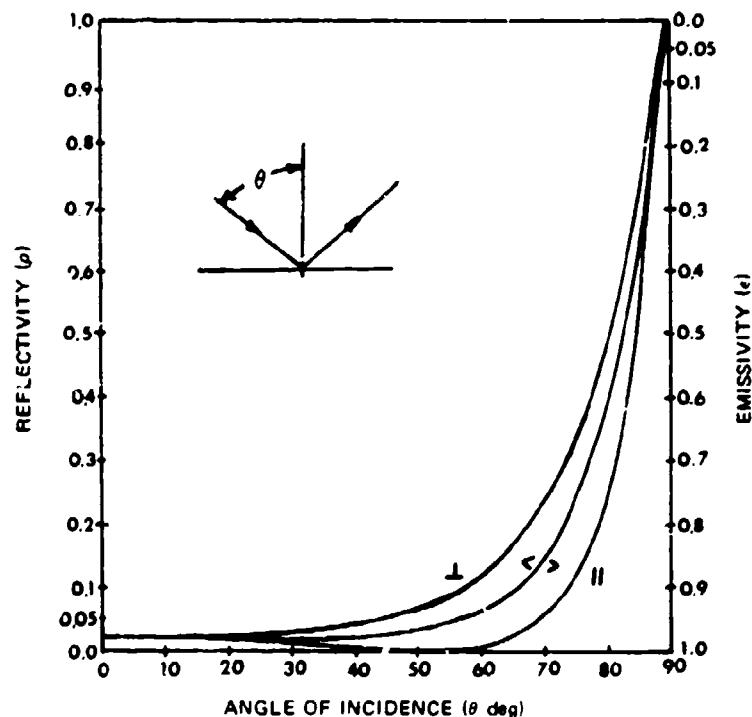


Fig. 2-3 — Reflectivity and emissivity of water for the parallel (||), average (< >) and perpendicularly (⊥) polarized light components vs angle of incidence in the visible spectrum

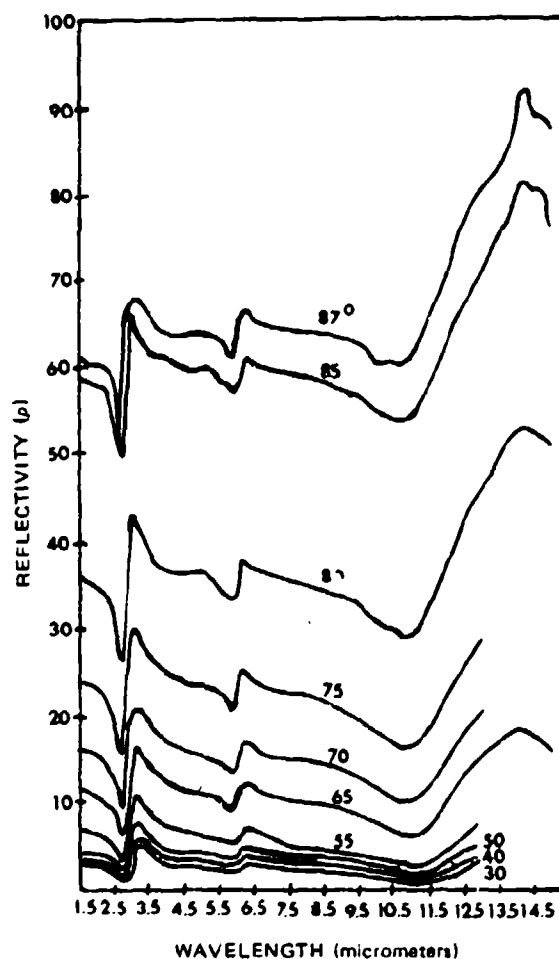


Fig. 2-4 — Spectral reflectance of water vs wavelength for various angles of incidence

Fig. 2-5. The sine wave sea is built up from sea-state descriptions of wavelength, height and period, etc. The sawtooth approximation, which is analytically much simpler, has shown good agreement with measured results in many cases. The sawtooth wave is inclined toward the sensor at an angle and equals about 15° for the average sea.

In Fig. 2-6, we show three viewing aspect angles over a water background. Along a substantially horizontal path just above the horizon through a dense air path, the sensor "sees" the air temperature. The air along the path may be considered to have an emissivity of unity and is thus a "blackbody sky." From a perpendicular to the surface, the water has an emissivity of unity and is thus a "blackbody sea." At the sea just below the horizon, a reflected ray would follow the dashed line if the sea were perfectly flat but since the sea is almost always disturbed, reflected rays from a higher source as shown by the solid line are observed. Experimentally, the upward angular displacement has been observed to be approximately 30° on the average

F. A. ROSELL

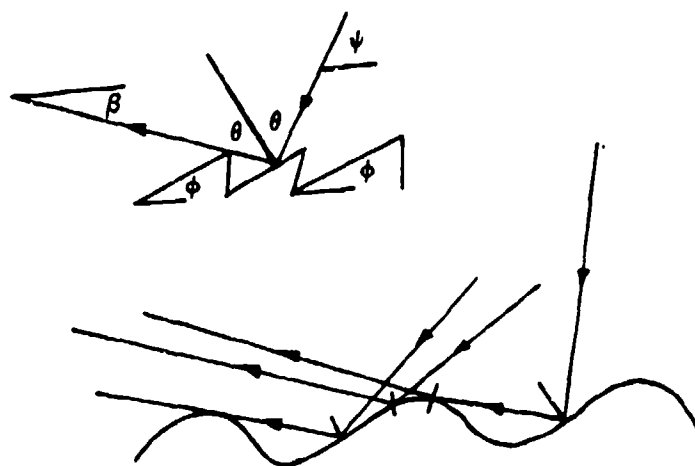


Fig. 2-5 — Sawtooth and sine wave approximations to a disturbed sea

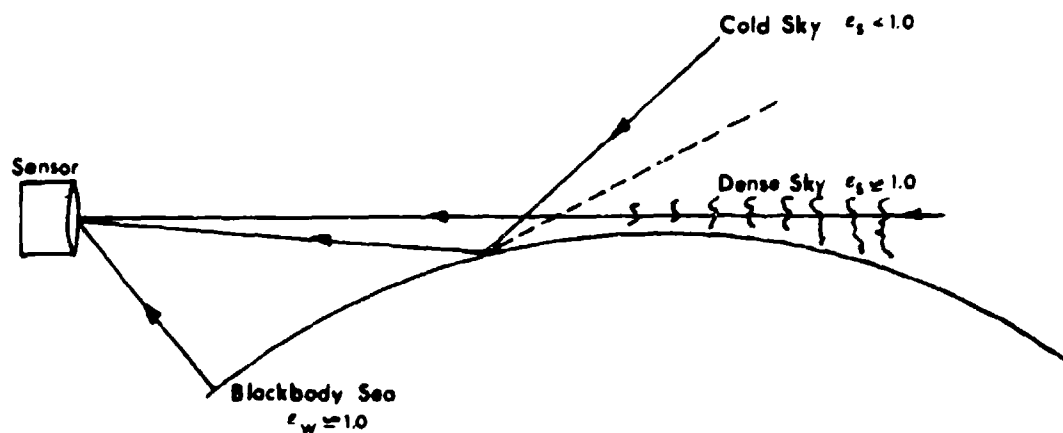


Fig. 2-6 — Background radiation sources in three viewing directions

giving credence to a sea model with an average slope of 15° . The thermal sensor viewing just below the horizon senses a combination of the radiation emitted from the sea and the mirrored reflection of a cold sky.

The variation in background temperature with the viewing aspect angle is illustrated in Fig. 2-7. Note that the sea background temperature dips just below the horizon and a ship which may be colder than either the air or the water may yet be imaged as hotter than either. The effect of an overcast sky is illustrated in Fig. 2-8. The sky temperature is seen to increase, and the dip in apparent temperature just below the horizon is decreased.

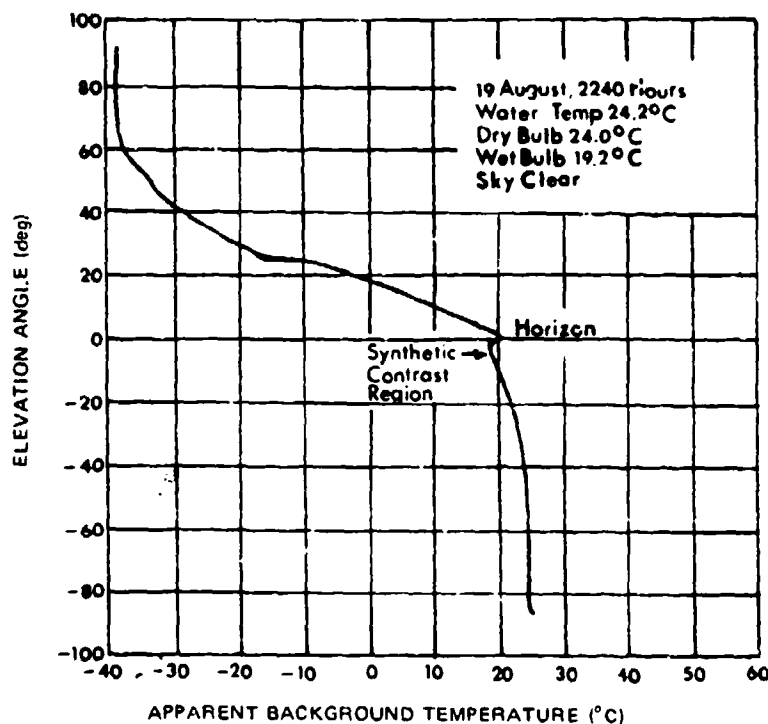


Fig. 2-7 — Effect of viewing angle on apparent background temperature of air and a disturbed sea

D. SCENE OBJECTS

A truck, when heated by nature looks very much like a truck on a FLIR display. The cavity under the truck may appear hot if viewed at an angle since by multiple reflection, this area has an emissivity of unity. The truck often has dark areas due to low-emissivity metal areas which reflect the sky. When idling, the engine and exhaust become very hot, exhibiting localized areas of radiation which may saturate the display. If the FLIR displays hot as white, the extreme brightness can aid detection but degrade recognition. Localized heating can cause the entire hood of the truck to appear very bright. By reversing the polarity to hot as black, the picture often appears more normal. If the truck is moving down the road there is again localized heating but not of the same type. The hood is cooled by the airstream to near the air temperature. The exhaust will still be hot and the undercarriage and tires will appear warm to hot.

Tanks have a large mass and generally lag the terrain in temperature when parked. The engine and exhaust can appear very bright when the tank is running and these features are in the field of view. When driven, the bogie wheels and treads as well as the rest of the tank heat to provide a natural looking picture. In Fig. 2-9, we show the various factors which influence the heating of a tank. The factors which must be considered are the insolation, the radiation exchange between the tank and its surround, convection due to wind or tank motion, internal heat sources such as the engine, and conduction to the earth. Conduction is of particular interest when the tank is parked in snow.

F. A. ROSELL

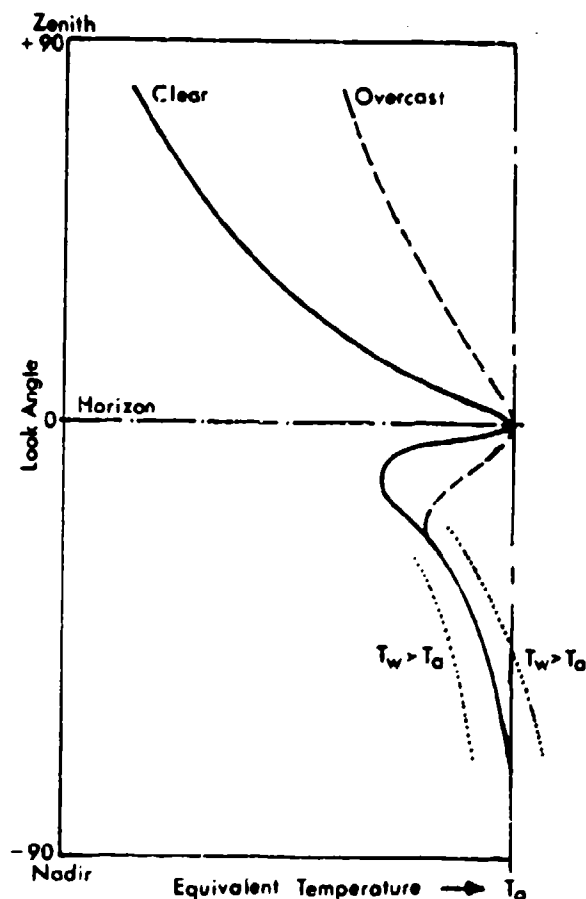


Fig. 2-8 — Effect of an overcast sky on the equivalent background temperature for various viewing angles

The signal obtainable from a scene object is a function of the viewing aspect angle and therefore the signals will be time dependent on even a very short time basis when the sensor is moving. A computed temperature profile of a tanklike object (parked) is shown in Fig. 2-10. The temperature curves show the effect of the sun passing from east to west. Temperatures of the eastern surfaces peak in midmorning and then slowly cool to equilibrium in midafternoon while the western surfaces do the opposite. South facing and roof surfaces rise to a pos:noon peak before they decay. The thermal lag of the tank is seen by the fact that the roof surface peaks later than the background.

The radiant contrast between the tank and a grass background is shown in Fig. 2-11. If it is desired to image the tank, it is seen that there is four times more thermal contrast on the east side of the tank at 9:00 a.m. Near noon, the tank will be more easily discerned in the north-south direction. In the late afternoon, the roof and the west sides of the tank provide higher contrasts.

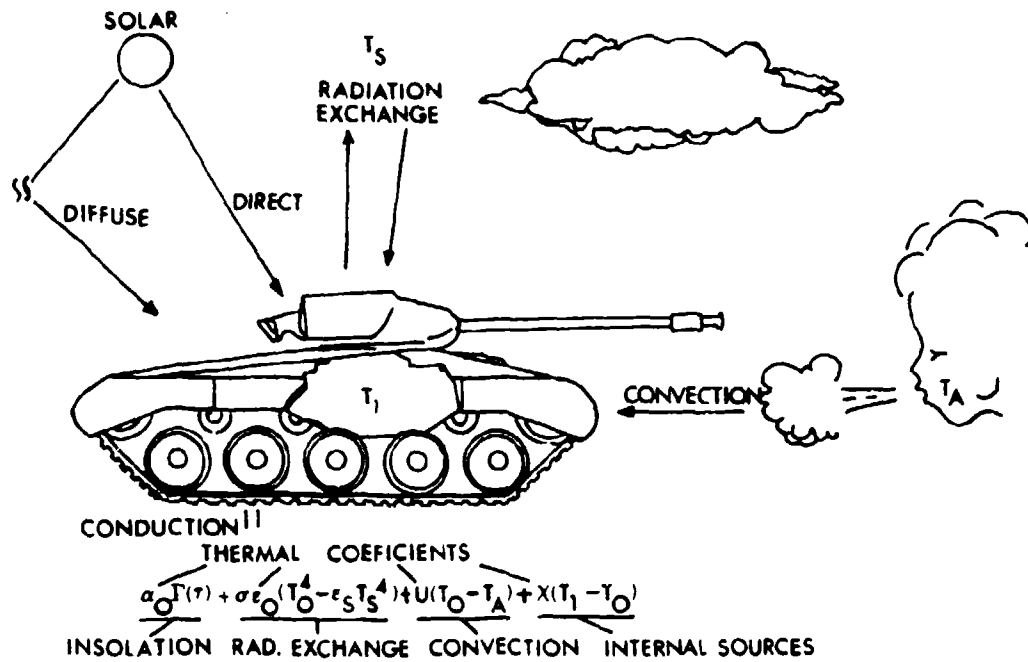


Fig. 2-9 — Factors to be considered in thermal modeling of a scene object

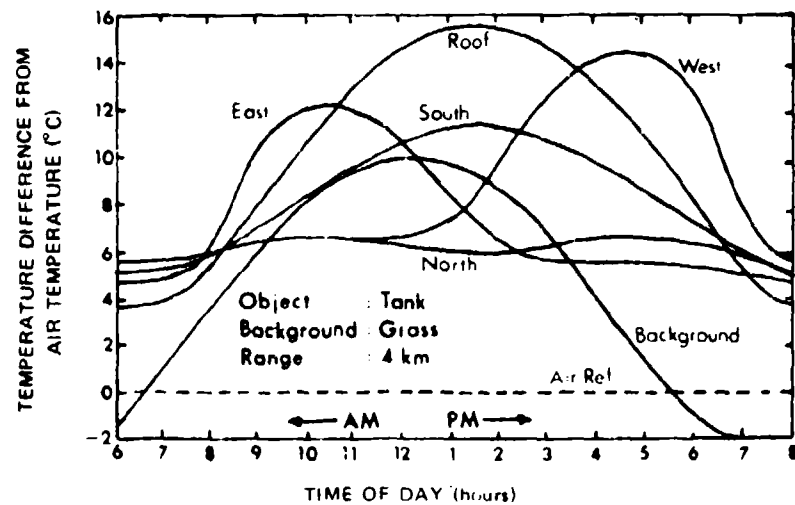


Fig. 2-10 — Temperature difference between a tank and air as a function of the time of day for various viewing directions

F. A. ROSELL

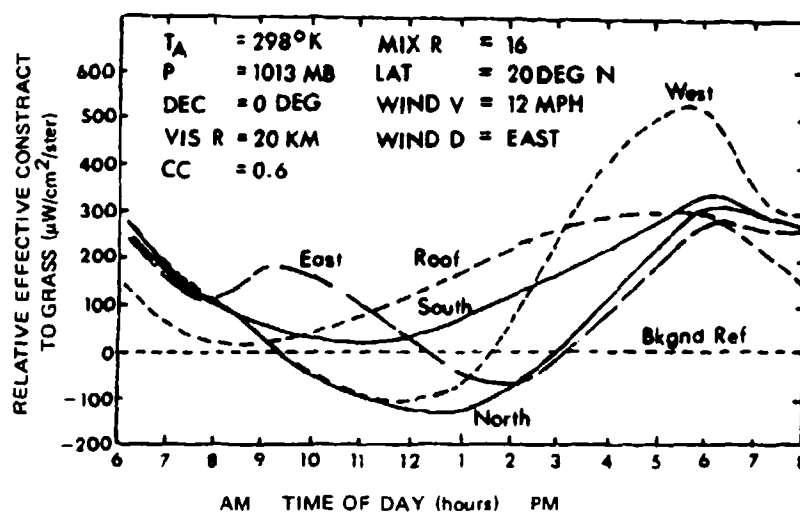


Fig. 2-11 — Effective radiant contrast between the tank and the grass background as a function of time of day for various viewing directions in the $8\text{-}12\text{ }\mu\text{m}$ spectral band

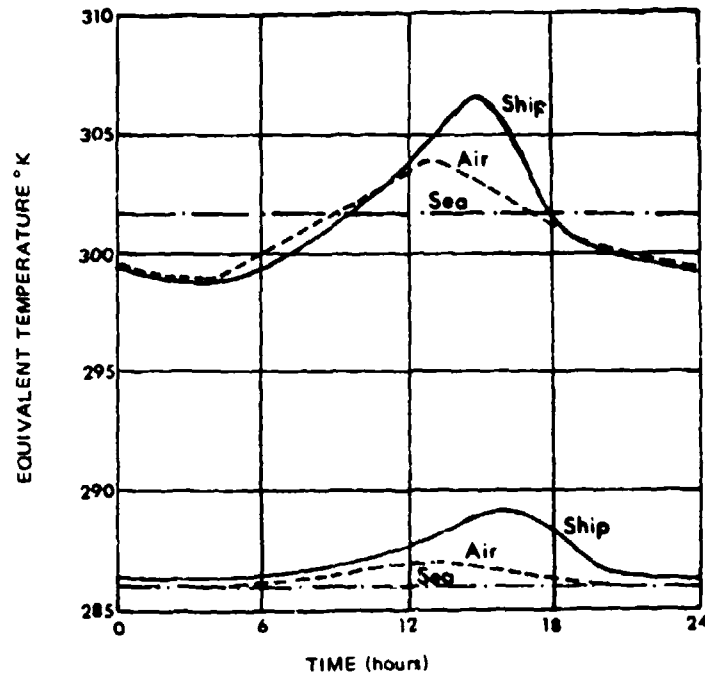


Fig. 2-12 — Equivalent temperature of a ship, the ambient air, and the sea in a semitropical and cold northern area vs time of day for a given set of operating conditions

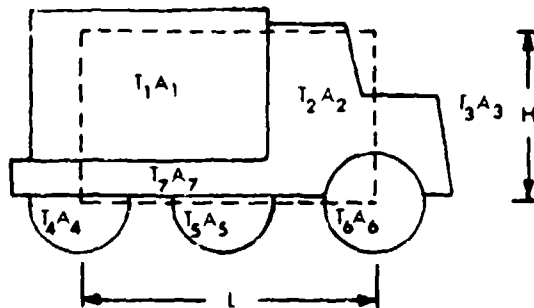


Fig. 2-13 — Geometrical considerations for the calculation of equivalent vehicle temperature and area

The thermal contrast of a ship against a sea and an air background is shown in Fig. 2-12 as a function of the time of day. The upper set of curves pertains to a semitropical warm sea. In the specific case analyzed, it can be seen that the ship can appear in positive or negative contrast relative to both the sea and the air. In the lower set of curves, a cold sea typical of the northern climes was assumed and for the specific case analyzed, the ship was always of positive contrast relative to the air and the sea. In making the above calculations the ships were assumed to be moving, there was a wind and partial cloud cover, and specific viewing angles were assumed. A stationary ship under a clear sky with no wind might be expected to undergo rather larger temperature excursions, but the same trends are expected.

E. EQUIVALENT TEMPERATURE DIFFERENCE

As noted above, the thermal signature of a scene object can be due to temperature differences, emissivity differences, and reflected radiation. To simplify calculations it is common to assume an equivalent object of unity emissivity and zero reflectivity because the sensitivity-resolution characteristics of a sensor are usually specified in terms of a minimum resolvable or detectable temperature difference vs angular spatial frequency. Another simplification which is often made is to average the temperature over the entire area of the scene object (Ref. 2-2). An example of a thermal signature of a truck is shown in Fig. 2-13. The truck is divided into *areas* A_i of substantially constant temperature T_i . Truck areas which are at the same temperature as the background are ignored. The approximate temperature of the whole truck for modeling purposes is taken to be

$$T_{ave} = \frac{\sum_i A_i T_i}{\sum A_i}$$

If we assume a uniform background at temperature T_B , the average truck temperature difference is

$$\Delta T_{ave} = T_{ave} - T_B$$

The equivalent truck is thus assumed to be a rectangle with the same area and a temperature difference ΔT_{ave} .

Some small areas of the truck may be very much hotter than some of the larger areas. Averaging dilutes the effect of the small hot areas, but this usually is not a modeling problem when the scene objects are fairly small relative to the field of view because the hot spots are smeared out by the sensor apertures and the eye can equally detect small hot objects and larger but cooler objects so long as the incremental signal integrated over the object areas are the same. At closer ranges, localized hot spots such as stacks on a ship which are otherwise of small extent may be of significant aid in detection and in recognition.

The minimum resolvable and detectable temperature differences are ordinarily measured using a 300 K background. If the scene object temperature differences are small and the background is approximately 300 K, the ΔT_{ave} approximation for the actual scene object radiance may be used. In other cases, the actual incremental radiance must be calculated because ΔT and the incremental radiance are not linearly related.

NRL REPORT 8311

REFERENCES

- 2-1 R.F. Higby and R.H. Daumit, Gaining Thermal Signature Insight Through Computer Simulation, Proc. Iris Imaging Specialty Group, June 1978 meeting.
- 2-2 J.A. Ratches, Static Performance Model for Thermal Imaging Systems, Optical Engineering, Vol. 15, No. 6, Nov-Dec 1976.
- 2-3 "Quantitative Thermal Signatures of Small Craft in Destin, Florida Coastal Waters for Maritime Search and Rescue," F. Zegel, W. Stump, S. Rodak, and P. Stamoulas, NV&EOL Report, July 74 (Unclassified).
- 2-4 "Thermal Signature Measurements of Four US Army Field Portable Power Generators," S. Rodak, F. Zegel and W. Stump, NV&EOL Report, August 1975 (Unclassified).

Chapter III

ATMOSPHERIC EFFECTS ON INFRARED SYSTEMS

*J.B. Goodell
R.E. Roberts*

A. INTRODUCTION

The atmosphere is an important, integral factor in the analysis and design of infrared (IR) systems. The spectral location of the atmospheric windows, for example, restricts the choice of materials for detectors and optics. Furthermore, within these windows, poor visibility substantially degrades the operation of IR imaging systems operations. On clear days of high absolute humidity, IR systems of equivalent sensitivity usually operate better in the 3-5 μm window, while hazy or limited visibility conditions generally favor operation in the 8-12 μm window. The atmosphere is undoubtedly one of the most important factors controlling the performance characteristics of FLIR devices and certainly must be taken into account both in the optimal choice of spectral bands and IR systems design.

This chapter provides the reader with a brief review and assessment of the LOWTRAN 3b* propagation code (Ref. 3-1) for evaluating atmospheric transmission and contains convenient computer-based tables derived from LOWTRAN 3b giving atmospheric contrast transmittances averaged with respect to a 10°C blackbody over the 3-5 and 8-12 μm atmospheric windows. From a knowledge of the local meteorological conditions (temperature, relative humidity or dew point, and visual range) the reader can simply and directly compute the transmittances corresponding to a selected range.

The chapter begins with a brief discussion of the main absorbing gases. It continues with a more detailed exposition of aerosol extinction together with an assessment of the aerosol modeling uncertainties. Following this is a description of the LOWTRAN 3b computer program for computing atmospheric transmittances as developed at the Air Force Geophysics Laboratory, Cambridge, Mass. It is currently the most widely accepted standard for computing atmospheric propagation and forms the basis for the data in this chapter. The model, however, does not include important man-made aerosols such as battlefield smoke and dust which are beyond the scope of this chapter. Detailed procedures for determining atmospheric attenuation from tables computed using LOWTRAN 3b conclude the chapter.

This chapter purposely avoids detailed expositions of meteorological variables such as seasonal variations of pressure and temperature, or the relative merits of different atmospheric models beyond LOWTRAN 3b. Nor does it include detailed discussions of molecular band absorption theory. The literature contains voluminous theory and data concerning all these topics which, of course, are crucial to atmospheric transmittance. The reader who wishes to probe deeper can consult references 3-2 to 3-42.

*LOWTRAN 4, which has provisions for calculating the radiance from atmospheric paths, is now available as a card deck from the National Climatic Center, Federal Building, Asheville, NC 28801 for a charge of \$20.00. (Address requests to Mr. R. Davis.) The transmittance portion of LOWTRAN 4 is essentially the same as LOWTRAN 3b.

B. ATMOSPHERIC MOLECULAR CONSTITUENTS

1. Water Vapor

Water vapor is the most important absorbing gas in the earth's atmosphere for infrared transmission and also the most variable. Local humidity conditions can easily double the water vapor content in the atmosphere in any locale in a matter of hours with a changing weather front, thus severely degrading the infrared imaging systems performance expectations (Ref. 3-43). Moreover, water vapor absorption primarily determines the atmospheric windows as Fig. 3-1 shows. For clear conditions these atmospheric windows vary in transparency primarily in response to the water vapor content. A dry (midlatitude winter) atmosphere (e.g. 3.5 g/m^3) is almost completely transparent in the windows. A wet tropical atmosphere (19 g/m^3) on the other hand almost completely blocks large portions of the atmospheric windows. Table 3-1 illustrates typical water content for various atmospheric models as given in the Air Force Geophysical Laboratories tabulation (Ref. 3-44).

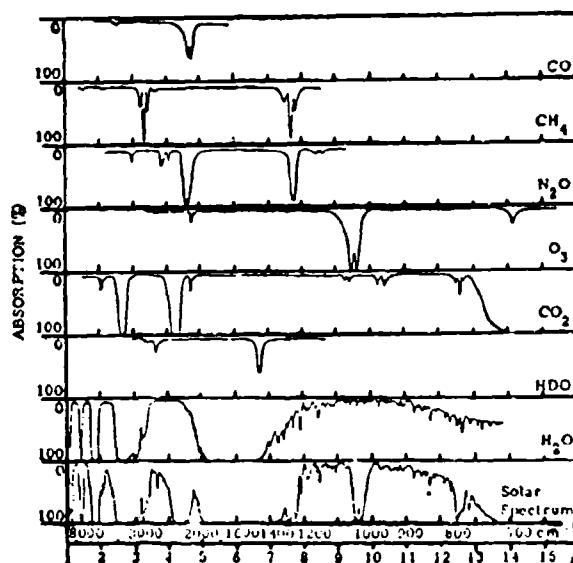


Fig 3-1 — Constituent absorption bands and atmospheric windows

Table 3-1 — Water Vapor Density (g/m^3) in the Atmosphere at Various Levels for Several Atmospheric Models

Alt (km)	Atmospheric Model					
	Tropics	Midlat. Summer	Midlat. Winter	Subartic Summer	Subartic Winter	U.S. Std.
0	19	14	3.5	9.1	1.2	5.9
1	13	9.3	2.5	6.0	1.2	4.2
2	9.3	5.9	1.8	4.2	0.94	2.9
3	4.7	3.3	1.2	2.7	0.68	1.8

Water vapor absorption occurs in two forms, molecular band absorption and continuum absorption. Very complex spectra characterize molecular absorption. Literally hundreds of vibration-rotation energy level transitions create the water vapor absorption bands. Figure 3-2 is a moderately high-resolution spectrum of water vapor in the spectral region from 5 to 7.69 μm . The water vapor continuum on the other hand has essentially a smooth spectral dependence and is present in both the 3-5 μm and 8-12 μm windows. A recent review (Ref. 3-45) of the 8-12 μm continuum absorption indicates that the contribution due to pure water vapor is quantitatively well understood both with respect to the spectral dependence between 8-12 μm as well as to the strong and important temperature dependence of that absorption. The only remaining uncertainty for this particular continuum absorption arises from the nitrogen-broadened portion of the water continuum. The overall contribution from this term is, however, small, and its effect on the uncertainty of FLIR performance is negligible.

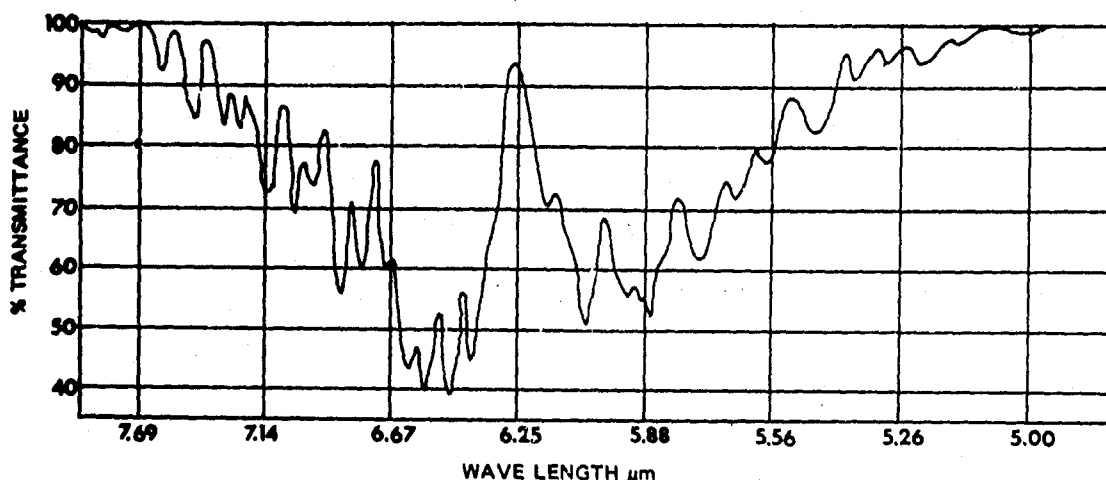


Fig. 3-2 — Moderate resolution H_2O spectrum, 5-7.69 μm

Much less is known about the 3-5 μm continuum. A best estimate for the extinction coefficient β_{cont} is $0.04\text{km}^{-1} \pm 0.04$ (Ref. 46-48). These values may be overly pessimistic for the 3-5 μm window since the water vapor continuum coefficient appears to attain its largest value near 4 μm . The relatively large uncertainty, of 0.04 km^{-1} , however, should not affect FLIR systems performance significantly although a possible exception may be long-range ship recognition which can be dominated by clear but humid transmission paths.

2. Carbon Dioxide CO_2

Carbon dioxide, unlike water vapor, has a constant weight ratio in standard atmospheres. Local perturbations such as automobile exhaust, dense foliage, and factory exhausts can, of course, alter the "standard" distribution.

Carbon dioxide is second in importance to water vapor in terms of infrared absorption in the clear atmosphere. It closes the 3-5 and 8-12 μm spectral windows. Figure 3-1 shows the carbon dioxide spectra together with the atmospheric spectra and those of other gases.

* β_{cont} , the extinction coefficient equals $-(\ln \tau)/R$, where τ is the transmittance and R is the range.

3. Nitrous Oxide (N_2O)

Nitrous oxide has an approximately constant concentration in the atmosphere. It has a strong absorption band, at about $4.5 \mu m$ and at about $8 \mu m$, otherwise its absorption is insignificant (see Fig. 3-1).

4. Methane (CH_4)

Methane has an approximately constant concentration in the atmosphere and generally occurs in small amounts except over swamps (marsh gas) where large quantities increase atmospheric absorption noticeably in two narrow infrared bands centered around 3.5 and $8 \mu m$ (see Fig. 3-1).

5. Ozone (O_3)

Ozone has a variable distribution in the earth's atmosphere. Solar ultraviolet dissociation of O_2 molecules causes O_3 concentration to peak at a height of about $24 km$. The very strong O_3 $9.6\text{-}\mu m$ absorption spike attenuates noticeably over long sea level paths in spite of the very small sea level ozone concentration (see Fig. 3-1). Normally, however, FLIR operation does not experience difficulty with the O_3 , $9.6\text{-}\mu m$ band.

6. Carbon Monoxide (CO)

Carbon monoxide has a nearly constant concentration in the atmosphere except where increased by pollutants, such as exhausts. Concentrations of carbon monoxide cause atmospheric absorption in a band between 3.6 and $3.8 \mu m$ (see Fig. 3-1).

7. Nitrogen (N_2)

The concentration of nitrogen in the earth's atmosphere is about 78.088 percent by volume. Nitrogen affects atmospheric transmission primarily through the nitrogen continuum in the $3\text{-}5 \mu m$ window.

8. Oxygen (O_2)

Molecular oxygen comprises 20.949 percent by volume in the earth's atmosphere. O_2 absorption should not be confused with O_3 (ozone) absorption which is strong at $9.6 \mu m$. Oxygen band absorption is negligible in the $3\text{-}5$ and $8\text{-}13 \mu m$ windows.

Table 3-2 shows the concentrations of the principal absorbing gases in the earth's atmosphere. The compositions are percent by volume. In a model atmosphere all important spectroscopic gases except H_2O and O_3 have nearly constant concentrations. The composite absorption of all these gases produces the results shown in Fig. 3-3, which is a transmission spectrum measured by Yates and Taylor over 5.5 and $16.25 km$ horizontal atmospheric paths.

Table 3-2 — Composition of the Atmosphere

Constituent	Percent by Volume	Constituent	Percent by Volume
Nitrogen	78.088	Krypton	1.14×10^{-4}
Oxygen	20.949	Nitrous Oxide	5×10^{-5}
Argon	0.93	Carbon Monoxide	20×10^{-5}
Carbon Dioxide	0.033	Xenon	8.6×10^{-6}
Neon	1.8×10^{-3}	Hydrogen	5×10^{-6}
Helium	5.24×10^{-4}	Ozone	variable
Methane	1.4×10^{-4}	Water Vapor	variable

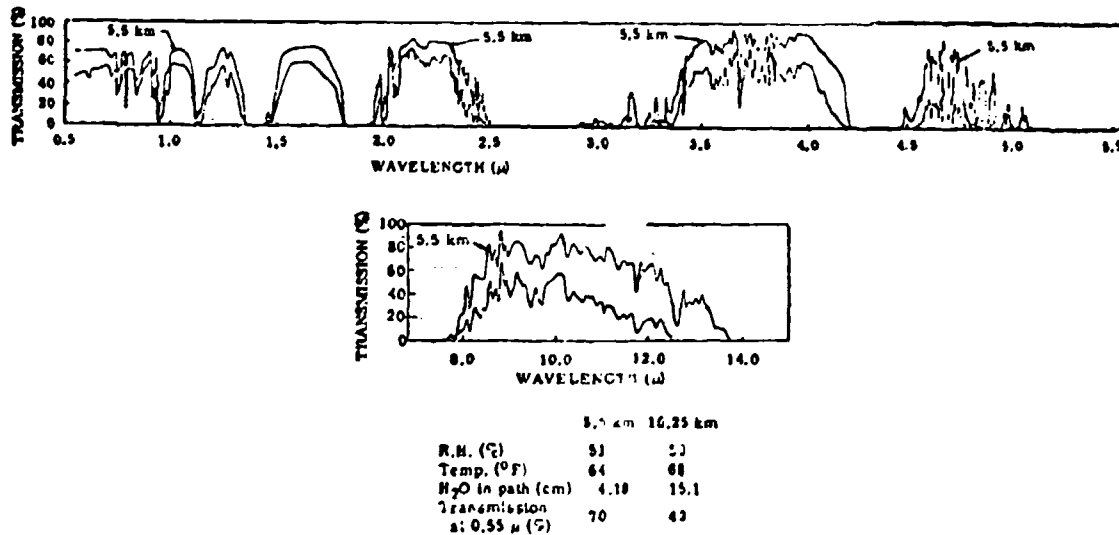


Fig. 3-3 — Atmospheric transmission at sea level over 5.5 and 16.25 km paths

C. AEROSOLS

The atmosphere also contains suspended particles such as dust, carbon particles, sand, ashes, water droplets, salt spray, and the like whose sizes and concentrations depend on local environments and can, therefore, vary not only with locale but temporally within a locale. Typical aerosol radii range from about $5 \times 10^{-3} \mu\text{m}$ up to about $20 \mu\text{m}$. Their number density can vary from almost zero up to about $10^5/\text{cm}^3$. The main contributors to aerosols are: sea spray; fog; haze; dust storms; and air pollution. Other contributors include forest fires, sea salt, rocks, soil, volcanos, meteoric dust, and biological materials.

Particulate extinction, especially the aerosol effects associated with limited visibility conditions, undoubtedly causes the largest uncertainty in the modeling of propagation for electro-optical systems. LOWTRAN 3b, for example, currently adopts three aerosol models applicable for low-altitude use (Ref. 3-1). Two of these are suggested for usage over land and are referred to as the urban and rural models. For the computation of extinction coefficients these models are nearly the same. The third low-altitude model employed on LOWTRAN 3b is

GOODELL AND ROBERTS

referred to as maritime. Also, for poor seeing conditions, such as visual ranges of 2 km or less, LOWTRAN 3b adopts a stopgap measure which amounts to equalizing the attenuation in all spectral bands. The equal attenuation aerosol methodology leads to a pessimistic result for the IR attenuation and in a sense, provides a lower bound to an expected infrared performance range. Such a spectrally flat extinction coefficient, however, may not be justified. Experiments with fogs and clouds as well as calculations based upon assumed particle distributions indicate that although the 3-5 μm attenuation is roughly that of the visible band, the 8-12 μm extinction is typically one half that of the other band. Thus an equal attenuation assumption can lead to extremely pessimistic predictions for 8-12 μm systems performance. This obviously has strong implications on the selection of an optimal spectral band for IR sensors (*i.e.*, 3-5 vs 8-12 μm).

The rural and urban models have gained widespread use for central European environments, particularly for the limited visibility conditions so often encountered during the winter months. They may not, however, be appropriate for limited visibility conditions. A misleading consequence of the use of these two models in any such application is that they tend to predict optimistic values of infrared transmission. For example, the urban and rural aerosol models predict higher transmissions in either the 3-5 or 8-12 μm bands than would be measured. These models tend to give optimistic results for IR propagation because of the low number density of large particles.

The maritime model particle distribution has a relatively higher concentration of large particles which is typically characteristic of hazes and fogs. Since optical properties used in generating the maritime model are very nearly those of liquid water again as found in continental fogs and hazes, the maritime model is most appropriate not only for oceanic environments but also for continental environments for fogs and hazy visibility conditions (Ref. 3-49). This statement tends to be borne out not only by theory in terms of what distributions are expected to look like for such conditions but also in terms of a comparison with the existing experimental data base for poor visibility conditions. If one is to adopt aerosol methodologies directly from the LOWTRAN 3b code, it is advisable to employ the maritime model both for at-sea use as well as for over land usage under poor seeing conditions. As one would expect, the application of the maritime aerosol algorithm is not nearly so optimistic for the infrared spectral bands as would be the case for the previous continental models. LOWTRAN is an evolutionary model which changes as the data base grows.

Most current aerosol models suffer considerably from reliance upon a single representative particle size distribution. The current LOWTRAN 3b aerosol models as discussed above use measured optical properties (representative of average continental, rural, urban, or maritime conditions) with a single assumed distribution to predict, via a Mie computation, a scaling model for the extrapolation of the visual range to IR transmission. The underlying assumption is that for a particular environment, such as a continental haze, the shape or functional form of the distribution remains unchanged. In many, if not most, cases this is not a valid representation. For example, in an evolving fog formation the water droplet distribution tends to change in the sense that there are relatively more large particles as the visibility becomes lower. Figure 3-4, which shows some representative particle size distributions for hazes and fogs from the recent Grafenwöhr field measurements (Ref. 3-50), illustrates this dramatically. Each of these distributions leads to a different spectral dependence for the aerosol extinction coefficient.

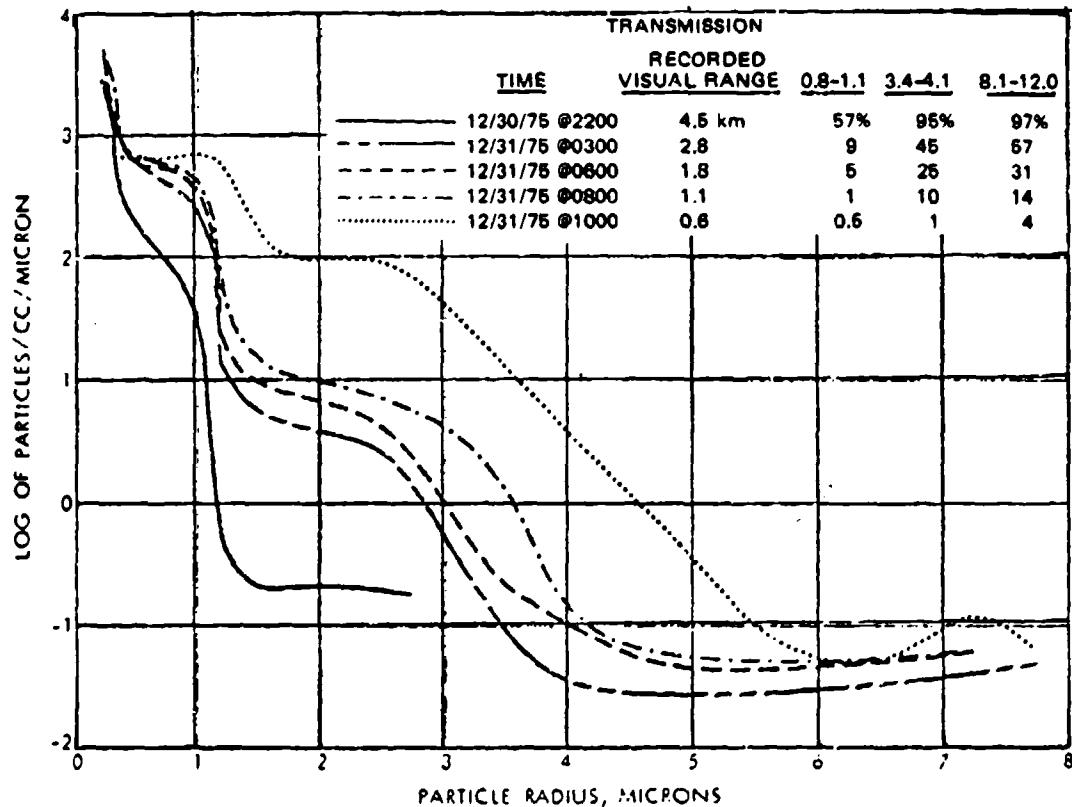


Fig. 3-4 — Change in aerosol droplet size as fogs build, December 30-31, 1975, at Grafenwöhr

A potentially useful method (Ref. 3-49) which is aimed at obtaining information directly related to IR propagation without reliance upon a single assumed distribution is the concept of correlating infrared propagation with the integrated liquid content along the transmission path. This approach has two advantages. First, it is insensitive to the shape or form of the assumed distribution. Second, it permits a remote measurement along the preferred line of sight (rather than a local measurement such as humidity, temperature, etc.) with, for example, a laser ranging system such as LIDAR for determining liquid content; thereby implying IR propagation directly on a real-time basis. Such a methodology can also be used to derive general scaling relationships between visibility statistics and propagation in other spectral bands. The relationships derived thus far, however, are not linear in the sense that LOWTRAN 3b is, and predict more general functional relationships between the IR and the visual bands.

Figure 3-5 illustrates that there is indeed a strong correlation of IR extinction by aerosols with the liquid content. The points are representative of the different distributions summarized by the recent review article of Tomasi and Tampieri (Ref. 3-51). The relative placement of the Grafenwohr measurements and LOWTRAN 3b maritime and rural cases are also shown. The points located toward the upper right corner are indicative of limited visibility conditions.

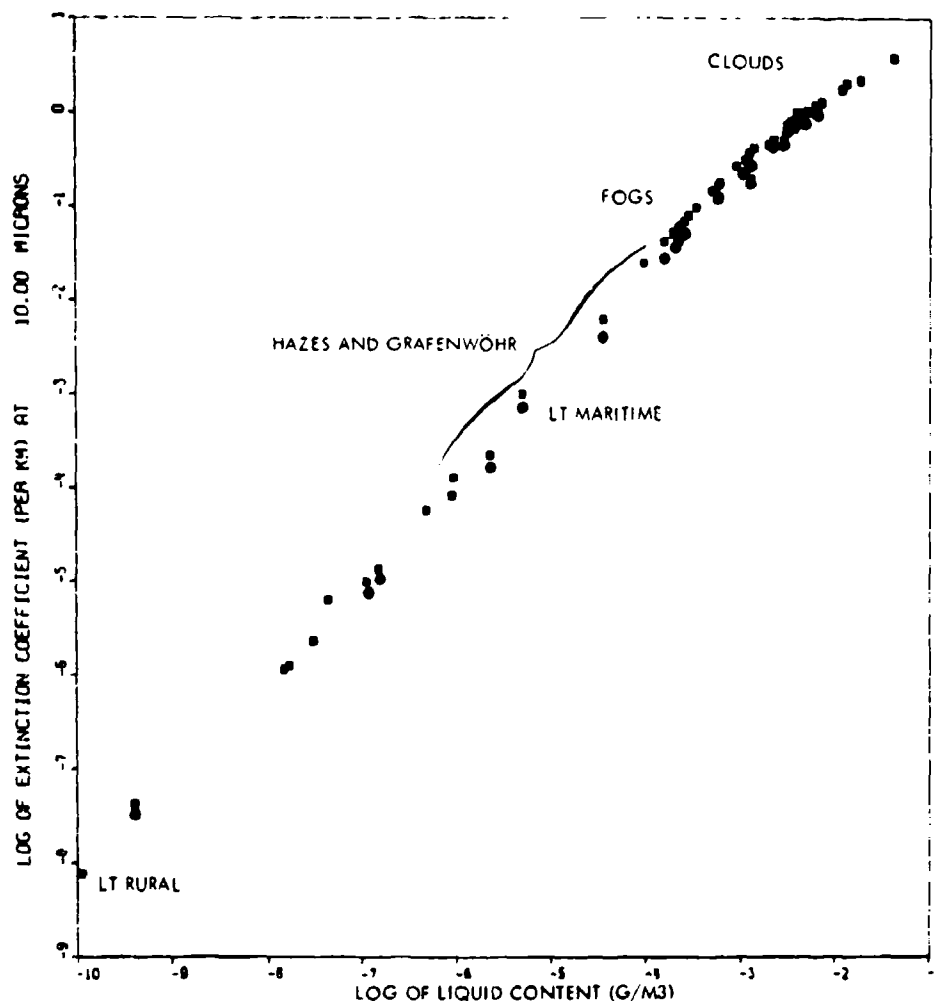


Fig. 3-5 — Correlation of 10- μ m extinction coefficient with liquid content. The distributions have been normalized to a total number density of one particle per cubic centimeter.

Most of our propagation models rely upon meteorological inputs as a driving parameter. For example, in the case of LOWTRAN 3b one uses an estimate of the visual range to imply multispectral aerosol effects. There is a serious problem in using such a meteorological parameter for estimating propagation either in IR channels or in the visible channels. The first problem is associated with the subjectivity of an observer making the observation. It is well known that different observers or even the same observer on different days can obtain drastically different results for the visual range under similar conditions. Secondly, an estimate of the visual range is usually at best a local measurement determined by a particular line of sight which the observer happens to take. In many cases this has little, if any, resemblance to the application being made. This is due to the vertical inhomogeneities associated with atmospheric aerosols. For example, an observer making a ground-based visual range estimate can obtain a result for the extinction which is orders of magnitude different from a similar estimate that might be made from a balloon-borne platform. Figure 3-6, again based upon the Grafenwöhr data base, illustrates this point dramatically.

NRL REPORT 8311

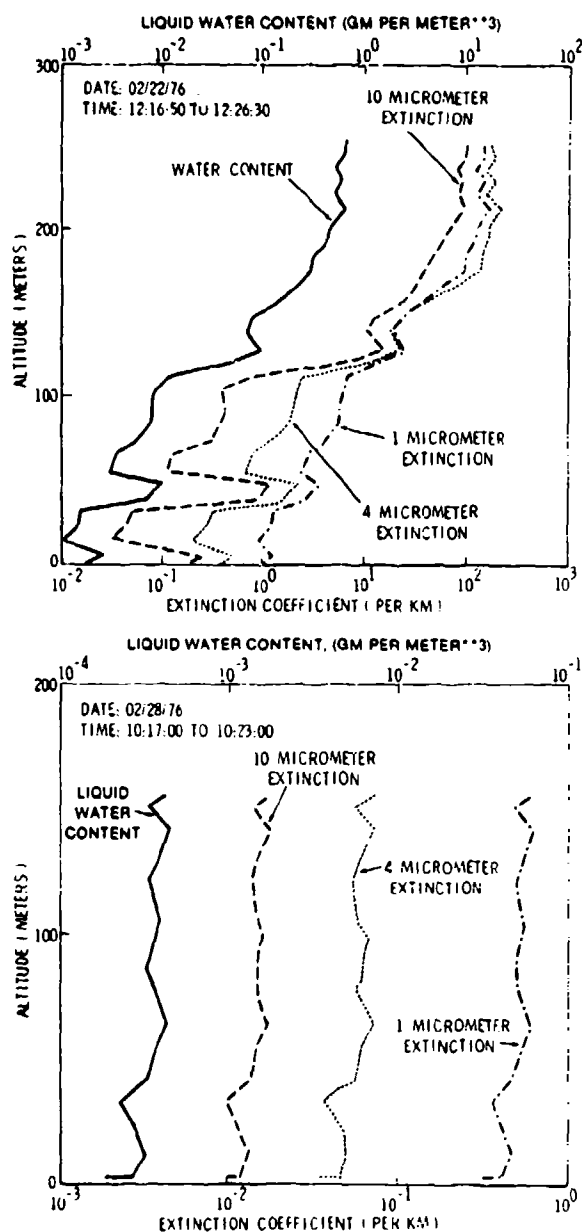


Fig. 3-6 — Effect of altitude upon the extinction coefficient of aerosols for limited visibility conditions

Sections B and C have reviewed and placed in perspective the three major categories of atmospheric transmission. It is fair to say that the first category, namely molecular absorption by the uniformly mixed gases, is fairly well understood. It also is apparent that the water vapor continuum from an engineering standpoint is fairly well understood in the 8-12 μm band but has a much larger discrepancy associated with it in the 3-5 μm band. Measures to remove this discrepancy are under way in several government laboratories. Finally, the largest problem that

we have in modeling the weather propagation effects for electrooptical (EO) sensors is associated with our uncertainties in the aerosol environment.

D. ATMOSPHERIC TRANSMISSION AND EXTINCTION

1. Transmission

When the gas quantities are known, the atmospheric transmittance over the corresponding line of sight path can be determined from the spectral absorption properties of the gases. The composite atmospheric transmittance is usually approximated by multiplying the transmittances of each separate component, averaged over some very narrow spectral band. Thus the average atmospheric transmittance over a line of sight path in a narrow spectral band is generally written as

$$\tau_A = \tau_{1A} \tau_{2A} \dots \tau_{NA},$$

where τ_1, \dots, τ_N are the transmittances of the individual absorbing species averaged over the narrow spectral band. The line of sight path determines the quantity of gas to be inserted into each individual τ .

In general, the calculation of the τ 's is very detailed and tedious because of the extreme complexity of the molecular spectra.

2. Extinction

For very narrow spectral intervals (essentially spectral lines) and/or weak wavelength dependence, Beer's Law, namely,

$$\tau = \exp(-\beta_{aim} R),$$

provides a useful approximation to atmospheric transmission. β_{aim} is the "extinction coefficient" associated with the composite atmospheric transmission, and R is the range, usually in kilometers. The approximation is generally fair for aerosol particles and the water vapor and nitrogen continua all of which display weak wavelength dependences.

The concept has two advantages for IR imaging system analysis. The first is that for an atmospherically limiting environment the range performance (such as detection or recognition range) for a given system directly relates to $1/\beta_{aim}$. Thus a doubling of the extinction coefficient degrades range performance by roughly half. A relative uncertainty in the extinction coefficient $d\beta_{aim}/\beta_{aim}$ produces a comparable uncertainty in the performance range, namely, dR/R .

The second advantage is that β_{aim} can be separated into various components, for example, $\beta_{mul}, \beta_{cont}, \beta_{aer}$, the extinction coefficients due to molecular band absorption, gas continuum absorption, and aerosol attenuation. This form provides a convenient mechanism for discussing the effects due to the dominant species, namely, continuum and aerosols.

Used with discretion and an understanding of its limits of validity, the concept of extinction provides useful insights into atmospheric influences on IR imaging system performance.

E. LOWTRAN COMPUTER PROGRAM

1. General Description

Many available computer programs today compute atmospheric transmittance over arbitrary slant paths from temperature, pressure, gas and aerosol lapse rates, and spectral line strength data. Most of them provide satisfactory values. Many are still evolving as new information advances the state of the art. Most of them are too complex for field use.

The LOWTRAN 3b computer program which forms the basis for the transmittance tables in this chapter was developed at the Air Force Geophysics Laboratory (AFGL) by J.E.A. Selby and R.A. McClatchey. LOWTRAN 3b predicts atmospheric transmittance along slant paths in the wavelength region from 0.25 to 28.5 μm . The LOWTRAN 3b program contains approximately 2000 cards. The program allows a choice of one of six model atmospheres or direct inputs of measured atmospheric data. LOWTRAN 3b includes the following atmospheric absorbing molecular species as discussed in Sections B and C.

1. Water vapor from 0.690 to 28.57 μm .
2. Uniformly mixed gases including CO_2 , N_2 , CH_4 , CO , and O_2 . Absorption is calculated in two bands: 1.241 to 20.00 μm ; 0.758 to 0.771 μm .
3. Ozone from 3.05 to 17.39 μm .
4. The N_2 continuum from 3.65 to 4.81 μm .
5. The water vapor continuum from 7.14 to 14.93 μm .
6. Ozone between 0.43 and 0.77 μm (the visible) and wavelengths shorter than 0.36 μm .

2. LOWTRAN 3b Aerosol Methodology

Although there are many gross uncertainties (as discussed in Section C) involved in the assessment of bad weather aerosol effects upon IR systems, one can at least develop a qualitative if not semiquantitative understanding of weather-sensor relationships by using the straight-forward aerosol models contained in the LOWTRAN 3b code. The assumptions embodied in this particular transmission algorithm ultimately lead to a set of fixed linear relationships between the subjective visibility estimate, V , and extinction in other spectral regions according to:

$$\beta_{\text{aer}}(\lambda) = C_{\lambda} \beta_{\text{aer}}(0.55\mu\text{m}).$$

where C_{λ} is determined via a Mie scattering calculation based upon a single representative size distribution and a set of optical properties. A different C_{λ} is obtained for the so-called maritime, urban, and rural cases. β_{aer} is in turn related to the visual range, V , with the well-known Koschmieder relationship:

$$\beta_{\text{aer}}(0.55\mu\text{m}) = 3.91/V,$$

derived using a 2% contrast requirement.

GOODELL AND ROBERTS

Since C_A for the LOWTRAN 3b program displays only a weak variation with λ over the 3-5 and 8-12 μm bands it is possible to describe the LOWTRAN 3b maritime, rural, and urban models quite simply and accurately with the following formulas.

Maritime:

$$\beta_{aer}^{3-5\mu\text{m}} = 2.24/V,$$

$$\beta_{aer}^{8-12\mu\text{m}} = 0.85/V.$$

Rural:

$$\beta_{aer}^{3-5\mu\text{m}} = 0.42/V,$$

$$\beta_{aer}^{8-12\mu\text{m}} = 0.43/V.$$

Urban:

$$\beta_{aer}^{3-5\mu\text{m}} = 0.60/V,$$

$$\beta_{aer}^{8-12\mu\text{m}} = 0.41/V.$$

The aerosol transmission factor is then obtained in a straightforward fashion via

$$\tau_{aer} = e^{-\beta_{aer} R}.$$

In light of the criticisms raised in Section C one would be well advised to use (within the context of the LOWTRAN 3b code) the maritime model for continental limited visibility (4 km) environments as well as oceanic conditions.

F. ATMOSPHERIC TRANSMISSION TABLES

1. Description

The atmospheric transmission tables in this chapter use spectrally weighted transmittances calculated from LOWTRAN 3B in two important atmospheric windows, 3-5 and 8-12 μm . The spectral contrast weighting produces the average transmittance of radiation from a blackbody source at 10°C in each of the two windows according to the formula,

$$\tau_{aim} = \frac{\int_{\Delta\lambda} \tau_{sys} \tau_{aim} \frac{\partial W}{\partial T} \lambda d\lambda}{\int_{\Delta\lambda} \tau_{sys} \frac{\partial W}{\partial T} \lambda d\lambda},$$

where τ_{sys} is an instrument function equal to unity over the spectral range included in the integration, and zero elsewhere, W is the blackbody function, T is temperature, and λ is the wavelength. Tables 3-3 through 3-10 include transmission data for horizontal line of sight ranges in factor of two increments from 0.5 to 32 km, dew point values from -20° to 40°C, in 5-deg steps, and temperature values (8-12 μm window only) from -20° to 40°C.

Transmittance values in the tables are due only to molecular band and continuum absorption. They do not include aerosol scattering which is computed separately.

2. Atmospheric Transmittance Determination

The tables require three inputs:

- Range
- Dew Point
- Temperature

NRL REPORT 8311

and also requires a measured visual range in order to assess aerosol effects. When these are known, use the following steps to determine atmospheric transmittance.

1. Select the range.
2. Choose the table corresponding to range and spectral region. (In the 3-5 μm window there is only one table for all ranges.)
3. Find the dew point column corresponding to the measured dew point temperature.
4. (8-12 μm) Go down the column to the proper temperature.
5. (3-5 μm) Go down the column to the proper range. Read the transmittance and go to step 6. (This is the "infinite visibility" transmittance.)
6. Compute the aerosol transmittance from the formula:

$$\bar{\tau}_{\text{aer}} = \exp(-\beta R),$$

where R is the selected range, V is the measured visual range, and

$$\beta = \begin{cases} \frac{0.85}{V} & \text{(8-12 } \mu\text{m band)} \\ \frac{2.24}{V} & \text{(3-5 } \mu\text{m band).} \end{cases}$$

7. Multiply the results of step 5 by the results of step 6 to complete the process.

3. Conversions

Relative humidity from absolute humidity (or use Fig. 3-7)

$$R_H = \frac{A_H \times T_a}{288.9P},$$

where

R_H is relative humidity

T_a is air temperature (K)

A_H is absolute humidity (g/m)

P is vapor pressure of water (use Table 3-11) (mm of Hg)

Dew point to absolute humidity

$$A_H = A \exp(18.9766 - 14.9595A - 2.4388A^2) \text{ g/m}^3$$

$$A = \frac{273.15}{273.15 + T_{dp}}$$

T_{dp} is dew point ($^{\circ}\text{C}$)

Torr to absolute humidity

$$A_H = \frac{1.05821}{1 + 0.0036t} P_{\text{Torr}} \text{ g/m}^3$$

t is air temperature ($^{\circ}\text{C}$)

Note that there is little difference between A_H and P_{Torr} for ambient conditions.

Examples

For a local temperature of 10°C, a dew point temperature of 5°C, and a visual range estimated to be 4 km, find the atmospheric transmittance over an 8 km horizontal path.

1. 8-12 μm Window

From Table 3-8, the "infinite visibility" transmittance is 0.445. The aerosol transmittance corresponding to the maritime model value of 0.85/V.R. for the 8-km path is 0.180. The composite atmospheric transmittance therefore is 0.081.

2. 3-5 μm Window

Temperature data is unnecessary in this window. From Table 3-3, the "infinite visibility" transmittance corresponding to a 5°C dew point temperature and an 8 km range is 0.260. From the maritime model, the aerosol transmittance corresponding to the extinction coefficient, $2.24/V$ is 0.011. The composite atmospheric transmittance is therefore 0.003.

3. Range Interpolation, 8-12 μm Window

For the same temperature (10°C), and dew point temperature (5°C), and visual range of 15 km, find the atmospheric transmittance over a 10-km path. The tables do not include values for 10 km so an interpolation is required. This example uses a *linear* interpolation.

From Table 3-8 the "infinite visibility" transmittance corresponding to an 8-km path is 0.445. From Table 3-9 the "infinite visibility" transmittance corresponding to a 16-km path is 0.234. The linear interpolation formula therefore is

$$\tau_{10km} = \tau_{8km} + \frac{\tau_{16km} - \tau_{8km}}{16km - 8km} (10km - 8km)$$

$$= 0.445 - 2 \times 0.211/8 = 0.392.$$

The aerosol transmittance, using the maritime model value of $0.65/V$, is 0.567 for a visual range of 15 km. The composite transmittance is therefore

$$0.567 \times 0.392 = 0.222.$$

The linear interpolation is simple and produces reasonable accuracy. It can be applied to interpolations between dew point temperatures, temperatures in the 8-12 μm window, and ranges in the 3-5 μm window.

4. 3-5 μm Transmittance Nomogram

Figure 3-8 is a transmittance nomogram prepared from the data in Table 3-3. It applies only to transmittance in the 3-5 μm band. The very high correlation between the logarithm of the negative logarithm of the transmittance and the logarithm of the range allows Figure 3-8 to predict transmittances in good agreement with those of Table 3-3.

NRL REPORT 8311

To use Figure 3-8 to predict atmospheric transmittance in the 3-5 μm band, lay a straight edge on the correct dew point temperature and the range. Read the transmittance where the straight edge intersects the transmittance column.

The nomogram also provides dew point temperature given range and transmittance, or range given dew point temperature and transmittance. Simply lay the straight edge on the two known quantities and read the third quantity where the straight edge intersects the corresponding column.

Table 3-3 - 3-5 μm Weighted Molecular Transmission
for Target Temperature of 10°C

Range (km)	T_{dp} (°C)												
	-20	-15	-10	-5	0	5	10	15	20	25	30	35	40
.5	.740	.725	.708	.689	.667	.644	.620	.595	.569	.542	.514	.487	.459
1.0	.683	.663	.640	.615	.589	.562	.533	.504	.474	.445	.417	.388	.359
2.0	.611	.585	.557	.529	.498	.467	.436	.405	.375	.345	.316	.288	.261
4.0	.524	.494	.463	.430	.397	.365	.333	.303	.273	.246	.220	.194	.170
8.0	.424	.391	.357	.324	.291	.260	.231	.204	.179	.155	.133	.111	.091
16.0	.314	.281	.248	.217	.189	.164	.140	.118	.098	.080	.063	.048	.035
32.0	.207	.177	.150	.126	.105	.086	.069	.054	.041	.029	.020	.013	.008

Table 3-4 - 8-12 μm Weighted Molecular Transmission for
Target Temperature of 10°C and Path Length $R = 0.5$ km

T_o (°C)	T_{dp} (°C)												
	-20	-15	-10	-5	0	5	10	15	20	25	30	35	40
-20	.971												
-15	.971	.965											
-10	.972	.966	.958										
-5	.972	.965	.959	.948									
0	.972	.967	.959	.948	.933								
5	.973	.967	.960	.950	.935	.912							
10	.973	.968	.961	.951	.936	.915	.882						
15	.973	.968	.961	.952	.938	.919	.887	.840					
20	.973	.968	.962	.952	.939	.920	.891	.847	.780				
25	.974	.969	.962	.953	.940	.922	.895	.853	.790	.699			
30	.974	.969	.962	.954	.941	.924	.898	.858	.799	.713	.594		
35	.974	.969	.963	.954	.942	.926	.901	.863	.807	.725	.612	.468	
40	.974	.969	.963	.955	.943	.927	.903	.868	.815	.737	.628	.489	.333

GOODELL AND ROBERTS

Table 3-5 — 8-12 μm Weighted Molecular Transmission for
Target Temperature of 10°C and Path Length $R = 1 \text{ km}$

T_a (°C)	T_{dp} (°C)												
	-20	-15	-10	-5	0	5	10	15	20	25	30	35	40
-20	.952												
-15	.953	.943											
-10	.953	.944	.931										
-5	.954	.945	.933	.914									
0	.954	.946	.934	.916	.889								
5	.955	.947	.935	.918	.893	.854							
10	.955	.947	.936	.920	.896	.859	.803						
15	.956	.948	.937	.921	.898	.864	.811	.732					
20	.956	.948	.938	.923	.901	.868	.818	.743	.636				
25	.957	.949	.938	.924	.903	.872	.825	.754	.652	.515			
30	.957	.949	.939	.925	.905	.875	.831	.764	.666	.535	.378		
35	.957	.950	.940	.926	.907	.878	.836	.772	.680	.554	.400	.241	
40	.958	.950	.940	.927	.908	.881	.841	.780	.692	.571	.421	.262	.127

Table 3-6 — 8-12 μm Weighted Molecular Transmission for
Target Temperature of 10°C and Path Length $R = 2 \text{ km}$

T_a (°C)	T_{dp} (°C)												
	-20	-15	-10	-5	0	5	10	15	20	25	30	35	40
-20	.924												
-15	.925	.910											
-10	.926	.911	.890										
-5	.926	.913	.892	.861									
0	.927	.914	.894	.865	.820								
5	.928	.915	.896	.868	.826	.760							
10	.929	.916	.898	.871	.831	.770	.677						
15	.929	.917	.899	.874	.836	.778	.691	.568					
20	.930	.918	.901	.877	.840	.785	.703	.586	.434				
25	.930	.919	.902	.879	.844	.792	.714	.602	.456	.292			
30	.931	.919	.903	.881	.848	.798	.724	.617	.476	.314	.163		
35	.932	.920	.904	.883	.851	.803	.732	.631	.495	.335	.182	.071	
40	.932	.921	.905	.884	.853	.808	.741	.664	.513	.356	.200	.083	.022

NRL REPORT 8311

Table 3-7 - 8-12 μm Weighted Molecular Transmission for
Target Temperature of 10°C and Path Length $R = 4 \text{ km}$

T_a (°C)	T_{dp} (°C)												
	-20	-15	-10	-5	0	5	10	15	20	25	30	35	40
-20	.881												
-15	.883	.850											
-10	.884	.861	.826										
-5	.886	.864	.831	.779									
0	.887	.866	.834	.786	.711								
5	.888	.868	.838	.792	.722	.618							
10	.890	.870	.841	.797	.731	.633	.497						
15	.891	.871	.843	.802	.739	.646	.516	.356					
20	.892	.873	.846	.806	.746	.658	.534	.378	.215				
25	.892	.874	.848	.810	.753	.669	.550	.399	.236	.102			
30	.893	.875	.850	.813	.759	.679	.565	.418	.256	.117	.035		
35	.894	.876	.852	.816	.764	.688	.579	.437	.276	.133	.043	.008	
40	.895	.877	.853	.819	.769	.696	.592	.454	.295	.149	.051	.010	.001

Table 3-8 - 8-12 μm Weighted Molecular Transmission for
Target Temperature of 10°C and Path Length $R = 8 \text{ km}$

T_a (°C)	T_{dp} (°C)												
	-20	-15	-10	-5	0	5	10	15	20	25	30	35	40
-20	.819												
-15	.822	.783											
-10	.824	.788	.731										
-5	.827	.792	.738	.656									
0	.829	.795	.744	.667	.554								
5	.831	.798	.750	.677	.570	.425							
10	.833	.801	.755	.686	.584	.445	.281						
15	.834	.804	.759	.693	.597	.463	.303	.150					
20	.836	.806	.763	.700	.608	.480	.323	.168	.059				
25	.837	.808	.767	.707	.619	.496	.342	.186	.070	.015			
30	.838	.810	.770	.712	.628	.510	.361	.204	.082	.020	.002		
35	.840	.812	.773	.717	.637	.523	.378	.222	.094	.025	.0030	.000	
40	.841	.814	.776	.722	.645	.535	.394	.239	.107	.030	.0040	.0000	.000

GOODELL AND ROBERTS

Table 3-9 - 8-12 μm Weighted Molecular Transmission for
Target Temperature of 10°C and Path Length $R = 16 \text{ km}$

T_a (°C)	T_{dp} (°C)												
	-20	-15	-10	-5	0	5	10	15	20	25	30	35	40
-20	.750												
-15	.735	.674											
-10	.739	.681	.595										
-5	.743	.688	.606	.487									
0	.746	.694	.616	.502	.354								
5	.749	.699	.625	.517	.373	.214							
10	.752	.704	.633	.530	.392	.234	.099						
15	.755	.708	.640	.541	.408	.253	.114	.031					
20	.757	.712	.646	.552	.424	.271	.129	.039	.006				
25	.759	.715	.652	.562	.438	.289	.144	.047	.0080	.000			
30	.761	.718	.658	.570	.451	.305	.159	.055	.010	.0010	.000		
35	.763	.721	.662	.578	.463	.320	.173	.064	.013	.0010	.0000	.000	
40	.765	.724	.667	.586	.474	.335	.188	.074	.017	.0020	.0000	.0000	.000

Table 3-10 - 8-12 μm Weighted Molecular Transmission for
Target Temperature of 10°C and Path Length $R = 32 \text{ km}$

T_a (°C)	T_{dp} (°C)												
	-20	-15	-10	-5	0	5	10	15	20	25	30	35	40
-20	.610												
-15	.617	.527											
-10	.624	.538	.417										
-5	.630	.548	.432	.286									
0	.635	.557	.446	.304	.157								
5	.640	.565	.459	.322	.174	.062							
10	.644	.572	.470	.337	.190	.073	.015						
15	.648	.579	.481	.352	.206	.084	.019	.002					
20	.651	.584	.490	.365	.222	.096	.024	.0030	.000				
25	.654	.590	.499	.378	.236	.108	.030	.0040	.0000	.000			
30	.657	.594	.506	.389	.250	.119	.036	.0050	.0000	.0000	.000		
35	.660	.599	.513	.400	.263	.131	.042	.0070	.0000	.0000	.0000	.000	
40	.662	.603	.520	.410	.276	.143	.049	.009	.0019	.0000	.0000	.0000	.000

Table 3-11 — Vapor Pressure of Water.^a
 Pressure of Aqueous Vapor over
 Water in mm of Hg.

Temp. (°C)	mm of Hg	Temp. (°C)	mm of Hg
-15	1.436	15	12.788
-14	1.560	16	13.634
-13	1.691	17	14.530
-12	1.834	18	15.477
-11	1.987	19	16.477
-10	2.149	20	17.535
-9	2.326	21	18.650
-8	2.514	22	19.827
-7	2.715	23	21.068
-6	2.931	24	22.377
-5	3.163	25	23.756
-4	3.410	26	25.209
-3	3.673	27	26.739
-2	3.956	28	28.349
-1	4.258	29	30.043
-0	4.579	30	31.824
0	4.579	31	33.695
1	4.926	32	35.663
2	5.294	33	37.729
3	5.685	34	39.898
4	6.101	35	42.175
5	6.543	36	44.563
6	7.013	37	47.067
7	7.513	38	49.692
8	8.045	39	52.442
9	8.609		

^a"Handbook of Physics and Chemistry,"
 Chemical Rubber Publishing Company.

G. PROCEDURE FOR CALCULATING DEW POINT TEMPERATURE FROM TEMPERATURE AND RELATIVE HUMIDITY

Variables

- T — Temperature (K)
- T_d — Dew point Temperature (K)
- RH — Relative humidity in decimals (% RH/100)
- e_s(T) — Saturation vapor pressure of water
 surface (dynes cm⁻²)
- e — Partial pressure of water vapor

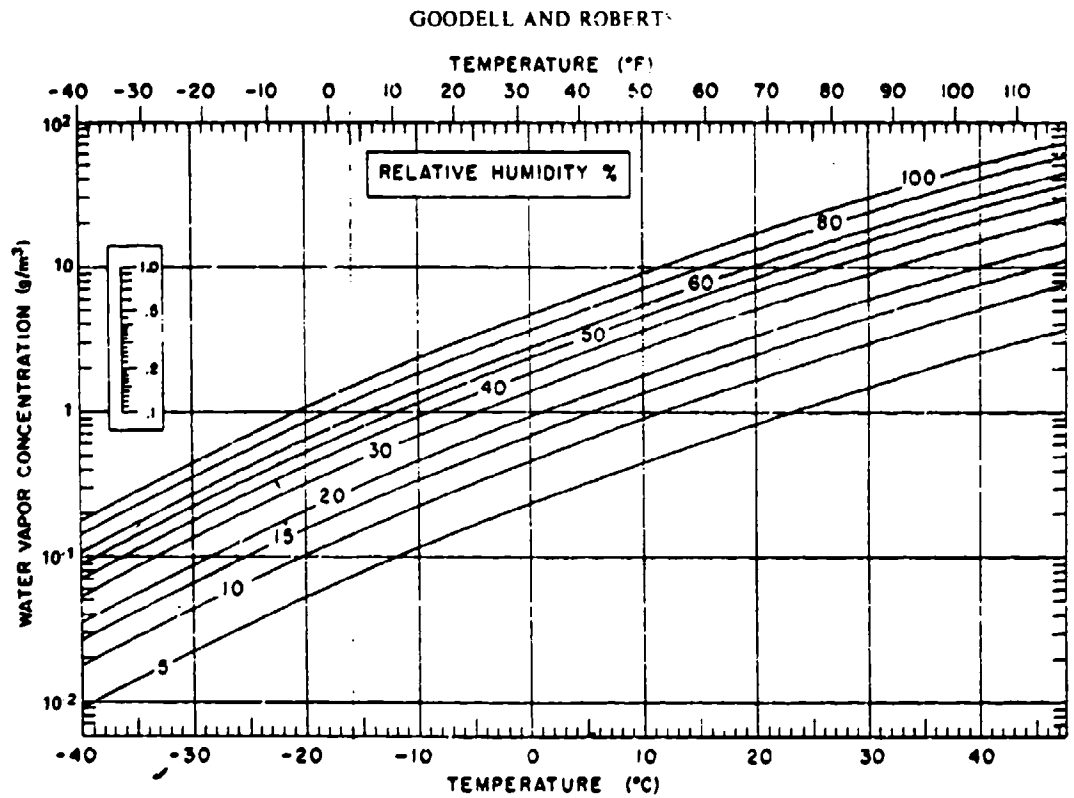


Fig. 3-7 — Water vapor concentration per kilometer path length as a function of temperature and relative humidity. Dew point corresponds to 100% relative humidity (top curve)

Constants

$$\begin{aligned} a &= 6108 \\ b &= 17.27 \\ c &= 273.16 \\ d &= 35.86 \\ \ln a &= 8.7173547 \end{aligned}$$

STEP 1

$$e_s(T) = a \exp [b(T - c)/(T - d)]$$

STEP 2

$$e = RH \cdot e_s(T)$$

STEP 3

$$a' = \ln e - \ln a$$

STEP 4

$$T_d = \frac{a' \cdot d - b \cdot c}{a' - b}$$

Restrictions

1. Valid for atmospheric pressure near standard value (*i.e.*, 1000 m bar 10^6 dynes cm^{-2}).
2. Use for temperatures above 0°C . Check accuracy before use at temperatures below 0°C .

Example

Given an ambient temperature of 70°F and a relative humidity of 60 percent find the dew point temperature at standard pressure conditions.

First express temperature in kelvins:

$$K = ^\circ\text{C} + 273.16 = \frac{5}{9} (^\circ\text{F} - 32) + 273.16$$

Thus $K = 294$

STEP 1

$$e_s(T) = 25\,000$$

STEP 2

$$e = 0.6 e_s(T) = 15\,000$$

STEP 3

$$a' = 0.9000$$

STEP 4

$$\begin{aligned} T_d &= 286\text{ K} \\ &= 13^\circ\text{C} \end{aligned}$$

(Values are stated to one figure accuracy.)

H. GRAPHICAL METHOD FOR RANGE INTERPOLATION

Figure 3-9 is a specially prepared graph on which the abscissas are the logarithms of the negative logarithms of the transmittances, $(\ln(-\ln \tau))$ and the ordinates are the logarithms of the ranges $(\ln R)$. This chart together with two transmittance values either in the 3-5 μm window or the 8-12 μm window provides transmittance values for other ranges under the same dew point temperatures. To use this method calculate and plot the chart two transmittances for two range points for a given set of conditions; then lay a straight edge along the two range-transmittance pairs. Transmittances at other ranges are read off at the intersections of the straight edge with the corresponding ranges.

This chart is possible because the transmittances in Tables 3-1 to 3-8 follow closely (correlation coefficient > 0.99) an exponential power law of the form:

$$\tau = e^{-aR^b},$$

where a and b are constants.

Taking the logarithm two times produces the relation:

$$\ln\{-\ln(\tau)\} = \ln(a) + b \ln(R)$$

which shows a linear relation with *slope* b and *intercept* a .

I. SUMMARY

The atmosphere strongly influences IR systems performance and therefore must be considered in any FLIR design. The major absorbing gases in the earth's atmosphere and the ones that primarily determine the atmospheric windows are water and carbon dioxide. Other gases include nitrous oxide, methane, ozone, nitrogen, and carbon monoxide. Water content varies widely depending on local weather conditions. Ozone concentration peaks at an altitude of about 24 km and normally does not substantially affect ground level operations. The other gases have fairly constant concentrations in the atmosphere.

Aerosols, many of which are water droplets, present many difficulties to FLIR performance analysis. They are extremely variable in particle size distribution and lapse rates. They are difficult to characterize by conveniently measurable quantities. The LOWTRAN 3b computer code offers three aerosol models: maritime, rural, and urban.

Extinction is often more useful than the transmittance itself for providing insights into FLIR performance. Thus the "extinction coefficient," which is the logarithm of the reciprocal of transmittance divided by the range, can often be expressed as the sum of extinction coefficients due to atmospheric attenuation components. The total extinction in these cases is the sum of the constituent extinctions. This concept is most effective with the water continuum and aerosol extinction.

The LOWTRAN 3b computer model for calculating atmospheric transmittance developed at the Air Force Geophysical Laboratories, Cambridge, Mass. provides the data in this chapter

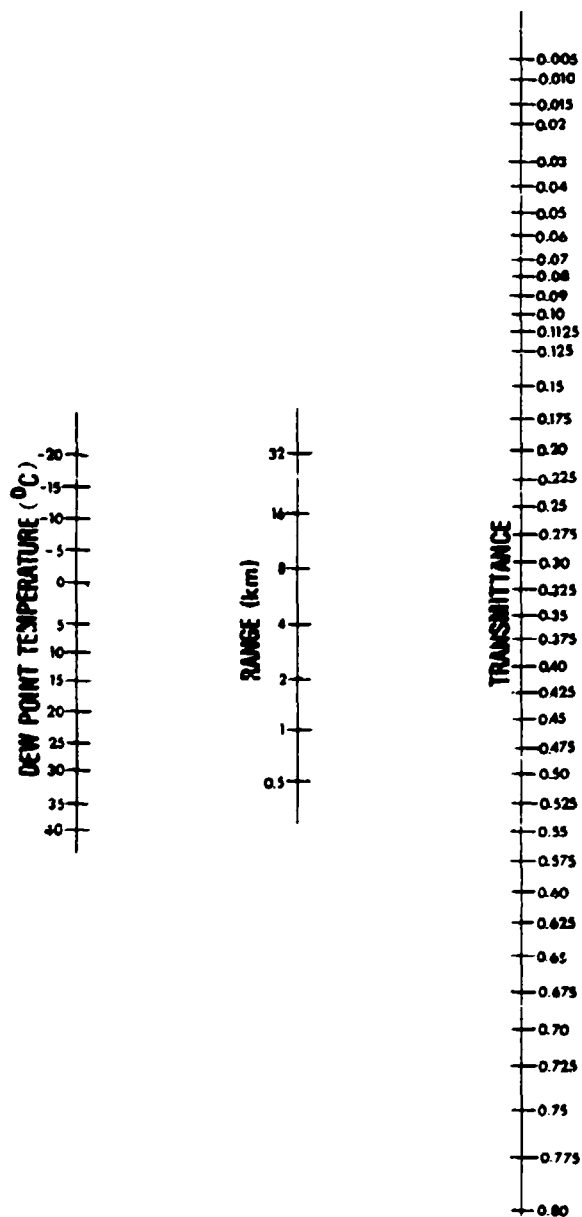


Fig. 3-8 — Nomogram for determining atmospheric transmittance in the 3-5 μm window

GOODELL AND ROBERTS

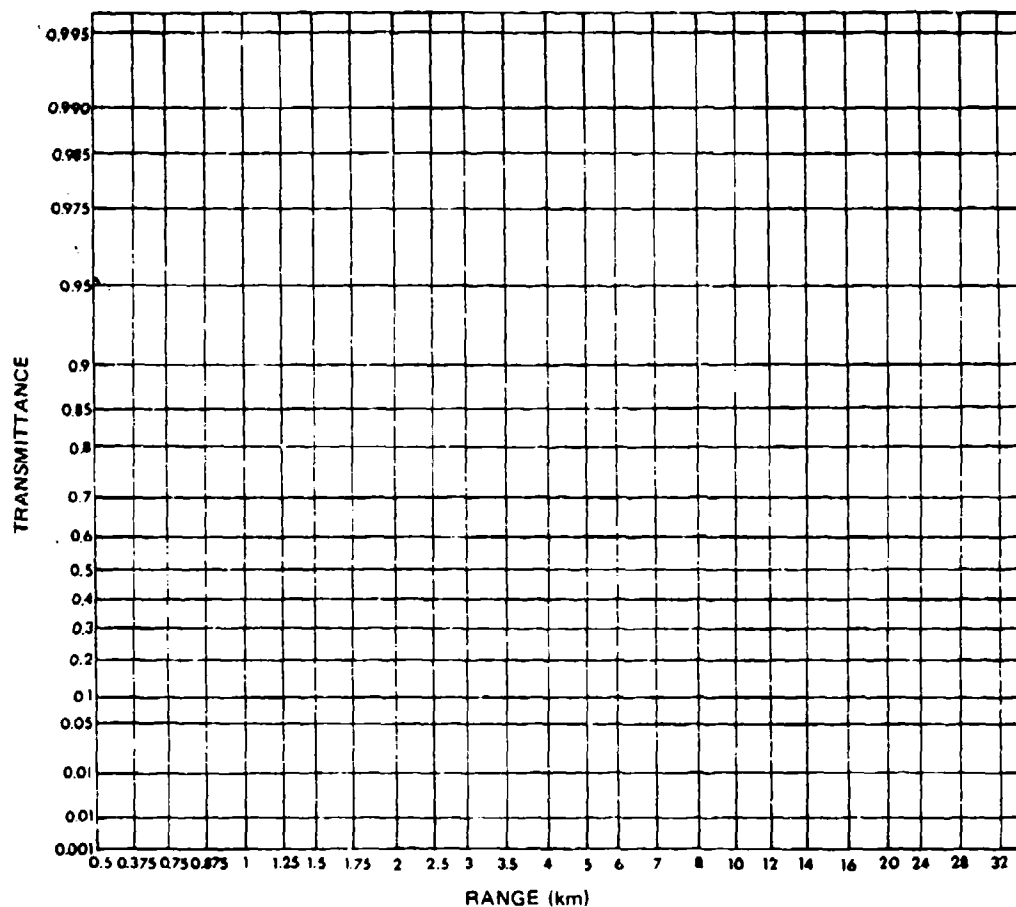


Fig 3-9 — Graph for interpolating range and/or transmittance in either spectral region

for determining transmittance. LOWTRAN 3b computes atmospheric transmittance by multiplying component transmittances of each of the constituent gases and one of the aerosol models. LOWTRAN 3b contains several model atmospheres and also provides for inputting meteorological parameters.

Tables 3-1 through 3-8 list contrast transmittances in the two main atmospheric windows (3-5 and 8-12 μm). These tables and the LOWTRAN 3b aerosol models provide the means for calculating atmospheric transmittance.

REFERENCES

- 3-1 J.E.A. Selby, E.P. Shettle, and R.A. McClatchey, "Atmospheric Transmittance From 0.25 to 28.5 μm : Supplement LOWTRAN 3B (1976)", Air Force Geophysics Laboratory, November 1976.
- 3-2 Handbook of Military Infrared Technology, Office of Naval Research, Department of the Navy.
- 3-3 *Handbook of Geophysics-Revised Edition*, Macmillan Company, New York (1960).
- 3-4 F. Stauffer and J. Strong, *App. Optics*, 1, (1962).
- 3-5 T.L. Altshuler, *Infrared Transmission and Background Radiation by Clear Atmospheres*, Document No. 615D199, Dec. 1961, General Electric Company, Missile and Space Vehicle Department, Philadelphia, Pa.
- 3-6 J.N. Howard and J.S. Garing, *The Transmission of the Atmosphere in the Infrared*, GRD, AFCRL, Cambridge, Mass. (1962).
- 3-7 A.J. Arnulf, J. Bricard, E. Cure and C. Veret, "Transmissions by Haze and Fog in the Spectral Region 0.35 to 10 Microns," *J. Opt. Soc. Am.* 47, 491 (1957).
- 3-8 S.S. Penner, *Quantitative Molecular Spectroscopy and Gas Emissivities*, Addison-Wesley Publishing Co., Inc., Reading, Mass. (1959).
- 3-9. G.N. Plass and D.I. Fivel, *Astrophys. J.*, 117, 225 (1953).
- 3-10. W.M. Elsasser, *Heat Transfer by Infrared Radiation in the Atmosphere*, *Harvard Meteor Studies* No. 6, Harvard University Press, Cambridge, Mass. (1942).
- 3-11. G.N. Plass, *J. Opt. Soc. Am.*, 48, 690 (1958).
- 3-12. G.N. Plass, *J. Opt. Soc. Am.*, 50, 868 (1960).
- 3-13. R. Ladenberg and F. Reiche, *Ann Physik.*, 42, 181 (1913)
- 3-14. G.N. Plass and D. I. Fivel, *Astrophys. J.*, 117, 225 (1953).
- 3-15. W.M. Elsasser, *Phys. Rev.*, 54, 126 (1938).
- 3-16. H. Mayer, *Methods of Opacity Calculations*, Los Alamos, LA-647 (1947).
- 3-17. P.J. Wyatt, V.R. Stull, and G.N. Plass, *J. Opt. Soc. Am.* (1962).
- 3-18. P.J. Wyatt, V.R. Stull, and G.N. Plass, *App. Optics*, 3 (1964); Aeronutronic Report U-1717, Aeronutronic Systems, Inc., Newport Beach, Calif. (1962).

GOODELL AND ROBERTS

- 3-19. V.R. Stull, P.J. Wyatt, and G.N. Plass, *App. Optics*, 3 (1964); Aeronutronic Report U-1718, Aeronutronic Systems, Inc., Newport Beach, Calif., 1962.
- 3-20. W.E.K. Middleton, *Vision Through the Atmosphere*, University of Toronto Press, Toronto, Canada (1952) Section 9.3.1.1.
- 3-21. H.C. Van De Hulst, *Light Scattering by Small Particles*, Wiley, New York (1957).
- 3-22. P. Kruse, L. McGlaughlin, and R. McQuistan, *Elements of Infrared Technology*, Wiley, New York (1962).
- 3-23. H.W. Yates and J.H. Taylor, *Infrared Transmission of the Atmosphere*, NRL Report 5453, U.S. Naval Research Laboratory, Wash., D.C. (1960).
- 3-24. J.A. Curcio, G.L. Knestrick, and T.H. Cosden, *Atmospheric Scattering in the Visible and Infrared*, NRL Report 5567, U.S. Naval Research Laboratory, Wash., D.C. (1961) ASTIA AD 250945.
- 3-25. L.P. Granath and E.O. Hulburt, "The Absorption of Light by Fog", *Phys. Rev.*, 34, No. 140 (1929).
- 3-26. M. Migeotte, L. Nevin, and J. Swensson, *The Solar Spectrum from 2.8 to 23.7 Microns, Part II. Measures and Identifications*, University of Liege, Contract AF 61 (514)-432, Phase A, Part II, Geophysics Research Directorate, AFCRC, Cambridge, Mass. ASTIA AD 210044.
- 3-27. M. Migeotte, L. Nevin, and J. Swensson, *An Atlas of Nitrous Oxide, Methane and Ozone Infrared Absorption Bands, Part I. The Photometric Records*, University of Liege, Contract AF 61(614)-432, Phase B, Part I, Geophysics Research Directorate, AFCRC, Cambridge, Mass. ASTIA AD 210045.
- 3-28. M. Migeotte, L. Nevin, and J. Swensson, *An Atlas of Nitrous Oxide, Methane and Ozone Infrared Absorption Bands, Part II. Measures and Identifications*, University of Liege, Contract AF 61(514)-432, Phase B, Part II, Geophysics Research Directorate, AFCRC, Cambridge, Mass. ASTIA AD 210046.
- 3-29. J.N. Howard and J.S. Garing, *Infrared Atmospheric Transmission: Some Source Papers on the Solar Spectrum from 3 to 15 Microns*, Air Force Surveys in Geophysics No. 142, AFCRL, Report No. 1098, Dec. 1961, Geophysics Research Directorate, AFCRL, Cambridge, Mass.
- 3-30. J.N. Howard, "Atmospheric Transmission in the 3 to 5 Micron Region," *Proc. IRIS*, 2, 59-75 (1957).
- 3-31. J.N. Howard, "Atmospheric Transmission in the 8 to 13 Micron Region," *Proc. of the Symposium on Optical Radiation from Military Airborne Targets*, Final Report No. AFCRL-TR-58-146, AFCRL, Cambridge, Mass., Contract No. AF 19(604)-2451, Haller, Raymond and Brown, Inc. State College, Pa. ASTIA AD 152411.

NRL REPORT 8311

- 3-32 D.E. Burch and D. Williams, *Infrared Absorption by Minor Atmospheric Constituents*, The Ohio State University Research Foundation, Scientific Report No. 1, Contract No. AF 19(604)-2633, Geophysics Research Directorate, AFCRI, Report No. TN-60-674, AFCRL, Cambridge, Mass. (1960) ASTIA AD 246921.
- 3-33 D.E. Burch, D. Gryvnak, and D. Williams, *Infrared Absorption by Carbon Dioxide*, The Ohio State University Research Foundation, Scientific Report No. 11, Contract No. AF 19(604)-2632. Geophysics Research Directorate, AFCRL Report No. 255, AFCRL, Cambridge, Mass. (1960) ASTIA AD 253435.
- 3-34 D.E. Burch, E.B. Singleton, W.L. France, and D. Williams, *Infrared Absorption by Minor Atmospheric Constituents*, The Ohio State University Research Foundation, Final Report, Contract No. AF 19(604)-2633. Geophysics Research Directorate, AFCRL Report No. 412, AFCRL, Cambridge, Mass. (1960) ASTIA AD 256952.
- 3-35 H.W. Yates and J.H. Taylor, *Infrared Transmission of the Atmosphere*, NRL Report 5453, U.S. Naval Research Laboratory, Wash., D.C. (1960) ASTIA AD 240188.
- 3-36 T. Elder and J. Stong, "The infrared Transmission of the Atmospheric Windows," *Journal of the Franklin Institute*, 255, No. 3, 189 Phila., Pa. (1953).
- 3-37 T.L. Altshuler, *Infrared Transmission and Background Radiation by Clear Atmospheres*, General Electric Company, Missile and Space Vehicle Department, Valley Forge, Pa., Docu-61SD199 (1961).
- 3-38 G.N. Plass, *App. Optics* 2, 515 (1963).
- 3-39 R. O'B. Carpenter, J.A. Wight, A. Quesada, and R.E. Swing, *Predicting Infrared Molecular Attenuation for Long Slant Paths in the Upper Atmosphere*, AFCRC Report No. TN-58-253, AFCRC, Cambridge, Mass (1957).
- 3-40 A.S. Zachor, *Near Infrared Transmission Over Atmospheric Slant Paths*, Report R-328, 2, Massachusetts Institute of Technology, Cambridge, Mass., Contract AF 33(6616)-6046 (1961).
- 3-41 A.E.S. Green and M. Griggs, *Appl. Optics* 2, 561 (1963).
- 3-42 G.N. Plass, *Transmittance of Carbon Dioxide and Water Vapor over Stratospheric Slant Paths*, Aeronutronic Report, Aeronutronic Systems, Inc., Newport Beach Calif. (1962); *Appl. Optics*, 3 (1964).
- 3-43 L.M. Biberman, "Effect of Weather at Hannover, Federal Republic of Germany, on Performance of Electrooptical Imaging Systems, Part I: Theory, Methodology, and Data Base", IDA Paper P-1123, August 1976.
- 3-44 R.A. McClatchey, R.W. Fenn, J.E.A. Selby, F.E. Volz, J.S. Garing, *Optical Properties of the Atmosphere*, AFCRL-72-0497.

GOODELL AND ROBERTS

- 3-45 R.E. Roberts, L.M. Biberman, and J.E.A. Selby, "Infrared Continuum Absorption by Atmospheric Water Vapor in the 8-12 μ m Window", IDA Paper P-1184, April 1976.
- 3-46 D.E. Burch, D.A. Gryvnak, and J.D. Pembroke, *Philco Ford Corp. Aeronutronic Report U-4897*, ASTIA AD 882876 (1971).
- 3-47 K.O. White, W.R. Watkins, T.W. Tuer, F.G. Smith, and R.E. Meredith, *J. Opt. Soc. Amer.*, **65**, p. 1201 (1975).
- 3-48 J. Dowling (private communication, Naval Research Laboratory, Washington, D.C.).
- 3-49 R.E. Roberts, "Atmospheric Transmission Modeling: Proposed Aerosol Methodology with Application to the Grafenwöhr Atmospheric Optics Data Base", IDA Paper P-1225, December 1976.
- 3-50 L.M. Biberman, R.E. Roberts, and L.N. Seekamp, *A Comparison of Electrooptical Technologies for Target Acquisition and Guidance. Part 2: Analysis of the Grafenwohr Atmospheric Transmission Data*, IDA paper P-1218 (August 1976).
- 3-51 C. Tomasi and F. Tampieri, *Size Distribution Models of Fog and Cloud Droplets in Terms of the Modified Gamma Functions*, *Tellus XXVIII*, **4**, 333 (1976).

Chapter IV

VIDEO, DISPLAY, AND PERCEIVED-IMAGE SIGNAL-TO-NOISE RATIOS

F.A. Rosell

A. INTRODUCTION

This chapter is devoted to the discussion of the basic concepts and the derivations of the fundamental mathematical relations used to describe and analyze thermal imaging systems. The models devised apply when the input test patterns are images of standardized and quantitatively describable objects such as rectangles or periodic bar patterns.

The first concept to be discussed is that of a display signal-to-noise ratio which is defined to be the SNR of an image appearing on the display of an electrooptical sensor. This image SNR takes into account the ability of an observer to integrate spatially and temporally but does not include other observer parameters such as the eye's modulation transfer function, retinal fluctuation noise, or dynamic range limitations. If these latter observer parameters were included, the image SNR would be that at the output of the observer's retina and would be designated the perceived SNR.

Following the derivation of the display SNR, various thermal imaging system configurations are discussed. Next the electrical signal-to-noise ratio which appears in a detector channel is quantitatively described along with basic concepts such as detector detectivity, reference channel bandwidth, detector cold shielding, and scan parameters such as interlace, overscan, and efficiency.

The noise-equivalent temperature difference or NE Δ T is obtained by equating the channel SNR to unity and by solving for the incremental scene temperature difference which produces this result. The NE Δ T has the advantage of being electrically measurable and is an indicator of sensitivity for systems which are identical. However NE Δ T is not a fundamental concept when an observer is the user of the displayed imagery since a system with a larger (inferior) NE Δ T may yet be more sensitive and produce higher resolution.

The channel SNR is converted to the video SNR which is used in turn to calculate the display SNR. In the initial analysis, the aperture responses of the various sensor elements such as the lens, detector, multiplexer, electrical circuits, and the display are ignored. As is well known, these effects are most easily analyzed in the spatial frequency domain by using Fourier analysis and the concepts of optical and modulation transfer functions. A number of typical modulation transfer functions for various sensor components are quantitatively described in this chapter.

Finally, a numerical example of a display SNR calculation is provided. In addition to the derivations in this chapter a number of appendixes are provided for those readers who desire more detail. In Appendix D, the synchronous integrator concept of modeling is described. In Appendix F, a number of parameters and fundamental relationships are described including the relation between video and display SNR, the detector channel SNR, detector detectivity, and responsivity. In Appendix G, the effects of imaging sampling are discussed.

The concepts of this chapter will be used to derive the minimum resolvable temperature difference (MRT) for a thermal imaging system in Chapter V which will also include a discussion of observer thresholds.

B. BASIC SIGNAL-TO-NOISE RATIO CONSIDERATION

Every man-made detector of radiant energy, whether radio, audio, or television generates a noise in converting the incident radiant energy to an electronic signal. It is easily shown that the ability to discern a signal is a function of noise generated in the signal conversion process or by noise subsequently added in the system. One common example of visually observable photo-to-electron conversion or system generated noise is the "snow" seen on a home television receiver when tuned in to a fringe area broadcast station. On the other hand, the existence of noises which are inherent in the detection process of the human eye or ear has been vigorously disputed by many workers; particularly in the field of psychophysical experimentation, analysis, and interpretation. The denial of a noisy detection process for the human observer has led to the reporting of psychophysical thresholds as minimum detectable contrast rather than threshold signal-to-noise ratio as is customary in engineering practice.

Engineers, for the past four decades, have assumed that the eye's and ear's detection process is noisy and have constructed quantitative models based on this premise. Foremost of these engineers is Dr. Otto Shade, Sr., whose contributions are only now becoming appreciated. Even among psychophysicists, the view of a noiseless detection by man's senses appears to be losing ground (Ref. 4-1).

For the bulk of the analysis presented herein, the existence of noise generated in the eye's photoprocess is academic; when the primary sensor is an electro-optical device, a photoconversion noise is generated which is electrically measurable. When the device is highly sensitive, these photoconversion noises are readily perceptible on the sensor's display at low input signal levels. The existence of these noises can neither be disputed nor ignored.

That noise could be limiting to visual perception of displayed imagery was suggested by Barnes and Czerny in 1932 (Ref. 4-2). In 1943, de Vries proposed that an image to be visually detectable must have a signal-to-noise ratio exceeding some threshold value. The noise level was assumed to be signal level dependent as postulated by fluctuation theory (Ref. 4-3).

It is readily appreciated that noise, whatever its source, will make an image more difficult to perceive. Clearly, the signal must equal or exceed the noise; speaking of noise in the conventional engineering sense. As will be seen, a SNR can be defined for an electro-optically generated image as viewed by an observer. Through psychophysical experimentation, the SNR required by an observer to detect the image at various levels of probability can be determined.

By matching the image SNR obtainable from the sensor to that required by the observer, the probability that the observer will detect the image can be surmised. This process is straightforward enough for images of simple geometry, but the image SNR is difficult to define for complex images of irregular geometry and contrast.

C. THE NOISE LIMITED CASE — RECTANGULAR IMAGES

Consider the schematic of an electro-optical imaging process as shown in Fig. 4-1. In this figure, a rectangular image of area a , amid a uniform background, has been projected onto a phototransducer by a lens. The phototransducer converts the photon image on it to a photoelectron image with 1:1 spatial correspondence. The incident photo image may be considered noise-free since the existence of a noisy "coherent" electron emission from a photosurface has yet to be demonstrated. This assumption is made to explain why "photon noise" is not observed in the phototransduced current (Ref. 4-4). The lens forming the image is characterized by an aperture,* or spatial frequency response, whose effect on image signals is analogous

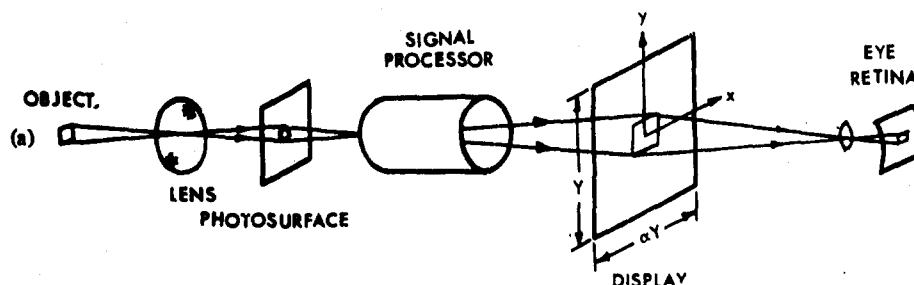


Fig. 4-1 — Schematic of the electro-optical imaging process

to the effect of a filter acting on electrical signals, i.e., the image is blurred. Similarly, other elements of the electro-optical sensor including the observer's eye have apertures which affect the image fidelity and SNR. These aperture effects will be assumed negligible in the initial analysis but will be discussed in Section IV-D. We note that the smaller the image size, the more important aperture effects are.

The lens of the electro-optical sensor does not directly generate noise, but the sensor's photon-to-electron conversion process is noisy and therefore an image SNR is established at the output of the photon transducer which will inherently limit the detectability of scene objects. After photoconversion, the image is passed to the signal processor whose main purpose is to amplify the image signals and noises alike, and perhaps, to magnify the image. Next, the electron image is converted to a visual image by a phosphor. The displayed image can be directly viewed or magnified before viewing by using a lens. If we suppose that no noise was added to the image in the signal processor or in the electron-to-photon conversion, then the image SNR

*The words *aperture* or *aperture response* as used in this document do not refer to the lens diameter (although relative aperture is often used in connection with the lens diameter). Instead, these words refer to the spatial impulse response or the effective size of the impulse response of various system components. In the case of the lens, its aperture is sometimes measured in terms of an effective blur circle size. The dimensions of a single infrared detector are exactly the dimensions of its aperture. The Fourier transform of a lens's aperture response is its optical transfer function. In electrical engineering, the Fourier transform of the impulse response of a component is its complex steady state frequency response and the modulus of this frequency response is the modulation transfer function.

on the display will be identical to that at the output of the primary phototransducer (the sensor's photosurface). Furthermore, if the gains and magnifications of the signal processor and display are sufficient so that the observer's eye is limited by neither light level nor image size, then the image SNR at the eye's retina will be identical to that on the display if due account is taken of the eye-brain combination's ability to integrate in space and time. These conditions can be achieved in practice for a wide range of image sizes, signal amplifications, apertures, display luminances, image magnifications, and observer-to-display viewing distances. In general, the image SNR is more often limited by the system than by the observer's eye although the case where the eye degrades image SNR is important and cannot be ignored.

Suppose that a perfectly sharp, well-defined rectangle is projected onto the sensor's input photosurface. Let the irradiance of the square be E_o , W/m^2 and let the irradiance of the square's background be E_b . If the phototransducer is linear, then the image irradiances E_o and E_b will result in the average photoelectron rates \dot{n}_o and \dot{n}_b photoelectrons/ $m^2 \cdot s$.^{*} In viewing the display, the eye seeks areas in which the photon density is higher than in others. The eye is aided in this process by being able to integrate over such areas in space and time. The eye (or eye-brain combination) has been termed a near-perfect synchronous integrator since it can completely integrate an image in space over a wide range of image areas. The incremental signal level is defined as

$$\begin{aligned}\Delta n &= n_o - n_b \\ &= (\dot{n}_o - \dot{n}_b) a T_e,\end{aligned}\quad (4-1)$$

where n_o is the average number of photoelectrons generated by the input photosurface in the image area a , during the eye's integration time T_e , while n_b is the average number generated in a similar equal sized comparison area of background in the same time. The noise associated with the inherent fluctuations in the photoprocess are assumed to follow the Poisson probability distribution which states that the fluctuations have a standard deviation or rms noise equal to the square root of the total number of photoconverted electrons integrated over the image area during the integration time. For the case of an object imaged against background, the total root mean square noise is assumed to be the average of the object and background photoelectrons summed in quadrature, i.e.,

$$\begin{aligned}\text{rms noise} &= [(n_o + n_b)/2]^{1/2} \\ &= [(\dot{n}_o + \dot{n}_b) a T_e / 2]^{1/2},\end{aligned}\quad (4-2)$$

and the image SNR_i is equal to

$$\begin{aligned}\text{SNR}_i &= \Delta n / [(n_o + n_b)/2]^{1/2} \\ &= \Delta \dot{n} (a T_e)^{1/2} / [\dot{n}_{av}]^{1/2},\end{aligned}\quad (4-3)$$

where $\dot{n}_{av} = (\dot{n}_o + \dot{n}_b)/2$. The above SNR is designated SNR_i to indicate that it is the SNR of the electron image at the output of the input photosurface after photoconversion of the scene photon image. Suppose the gain of the signal processor is G and that the conversion efficiency of the phosphor is K_p lumens per electron. Then, the SNR_p at the output of the display is

^{*}The dot and prime used in connection with 'n' denotes that the quantity is a derivative with respect to space and time.

$$\begin{aligned} \text{SNR}_D &= GK_p \Delta \dot{n}' (a T_c)^{1/2} / [K_p^2 G^2 \dot{n}_{av}]^{1/2} \\ &= \Delta \dot{n}' (a T_c)^{1/2} / [\dot{n}_{av}]^{1/2}. \end{aligned} \quad (4-4)$$

That is, the display SNR is independent of the gain of the signal processor and the phosphor electron-to-photon conversion efficiency and is equal to the image SNR at the output of the input photosurface. However, this is true only if the image is not degraded in the signal processing by either image deformation or noise addition in the reimaging process.

In the above, we have defined an image SNR which is proportional to the square root of the product of image area and integration time. This SNR could be measured on a display using a photometer whose spot size on display perfectly matches the displayed image area, a . The integration time is that of the photometer or that of the sensor, whichever is larger. The SNR_D , whether calculated or measured, is that obtainable from the sensor. An image may or may not be detectable depending on its SNR_D . In the particular case where the final detector is a human observer, it is assumed that the eye will integrate over the area a (within limits to be defined) and that the integration time will be 0.1 s for display luminances in the 0.2 to 10 ft-lambert range. Actually, the eye's integration time is variable from about 0.05 s at very high light levels to about 0.2 s at very low light levels (Ref. 4-5). Lavin (Ref. 4-6) estimated 0.1 s using photographs of televised images. In practice, the actual value is relatively unimportant because it is included in the measured threshold signal-to-noise ratio. However it is important, when making calculations, to use the value of integration time that was assumed in making the threshold measurement.

We have inferred that the rectangular image will be detectable if its SNR_D exceeds some threshold value which we will designate as SNR_{DT} . Rose (Ref. 4-7) performed experiments using noisy photographs and concluded that the required SNR_{DT} ranged between 3 and 7 and preferred the value 5. For dynamic images as exemplified by TV, a value of SNR_{DT} of 2.8 appears appropriate based on more recent psychophysical experimentation and an assumed value of 0.1 s for the eye's integration time. By dynamic images, we infer the type of image displayed on a real time TV or FLIR display wherein three images are typically presented to the observer during the 0.1-s integration period. The observer coherently sums the signal while incoherently summing the noise when the images are stationary in space. Thus the image SNR improves by about $\sqrt{3}$. By contrast, a photographic image represents a single sample in time and no use is made of the observer's temporal integration capability.

In television practice, the signal current, i , can be related to the rate of photoelectron generation, \dot{n}' , through the equation

$$i = \dot{n}' e A, \quad (4-5)$$

where e is the charge of an electron and A is the sensor's total effective photosensitive area. When Eq. (4-5) is substituted into Eq. (4-4), one obtains

$$\text{SNR}_D = \left[\left(\frac{a}{A} \right) T_c \right]^{1/2} \frac{\Delta i}{[e \dot{n}_{av}]^{1/2}}, \quad (4-6)$$

where Δi corresponds to $\Delta \dot{n}'$ and \dot{n}_{av} to \dot{n}_{av} . We arbitrarily multiply the numerator and denominator of the above equation by $2\Delta f_v$, where Δf_v is the video bandwidth, giving

$$\text{SNR}_D = \left[2\Delta f_v T_c \left(\frac{a}{A} \right) \right]^{1/2} \frac{\Delta i}{[2e \dot{n}_{av} \Delta f_v]^{1/2}}. \quad (4-7)$$

The term to the right will be recognized by those who are familiar with video circuitry as the video signal-to-noise ratio SNR_V and thus

$$\text{SNR}_D = \left[2\Delta f_v T_c \left(\frac{a}{A} \right) \right]^{1/2} \text{SNR}_{V0} \quad (4-8)$$

For future convenience, the subscript zero has been added to SNR_V to indicate that it is measured using an image of spatial extent which is large relative to the overall sensor's aperture (or effective "blur" dimensions). The case where the image is small will be treated in Section IV-D.

As shown in Appendix F(A), Eq. (4-8) also applies to thermal imaging or FLIR systems when A is interpreted as the total image plane area regardless of the area of the detectors within that area. This equation will serve as the starting point for the SNR_D calculation.

Again, we observe that the image signal is proportional to the square root of the product of the image area and the observer's integration time because of the observer's ability to integrate in space and time. The display SNR is usually larger than the video SNR as can be seen by inserting typical numbers in Eq. (4-8), suppose the ratio of image area to total image plane area $(a/A) = 1/1000$ and let $\Delta f_v = 4 \times 10^6 \text{ Hz}$ and $T_c = 0.1 \text{ s}$, then $\text{SNR}_D = 800 \text{ SNR}_{V0}$. To gain further insight into this relationship consider Fig. 4-2. The photoconverted electron image in Fig. 4-2(a) is a rectangle of size $\Delta x \cdot \Delta y$ and is of incremental current amplitude Δi . The SNR_V is measured by use of a line selector oscilloscope. The assumed image is shown as subtending three scan lines in the y direction in Fig. 4-2(b), but only a single line is used in the SNR_V measurement as shown in Fig. 4-2(c). The incremental current Δi represents the signal, while the square root of the average sum of the mean square noise currents in the image blacks and whites represents the rms noise. To contrast the key difference between SNR_V and SNR_D , observe that the SNR_V does not include the image dimensions or frame-to-frame signal integration. The observer, on the other hand, spatially integrates each line in the horizontal, from line-to-line in the vertical and over a number of frame times (usually about three in conventional TV).

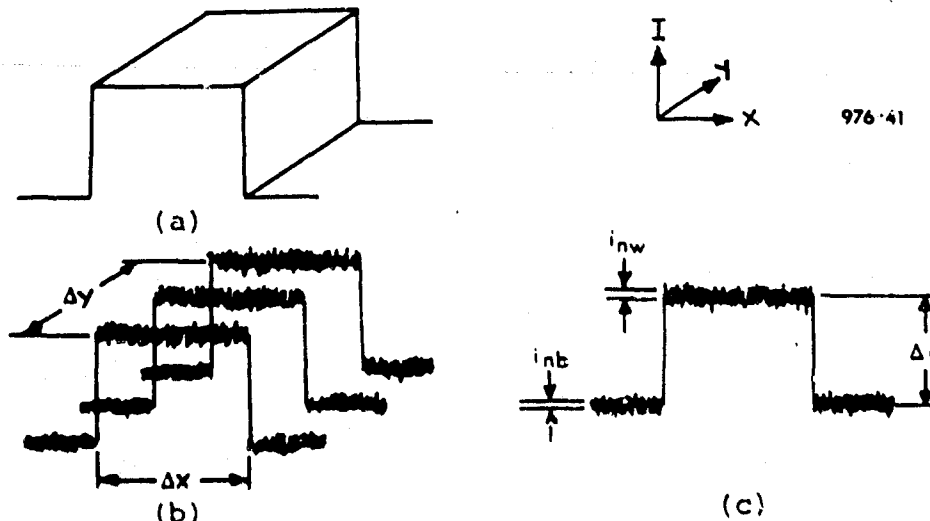


Fig. 4-2 - (a) Image intensity distribution, (b) image waveform after raster scanning, and (c) single line used in measurement of the video signal-to-noise ratio

Before proceeding, we wish to make a strong distinction between the terms *perceived signal-to-noise ratio*, SNR_p , and the *display signal-to-noise ratio*, SNR_D . When the observer's ability to discern or resolve an image is primarily limited by sensor apertures and sensor generated noises, the SNR_p equals the SNR_D . However, as will be discussed, the observer's ability may be primarily limited by his own eye apertures and noise in which case, the SNR_p can be far different from the SNR_D . In the current state-of-the-art, most models do not include eye parameters at all. In certain cases, the MTF of the eye is taken into account but efforts to include retinal fluctuation noise are rarely made. If eye parameters are ignored in a model, except for the eye's ability to spatially and temporarily integrate, it is recommended that the term SNR_D be used. If all eye parameters are included, to the extent that the state of the art permits use SNR_p . If a partial inclusion of eye parameters are included, it is tentatively proposed to use the term SNR_{Dp} .

D. APPLICATION OF THE NOISE-LIMITED CASE TO VARIOUS FLIR CONFIGURATIONS

The most commonly employed FLIR configuration is schematically shown in Fig. 4-3. The photon image of the scene is mechanically scanned over the detector array in the horizontal direction by use of rotating mirrors or prisms. The detectors are usually in a line array and are often spaced by some distance for ease of manufacture. An interlace feature to reduce flicker in the display is often provided. Typically, one field is scanned in 1/60 s and, prior to the second field, the optical line-of-sight is depressed by the angular subtense of 1/2 the detector's center-to-center or pitch dimension to scan the alternate field.

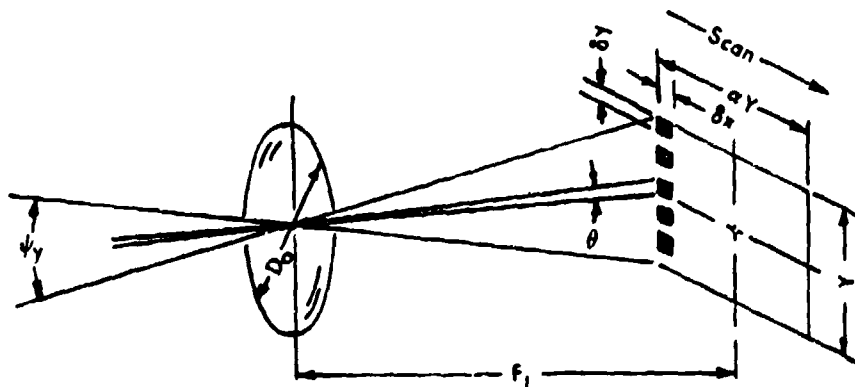


Fig. 4-3 -- Schematic of the basic FLIR configuration

The detectors may number several hundred with each detector having its own preamplifier whose purpose is to build up the detected signal prior to multiplexing. The purpose of the multiplexer is to provide a single sequential signal which can be displayed on a conventional TV display using a single electron scanning beam. The multiplexer can be an electronic sampler as shown in Fig. 4-4. The output of each detector channel is sampled one or more times in the time that it takes the scanned image to move one detector width in the horizontal. The sampled image is amplified and reconstructed by the display. Note that the raster lines are vertical when this configuration is used. A TV camera can also be used as a multiplexer. In this case, the amplified output of each detector is connected to a light-emitting diode or LED. The LED

F. A. ROSELL

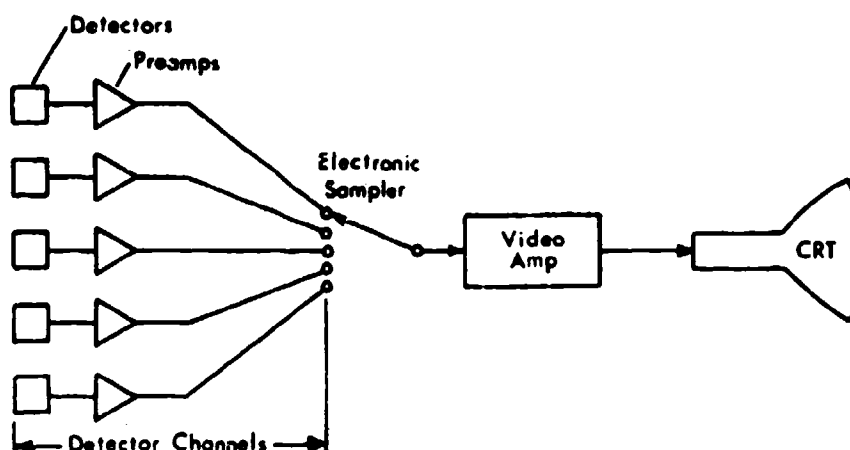


Fig. 4-4 - Schematic of the electronic sampling process

array, whose light outputs are proportional to the detector outputs, is mechanically scanned in synchronism with the detector array.* The LED array is viewed by the TV camera which converts the image generated to a video signal.

In the case of an electronic multiplexer, the output signal represents sampled data in both directions by virtue of the discrete detector dimensions in the vertical and the electronic sampling in the horizontal. In the case where a TV camera is used as a multiplexer, the TV scan lines are in the same direction as the detector scan so that the signals are essentially analog in the horizontal. However, the signals are doubly sampled in the vertical; first by the discrete nature of the detectors and second by the TV camera raster. In practice, the number of TV scan lines are made larger than the number of detectors in order to avoid aliasing effects. The sampling process, whether caused by the discrete nature of the detectors or by the multiplexing process, will affect both signals and noises. In the initial analysis the effects of sampling will be assumed negligible, but sampling effects will be discussed in Appendix G.

A number of different scan configurations such as those shown in Figs. 4-5 and 4-6 can be used. The case (1) scan configurations of Fig. 4-5 are generally referred to as *serial scan* while the case (2) configurations are referred to as *parallel scan*. In case 1(a) a single detector is used to sequentially scan the image without interlace and without overscan (to be defined). In case 2(a), a row of contiguous detectors is used to scan the image plane and has the merits of increasing system sensitivity (by the square root of the number of detectors) and of reducing detector channel bandwidth (by the number of detectors directly). In cases 1(b) and 2(b) an interlace feature is used to scan the image plain for the purpose of reducing display flicker. Also case 2(b) does not require contiguous detectors which are sometimes difficult to manufacture.

In cases 1(c) and 2(c) the scan lines are only 1/2 a detector height apart. This mode of operation is called overscan and as will be discussed further, overscan results in an increase in the system resolution which is theoretically possible for a detector of a given size because the

*See Sections IV-E for a more detailed description of a FLIR with a TV camera multiplexer.

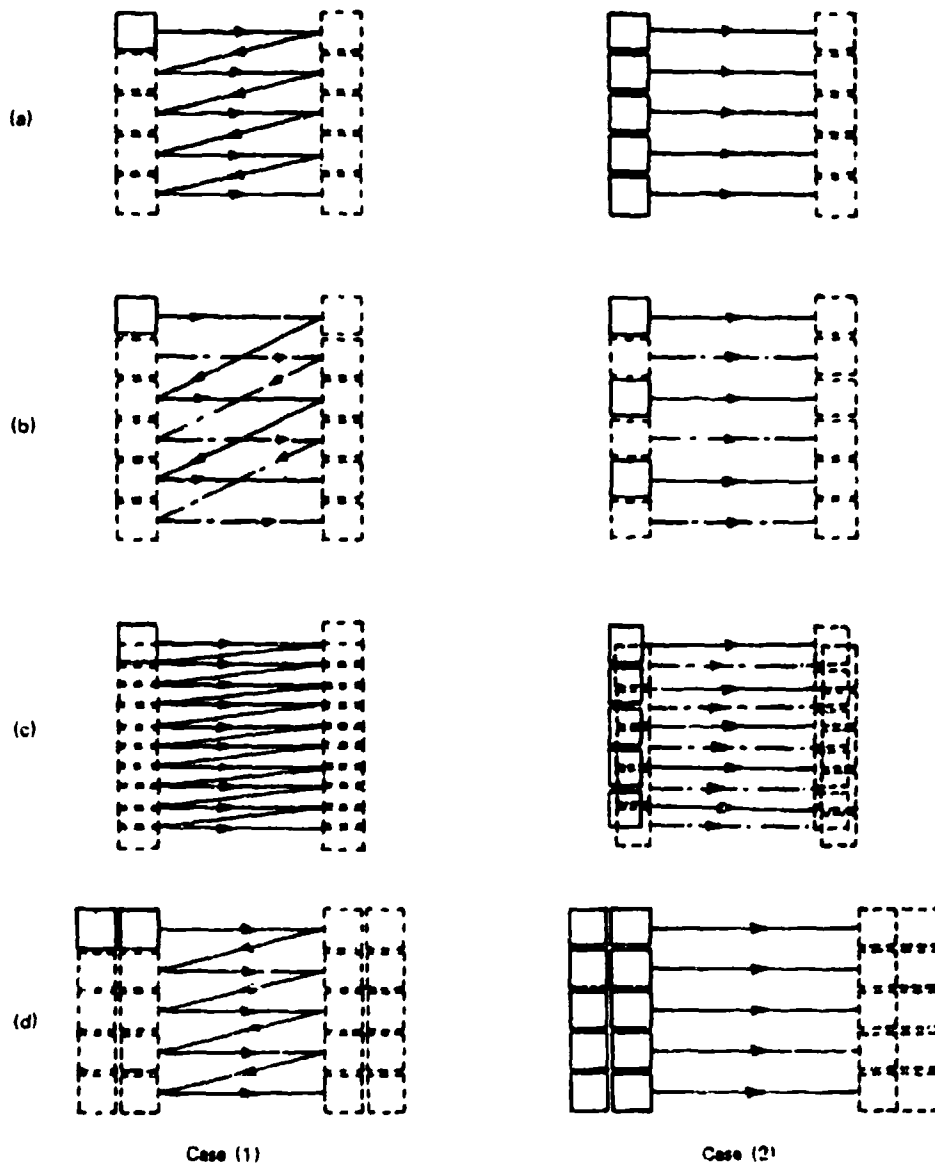


Fig. 4-5 — Various scan configurations employing serial and parallel scan. Also shown are configurations which include interlace and time delay integration.

F. A. ROSELL

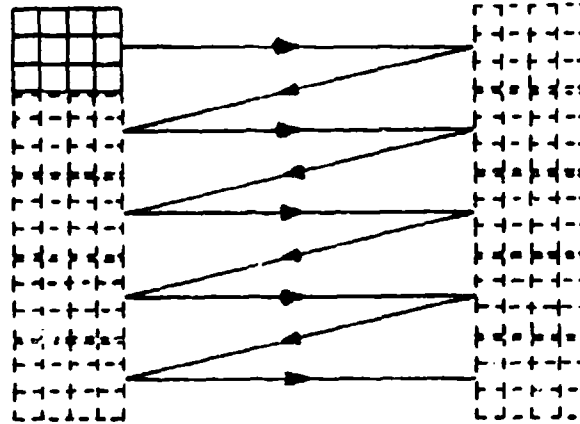


Fig. 4-6 — Serial-parallel scan configuration including time delay integration

Nyquist spatial frequency limit is increased. The amount of overscan need not be exactly a factor of two as shown but is generally between 1 and 2. We define *overscan* as the ratio of the detector height divided by the scan line pitch, where pitch is the distance between adjacent scan lines.

In cases 1(d) and 2(d) we show two detectors in the scan direction. The signals from the first detector are time delayed by one detector dwell time and added to the output of the second. The signal currents add coherently while the noises add incoherently resulting in a sensitivity improvement by the square root of the number of detectors added in the scan direction while detector channel bandwidth remains unchanged. This mode of operation is sometimes called time delay and integration or *TDI*. Another configuration used is a combination of serial, parallel, and time delay integration as shown in Fig. 4-6. The disadvantage of this format is that each of the signals in the parallel channels must be stored for the duration of a line.

In thermal imaging systems practice, it is common to first define a signal-to-noise ratio SNR_{co} for a particular detector (or a number of detectors when a *TDI* scan mode is used) before progressing to the video SNR_{vo} . This intermediate SNR will be defined as the channel SNR_{co} and as shown in Appendix F(B) is equal to*

$$SNR_{co} = \frac{\pi \eta_o}{4 f^2} \frac{(\eta_l a_d \eta_s)^{1/2} D^*(\Omega) K_m \Delta T}{[\Delta f_c]^{1/2}}, \quad (4-9)$$

where

- η_o = transmittance of the objective lens.
- f = focal ratio of the objective lens (focal length/diameter)
- n_l = number of detectors in the *TDI* (or scan) direction

In these preliminary derivations, we will ignore the spectral wavelength dependence of terms such as the optical transmittance, and $D^(\Omega)$ as discussed in Appendix F.

a_d = detector area (cm^2)

η_s = scan efficiency*

$D^*(\Omega_c)$ = detector detectivity for viewing angle Ω_c ($\text{cm Hz}^{1/2} \text{ W}^{-1}$)

K_M = conversion factor between radiance and ΔT ($\text{W cm}^{-2} \text{ sr}^{-1} \text{ K}^{-1}$)

ΔT = temperature difference between scene object and background ($^\circ\text{C}$)

Δf_{co} = detector channel bandwidth (Hz)

Observe that the subscript zero has been added to SNR_c to imply that its measurement was made with a broad area image as discussed in connection with Eq. (4-8)

A reference bandwidth† is defined here as

$$\Delta f_{cr} = 1/2 T_d \quad (4-10)$$

where T_d is the time that a detector dwells on a point on the scene. In general, T_d is given by

$$\begin{aligned} T_d &= \frac{\eta_s n_p \omega_l T_f}{O_s \Omega} \\ &= \frac{\eta_s n_p \omega_l}{O_s F_R \Omega} \end{aligned} \quad (4-11)$$

so that

$$\Delta f_{cr} = \frac{O_s F_R \Omega}{2 \eta_s n_p \omega_l} \quad (4-12)$$

where n_p is the number of detectors in the parallel scan direction, O_s is the overscan ratio, Ω is the total field of view ($\phi_x \phi_y$), ω is the instantaneous field of view ($\theta_x \cdot \theta_y$) of a detector, T_f is the frame time, and F_r is the frame rate.

The factor K_M , which relates incremental scene radiance to incremental temperature difference, is defined and derived in Appendix F (B). The quantity K_M , evaluated between the limits 0 to λ_2 , is provided in Table 4-1 for λ_2 from 2 to 13.9 μ . To find the value of K_M for any spectral interval inbetween, the procedure is to subtract the value obtained at the higher limit from that given at the lower limit. For example

$$K_M(0-13 \mu\text{m}) = 12.40 \times 10^{-5}$$

$$K_M(0-8 \mu\text{m}) = 5.15 \times 10^{-5}$$

$$K_M(8-13 \mu\text{m}) = 7.25 \times 10^{-5} \text{ W cm}^{-2} \text{ sr}^{-1} \text{ K}^{-1}$$

*Scan efficiency is the ratio of the time actually spent by the detector in scanning the entire image plane to the frame time

†The reference bandwidth is quite often defined as $\pi/4 T_d$ which is the result of assuming that the channel bandwidth is limited by a simple RC filter with a 3 dB downpoint at $1/2 T_d$. Using this formulation results in an SNR_{cr} that is 0.89 times as large as that using $\Delta f_{cr} = 1/2 T_d$. See Appendix C

Table 4-1—Value* of K_M Integrated from 0 to λ_2 Micrometers in W/cm^2 -sr-K

λ_2	K_M		λ_2	K_M		λ_2	K_M		λ_2	K_M		λ_2	K_M	
2.0	1.14	E-10	4.0	1.38	E-6	6.0	1.80	E-5	8.0	5.15	E-5	10.0	8.59	E-5
2.1	2.96		4.1	1.69		6.1	1.94		8.1	5.33		10.1	8.75	
2.2	6.99		4.2	2.05		6.2	2.09		8.2	5.51		10.2	8.90	
2.3	1.52	E-9	4.3	2.45		6.3	2.23		8.3	5.69		10.3	9.05	
2.4	3.09		4.4	2.91		6.4	2.39		8.4	5.87		10.4	9.20	
2.5	6.00		4.5	3.42		6.5	2.54		8.5	6.05		10.5	9.35	
2.6	1.06	E-8	4.6	3.99		6.6	2.70		8.6	6.22		10.6	9.50	
2.7	1.83		4.7	4.61		6.7	2.86		8.7	6.40		10.7	9.64	
2.8	3.01		4.8	5.30		6.8	3.03		8.8	6.58		10.8	9.78	
2.9	4.76		4.9	6.04		6.9	3.20		8.9	6.75		10.9	9.93	
3.0	7.28		5.0	6.84		7.0	3.37		9.0	6.93		11.0	1.01	E-4
3.1	1.08	E-7	5.1	7.70		7.1	3.54		9.1	7.10		11.1	1.02	
3.2	1.56		5.2	8.62		7.2	3.71		9.2	7.27		11.2	1.03	
3.3	2.19		5.3	9.60		7.3	3.89		9.3	7.44		11.3	1.05	
3.4	3.01		5.4	1.06	E-5	7.4	4.07		9.4	7.61		11.4	1.06	
3.5	4.04		5.5	1.17		7.5	4.24		9.5	7.78		11.5	1.07	
3.6	5.34		5.6	1.29		7.6	4.42		9.6	7.95		11.6	1.09	
3.7	6.92		5.7	1.41		7.7	4.60		9.7	8.11		11.7	1.10	
3.8	8.83		5.8	1.53		7.8	4.78		9.8	8.27		11.8	1.11	
3.9	1.11	E-6	5.9	1.67		7.9	4.96		9.9	8.43		11.9	1.12	

*T = 300 K (ambient)

The noise equivalent temperature difference or NE Δ T is defined as the scene temperature difference above some reference temperature which is just large enough to provide a SNR $_{co}$ equal to 1.0. The two conditions imposed are that the test image be large enough so that the signal amplitude will not be reduced by sensor apertures and that the channel bandwidth be the reference bandwidth defined by Eq. (4-12). By setting SNR $_{co} = 1$ in Eq. (4-9), ΔT becomes NE Δ T and,

$$NE\Delta T = \frac{4f^2}{\pi\eta_o} \frac{[\Delta f_{cr}]^{1/2}}{(n_1 a_d \eta_s)^{1/2} K_M D^*(\Omega)} \quad (4-13)$$

since $f = F_L/D_o$ and since

$$F_L^2 = a_d/\omega_l \quad (4-14)$$

Equation (4-13) may be written as

$$NE\Delta T = \frac{4}{\pi\eta_o} \frac{[a_d \Delta f_{cr}]^{1/2}}{D_o^2 (n_1 \eta_s)^{1/2} \omega_l K_M D^*(\Omega_l)} \quad (4-15)$$

Another form which is sometimes convenient is

$$NE\Delta T = \frac{4f}{\pi\eta_o D_o} \frac{[\Delta f_{cr}]^{1/2}}{(n_1 \omega_l \eta_s)^{1/2} K_M D^*(\Omega_l)} \quad (4-16)$$

The above equation together with Eq. (4-12) becomes

$$NE\Delta T = \frac{4f}{\pi\eta_o D_o} \frac{[O, F_R \Omega]^{1/2}}{[2n_1 \eta_s]^{1/2} \omega_l \eta_s K_M D^*(\Omega)} \quad (4-17)$$

NRL REPORT 8311

The incremental irradiance ΔE as used in the above equations is a value which is integrated over wavelength and D^* is integrated with respect to the spectral distribution of the background irradiance. It is further assumed that the spectral distribution of the scene object which is of interest is similar to that of the background. These assumptions lead to the simplified form of the above equation.* (Also see Appendix F.)

The detectivity may be limited by background fluctuation noise generated in the primary photon-to-electron conversion process, by noise generated in the internal semiconductor processes within the detector, by preamp noise, or by a combination of all three. In some cases an effective D^* is quoted which includes noises such as preamp noise as discussed in Appendix F(C). Also, the special case where the major noise is due to photoconversion of background photons is discussed in this appendix. The detector in this case is said to be background limited and the detectivity in this case is often written as D^*_{BLIP} .

A detector in a TIS can detect photons from sources which are outside the field of view such as the lens housing. These photons after detection constitute an additive noise. However these noises can be reduced considerably by cold shielding. The detector is discussed in Appendix F(C). The intent of the cold shield is to restrict the detector viewfield to the solid angle subtended by the objective lens. If this is the case,

$$D^*(\Omega_c) = 2f\eta_c D^*(2\pi), \quad (4-18)$$

where η_c is the efficiency of the cold shield relative to a perfect cold shield and $D^*(2\pi)$ is the detectivity when the detector is viewing a solid angle of 2π sr of background radiation.

With Eq. (4-18), Eq. (4-16) becomes

$$NE\Delta T = \frac{2}{\pi\eta_o D_o} \frac{[\Delta f_{cr}]^{1/2}}{(n_f \omega_f \eta_s)^{1/2} K_M D^*(2\pi)} \quad (4-19)$$

and Eq. (4-17) becomes

$$NE\Delta T = \frac{2}{\pi\eta_o D_o} \frac{[O_s F_R \Omega]^{1/2}}{[2n_f n_p]^{1/2} \omega_f \eta_s K_M D^*(2\pi)} \quad (4-20)$$

The NE ΔT has the advantage of being electrically measurable and is an indicator of sensor sensitivity. As will be discussed it is not an absolute indicator since a system with an NE ΔT which is inferior (larger) to another may yet produce a superior image on the display to the observer. The NE ΔT is of direct interest to video tracker designers since

$$SNR_{co} = \frac{\Delta T}{NE\Delta T} \quad (4-21)$$

In the case where the detector channels are multiplexed at a rate of one sample per dwell time, the video SNR becomes n_p times the channel bandwidth. To compute the video SNR in this case we observe that the signal, the mean square noise, and the bandwidth all increase directly as the number of detectors in parallel. Thus

$$SNR_{co} = \frac{\pi\eta_o}{4f^2} \frac{n_p (n_f a_d \eta_s)^{1/2} [D^*(\Omega_c)/n_p^{1/2}] K_M \Delta T}{[n_p \Delta f_{cr}]^{1/2}} \quad (4-22)$$

*The simplified forms above also assume that average values of spectrally dependent quantities such as optical efficiency, η_o , taken over the spectral bandpass of the system can be used which is a usual engineering approximation.

and as can be seen, n_p cancels out and thus the broad area video SNR is identical to the SNR_{co} of Eq. (4-9) for the case where the multiplexing rate is one sample per dwell time. In some cases, the detector output may be, for example, sampled twice per dwell time which would have the effect of doubling the video bandwidth and would increase the measured NE ΔT by $\sqrt{2}$. The quality of the image viewed by the observer will, however, increase instead of decrease because overall sensitivity stays the same while the increased sample rate improves sensor MTF and decreases aliasing effects as will be discussed in Appendix G.

The interest in the channel and video SNR stems in part from the relationship given in Eq. (4-8) which relates the SNR_D to the SNR_{vo} . The video bandwidth in the simplified derivation leading to Eq. (4-8) is immaterial in principle so long as it is the same as that used to measure SNR_{vo} . If, however, NE ΔT is used to compute SNR_{vo} , then the video bandwidth must be $n_p \Delta f_{cr}$. Strictly speaking, Eq. (4-8) applies only when the noise is band-limited white noise, i.e., noise which has a uniform spectral power density within the video bandpass. The case where the noise is nonwhite is treated in Appendix D.

Because it is wished to employ Fourier methods of analysis when sensor aperture affects are to be taken into account in later sections, it is convenient to describe the image dimension in terms of its reciprocal dimensions. Therefore, we define the image at this point to be a rectangle of size

$$a = \Delta x \Delta y = \epsilon \Delta x^2, \quad (4-23)$$

where $\epsilon = \Delta y / \Delta x$. Also, we define the quantity N , which will be termed a spatial frequency, as

$$N = Y / \Delta x, \quad (4-24)$$

where Y is the effective height of the image focal plane as shown in Fig. 4-3. The units of N are reciprocal picture heights or, more commonly, lines per picture height. The virtue of N as a measure of spatial frequency is that it is dimensionless which is a convenience when computing overall sensor modulation transfer function, and N relates most directly to the displayed information that the sensor is capable of displaying. With the above definitions, Eq. (4-8) become

$$\begin{aligned} \text{SNR}_D &= \left[\frac{2 T_c \epsilon \Delta x^2 \Delta f_s}{\alpha Y^2} \right]^{1/2} \text{SNR}_{vo} \\ &= \left[\frac{2 T_c \epsilon \Delta f_s}{\alpha} \right]^{1/2} \frac{1}{N} \text{SNR}_{vo} \end{aligned} \quad (4-25)$$

where $A = \alpha Y^2$ is the effective image focal plane area when α is the picture aspect ratio (horizontal to vertical). Note that α may be written as φ_H / φ_V , the ratio of the horizontal to the vertical field of view.

By rewriting Eq. (4-22) in terms of a video bandwidth, we obtain

$$\text{SNR}_{vo} = \frac{\pi \eta_o}{4 f^2} \frac{(n_p a_f \omega_f / \eta_s)^{1/2} D^*(\Omega_c) K_M \Delta T}{[\Delta f_s]^{1/2}}, \quad (4-26)$$

and by substitution of Eq. (4-26) into Eq. (4-25), the relation

$$\text{SNR}_D = \left[\frac{2 T_c \epsilon}{\alpha} \right]^{1/2} \frac{1}{N} \frac{\pi \eta_o (n_p n_f a_f \eta_s)^{1/2} D^*(\Omega_c) K_M \Delta T}{4 f^2}, \quad (4-27)$$

or by use of Eq. (4-14),

$$\text{SNR}_D = \left[\frac{2T_c \epsilon}{\alpha} \right]^{1/2} \frac{1}{N} \frac{\pi \eta_o D_o (n_f n_p \omega_f n_s)^{1/2} D^*(\Omega_c) K_M \Delta T}{4f} \quad (4-28)$$

or by use of Eq. (4-18) for the BLIP detector case with cold shield,

$$\text{SNR}_D = \left[\frac{2T_c \epsilon}{\alpha} \right]^{1/2} \frac{1}{N} \frac{\pi \eta_o D_o (n_f n_p \omega_f n_s)^{1/2} \eta_c D^*(2\pi) K_M \Delta T}{2} \quad (4-29)$$

Note that the video bandwidth cancels out.

The use of N measured in lines or half-cycles per picture height is standard in television practice not only because of the analytical benefits noted above but because TV camera lenses can be changed at will. FLIR lenses are generally designed in because of cold shielding requirements. As a result one measure of spatial frequency which is commonly used in FLIR analysis and design is k_θ which is measured in line pairs or cycles per milliradian. The conversion of N to k_θ is given by

$$N = \frac{2000 Y k_\theta}{F_L} \quad (4-30)$$

and because the vertical field of view φ_v is approximately Y/F_L ,

$$N = 2000 \varphi_v \quad (4-31)$$

where φ_v is measured in milliradians. Equation (4-31) can be substituted into either Eqs. (4-28) or (4-29) directly.

Equation (4-28) can be rearranged to read

$$\text{SNR}_D = \left[\frac{2T_c \eta_p \Delta f_r}{\alpha} \right]^{1/2} \frac{1}{N} \frac{\pi \eta_o D_o (n_f \omega_f \eta_s)^{1/2} D^*(\Omega_c) K_M \Delta T}{4f [\Delta f_r]^{1/2}} \quad (4-32)$$

where we have also multiplied the numerator and denominator by $\Delta f_r^{1/2}$. The term to the far right can be recognized as being equal to $\Delta T/NE\Delta T$ by comparison with Eq. (4-16) and if we define $\eta_p \Delta f_r$ as the reference video bandwidth, Δf_r , Eq. (4-32) becomes

$$\text{SNR}_D = \left[\frac{2T_c \epsilon \Delta f_r}{\alpha} \right]^{1/2} \frac{1}{N} \frac{\Delta T}{NE\Delta T} \quad (4-33)$$

This form is convenient when noise sources are of a simple form and when there is no need to take into account the detailed effects of sensor apertures on the noises.

In FLIR modeling practice, it is usual to calculate $NE\Delta T$ but it has not been customary to calculate SNR_D or SNR_B . The reason is that the first generations of FLIR have been comparatively simple and it has been generally possible to specify the detectivity of the detectors by a simple number or an equivalent detectivity including perhaps an additional noise as shown in Appendix F(C). In this case, it is usually simpler to calculate the minimum resolvable temperature, or MRT, directly as shown in Chapter V without an intermediate SNR_D step. This procedure will probably change in the future both as our understanding of the modeling process increases and with the advent of more advanced FLIRs. For example, if observer retinal noise characteristics are added in, then its noise would be difficult to put into the detectivity definition. Also multiple noises with rather widely varying bandwidths may be involved which

makes the simple lumped detectivity concept very cumbersome. Even with current systems the simple approach begins to break down if it is wished to make the calculations by using the actual noise power of the detector and if aperture correction of either the preamp, the multiplexer, or the display is used.

E. THE EFFECTS OF FINITE SENSOR APERTURES

If an imaging sensor were perfect, the image of a point source would appear as a point in the displayed image and all images would be transmitted through the sensor with perfect fidelity. In reality, the displayed image will differ from the scene object in amplitude, shape, position, or all three due to finite sensor apertures such as the lens, the finite dimensions of the detector, the multiplexer, the finite dimensions of the displays electron scanning beam, *etc.* To illustrate the effect of an aperture, consider the point source object of Fig. 4-7 (a). Due to diffraction, chromatic and geometric aberrations, and imperfect focus, a point in object space will be imaged by the lens as a blur in image space. An equation representing the image intensity vs the x, y coordinates in the image plane is known as the *point spread function*. Similarly, an equation representing the blurred line of Fig. 4-7 (b) is known as the *line spread function*. If the aperture responses are linear, the point and line spread functions can be Fourier transformed and the sensory system can be analyzed in the frequency domain.

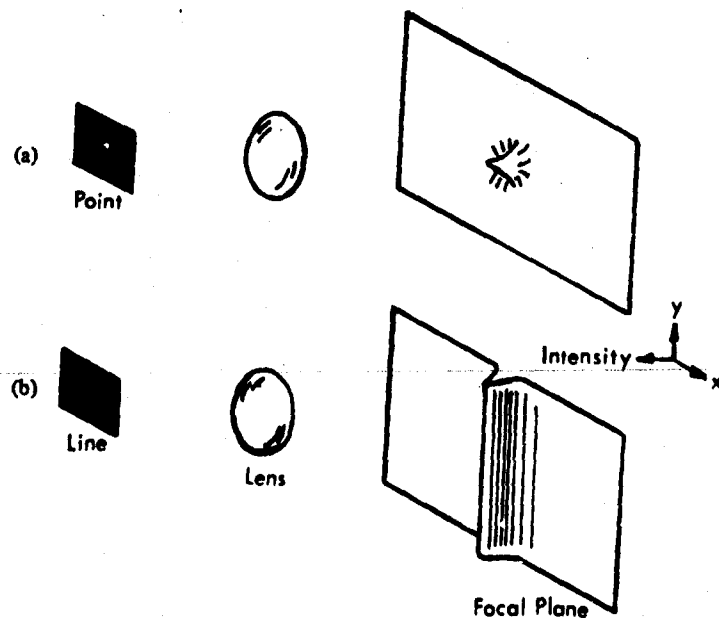


Fig. 4-7 — Effect of a finite aperture on a point and line source image

The methods of analyses are discussed extensively in Appendix D. Appendix C discusses a model using a matched filter concept for the human eye while Appendix D treats the eye as a synchronous integrator. Both approaches give similar results. The methods and results of Appendix D will be used in the treatment which follows.

To illustrate the methods of analysis, we will first consider the system of Fig. 4-8 which employs a TV camera to perform the multiplexing operation. The image of the scene is projected onto the line array of detectors by the first lens. The output of each detector is amplified and used to modulate a light-emitting diode or LED. The detectors and the LED's are scanned in the horizontal direction by mirrors (not shown). During each scan, the TV camera stores the image created by the LED array and the stored image is subsequently read out by the TV pickup tube's electron scanning beam. The resulting signals are amplified and used to modulate the display beam which creates a visible light image on the CRT phosphor of contrast proportional to the radiation contrast of the photoconverted scene. In the horizontal direction, the signals are analog so that sampling effects need not be considered. However this is not true in the vertical direction.

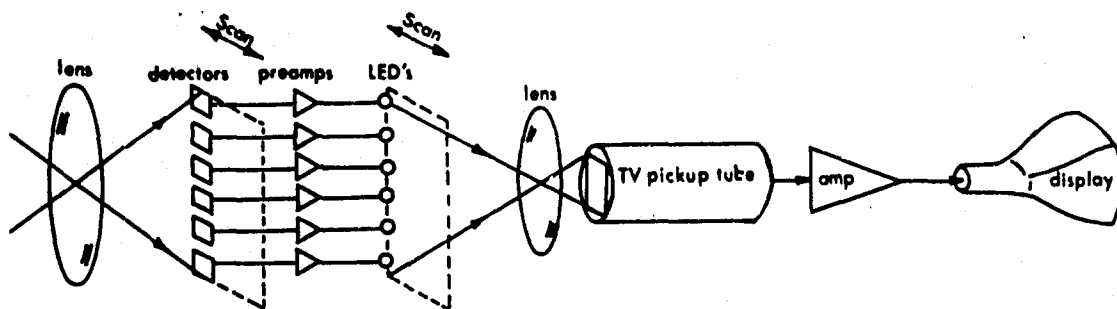


Fig. 4-8 — Schematic representation of a basic FLIR configuration

We will consider two basic types of test objects which are aperiodic objects (defined here to be isolated rectangular images on a uniform background) and periodic bar patterns. To focus on first-order effects, we will initially consider the rectangles and bars to be long relative to their width so that the effects of the sensor apertures on bar length can be considered trivial. The analysis can then proceed on a one-dimensional basis so far as the apertures are concerned. It is further assumed that the perception of the displayed image is limited by sensor-generated, rather than retinal fluctuation, noise.

The most prominent and usually dominant noise generated within the usual FLIR system is due to the photoconversion of photons to electrons by the detectors. Other noises such as inverse frequency-dependent noise and preamp noise which may occur are frequently lumped and incorporated in the D^* specification. In first-order analysis, it is common to consider there to be only one noise source and that the character of the noise is white. These assumptions are by no means necessary: multiple noise sources of nonwhite character are readily treated as discussed in Appendix D but we shall assume only one noise source in the analysis that immediately follows.

In the synchronous integrator concept of the human eye-brain combination as discussed in Appendix D, it is assumed that while the image of an aperiodic object is smeared out or blurred by the finite sensor apertures, the observer will extend his limits of spatial integration as required so as to recover all of the signal. However, in extending the integration distance to recover the signal, more background noise is also integrated. Since a sensor aperture is also a filter, the aperture may also reduce the noise of the aperture follows a point of noise insertion. Thus, while an aperture can both increase and decrease if the noise an observer will perceive,

the increase will always be larger than the decrease and the net effect on the SNR_D will always be a decrease.* A functional block diagram of the sensor apertures corresponding to the system of Fig. 4-8 is shown in Fig. 4-9. The sensor optical transfer functions are symbolically denoted as $R_o()$ and the magnitudes of $R_o()$ are called the aperture's modulation transfer function or MTF.

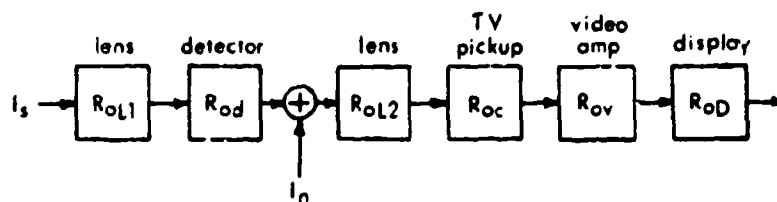


Fig. 4-9 — Functional diagram for the system of Fig. 4-7 showing sensor apertures and point of noise insertion

The equations that describe the effects of apertures on the models for bar pattern detection differ substantially from those used to model simple rectangle detection because of the effects the apertures have on the signal waveform and not because of any substantial difference in the observer's detection process (although some differences exist). In the aperiodic case, the displayed images waveform is smeared out and may be reduced in amplitude by apertures. However the area under the output waveform is identical to the area under the input waveform. As noted above, it is assumed that the observer will simply extend his spatial integration limits to recover all of the signal. However, in the process, the amount of noise perceived increases since the limits of signal integration now include more noise from the background. This is discussed in detail in connection with Fig. D-2 of Appendix D. In the periodic case, the image of a bar pattern is also blurred by apertures but the period of the output waveform is identical to the period of the input waveform and it is therefore assumed that the noise integration distance remains unchanged by aperture effects. The primary effect of apertures on bar pattern detection is to reduce signal amplitude (more correctly, the area under the output waveform decreases as discussed in connection with Fig. D-12 of Appendix D). To summarize, the effect of apertures on aperiodic test objects is to increase the noise integration distance leaving the integrated signal unchanged while in the periodic test object case, the effect is to reduce integrated signal leaving the noise integration distance unchanged.

The periodic bar pattern is the most commonly used test pattern and sensor performance is generally specified in terms of the highest spatial frequency that an observer can resolve on the sensor's display as a function of the pattern's radiant exitance or temperature differential. For the basic FLIR configuration shown schematically in Fig. 4-8 and functionally as a block diagram in Fig. 4-9, the SNR_D may be written as

$$SNR_D = \left[\frac{2T_s \epsilon \Delta f_{sc}}{\alpha} \right]^{1/2} \frac{R_s(N)}{N \cdot \beta(N)^{1/2}} SNR_{im} \quad (4-34)$$

where $R_s(N)$, the square wave flux response and $\beta(N)$ the noise filtering function are to be defined. The SNR_D , as in the case of the aperiodic object, is computed on the basis of a single

*The net SNR_D will always be a decrease except possibly in the sampled data direction where the apertures are a part of the pre- and postfiltering operation and thus are both necessary to image reconstruction and to the prevention of spurious response.

bar; the assumption being that an observer, to resolve the presence of a bar pattern, must resolve a single bar in the pattern. In the periodic case, all of the apertures shown on the block diagram of Fig. 4-9 act to reduce the integrated signal under the output waveform. If the individual aperture responses are linear, then all of the aperture responses may be lumped as follows.*

$$R_{os}(N) = R_{oL}(N) \cdot R_{od}(N) \cdot R_{oL2}(N) \cdot R_{oc}(N) \cdot R_{ov}(N) \cdot R_{oD}(N), \quad (4-35)$$

where $R_{os}(n)$ is the oversensory system MTF. The square wave flux response is determined from the above equation and

$$R_{sf}(N) = \frac{8}{\pi^2} \sum_{k=1}^{\infty} \frac{R_{os}[(2k-1)N]}{(2k-1)^2}. \quad (4-36)$$

The noise filtering factor $\beta(n)$ includes only those MTFs that follow the point of noise insertion which are

$$R_{of}(N) = R_{oL2}(N) \cdot R_{oc}(N) \cdot R_{ov}(N) \cdot R_{oD}(N) \quad (4-37)$$

and $\beta(N)$ is obtained from the approximation

$$\beta(N) = \frac{\int_0^{\infty} R_{of}^2(N) dN}{N_{ef}} \quad (4-38)$$

Alternatively $\beta(N)$ can be obtained from the approximation

$$\beta(N) = 1/[1 + (N/N_{ef})^2]^{1/2}, \quad (4-39)$$

where N_{ef} , the noise equivalent bandwidth of those apertures which follow the point of noise insertion, is given by

$$N_{ef}(N) = \int_0^{\infty} R_{of}^2(N) dN. \quad (4-40)$$

$R_{of}(N)$, $\beta(N)$, and $N_{ef}(N)$ are usually evaluated numerically.

It is observed that a bar pattern is periodic in one direction and aperiodic along the length of the bar. Usually the length of the bars are sufficiently long so that the noise increase and filtering effects along the bar can be ignored. If the bar lengths are short, then Eq. (4-34) would be written as

$$\text{SNR}_D = \left[\frac{2T_e \Delta f_w}{\alpha} \right]^{1/2} \frac{R_{sf}(N)}{[\Gamma_y(N) \xi_y(N) \beta_x(N)]^{1/2}} \text{SNR}_{vo}, \quad (4-41)$$

where the bars are assumed to be periodic in x and aperiodic in y and, $\Gamma_y(N)$ and $\xi_y(N)$ are the noise filtering and increase factors respectively. Assuming that these factors can be neglected, Eq. (4-34) together with Eq. (4-28) may be written as

$$\text{SNR}_D = \left[\frac{2T_e \epsilon}{\alpha} \right]^{1/2} \frac{R_{sf}(N)}{\beta(N)^{1/2}} \frac{\pi \eta_o D_o (\eta_f \eta_p \omega_f \eta_s)^{1/2} D^* (\Omega_c) K_M \Delta T}{4f}. \quad (4-42)$$

*The spatial frequency may be expressed in other units such as k/μ if care is exercised in scaling the MTFs as previously discussed. The chance of error is reduced if the overall MTFs and specialized terms are carried forward as dimensionless units until the end and then converted to the dimensional units desired.

F. A. ROSELL

The noise equivalent bandwidth of any aperture is defined in general by

$$N_e = \int_0^\infty R_o^2(N) dN \quad (4-43)$$

or

$$N_e = 2 \int_0^\infty R_o^2(k_\rho) dk_\rho$$

and the noise equivalent aperture is defined in general by

$$\delta_e = \frac{1}{N_e} \quad (4-44)$$

The meaning of δ_e can be visualized by reference to Fig. 4-10. If an image impulse (a point source) is passed through a Gaussian filter, the output waveform will be as shown in the figure. The shaded area bounded by δ_e is the distance over which the eye is assumed to integrate noise. This is less than the distance over which the signal was assumed to be integrated, but some means had to be found to bound the noise integration limits. However the difference is not large in effect because the shaded area in Fig. 4-9 is 0.92 times the total area integrated over infinite limits. The quantity δ_e may be thought of as a noise equivalent blur distance. When a number of apertures are cascaded the following approximations are sometimes useful.

$$\delta_{e1}^2 = \delta_{e1}^2 + \delta_{e2}^2 + \delta_{e3}^2 + \dots + \delta_{en}^2 \quad (4-45)$$

$$\frac{1}{N_{e1}^2} = \frac{1}{N_{e1}^2} + \frac{1}{N_{e2}^2} + \frac{1}{N_{e3}^2} + \dots + \frac{1}{N_{en}^2} \quad (4-46)$$

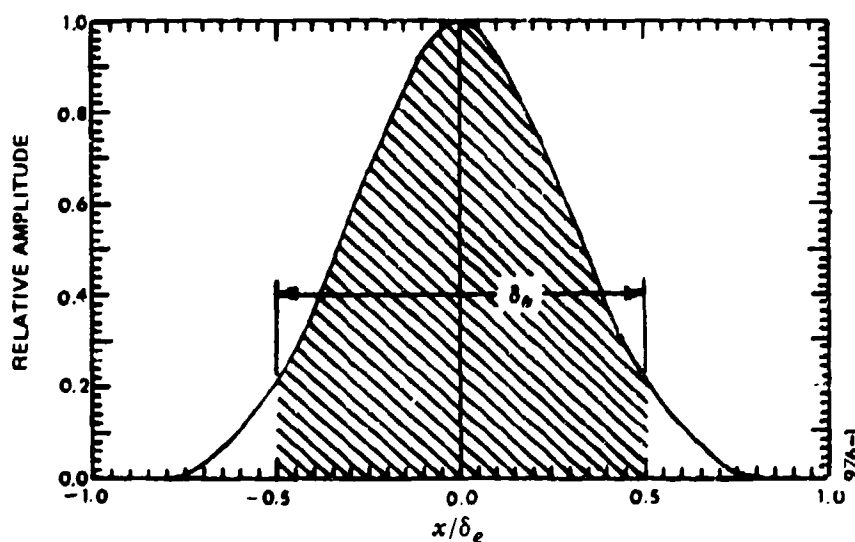


Fig. 4-10 — Noise integration distance for a point image after the image has passed through a Gaussian aperture

The aperiodic model is seldom used in either analytical modeling or in laboratory or field testing of TIS. However since it is the appropriate model to use when the task is the detection of small objects on a uniform background, the aperiodic model will be reviewed. Equation (4-25) modified to include aperture effects on aperiodic images becomes

$$\text{SNR}_D = \left[\frac{2T_e \epsilon \Delta f_{vr}}{\alpha} \right]^{1/2} \frac{1}{N} \frac{\text{SNR}_{v0}}{[\Gamma(N)\xi(N)]^{1/2}}, \quad (4-47)$$

where $\xi(N)$ is a noise increase factor and $\Gamma(N)$ is a noise filtering factor.

Precise integral expressions are available in Appendix D for the purpose of calculating the noise increase and filter factors but for the purpose of clarity and physical insight, we will use the approximations developed. The approximate noise increase factor is given by

$$\xi(N) = \left[1 + \left(\frac{N}{N_{es}} \right)^2 \right]^{1/2}, \quad (4-48)$$

where N_{es} is the noise equivalent bandwidth as defined by Eq. (4-43) and calculated by using the overall system MTF as given by Eq. (4-35). Alternatively, Eq. (4-48) can be written as

$$\xi(\Delta x) = \left[1 + \left(\frac{\delta_{es}}{\Delta x} \right)^2 \right]^{1/2}, \quad (4-49)$$

where δ_{es} is the overall system noise equivalent aperture as defined by Eq. (4-44) and Δx is the width of the input test pattern in compatible units. It can be seen that when the width of the test object is large relative to the noise equivalent aperture (or "blur diameter"), the noise increase factor is near unity. The noise filtering factor $\Gamma(N)$ is given by

$$\Gamma(N) = \frac{\left[1 + \left(\frac{N}{N_{en}} \right)^2 + \left(\frac{N}{N_{ef}} \right)^2 \right]^{1/2}}{\left[1 + \left(\frac{N}{N_{en}} \right)^2 + 2 \left(\frac{N}{N_{ef}} \right)^2 \right]^{1/2}}, \quad (4-50)$$

where N_{en} is the noise equivalent bandwidth for all of the apertures that precede the point of noise insertion and N_{ef} is the same parameter for all of the apertures that follow the point of noise insertion, i.e., for the block diagram of Fig. 4-8, $R_{on} = R_{oL1} \cdot R_{od}$ and $R_{of} = R_{oL2} \cdot R_{oc} \cdot R_{ov} \cdot R_{oD}$. Now, by analogy to Eq. (4-42) we can write the typical SNR_D equation including apertures for the aperiodic target case as

$$\text{SNR}_D = \left[\frac{2T_e \epsilon}{\alpha} \right]^{1/2} \frac{1}{N} \frac{\pi \eta_o D_o (n_i n_p \omega_f \eta_s)^{1/2}}{[\Gamma_x(N)\xi_x(N)\Gamma_y(N)\xi_y(N)]^{1/2}} \frac{D^*(\Omega_c) K_M \Delta T}{4f}, \quad (4-51)$$

where we have included the effects of the apertures in both directions. In this formulation we have assumed that the spatial dependences of the aperture responses are independent and separable in x and y .

The principal sensor MTFs may include the lens, the instability of sightline, the detector, the multiplexer, and the display. In good design, the lens will be close to diffraction limited. The diffraction limit is of course wavelength dependent. However, to gain some appreciation of the diffraction problem, we have used the simple diffraction equation given by

$$R_{oL}(\nu) = \frac{2}{\pi} \left\{ \cos^{-1} \frac{\nu}{\nu_0} - \frac{\nu}{\nu_0} \left[1 - \left(\frac{\nu}{\nu_0} \right)^2 \right]^{1/2} \right\}, \quad (4-52)$$

where ν is the spatial frequency in arbitrary units. When ν is given in terms of N lines/pict. ht.,

F. A. ROSELL

$$N_0 = \frac{2000 Y}{\lambda f} = \frac{2000 Y D_0}{\lambda F_L} = \frac{2000 \psi_v D_0}{\lambda} \quad (4-53)$$

where λ is the wavelength in μm , ψ_v is the vertical field of view in radians, and D_0 is the diameter of the lens in mm. We plot Eq. (4-53) in Fig. 4-11 for $\lambda = 10\mu\text{m}$ and a ψ_v of 2° for various lens diameters. When ν is given in terms of k_θ cycles/mrad,

$$k_{\theta 0} = \frac{D_0}{\lambda}, \quad (4-54)$$

where D_0 is in mm and λ is in μm . Again, we plot Eq. (4-52) in Fig. 4-12 for $\lambda = 4$ and $10\mu\text{m}$ and the same lens diameter as before. When using k_θ units, the MTFs are independent of the fields of view.

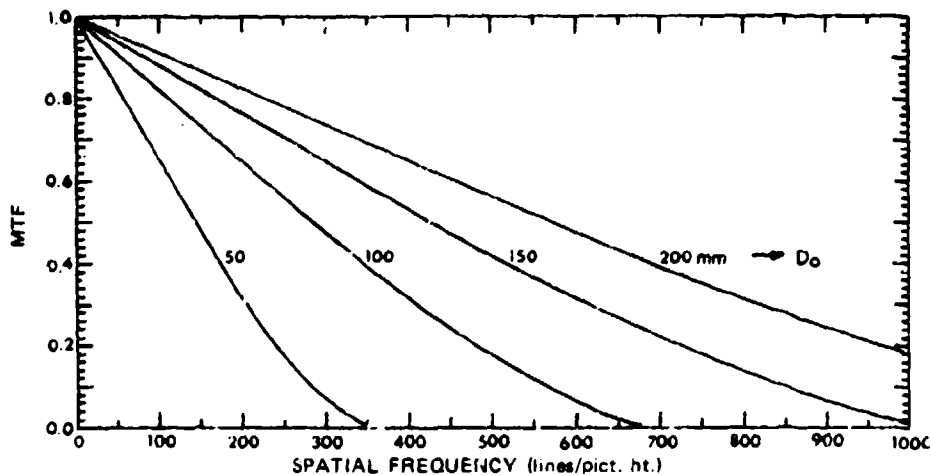


Fig. 4-11 — MTF of diffraction-limited circular lens at $10\mu\text{m}$ with a vertical field of view of 2° . The MTFs are plotted for various lens diameters.

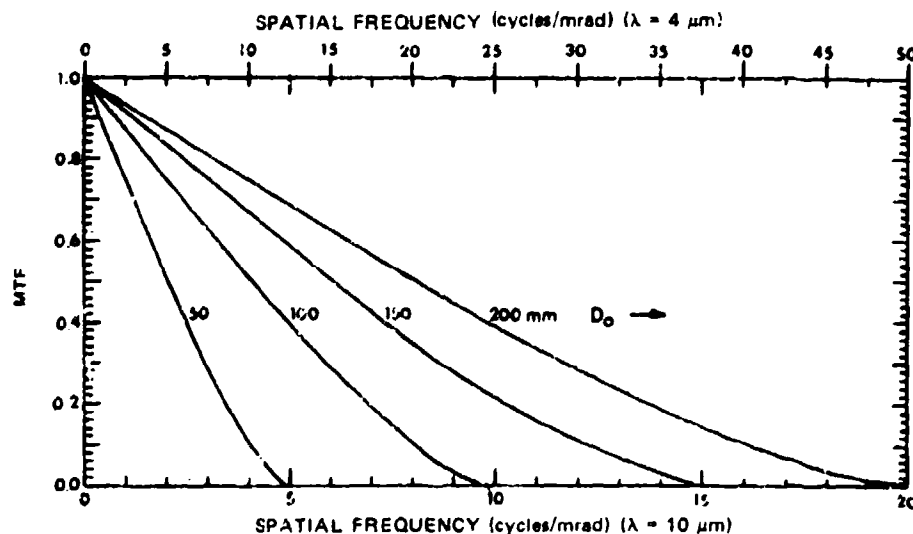


Fig. 4-12 — MTF of diffraction limited circular lens at 4 and $10\mu\text{m}$ for various lens diameters

The effects of sightline instability are well known for television cameras which are integrating sensors but the effects on FLIR systems are not. In the television case, image blur due to instability takes place before readout and therefore each displayed image is blurred and each point in the picture is blurred by about the same amount. In the case of a FLIR using electronic multiplex, each picture displayed should be relatively unblurred since the exposure time over which the motion is integrated is only equal to the detector dwell time rather than the much longer sensor frame time. Each point in the picture can be somewhat displaced from its true position, and the displacement of any given point may be different from that of any other point. When the sightline motion is of the random amplitude variety, each point in the picture will be displaced from the next by an unpredictable and variable amount. The primary integration of the motion will take place in the observer's eye. When the TV camera tube is used as the multiplexer, the motion is still not completely integrated as in conventional TV case although some TV camera tube lag effects may come into play. The psychological experimentation necessary to determine sightline instability effects for FLIR has not been performed. Therefore, the usual procedure is either to ignore motion entirely, which seems rather optimistic, or, to use the TV-derived motional MTFs, which is probably somewhat pessimistic. For random sightline motion, the MTF for TV is given by

$$R_{0m}(N) = \exp - \left[\frac{\pi \theta_A N}{\sqrt{2} \psi_1} \right]^2, \quad (4-55)$$

when N is given in lines/pict. ht. and as

$$R_{0m}(k_\theta) = \exp - [\pi \sqrt{2} \theta_A k_\theta]^2 \quad (4-56)$$

when k_θ is in cycles/mrad and θ_A is in mrad. The quantity θ_A is the rms amplitude of the sightline motion. Equations (4-55) and (4-56) are plotted in Figs. 4-13 and 4-14 respectively. Again, observe that R_{0m} is field-of-view dependent when given in units of N .

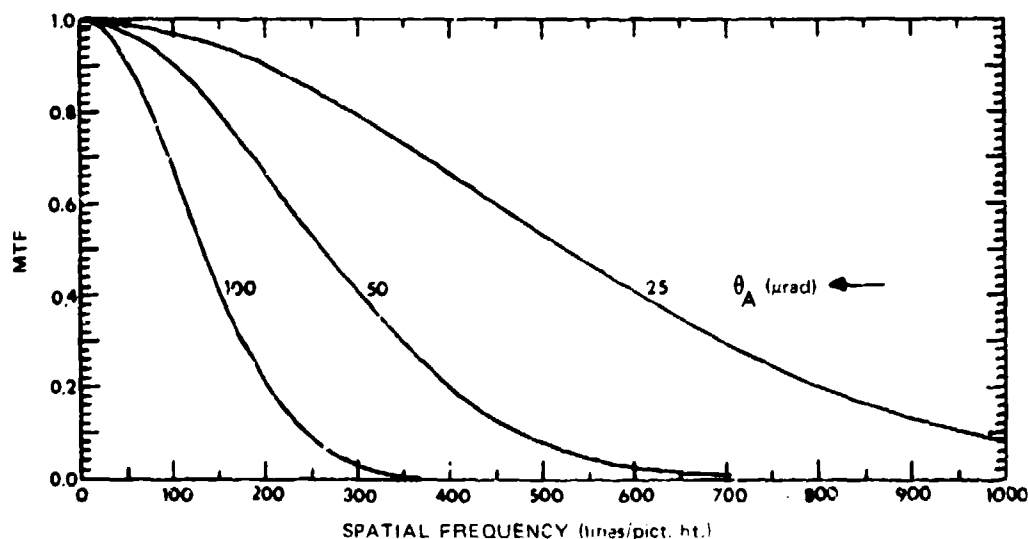


Fig. 4-13 - MTFs due to random sightline motions of amplitude θ_A for a vertical field-of-view of 2.5°

F. A. ROSELL

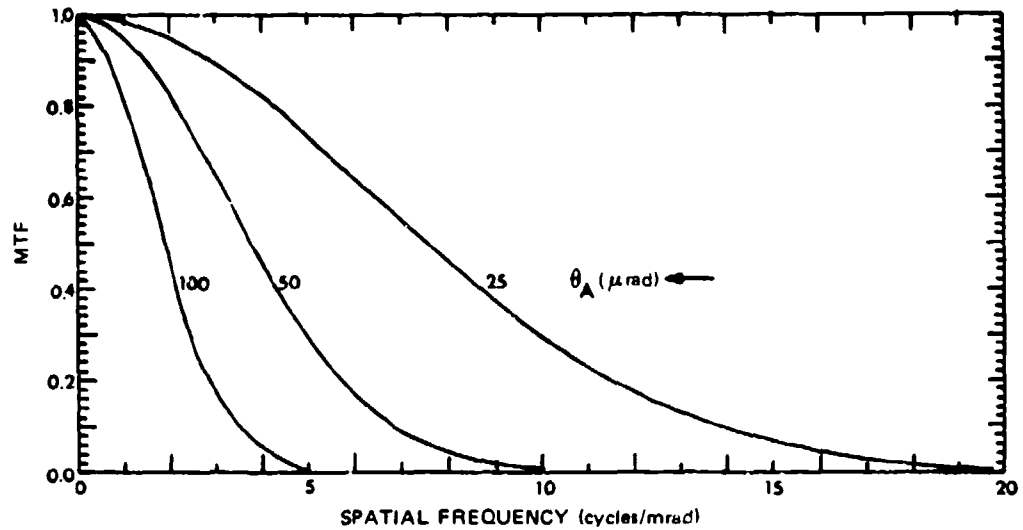


Fig. 4-14 — MTFs due to random sightline motions of amplitude θ_A

The MTF of a detector of size δ in one direction is given by

$$R_{0d}(N) = \frac{\sin(\pi\delta N/2F_L\psi_v)}{\pi\delta N/2F_L\psi_v} \quad (4-57)$$

when N is in lines/pict. ht. Alternatively

$$R_{0d}(N) = \frac{\sin(\pi\theta N/2\psi_v)}{\pi\theta N/2\psi_v} \quad (4-58)$$

where θ is the instantaneous field-of-view of the detector in the appropriate direction. For k_θ in cycles/mrad,

$$R_{0d}(k_\theta) = \frac{\sin(1000\pi\delta k_\theta/F_L)}{1000\pi\delta k_\theta/F_L} \quad (4-59)$$

or

$$R_{0d}(k_\theta) = \frac{\sin\pi\theta k_\theta}{\pi\theta k_\theta} \quad (4-60)$$

when θ is the instantaneous field-of-view in mrad. The above equations apply to the analog scan direction. The case where the signals are sampled is discussed in Appendix G. We plot the detector MTF for $\phi_v/\theta=360$ in Fig. 4-15 and by use of the scale at the top of the graph, the MTF is shown vs k_θ for $\theta = 0.1$ mrad. The various MTFs discussed above plus the MTFs assumed for a TV camera multiplexer and a typical 5" display are shown in Fig. 4-16. The lens MTF assumes a 200-mm diameter, and the sightline motion was assumed to be $50 \mu\text{rad}$ rms. The overall system MTF is shown as R_{0s} . The MTFs due to the LED's and reimaging lens used in the basic FLIR configuration of Fig. 4-8 are assumed to be unity. In Fig. 4-17, we show the overall system square wave amplitude response $R_{sq}(N)$, the sine wave amplitude response $R_0(N)$, or MTF, and the square wave flux response $R_{\phi}(N)$. Also shown is the noise-filtering function, $\beta(N)$, for periodic patterns.

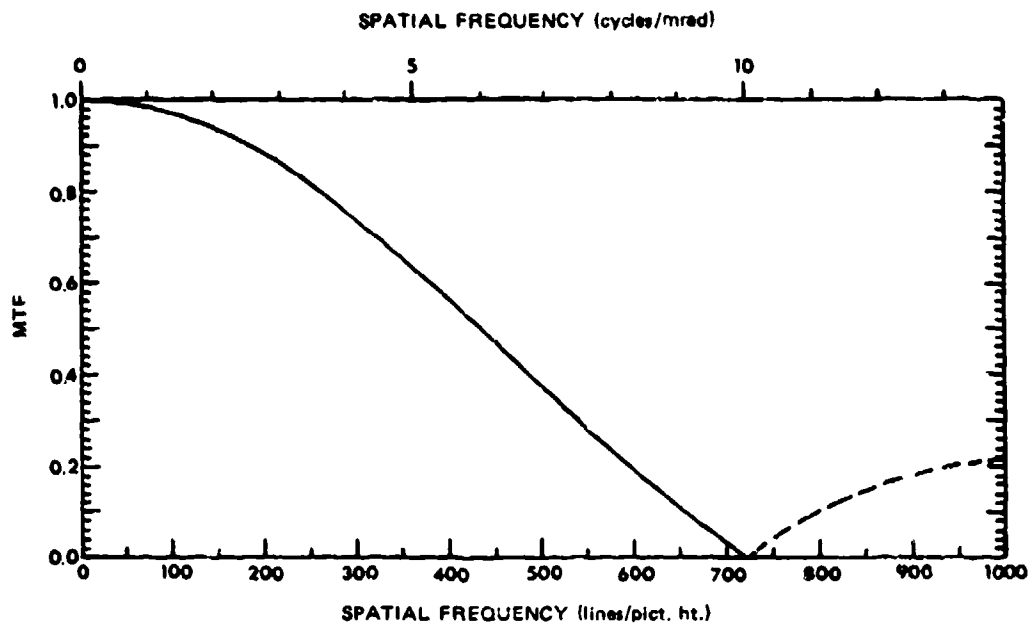


Fig. 4-15 — MTF for a detector vs N for a ϕ_s/θ ratio of 360 and νk_s for an instantaneous field of view of 0.1 mrad

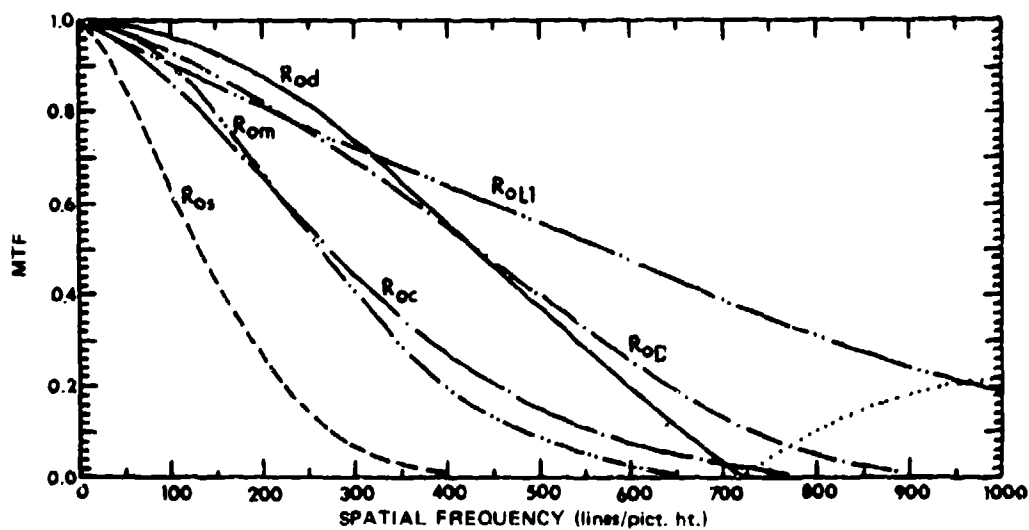


Fig. 4-16 — Overall system MTF, $R_{0i}(N)$, and component MTFs including R_{0L1} (lens), R_{0m} (motion), R_{0d} (detector), R_{0c} (camera tube), and R_{0D} (display)

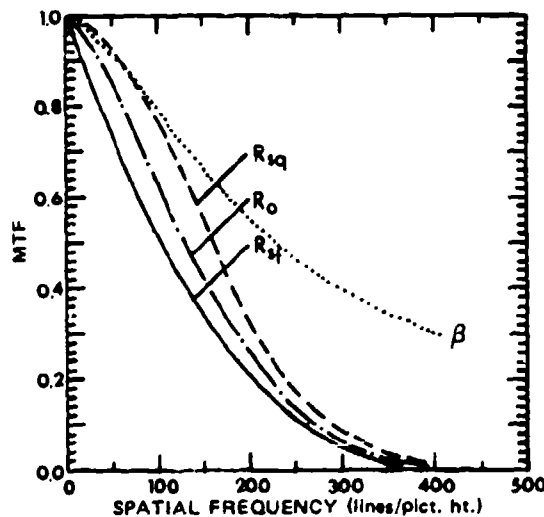


Fig. 4-17 — Square wave amplitude response $R_{sq}(N)$, sine wave amplitude response $R_o(N)$, square wave flux response $R_{sf}(N)$, and noise filtering function, $\beta(N)$ for the assumed sensory system

In low light level television systems, the image blurring takes place in the TV camera tube's gain-storage target which follows the point of photoelectron noise generation (at the photosurfaces) and thus the motion MTF filters the noise and is included in $\beta(N)$. If the blurring takes place in the observer's eye, then again the noise is filtered and would be included in $\beta(N)$. This was assumed in calculating $\beta(N)$ of Fig. 4-17.

The component MTFs used above for illustrational purposes are by no means all inclusive. Other MTFs such as the preamp and video-amplifier responses, the MTF of the LED reimaging system, and even the MTF of the observer's eye may be involved in the overall imaging process.

It should also be observed that certain MTFs can be partially compensated (Ref. 4-8). If an aperture has the functional frequency response $R_o(N)$, the ideal corrector would be $R_o^{-1}(N)$. Note that the corrector's response must be the inverse of both the magnitude and phase terms of $R_o(N)$. In the example described by the functional block diagram of Fig. 4-8, it will be found that an attempt to compensate the lens and detector will be unfruitful because these apertures precede the point of noise insertion and both signals and noises will be amplified alike by the compensator. However, it is possible to compensate the reimaging lens, R_{oL2} , and the TV camera, R_{oc} , which follows the noise. In this case, it will be found that compensation increases both signal and noise but the signal increases faster. It has been found in practice that the improvement obtainable can be appreciable for this specific case.

F. NUMERICAL EXAMPLE

In Table 4-2, the parameters of a hypothetical FLIR are summarized. It is assumed that the basic FLIR configuration of Fig. 4-8 is used. A vertical array of 180 detectors interlaced 2:1 is used to provide 360 scan lines without overlap. The reference channel bandwidth from Eq. (4-12) may be written as

$$\Delta f_{cr} = \frac{O, F_R \Omega}{2\eta_s \eta_p \omega_l} = \frac{1 \cdot 30 \cdot 36 \cdot 48}{2 \cdot 0.75 \cdot 180 \cdot 0.1 \cdot 0.1} = 19,200 \text{ Hz.}$$

NRL REPORT 8311

Table 4-2 — Hypothetical FLIR Parameters

Field of View	Ω	36×48 mrad
Instantaneous Field of View	ω_I	0.1×0.1 mrad
Lens		
Diameter	D_o	200 mm
Focal Length	F_L	500 mm
Focal Ratio	f	2.5
Efficiency	η_o	0.65
Picture Aspect Ratio	α	4/3
Frame Rate	F_R	30/s
Interlace Ratio	K_{I_0}	2/1
Detectors		
Size	$\delta_x \delta_y$	$.05 \times .05$ mm
Number	η_p	180
Scan Efficiency	η_{sc}	0.75
Detectivity	$D^* (2\pi)$	1.3×10^{10} cm Hz ^{1/2} W ⁻¹
Cold Shield Efficiency		0.7
Incremental Scene Radiance		
Spectral Band	$\Delta\lambda$	8.0 — 11.5 μ m
Temperature	T	300 K
ΔT Proportionality Factor	K_M	5.55×10^{-5} W/cm ² -sr-K

by using the parameters of Table 4-2. The NE ΔT calculated from Eq. (4-19) is

$$\begin{aligned}
 \text{NE}\Delta T &= \frac{2}{\pi \eta_o D_o} \frac{[\Delta f_c]^{1/2}}{(\eta_I \omega_I \eta_s)^{1/2} K_M D^* (2\pi)} \\
 &= \frac{2[19, 200]^{1/2}}{\pi \cdot 0.65 \cdot 20 \cdot 0.7 (1 \times 10^{-8} \times 0.75)^{1/2} \cdot 5.5 \times 10^{-5} \cdot 1.3 \times 10^{10}} = 0.157^\circ.
 \end{aligned}$$

The SNR_D obtainable from the sensory system assuming a unity MTF is calculated from Eq. (4-33) as follows

$$\begin{aligned}
 \text{SNR}_D &= \left[\frac{2 T_c \epsilon \Delta f_c}{\alpha} \right]^{1/2} \frac{1}{N} \frac{\Delta T}{\text{NE}\Delta T} \\
 &= \left[\frac{2 \cdot 0.1 \cdot 7 \cdot 3.46 \cdot 10^6}{4/3} \right]^{1/2} \frac{1}{N} \frac{\Delta T}{0.157} \\
 &= 12,140 \frac{\Delta T}{N}.
 \end{aligned}$$

F. A. ROSELL

where a bar pattern image of 7:1 length-to-width aspect is assumed. This equation is plotted in Fig. 4-18 for various values of ΔT . When the test image is an isolated rectangle and when the principal noise is white noise developed in the detector's photoconversion process, then

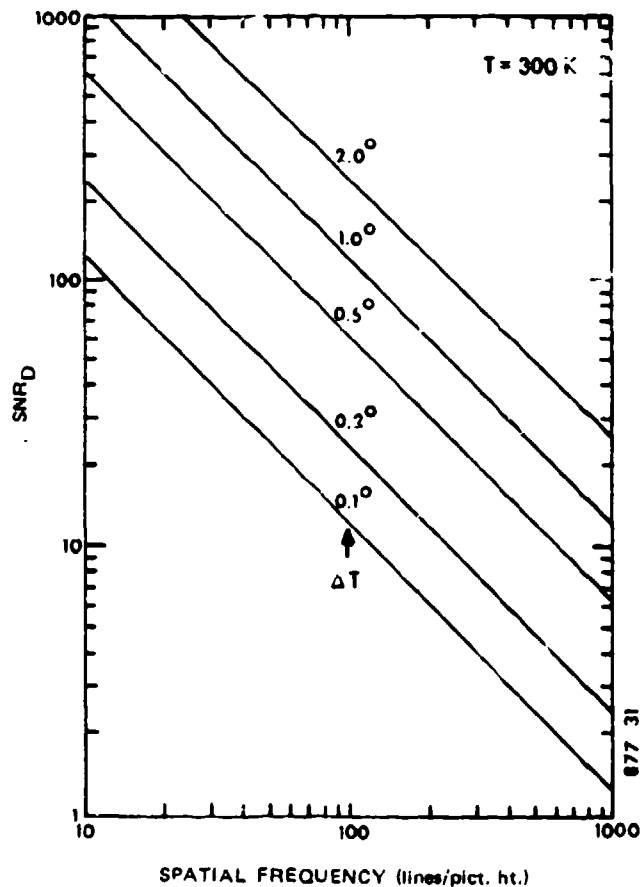
$$SNR_D = \frac{12,140 \Delta T}{N[\Gamma(N) \xi(N)]^{1/2}}$$

where in the above, we have included the effects of the sensor's finite apertures in the horizontal direction. For periodic bar patterns, the corresponding equation under the same condition is

$$SNR_D = 12,140 \Delta T \cdot \frac{R_{sf}(N)}{N \cdot \beta^{1/2}(N)}$$

The above three equations are plotted in Fig. 4-19 by using the MTFs of Section D for $\Delta T = 1^\circ$. In the above calculations, it is assumed that the bar patterns are vertically oriented and that the effects of the apertures in the vertical direction can be neglected. Observe that the effect of the apertures is to decrease the SNR_D obtainable at the higher line numbers and that the effect of the apertures is much more severe on periodic than aperiodic images.

Fig. 4-18 — SNR_D vs spatial frequency for the assumed sensor with unity MTF



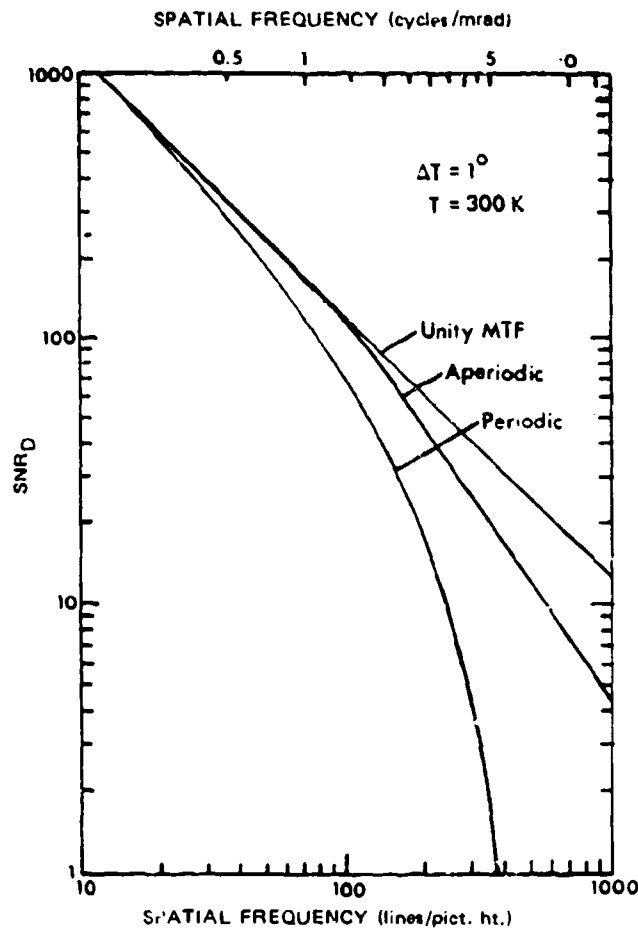


Fig. 4-19 — SNR_D vs spatial frequency for the assumed sensor with unity MTF and for the assumed MTF with periodic and aperiodic test patterns

G. SUMMARY OF THE SIGNIFICANT EQUATIONS

In this section we summarize the more significant equations. The equation numbering corresponds to the original equation numbers as they appeared earlier in this chapter.

Display Signal-to-Noise Ratio

$$SNR_D = \left[2T_e \Delta f_v \left(\frac{a}{A} \right) \right]^{1/2} SNR_{v0} \quad (4.8)$$

SNR_D = display signal-to-noise ratio

T_e = observer's integration time (s)

F. A. ROSELL

Δf_v = video bandwidth (Hz)

a = image area in focal plane (m²)

A = total focal plane area (m²)

e = charge of an electron (coul)

SNR_{v0} = video signal-to-noise ratio

Channel Signal-to-Noise Ratio

$$\text{SNR}_{co} = \frac{\pi \eta_o}{4f^2} \frac{(n_I a_d \eta_s)^{1/2} D^*(\Omega_c) K_M \Delta T}{[\Delta f_c]^{1/2}} \quad (4-9)$$

SNR_{co} = channel signal-to-noise ratio

η_o = lens transmittance

f = lens focal ratio

n_I = no. of TDI detectors

a_d = area of 1 detector (cm²)

η_s = scan efficiency

$D^*(\Omega_c)$ = detector detectivity (cm Hz^{1/2} W⁻¹)

K_M = ΔT conversion factor (W cm⁻² sr⁻¹ K⁻¹)

Δf_c = channel bandwidth (Hz)

ΔT = incremental temperature (K)

Detector Channel Bandwidth (Reference)

$$\Delta f_{cr} = \frac{O_s F_R \Omega}{2 \eta_s n_p \omega_I} \quad (4-12)$$

Δf_{cr} = reference channel bandwidth (Hz)

O_s = overscan ratio

F_R = frame rate (s⁻¹)

Ω = total field of view (sr)

η_s = scan efficiency

n_p = number of parallel detectors

ω_I = instantaneous field of view (sr)

Noise Equivalent Temperature Difference (General)

$$NE\Delta T = \frac{4f^2}{\pi\eta_o} \frac{[\Delta f_{cr}]^{1/2}}{(n_I a_d \eta_s)^{1/2} K_M D^* (\Omega_c)} \quad (4-13)$$

$$= \frac{4}{\pi\eta_o D_o^2} \frac{[a_d \Delta f_{cr}]^{1/2}}{(n_I \eta_s)^{1/2} \omega_I K_M D^* (\Omega_c)} \quad (4-15)$$

$$= \frac{4f}{\pi\eta_o D_o} \frac{[\Delta f_{cr}]^{1/2}}{(n_I \omega_I \eta_s)^{1/2} K_M D^* (\Omega_c)} \quad (4-16)$$

$$= \frac{4f}{\pi\eta_o D_o} \frac{[O_s F_R \Omega]^{1/2}}{[2n_I n_p]^{1/2} \omega_I \eta_s K_M D^* (\Omega_c)} \quad (4-17)$$

Detectivity (BLIP Detectors)

$$D^* (\Omega_c) = 2f \eta_c D^* (2\pi). \quad (4-18)$$

$D^* (\Omega)$ = detectivity for view angle Ω sr

η_c = cold shield efficiency

$D^* (2\pi)$ = detectivity for 2π sr viewing angle

Noise Equivalent Temperature Difference (BLIP Detectors)

$$NE\Delta T = \frac{2}{\pi\eta_o D_o} \frac{[\Delta f_{cr}]^{1/2}}{\eta_c (n_I \omega_I \eta_s)^{1/2} K_M D^* (2\pi)} \quad (4-19)$$

$$= \frac{2}{\pi\eta_o D_o} \frac{[O_s F_R \Omega]^{1/2}}{[2n_I n_p]^{1/2} \omega_I \eta_s \eta_c K_M D^* (2\pi)} \quad (4-20)$$

Channel Signal-to-Noise Ratio

$$SNR_{c,0} = \frac{\Delta T}{NE\Delta T} \quad (4-21)$$

Video Signal-to-Noise Ratio (Broad Area Imager)

$$SNR_{v,0} = \frac{\pi\eta_o}{4f^2} \frac{(n_I a_d \omega_I \eta_s)^{1/2} D^* (\Omega_c) K_M \Delta T}{[\Delta f]^{1/2}} \quad (4-26)$$

$SNR_{v,0}$ = broad area video SNR

Δf_v = video bandwidth (Hz)

F. A. ROSELL

Image Dimensions and Spatial Frequency

$$a = \Delta x \Delta y = \epsilon \Delta x^2. \quad (4-23)$$

$$N = Y/\Delta x. \quad (4-24)$$

$$k_\theta = N/2000\varphi_v. \quad (4-31)$$

ϵ = image aspect ratio $\Delta y/\Delta x$

N = spatial frequency (lines/pict.ht.)

Δx = minimum image dimension (mm)

Y = image plane height (mm)

k_θ = spatial frequency (cycles/mrad)

φ_v = vertical field of view (rad)

SNR_D for General Ideal Sensor (MTF = 1.0)

$$\text{SNR}_D = \left[\frac{2T_e a}{\alpha} \right]^{1/2} \frac{1}{N} \frac{\pi \eta_o (n_p n_i a_s \eta_s)^{1/2} D^* (\Omega_c) K_M \Delta T}{4f^2}. \quad (4-27)$$

SNR_D = display SNR

α = picture aspect ratio (φ_H/φ_v)

φ_H = horizontal field of view (rad)

$$\text{SNR}_D = \left[\frac{2T_e a}{\alpha} \right]^{1/2} \frac{1}{N} \frac{\pi \eta_o D_o (n_p n_i \omega_i \eta_i)^{1/2} D^* (\Omega_c) K_M \Delta T}{4f}. \quad (4-28)$$

$$\text{SNR}_D = \left[\frac{2T_e a \Delta f_w}{\alpha} \right]^{1/2} \frac{1}{N} \frac{\Delta T}{NE\Delta T} \quad (4-33)$$

Δf_w = the reference video bandwidth = $n_p \Delta f_c$ (Hz).

SNR_D for Ideal BLIP Sensor (MTF = 1.0)

$$\text{SNR}_D = \left[\frac{2T_e a}{\alpha} \right]^{1/2} \frac{1}{N} \frac{\pi \eta_o D_c (n_p n_i \omega_i \eta_i)^{1/2} \eta_r D^* (2\pi) K_M \Delta T}{2}. \quad (4-29)$$

NRL REPORT 8311

SNR_D for Periodic Images

$$\text{SNR}_D = \left[\frac{2T_e \Delta f_{\pi}}{\alpha} \right]^{1/2} \frac{R_{sf}(N)}{N \cdot \beta(N)^{1/2}} \text{SNR}_{\infty} \quad (4-34)$$

$R_{sf}(N)$ = square wave flux response

$\beta(N)$ = noise filtering function

Square Wave Flux Response—Periodic Images

$$R_{sf}(N) = \frac{8}{\pi^2} \sum_{k=1}^{\infty} \frac{R_{0s}[(2k-1)N]}{(2k-1)^2} \quad (4-36)$$

Noise Filtering Function for Periodic Images

$$\beta(N) = \frac{\int_0^N R_{sf}(N) dN}{N} \quad (4-38)$$

SNR_D for Aperiodic Images

$$\text{SNR}_D = \left[\frac{2T_e \Delta f_{\pi}}{\alpha} \right]^{1/2} \frac{1}{N} \frac{\text{SNR}_{v0}}{[\Gamma(N) \xi(N)]^{1/2}} \quad (4-47)$$

$\text{SNR}_{v0} = \text{SNR}_{r0}$

$\Gamma(N)$ = noise filtering function

$\xi(N)$ = noise increase function

Noise Increase Function for Aperiodic Images

$$\xi(N) = \left[1 + \left(\frac{N}{N_{es}} \right)^2 \right]^{1/2} \quad (4-48)$$

N_{es} = noise equivalent bandwidth for the overall system

Noise Equivalent Bandwidth

$$N_{es} = \int_0^{\infty} R_0(N) dN \quad (4-43)$$

$R_0(N)$ = modulation transfer function

F. A. ROSELL

Noise Filtering Function

$$\Gamma(N) = \frac{\left[1 + \left(\frac{N}{N_{en}}\right)^2 + \left(\frac{N}{N_{ef}}\right)^2\right]^{1/2}}{\left[1 + \left(\frac{N}{N_{en}}\right)^2 + 2\left(\frac{N}{N_{ef}}\right)^2\right]^{1/2}} \quad (4-50)$$

N_{en} = noise equivalent bandwidth for all apertures
preceding the point of noise insertion

N_{ef} = noise equivalent bandwidth for all apertures
following a point of noise insertion

MTF for a Diffraction Limited Lens

$$R_{0L}(\nu) = \frac{2}{\pi} \left\{ \cos^{-1} \frac{\nu}{\nu_0} - \frac{\nu}{\nu_0} \left[1 - \left(\frac{\nu}{\nu_0} \right)^2 \right]^{1/2} \right\} \quad (4-52)$$

$$N_0 = \frac{2000\psi_v D_0}{\lambda} \quad (4-53)$$

$$k_{\theta 0} = \frac{D_0}{\lambda} \quad (4-54)$$

ψ_v = vertical field of view (rad)

λ = wavelength (μm), when D_0 is in mm

MTF for Random Sightline Motion

$$R_{0m}(k_\theta) = \exp - [\pi \sqrt{2} \theta_A k_\theta]^2 \quad (4-56)$$

$$R_{0m}(N) = \exp - \left[\frac{\pi \theta_A N}{\sqrt{2} \psi_v} \right]^2 \quad (4-55)$$

θ_A = rms angular amplitude of motion

MTF of a Detector in Scan Direction

$$R_{0d}(N) = \frac{\sin(\pi \theta N / 2 \psi_v)}{\pi \theta N / 2 \psi_v} \quad (4-58)$$

NRL REPORT 8311

$$R_{0d}(k_\theta) = \frac{\sin(1000\pi\delta k_\theta/F_L)}{1000\pi\delta k_\theta/F_L} \quad (4-59)$$

$$R_{0d}(k_\theta) = \frac{\sin\pi\theta k_\theta}{\pi\theta k_\theta} \quad (4-60)$$

δ = detector dimension

θ = instantaneous field of view

MTF of a Detector in the Across Scan Direction

$$MTF = R_{0d}^2(N) = \frac{\sin^2(\pi\theta N/2\psi_v)}{(\pi\theta N/2\psi_v)^2} \quad (G-2)$$

REFERENCES

- 4-1 Stevens, S.S., A Neural Quantum in Sensory Discrimination, *Science*, **177**, No 4051, Sept 1972.
- 4-2 Barnes, R&M. Czerny, *Z. Physik*, **79** (1932).
- 4-3 de Vries, Hessel, The Quantum Character of Light and Its Bearing Upon Thresholds of Vision, the Differential Sensitivity and Visual Activity of the Eye, *Physica* **10** (7): 553-564 (1943)
- 4-4 Schade, Otto H., Sr., The Resolving-Power Functions and, Quantum Processes of Television Cameras, *RCA Rev.* **28** (3) 1967, 460-535.
- 4-5 Schade, Otto H., Sr., Optical and Photoelectric Analog of the Eye *JOSA*, **46** (9) 1956: 721-739.
- 4-6 H. P. Lavin, Systems Analysis, Chapter 15, Photoelectronic Imaging Devices, Vol 1, Plenum Press, New York 1971
- 4-7 Rose, Albert, The Sensitivity Performance of the Human Eye on an Absolute Scale. *JOSA* **38**(2) 1948: 196-208
- 4-8 Rosell, F. A., Performance of Electro-optical Sensors Final Technical Report, EOTM No. 575, Contract No. DAAK-53-75-C-0225, Night Vision Laboratory, Ft. Belvoir, Va., Feb. 1977: 154-187.

Chapter V

LABORATORY PERFORMANCE MODEL

F. A. Rosell

A. INTRODUCTION

In Chapter IV, we discussed the notion of an image SNR and methods of calculating the image SNR obtainable on a sensor's display for test images of simple geometry such as rectangles and periodic bar patterns. If the observer's image SNR requirements were known, then the probability that an observer will discern a particular image under a given set of operating conditions can be analytically predicted. The ability to perform such predictions is of considerable aid in the process of designing sensory systems and in the evaluation of proposed designs.

The most commonly used and specified measure of a thermal imaging system's sensitivity and resolution has been designated the minimum resolvable temperature or MRT. The use of this term implies that the test image is a four-bar pattern with the length of each bar in the pattern being seven times its width. The MRT measure is adapted from and is directly analogous to a similar measure devised by television engineers. In the TV case, threshold spatial resolution is plotted as a function of the test patterns irradiance level while in the thermal imaging system (TIS), the threshold incremental temperature difference about a given background temperature, is plotted as a function of the bar pattern spatial frequency. Aside from the interchange of coordinates, the measures used for TIS and TV systems are conceptually identical. The difference in presentation of data is probably due to practical considerations. In the visible spectrum, bar patterns are easy to make and the test procedure most often used is to simultaneously image a number of patterns of different spatial frequency. At a given light level, the observer is asked to select the pattern of highest spatial frequency that he can just barely resolve as a bar pattern. In the TIS case, where patterns are difficult to construct, it was more usual to image a single pattern and then increase or decrease its temperature differential until the pattern becomes just barely perceptible. However more sophisticated test equipment with multiple test patterns are now available for testing TIS systems.

A less commonly used measure for TIS systems is the minimum detectable temperature or MDT. This measure implies that the test image is a square. MDT is plotted as a function of the square's dimensions and thus, it is also a measure of sensitivity and resolution as is MRT. However, MDT is a much less sensitive measure of the effects of the sensor's aperture response. Both MRT and MDT are appropriate measures when the final user of the displayed information is a human observer, since these measures include the ability of the observer to integrate spatially and temporally, and the threshold SNR which determines MRT and MDT is that which has been experimentally determined for observers.

In Section B of this chapter the observer threshold SNRs are briefly summarized. The MRT and MDT equations are derived in terms of these thresholds, and some sample calculations are performed. In Section C, the observer thresholds and the limitations of the threshold measurements are briefly discussed. The psychophysical experiments which led to the threshold value are discussed further in Appendix H.

B. MINIMUM RESOLVABLE TEMPERATURE (MRT) AND MINIMUM DETECTABLE TEMPERATURE (MDT)

The display SNR_D 's obtainable from a sensor when the test images are simple rectangles or periodic bar patterns were derived in Chapter IV. In Section C of this chapter, the results of psychophysical experimentation performed for the purpose of determining the SNR_D required by the observer to discern the simple test images at a given level of probability will be discussed. By matching the SNR_D obtainable from the sensor to that required by the observer, the probability of discerning the image on the sensor's display can be determined. In particular, when the SNR_D required by the observer is set equal to its threshold value for which the probability of discerning a particular image is 50% and when the SNR_D obtainable from the sensor is equal to this threshold value, a measure of sensor resolution and sensitivity is obtained. In the case of a TIS or FLIR, the measure is known as the *minimum resolvable temperature* or MRT when the input test image is a bar pattern and, the *minimum detectable temperature* or MDT when the test image is a square.

The MRT measure is by far the most commonly used. In making the MRT measurement for a real sensor, an observer views the displayed image of a four-bar pattern of 7:1 bar aspect ratio as the temperature differential between it and a uniform background of a fixed temperature is varied either continuously or randomly. In principle, that temperature at which the pattern is discerned 50% of the time by a number of observers or an ensemble of observations is known as the MRT for the spatial frequency of the pattern used. In practice, the measurement is usually made by a trained observer who varies the temperature differential until the pattern can just barely be "resolved." These two methods of measurement have been shown to be fairly comparable and to give consistent results for any given observer and also, between trained observers (Ref. 5-1). The MRT is plotted as a function of spatial frequency.

During the measurement of MRT, the observer is generally free to optimize his viewing distance and to optimize the displayed image contrast and light level. These conditions are not always realizable when viewing real scenes of large dynamic range. The MRT should be interpreted as the absolute minimum temperature difference observable under optimum viewing conditions. From time-to-time a resolvable temperature or RT concept, which includes dynamic range constraints, is proposed but standards for this measurement have not been established.

MDT is not often used in either system design, analysis, or specification although it may be relevant to certain sensory system applications. Its measurement and its condition of measurement are similar to that used to obtain MRT except that the test image is a square. Both MRT and MDT are analytically predictable and if the system parameters are accurately known, the accuracy of the prediction should be within the accuracy of the measurement.

For a 50% probability of detecting rectangles and bar patterns, and an observer integration time of 0.1 s, the recommended values of observer thresholds are as follows.

For Rectangles

If the observer is free to vary his display viewing distance at will, as in making an MDT measurement, the recommended value of the threshold SNR_{DT} is 2.8.

If the display viewing distance is fixed, the recommended value for SNR_{DT} is 2.8 for squares if the angular subtense of the displayed image is neither less than about 4' nor greater

than about 30' of arc relative to the observer's eye. If this is not the case, the threshold value may be obtained from Fig. 5-5.

If the display viewing distance is fixed, the recommended value of threshold SNR_{DT} is 2.8 for rectangles so long as the angular subtense of the rectangle is not greater than about 30' of arc relative to the observer's eye in both dimensions simultaneously. The displayed rectangular image can subtend up to 6° or more in one direction and an SNR_{DT} of 2.8 is still appropriate. If both dimensions are greater than about 30' of arc, assume that the eye integrates an area around the perimeter which has an angular subtense of 8' to 10' of arc* relative to the observer's eye.

For Periodic Bar Patterns

If the observer is free to vary this display viewing distance at will, as in making an MRT measurement, the recommended value of the threshold SNR_{DT} is 2.5. This value generally holds for the lower line numbers but will give somewhat pessimistic threshold resolution predictions at the higher spatial frequencies. (See Figs. 5-6 and 5-7).

If the observer viewing distance is fixed, the threshold value of SNR_D tends to increase at the lower spatial frequencies and decrease at the higher spatial frequencies at short viewing distances and conversely (see Fig. 5-6).

In the aperiodic (rectangular image) case, the SNR_D required to achieve either higher or lower probabilities of detection can be estimated from Table 5-1. The same table can be used for periodic case by use of the ratio column, and by noting that an SNR_{DT} of 2.5 is usual for bar patterns rather than 2.8 as for rectangles.

Table 5-1 — SNR_D Required to Achieve a Given Level of Detection Probability for Rectangular Images

P_d	SNR_D	$\frac{SNR_D}{SNR_{DT}}$	P_d	SNR_D	$\frac{SNR_D}{SNR_{DT}}$
0.1	1.40	0.50	0.7	3.36	1.23
0.2	1.28	0.67	0.8	3.72	1.45
0.3	2.44	0.80	0.9	4.20	1.71
0.4	2.52	0.90	0.95	4.59	1.84
0.5	2.80	1.00	0.99	5.32	1.90
0.6	3.08	1.11	0.995	5.60	2.00

*The 8' to 10' of arc does not appear consistent with the 30' dimension but as is discussed in Section V-C the error in assuming complete spatial integration does not become appreciable until the angular subtense of the image becomes greater than about 30' relative to the eye.

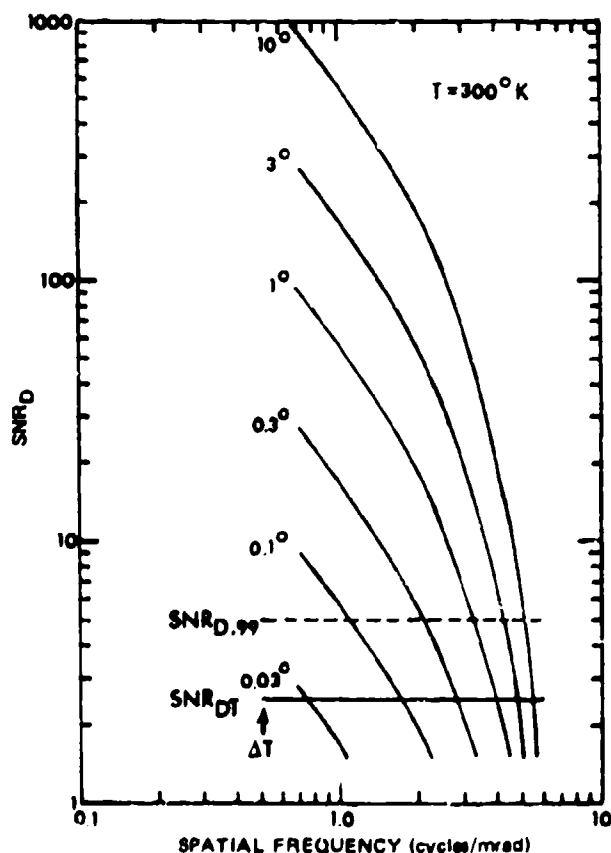
The MRT is quantitatively determined by setting the SNR_D equation equal to its threshold SNR_{DT} value and solving for ΔT which now becomes the MRT. When there are several significant noise sources it is sometimes necessary to plot the SNR_D as shown in Fig. 5-1 for various values of ΔT . The threshold value, assumed to be 2.5, is also plotted as the solid horizontal line in the figure. The intersections of the SNR_D curves with the SNR_{DT} curve give the threshold resolution for the given value of ΔT which is then also the MRT. If a higher value of probability is desired, the value of SNR_{DT} is increased. By use of Table 5-1 we see that a 0.995 probability requires 2 times the SNR_D as a probability of 0.5 and thus a horizontal dashed line is drawn at $\text{SNR}_D = 5$ in Fig. 5-1 and again the intersections give the spatial frequency required at any given value of ΔT . When a single noise term suffices, the MRT may be written in general from Eq. (4-42) as

$$\text{MRT} = \text{SNR}_{DT} \cdot \left[\frac{\alpha}{2\epsilon T_e} \right]^{1/2} \frac{N\beta^{1/2}(N)}{R_{sf}(N)} \frac{4f}{\pi\eta_0 D_0 (n_i n_p \omega_i \eta_s)^{1/2} D^*(\Omega_c) K_M} \quad (5-1)$$

or if the detectors are BLIP

$$\text{MRT} = \text{SNR}_{DT} \cdot \left[\frac{\alpha}{2\epsilon T_e} \right]^{1/2} \frac{N\beta^{1/2}(N)}{R_{sf}(N)} \frac{2}{\pi\eta_0 D_0 (n_i n_p \omega_i \eta_s)^{1/2} \eta_c D^*(2\pi) K_M} \quad (5-2)$$

Fig. 5-1 — Display SNR_D vs spatial frequency for various values of ΔT . Also shown are the SNR_D values at threshold and for a 99% probability of detection.



In either case, by modification of Eq. (4-33) to include MTF parameters,

$$MRT = SNR_{DT} \cdot \left[\frac{\alpha}{2\epsilon T_e \Delta f_w} \right]^{1/2} \frac{N\beta^{1/2}(N)}{R_{sf}(N)} NE\Delta T. \quad (5-3)$$

By using the parameters of Table 4-2 and Section F of Chapter IV,

$$\begin{aligned} MRT &= 2.5 \cdot \left[\frac{4/3}{2 \cdot 0.1 \cdot 7 \cdot 3.46 \times 10^6} \right]^{1/2} \frac{N\beta^{1/2}(N)}{R_{sf}(N)} \cdot 0.157 \\ &= 2.06 \times 10^{-4} \frac{N\beta^{1/2}(N)}{R_{sf}(N)}. \end{aligned} \quad (5-4)$$

Also, for the parameters of Table 4-2, $N = 72k_\theta$ so that

$$MRT = 1.48 \times 10^{-2} \frac{k_\theta \beta^{1/2}(K_\theta)}{R_{sf}(k_\theta)}. \quad (5-5)$$

which is plotted in Fig. 5-2 by use of the MTF data of Section E of Chapter IV.

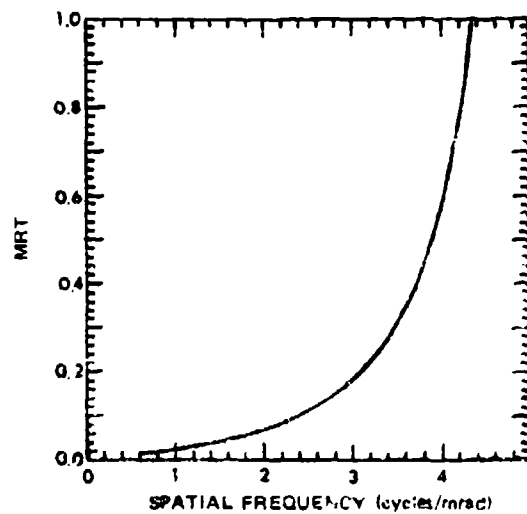


Fig. 5-2 - MRT vs. spatial frequency for the assumed basic FLIR configuration

The procedure for determining the MDT is similar to that used to determine the MRT. For the case where there is a single source of noise, Eqs. (5-1), (5-2), and (5-3) can be used if

$$\frac{N\beta^{1/2}(N)}{R_{sf}(N)} \text{ is replaced by } N[\Gamma(N)\xi(N)].$$

For example, Eq. (5-3) becomes

$$MDT = SNR_{DT} \cdot \left[\frac{\alpha}{2T_e \Delta f_w} \right]^{1/2} N[\Gamma(N)\xi(N)] NE\Delta T. \quad (5-6)$$

Note in this derivation we have assumed a square image ($\epsilon = 1$) and that the MTF is the same in both the vertical and horizontal direction so that $[\Gamma_v(N) \cdot \Gamma_h(N) \cdot \xi_v(N) \cdot \xi_h(N)]^{1/2} = [\Gamma(N)\xi(N)]$. In general, the horizontal and vertical MTFs are not of course equal.

Again, by using the parameters of Table 4-2 and Section F of Chapter 4,

$$\begin{aligned} \text{MDT} &= 2.8 \cdot \left[\frac{4/3}{2 \cdot 0.1 \cdot 3.46 \times 10^6} \right]^{1/2} N[\Gamma(N)\xi(N)] \cdot 0.157 \\ &= 6.10 \times 10^{-4} N[\Gamma(N)\xi(N)]. \end{aligned} \quad (5-7)$$

Or alternatively

$$\text{MDT} = 4.39 \times 10^{-2} k_\theta [\Gamma(k_\theta)\xi(k_\theta)]. \quad (5-8)$$

Because both N and k_θ are awkward units when describing a square image, the angular subtense of the square image $\Delta\theta = 1/2k_\theta$ is often used, in which case

$$\text{MDT} = \frac{2.19 \times 10^{-2}}{\Delta\theta} [\Gamma(\Delta\theta)\xi(\Delta\theta)]. \quad (5-9)$$

This equation is plotted in Fig. 5-3 using the parameters of Table 4-2 and the MTF data of Section E of Chapter IV.

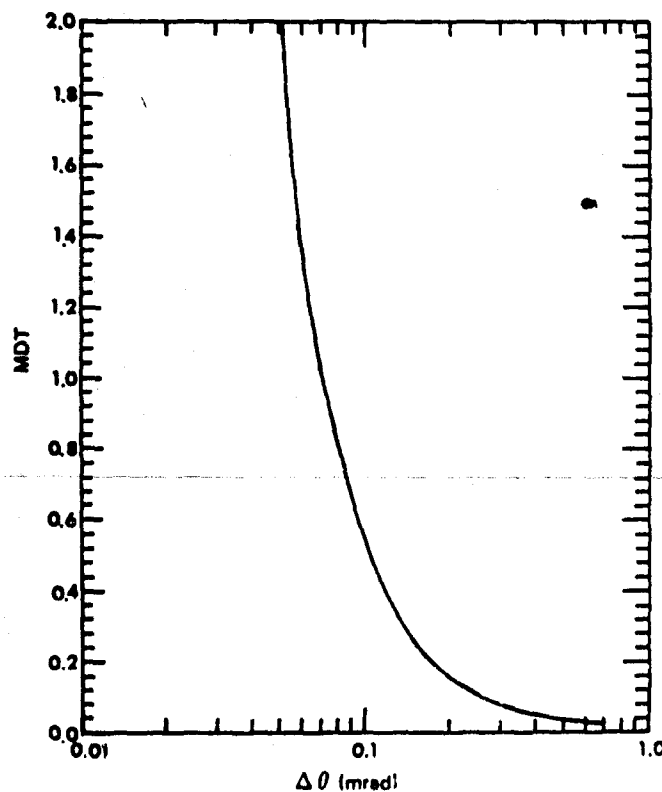


Fig. 5-3 — MDT vs angular subtense of a square image for the assumed basic FLIR configuration

C. OBSERVER THRESHOLDS

The two standardized test objects for thermal imaging systems are the aperiodic square and the periodic four-bar patterns with each of its bars being seven times its length. However,

the models developed herein apply to other aperiodic and periodic test objects within certain limits to be discussed. The observer threshold signal-to-noise ratios have been measured through psychophysical experimentation. A few of these experiments are reviewed in Appendix H.

Generally, the procedure was to generate an image either electronically or by use of a TV camera tube, add white noise of Gaussian distribution in the video channel, and display the noisy image on a CRT monitor. For aperiodic objects, the location of the image on the display and the SNR_D of the image was randomly varied. The observer, under a forced choice criterion, was asked to specify the image location whether he could see it or not. The data were corrected for chance.

For periodic images, the location of the pattern was fixed while the SNR_D was varied. Two methods of determining threshold resolution were used. In the method of random SNR_D variation, the pattern was of fixed spatial frequency. The probability of discerning the bars within the pattern was then determined as a function of SNR_D . In the method of limits, a number of bar patterns of different spatial frequencies were simultaneously imaged and the SNR_D was systematically increased or decreased. The SNR_D level at which the bar pattern could be just barely discerned was taken to be the threshold* SNR_{DT} . The threshold SNR_{DT} determined by using the method of limits was found to be identical to that determined by using the method of random SNR_D variation to within the experimental error. The value of the SNR_{DT} was found to be 2.5.

The corrected probability of detection for rectangular images is plotted vs SNR_D in Fig. 5-4. The rectangles in all cases were 4 TV scan lines wide and from 4 to 180 scan lines high. The angular subtense of the rectangles relative to the observer's eye varied from $0.13^\circ \times 0.13^\circ$ to $0.13^\circ \times 6.02^\circ$. The ability of the eye to integrate over an angle as large as 6° or possibly more was an unsuspected result. Therefore the experiment was repeated using squares with the result shown in Fig. 5-5. The uptilt of the threshold SNR_{DT} for the smallest square is attributed to eye MTF effects since the image is near the size of the eye's effective blur circle diameter (about $3.2'$ of arc or 0.053°). When the image becomes larger than 0.27° or 16 min of arc the apparent SNR_{DT} , which was calculated assuming that the observer spatially integrates all of the image area, begins to slowly increase but the increase is not large until the displayed image becomes larger than about 0.5° on a side. This result is attributed to the eye's acting as a differentiator at the higher light levels and as a result, the eye only integrates around the perimeter of a large image. In the above experiment, the observer was 28" from an 8" high monitor and as can be seen from Fig. 5-5, the eye's apparent threshold SNR_{DT} is only approximately constant for images which are smaller than about 16×16 scan lines in size for a conventional television monitor with 490 active scan lines.

The probability model used to fit the experimental points of Fig. 5-4 is based on a model discussed in detail by Legault (Ref. 5-2). In this model it is assumed that the mean number of photoconverted electrons within the sampling area and period has become sufficiently large so that the Gaussian or normal probability distribution law given by

$$f_z(z) = [\exp(-z^2/2)]/(2\pi)^{1/2} \quad (5-10)$$

*By threshold, a 50% probability of detection is implied.

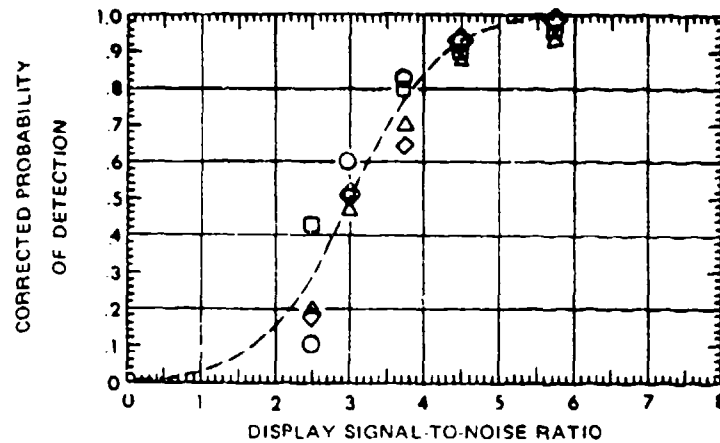


Fig. 5-4 -- Corrected probability of detection vs SNR_D required for rectangular images of size $\circ 4 \times 4$, $\square 4 \times 64$, $\triangle 4 \times 128$, and $\nabla 4 \times 180$ scan lines

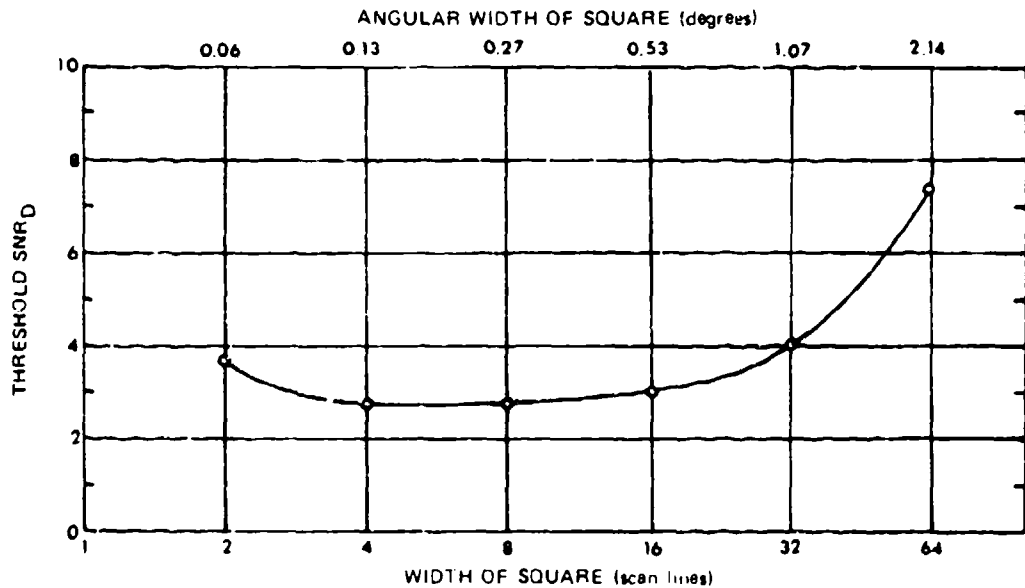


Fig. 5-5 -- Threshold SNR_D required to detect square images of various size and angular extent

becomes a good approximation to the Poisson distribution law, which actually represents the signal and noise processes. In the above, Z is a random variable numerically equal to

$$Z = SNR_D - SNR_{DT} \quad (5-11)$$

where SNR_{DT} is the threshold display signal-to-noise ratio, which is defined to be that needed to obtain a detection probability of 0.5. The random variable Z is of unit mean and variance. Other values of probability are obtained from the formula

$$P(-\infty < Z < z) = (1/2\pi^2) \int_{-\infty}^{z^2} \exp(-z^2/2) dz. \quad (5-12)$$

which cannot be integrated in closed form but is widely available in standard mathematical tables. In Table 5-1, the SNR_D required to obtain various levels of detection probability are given based on a value of SNR_{DT} of 2.8 for a 50% probability of detection.

The value of 2.8 for the threshold SNR_{DT} results in part from the assumed value of 0.1 s for the eye's integration time. If a different value had been assumed value had been assumed, a different value for the threshold would have been obtained. In other words, the SNR_D is a derived quantity based on a measured threshold video SNR and an assumed ability of the eye to integrate perfectly in space and time.

The threshold SNR_{DT} curve for bar pattern images which were generated by a TV camera are shown in Fig. 5-6 for three viewing distances. As one might intuitively expect, the low-frequency bar patterns were most easily seen at a large viewing distance while the high-frequency patterns were most easily seen as indicated by a lower SNR_{DT} at the shorter distance. In Fig. 5-7, the SNR_{DT} required at a 28" viewing distance is compared to that required when viewing distance was optimized by the observer.

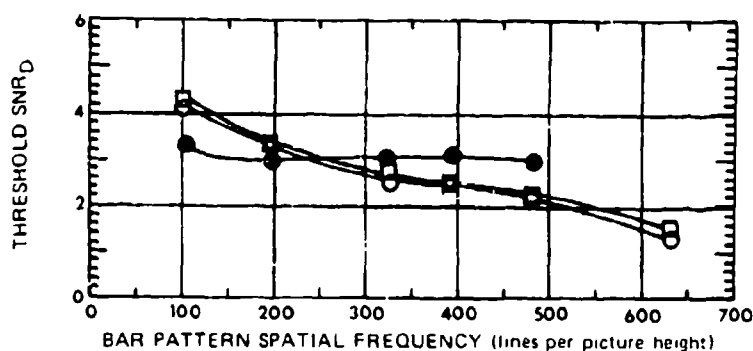


Fig. 5-6 — Threshold display signal-to-noise ratio vs bar pattern spatial frequency for display to observer viewing distance of \circ 14" \square 28" and \bullet 56". Televised images at 25 frames/s and 875 scan lines. Display was 8" high.

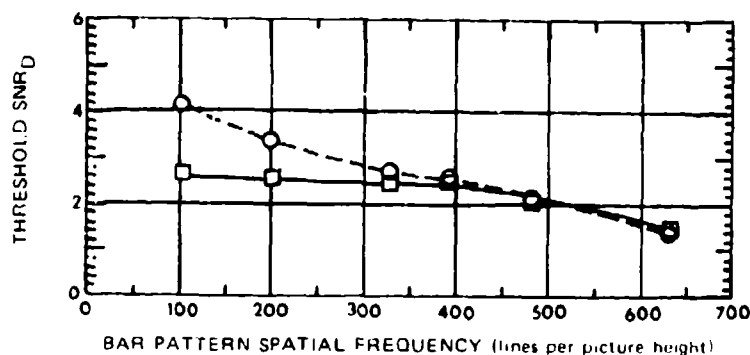


Fig. 5-7 — Threshold display signal-to-noise ratio vs bar pattern spatial frequency for optimum viewing distances and \circ 28" viewing distance from one observer. Display was 8" high.

The threshold value of SNR_D for bar patterns is seen to be generally less for bar patterns than for isolated rectangles when the measurement is made at optimum viewing distance. A value of 2.5 rather than 2.8 would appear appropriate for the range of spatial frequencies from 0 to 500 l/p.h. This difference in threshold may be due in part to the method of measurement. With bar patterns, the location of the pattern is known, no chance is involved, and the definition of discerning or detecting a bar pattern is of a very subjective nature.

Both the MRT and MDT are measured under optimum laboratory conditions. In general, the dynamic temperature range of the test patterns is small and the display gain (contrast) control can be set at a very high value. When viewing a real scene with a wide dynamic temperature range the ability to adjust display gain may become limited. As discussed in Appendix H, retinal fluctuation noise, rather than system generated noise can be the principal noise limiting threshold resolution.

D. SUMMARY OF SIGNIFICANT EQUATIONS

Minimum Resolvable Temperature (General)*

$$MRT = SNR_{DT} \left[\frac{\alpha}{2\epsilon T_e} \right]^{1/2} \frac{N \beta^{1/2}(N)}{R_{s,f}(N)} \frac{4f}{\pi \eta_o D_o (n_l n_p \omega_l \eta_s)^{1/2} D^*(\Omega_l) K_M} \quad (5-1)$$

- MRT = minimum resolvable temperature (°C)
- SNR_{DT} = threshold display SNR
- α = picture aspect ratio (W/H)
- ϵ = bar length to width ratio
- T_e = eye integration time (s)
- N = spatial frequency (lines/pict. ht.)
- $\beta(N)$ = noise filtering function
- $R_{s,f}(N)$ = square wave flux response
- f = lens focal ratio
- η_o = lens transmittance
- D_o = lens diameter (cm)
- n_l = number of detectors in series
- n_p = number of detectors in parallel
- ω_l = instantaneous field of view (sr)
- η_s = scan efficiency
- $D^*(\Omega)$ = detectivity for viewing solid angle Ω (cm Hz^{1/2} W⁻¹)
- K_M = ΔT conversion factor (W cm⁻² sr⁻¹ K⁻¹)

Spatial Frequency Conversion

- N = 2000 $\phi_v k_\theta$
- ϕ_v = vertical field of view (rad)
- k_θ = spatial frequency (cycles/mrad)

*Use when system noise can be described by a single noise source assuming MTF equal in x and y directions. If not, use $[(R_{s,f}(N))^2 + (R_{s,f}(N))^2]^{1/2}$

Minimum Resolvable Temperature (BLIP)*

$$\text{MRT} = \text{SNR}_{DT} \cdot \left[\frac{\alpha}{2\epsilon T_e} \right]^{1/2} \frac{N^{1/2} \beta(N)}{R_{sf}(N)} \frac{2}{\pi \eta_o D_o (n_l n_p \omega_l \eta_s)^{1/2} \eta_c D^*(2\pi) K_M} \quad (5-2)$$

η_c = cold shield efficiency
 $D^*(2\pi)$ = detectivity viewing solid angle of 2π sr

Minimum Resolvable Temperature (General)*

$$\text{MRT} = \text{SNR}_{DT} \cdot \left[\frac{\alpha}{2\epsilon T_e \Delta f_{vr}} \right]^{1/2} \frac{N \beta^{1/2}(N)}{R_{sf}(N)} NE \Delta T \quad (5-3)$$

Δf_{vr} = reference video bandwidth
 $NE \Delta T$ = noise equivalent temperature difference

Minimum Detectable Temperature

The Eqs. (5-1), (5-2), and (5-3) also apply to MDT if $N \beta^{1/2}(N)/R_{sf}(N)$ is replaced by $N[\Gamma(N) \xi(N)]$.^{*} For example, Eq. (5-3) becomes

$$\text{MDT} = \text{SNR}_{DT} \left[\frac{\alpha}{2 T_e \Delta f_{vr}} \right]^{1/2} N [\Gamma(N) \xi(N)] \cdot NE \Delta T \quad (5-6)$$

$\Gamma(N)$ = noise filtering function
 $\xi(N)$ = noise increase function.

REFERENCES

- 5-1 Rosell, F.A., and Willson, R.H., Chapter 5, Perception of Displayed Information, edited by L.M. Biberman, Plenum Press, New York, 1973.
- 5-2 Legault, R. R., Chapter 4, Photoelectronic Imaging Devices, Vol. 1, Plenum Press, New York, 1971.

^{*}Use when system noise can be described by a single noise source assuming MTF equal in x and y directions. If not, use $[\Gamma_x(N) \Gamma_y(N) \xi_x(N) \xi_y(N)]^{1/2}$.

Chapter VI

STATIC FIELD PERFORMANCE MODELS

F. A. Rosell

A. INTRODUCTION

The analytical models developed in Chapters IV and V can be used to predict the incremental temperature difference about a given temperature that is required to detect either aperiodic (isolated rectangles) or periodic (bar patterns) images of known geometry. That is all the models can be expected to do. However there are continuing efforts to correlate threshold resolution as measured or predicted with the ability to discriminate images of real scene objects. The levels of visual discrimination typically include simple detection, orientation, recognition, and identification, but other levels may be appropriate to specific tasks. If we are to predict the sensor's static field performance, we must correlate sensor resolution with visual discrimination levels and include environmental factors such as atmospheric transmission, atmospheric turbulence, scene temperature, and dynamic range. By static field performance it is usually meant that we desire to estimate the range at which a real object can be discriminated on the display at the desired level assuming that the object is in the sensor's field of view and that the observer is looking at the object. The scene object may be moving, but by use of the word static we imply that search is not part of the observer's tasks.

In attempting to apply the MRT or MDT models to the visual discrimination of displayed images of real scene objects, the basic premise is that the higher the resolving power of the sensor, the higher will be the level of visual discrimination. It is intuitively obvious that this statement is generally true, but it is not so obvious that the sensor resolution as measured in the threshold sense in the laboratory under optimum conditions will in fact be realized in a field environment. Recall that the MRT measurements are made under conditions where the display can be optimized for a test pattern scene of very small dynamic range. In a real environment, the sensor resolution can be degraded considerably by dynamic range limitations imposed by either the sensor, the display, or the observer. The current sensor models in use assume that if the incremental displayed image signal exceeds the noise due to background fluctuations or other system noise by a certain amount, the observer will detect it given that he is looking at it regardless of the contrast of the displayed image. Displayed image contrast and display image SNR are not related quantities, *e.g.*, a large low-contrast image can have the same SNR_D as a small bright one. Also as is discussed in this chapter and Appendix I, the observer appears to require more sensor resolution when the resolution is noise as opposed to spatial frequency response limited.

In some cases, a level of visual discrimination can be defined easily but there can be considerable difficulty in others. An aircraft may be easily detected against a cloudless sky given that it is close enough and that the observer is looking at it. The meaning of detection is clear in this case. The detection of a vehicle against a complex background such as a forest may be very difficult and in fact, it may be necessary to recognize the vehicle before it can be said to be detected. Alternatively, a vehicle may be considered recognized at times because of some

characteristics of its image or because of its location or velocity even though the sensor resolution is insufficient to perform a classical shape recognition. In field trials, the number of objects such as vehicles which can be employed when performing recognition trials is usually limited. After a short period of training, observers are often able to "recognize" without discerning shape because of certain object peculiarities such as relative size, location of hot spots, and use of comfort heaters. The recognition criteria in these cases may be more a "telling the difference between." Thus even "measured" recognition or identification data may not truly reflect the level of discrimination implied.

In spite of the limitations discussed above, the models developed in Chapters IV and V are used to predict the range at which real scene objects can be discriminated and over a fairly wide range of conditions, the predictions will hold if the analyst exercises good judgment in selecting the discrimination criteria based on either experimentally measured results, by analogy to these results, or by prior experience.

B. LEVELS OF VISUAL DISCRIMINATION OF DISPLAYED IMAGES

One of the earliest attempts to relate functionally threshold resolution with the visual discrimination of images of real scenes is attributed to John Johnson Ref. 6-1. The levels of visual discrimination were arbitrarily divided into four categories: detection, orientation, recognition, and identification, with detection being the lowest and identification being the highest discrimination level. The basic experimental scheme was to move a real scene object such as a vehicle out in range until it could be just barely discerned on a sensor's display at a given discrimination level. Then the real scene object was replaced by a bar pattern of contrast similar to that of the scene object. The number of bars in the pattern per minimum object dimension was then increased until the bars could just barely be individually resolved. In this way the detectability, recognizability, *etc.* of the scene object can presumably be correlated with the sensor's threshold bar pattern resolution. The basic idea makes sense—the better the sensor's resolution, the higher the level of visual discrimination should be. Johnson's basic notion is shown schematically in Fig. 6-1. The real scene object is replaced by a bar pattern whose bar spacing is some function of the minimum dimension of the object and the level of visual discrimination desired. The definitions of the various levels of discrimination are given in Table 6-1 in addition to the resolution required in lines or half cycles per minimum object dimension. In addition to sufficient resolution, Johnson noted that image SNR had to be sufficient but the definition of image SNR was not clear.

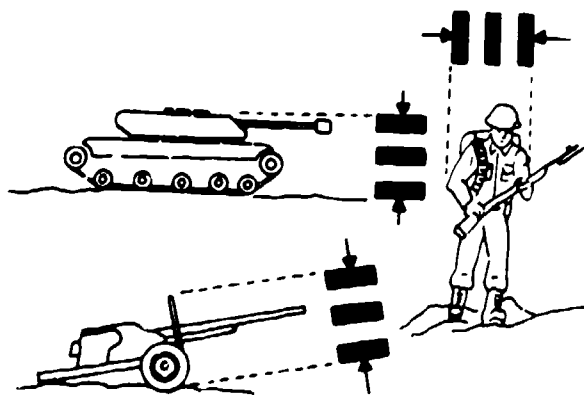


Fig. 6-1 — Schematic representation of the Johnson approach to resolution vs. level of visual discrimination

Table 6-1 — Definition of Visual Discrimination Level and Resolution Required per Minimum Object Dimension

Discrimination Level	Meaning	Resolution Required per Minimum Object Dimension (lines or half cycles)
Detection	An object is present	$2_{-0.5}^{+1}$
Orientation	The object is approximately symmetrical or unsymmetrical and its orientation may be discerned	$2.8_{-0.4}^{+0.8}$
Recognition	The class to which the object belongs may be discerned (e.g., tank, truck, man)	$8.0_{-1.4}^{+1.6}$
Identification	The target can be described to the limit of the observer's knowledge (e.g., T-34 tank, friendly jeep)	$12.8_{-2.8}^{+3.2}$

It has become evident in field trials that more levels of visual discrimination than the four originally proposed by Johnson would be desirable. In particular, the gap between detection and recognition is considered to be too large. As noted previously, scene objects may often be "recognized" even when the resolution available is inadequate to perform a classical shape recognition. The Night Vision Laboratory has proposed one intermediate step between detection and recognition. This step is called classification, which is defined to be a resolving capability that is insufficient to recognize a specific type of vehicle but sufficient to differentiate between say a wheeled and a tracked vehicle. This intermediate level appears desirable, but the word classification has a specific different meaning in naval ship discrimination and should be avoided. In Table 6-2 a more detailed discrimination level breakdown is proposed which fits a wider set of field conditions. Observe that the orientation level, which has been little used in the past, has been dropped. The increase in the number of detection levels has been made to make note of the fact that many objects are recognized correctly even though the resolution at the object is far below that required to recognize shape.

Since the early Johnson results, it has been found that the resolution required to visually discriminate real scene objects is much more variable than Table 6-1 suggests. In particular, the viewing aspect has a pronounced effect as shown in Appendix I. For example, it was found to be possible to recognize a destroyer with only 6 lines per minimum dimension on a beam viewing aspect but 20 lines are required on a bow or stern viewing aspect. Table 6-3 is felt to be somewhat more representative of the resolution required for targets in various viewing aspects for the tasks of Table 6-2. Also it is felt that the Table 6-3 applies primarily to fairly high video SNR conditions. The number of lines required may more than double under low SNR conditions as will be discussed.

Table 6-2 — Levels of Visual Discrimination

Discrimination Task	Level	Description	Example
Detection	0	A blob has been discerned that may or may not warrant further investigation. Probability of false alarm is high.	A bright spot in a scene may be a tank, a smudge pot, a tree, an animal, a campfire, etc. No appreciable cues.
	1	A blob has been discerned that has a reasonable probability of being the object sought, because of auxiliary but limited cues that definitely warrant further investigation if possible. Probability of false alarm is moderate.	A stationary blob on a road has a reasonable probability of being a vehicle but could also be a puddle or a tree shadow.
	2	A blob has been discerned that has a high probability of being the object sought because of strong cues such as location, motion, radiant signature, and reported location scale. Evidence is sufficient to abandon other search. Probability of false alarm is low to moderate.	A blob moving at high speed on the horizon sky has a high probability of being an aircraft. A hot moving object on a road is probably a vehicle.
Type Recognition	3	An object has been discerned with sufficient clarity that its general class can be differentiated.	Differentiate between a tracked and a wheeled vehicle.
Classical Recognition	4	An object has been discerned with sufficient clarity that its particular class can be definitely established.	Passenger car, van, pickup truck, tank, armored personnel carrier.
Identification	5	An object has been discerned with sufficient clarity not only to establish the particular class of object but also, the specific type within the class.	M-60 tank, F-4 aircraft, a particular person, etc.

Table 6-3 — Resolution Required for Various Levels of Visual Discrimination

Discrimination Task	Level	Estimated Resolution Required per Minimum Object Dimension (lines or half cycles)
Detection	0	1-3
	1	2-4
	2	2-5
Type Recognition	3	4-10
Classical Recognition	4	4-20
Identification	5	9-30

The spread in values for required resolution in Table 6-3 could perhaps be reduced if some method of taking aspect ratio into account were developed. One such effort by Rosell and Willson (Ref. 6.2) is shown in Fig. 6-2. An equivalent bar pattern is created in object space which has bars of width equal to the minimum dimension of the scene object divided by k_d , the discrimination factor which is the number of lines required per minimum object dimension for the discrimination level desired. The lengths of the bars in the equivalent bar pattern are made equal to the maximum dimension of the scene object. Thus, as the *aspect ratio* ϵ ($\max \div \min$ dimension) of the scene object increases, the bars increase in length by ϵ and the SNR_D increase as $\epsilon^{1/2}$.

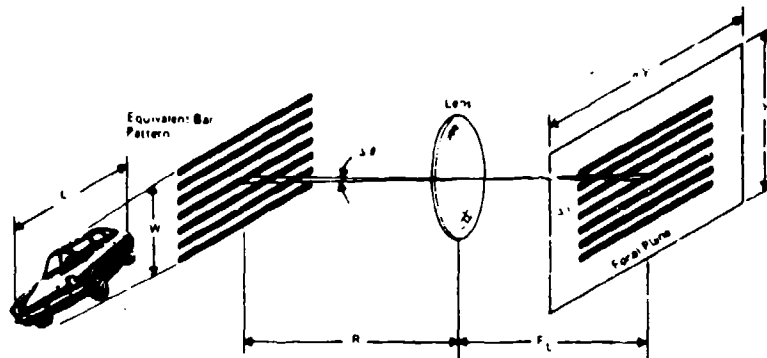


Fig. 6-2 — The equivalent bar pattern for the identification of a real scene object

The Naval Air Development Center, Warminster, Pa., has used a pixel approach in determining resolution requirements for discrimination of ships. If the sensor resolution of the scene object is ΔX as determined from threshold resolution measured in the horizontal direction for TV or in the scan direction for FLIR, then the number of pixels is equal to the area of the scene object divided by ΔX^2 instead of the k_d criteria for the various levels of visual discrimination. A table similar to Table 6-3 is made up by use of a pixel requirement. For example, for a specific ship viewed broadside, it was found that 36 pixels were needed for simple detection, 100 to discern that the object was a ship, 500 to determine superstructure location, etc. The pixel approach includes object viewing aspect ratio considerations since as the number of pixels increase the aspect ratio increases.

Objects such as airplanes and tanks are generally more recognizable from the sides than the frontal aspect and taking viewing aspect into account either in calculating SNR_D or in setting the resolution requirement would appear desirable. However, the amount of correction required is highly variable and in many cases, totally unwarranted. In general, it has been customary to include an aspect ratio in predicting the range at which real objects can be discriminated whether it is correct to do so or not. In the following, the k_d criteria of Table 6-1 together with the scene object aspect ratio ϵ will be used in predicting range.

C. RANGE PREDICTION

If we could correlate the sensory system resolution with levels of real object discrimination and if we knew enough about the scene characteristics including the thermal signature of a scene object and its background, the effects of the atmosphere intervening between the scene and sensor, the interactions between the scene, sensor, display and observer dynamic ranges, etc., then it should be possible to predict the range at which a sensor-augmented-observer can discriminate a real scene object. In the current state-of-the-modeling art, not all of the factors will be well enough known and great range prediction accuracy cannot be expected. Nevertheless, the accuracy can be good enough in many cases to be useful for system design purposes.

In the following, we will show the traditional methods of predicting the range at which an object can be discriminated at the 50% level of probability. The cumulative probability of discrimination will be determined by using the NVL resolution dependent method, assuming an atmospheric transmission of unity. The effect of atmospheric transmission, which is both to shorten the ranges at which the 50% probability level of discrimination occurs and to make the cumulative probability vs range curve steeper, will be shown next. Finally the noise vs resolution-limited effects discussed in Appendix I will be included. As the level of complexity in the range prediction increases, the confidence in the prediction methods may decrease even though the trends obtained through use of the more complex methods are in general consonance with experimentally observed results. Verification and or modification as may be required to bring the new methods into closer agreement with reality should be easily obtainable through continued psychophysical experimentations.

As conventionally performed the first step in range prediction is to convert the MRT to take into account the scene object aspect ratio (maximum to minimum object dimension) if use is to be made of the concept that an object is more readily discerned if the aspect ratio is greater than unity. The MRT is computed or measured with a bar aspect ratio, ϵ , of 7. For simple detection by use of the two line or one cycle per minimum scene object dimension, the

quantity ϵ will be 2 for an object of 1:1 aspect and 4 for an object of 2:1 aspect. For the latter case,

$$\begin{aligned} \text{MRT}' (2:1 \text{ object aspect, detection}) &= \text{MRT} \sqrt{7\epsilon} \\ &= \text{MRT} \sqrt{7/4}, \end{aligned} \quad (6-1)$$

where MRT' is an adjusted MRT for the specific case of detection. On the other hand, if the visual discrimination level is recognition of an object of 2:1 aspect with an eight line or four cycle per minimum object dimension criterion, $\epsilon = 16$ and

$$\text{MRT}' (2:1 \text{ object aspect, recognition}) \approx \text{MRT} \sqrt{7/16} \quad (6-2)$$

and the MRT' is seen to be smaller than the measured MRT. Observe that at any given scene object range, recognition requires a spatial resolution that is four times better than for detection by using the classical Johnson criteria.

The use of ϵ , the bar aspect ratio, to compute the discernability of bar patterns is warranted on the basis of experimental psychophysical evidence. Its use for the purpose of trying to quantitatively indicate that a scene object of larger aspect is more recognizable or identifiable than one of smaller aspect is somewhat questionable. The resolution required for recognition and identification of several scene objects including a tank, a destroyer, and an aircraft carrier are shown as a function of viewing aspect angle in Figs. 1-12, 1-14, and 1-15 of Appendix 1. It was found that a tank that is of about 2:1 aspect requires about 11 to 12 lines for recognition viewed broadside while 16 lines are required frontally where the aspect is near unity. In this case, the ϵ criteria which increases SNR_D by $\sqrt{2}$ when the aspect changes from frontal to broadside appears reasonable even though a $\sqrt{2}$ increase in SNR_D may not result in a $\sqrt{2}$ improvement in resolution.

As a minimum it can be said that for tanks, the use of ϵ should result in some improvement in prediction accuracy. For the aircraft carrier, the recognition criteria are almost independent of aspect, which may increase by a factor of 50 from the bow or stern to broadside. A broadside view would increase the SNR_D by a factor of $\sqrt{50}$, or about 7 over the bow or stern view. Clearly, the ϵ concept is not applicable in this case. For a destroyer where the frontal view requires nearly four times more resolution than broadside, the ϵ concept would appear to be somewhat more reasonable. The typical ship, excluding aircraft carriers, is probably nearly unrecognizable from the bow or stern and rather highly recognizable viewed broadside. But whether a ship is 100 or 500 meters long is probably less significant than the detail which can be seen on the superstructure. The use of a large ϵ in the case of ships does not seem to be appropriate particularly for the higher levels of visual discrimination. The alternative to using ϵ is to use the MRT curves as is and to adjust the resolution required as a function of viewing angle by using experimentally measured curves to the extent that such curves are available or by using judgment. This is considered to be a better approach but much more work is needed in this area.

The second step in conventional range analysis is to convert the MRT vs spatial frequency to MRT (or MRT') vs range curves. This step is required in order to include atmospheric transmittance effects that are range dependent. To convert spatial frequency to range, it is necessary to select scene object dimensions, the desired level of visual discrimination, and the resolution requirement appropriate to the level of visual discrimination. To begin, we assume an object of minimum dimension X and a bar pattern resolution based on a bar width ΔX equal to

F. A. ROSELL

$$\Delta X = \frac{X_o}{k_d}, \quad (6-3)$$

where k_d represents the number of lines required per minimum scene object dimension to obtain the desired discrimination level. The angular subtense, $\Delta\theta$, of ΔX at range R is given by

$$\Delta\theta \approx \Delta X/R, \quad (6-4)$$

and since $k_u = 1/2 \Delta\theta$,

$$R = 2\Delta X k_u. \quad (6-5)$$

If ΔX is in meters, and k_u is in cycles/mrad, R will be in kilometers.

The MRT curve of Fig. 5-2 is converted to a function of range if we assume 1:1 scene object aspect ratio and a recognition level of discrimination. The resulting MRT curves are plotted in Fig. 6-3 for several values of scene object size using bar widths for 1/3 to 2 m for the equivalent bar pattern. We assume a scene object to have a temperature differential of 5° about a 300°F background. If the atmospheric transmittance is unity, the apparent scene object ΔT will equal 5° at all ranges. The intersection of the τ_{at} line representing this case with the MRT curves gives the threshold ranges for each bar width assumed. In the special case of $\tau_a = \tau_{at} = 1.0$, it is found that $\Delta\theta_T = \Delta X/R = \text{constant}$ and we plot $\Delta\theta$ vs range in Fig. 6-3. Atmospheric transmission at the long infrared wavelengths can often be approximated by an exponential so that

$$\Delta T(R) = \Delta T_o \exp [-\sigma R], \quad (6-6)$$

where ΔT_o is the object temperature at zero range and σ is the atmospheric extinction coefficient. The curve τ_{at} in Fig. 6-3 corresponds to a dry air, cold weather condition for which the atmospheric transmittance is high while curve τ_{a2} represents a fairly low transmittance due to moist warm air condition. The effect of the atmosphere is to cause the threshold angular resolution $\Delta\theta$, to increase with range as shown in Fig. 6-4 with the largest increase for τ_{a2} .

As noted in connection with Table 6-3, the sensor resolution required, as measured in the threshold sense, to visually discriminate real scene objects appears to increase when the video SNR is low. Thus the effective sensor resolution is less than the measured threshold resolution. The ratio of effective to measured threshold angular resolution ($\Delta\theta_e/\Delta\theta_T$) is shown as a function video SNR in Fig. 6-5. This particular curve was derived from measurements by O'Neill using images of ship silhouettes (Refs. 6-6,4,5) as discussed in Appendix I. It should be emphasized that the curve of Fig. 6-5 is based on very little data derived from an experiment which was not specifically designed to determine a correlation between video SNR and resolution criteria. However, it is believed that the curve is of the correct form if not of precise values.

The interpretation of the curve is as follows: suppose that the threshold resolution of a system at a particular range is $\Delta\theta_T$ equal to $100 \mu\text{rad}$. Further suppose that the video SNR_{thr} is calculated for that range from the relation

$$\text{SNR}_{thr} = \frac{\Delta T_o}{NE\Delta T} e^{-\sigma R}, \quad (6-7)$$

where ΔT_o is the temperature of a specific object at zero range, σ is the atmospheric extinction coefficient, and the calculated value of $\text{SNR}_{thr} = 1.0$. Then, from Fig. 6-5 it is found that

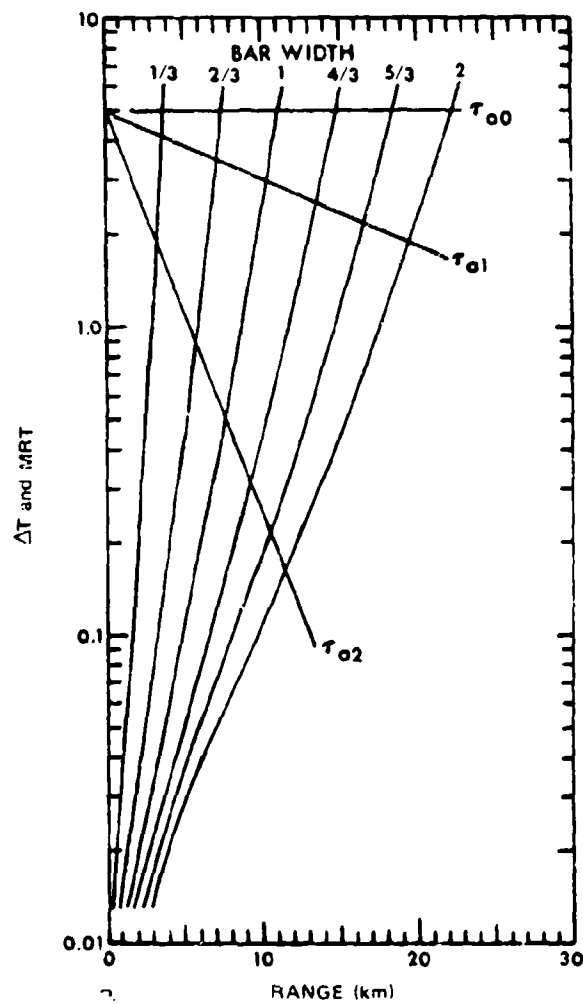


Fig. 6-3 - MRT plotted vs range for various equivalent bar pattern widths and scene object ΔT vs range for atmospheric transmissions of τ_{o0} (no atmosphere), τ_{o1} (dry air, cold), and τ_{o2} (moist air, warm)

F. A. ROSELL

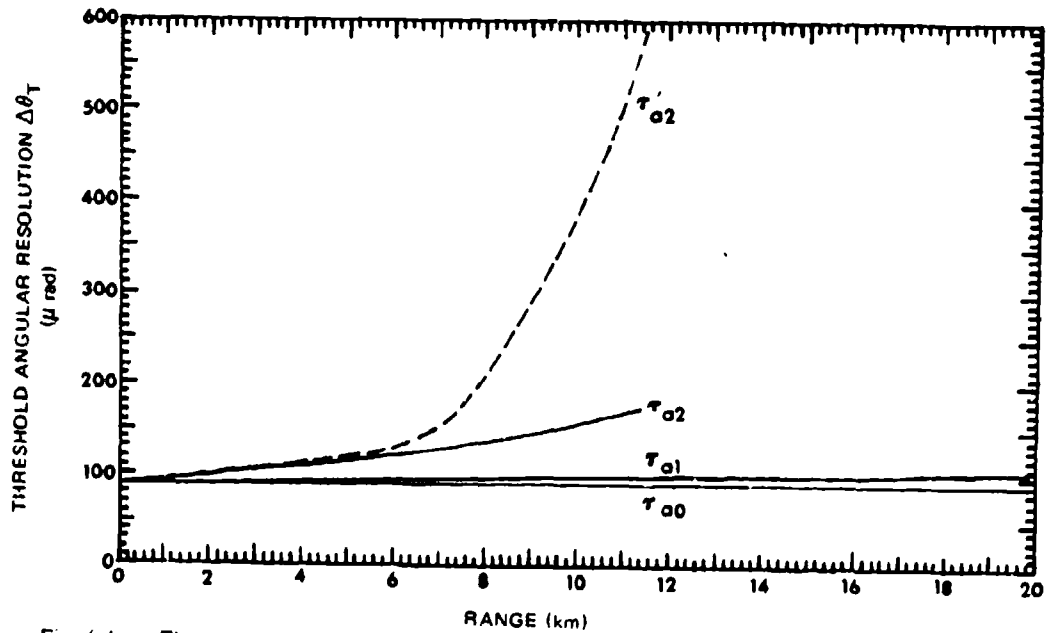


Fig. 6-4 — Threshold angular resolution vs. range for the assumed system for three atmospheric transmittances and, the effective angular resolution for the atmospheric case τ_{a2} as modified to include loss in video SNR_{v0} with range

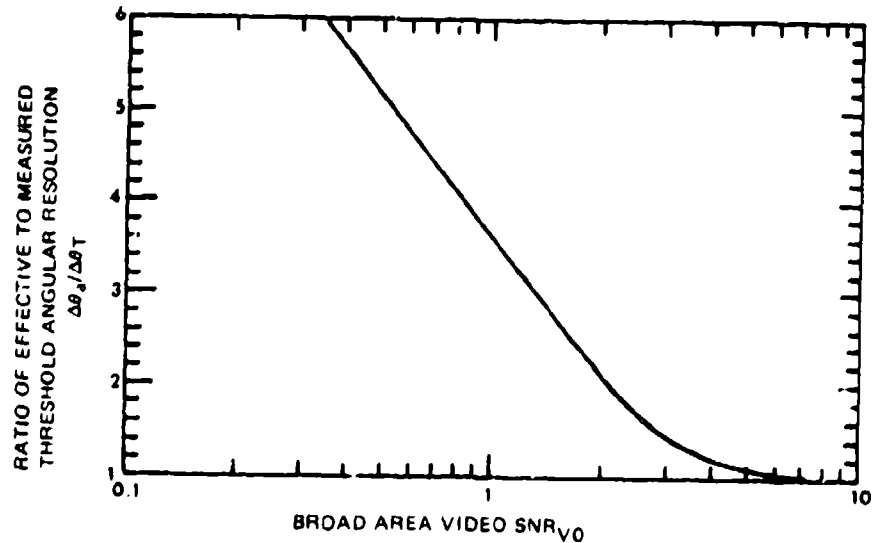


Fig. 6-5 — Ratio of effective to measured angular resolution required to visually discriminate the ship silhouette as a function of the broad area video SNR

$\Delta\theta_a/\Delta\theta_T = 3.6$. Then, the effective sensor resolution so far as visual discrimination of real scene objects is $\Delta\theta_a = 3.6 \Delta\theta_T = 360 \mu\text{rad}$.

A graphical method of including the above effect in range prediction is shown in Fig. 6-6 where we have plotted Eq. (6-7) with the MRT curves of Fig. 6-3 and the $\Delta\theta_a/\Delta\theta_T$ curve of Fig. 6-5. The curves are used as follows. For the τ_{a2} atmospheric curve, the threshold range for a 2-m object with a ΔT of 5° at zero range is 11 km and the threshold angular resolution is thus $174 \mu\text{rad}$. The video SNR_{vo} under these conditions is about 1.1 and $\Delta\theta_a/\Delta\theta_T = 3.4$ and $\Delta\theta_a = 590 \mu\text{rad}$ which is plotted as one of the points on the dashed curve τ_{a2} in Fig. 6-4. Observe that the correction for SNR_{vo} is trivial for ranges shorter than 6 km for the assumed case but the effect is large beyond 8 km.

D. CUMULATIVE PROBABILITY OF VISUAL DISCRIMINATION VS RANGE

One commonly desired format in plotting predicted range is the cumulative probability that a scene object will be visually discriminated at a range equal to or less than a given range vs range. To obtain this curve, we use the methods of the previous section to obtain the threshold angular resolution of the sensor for a specific object. Assume that the object is a bar of width 1 m with a ΔT_o of 5° . Then if the atmospheric transmittance is unity, the Ta_o curve of Fig. 6-3 intersects the MRT curve for a 1-m bar width at about 11 km and the threshold angular resolution of the sensor is about $90 \mu\text{rad}$ at that range. Next, $\Delta\theta_o$, the angular subtense of a 1-m bar width, is plotted as a function or range in Fig. 6-7(b). The sensor's threshold angular resolution, when the atmospheric transmittance is unity, is actually independent of range and thus, $\Delta\theta_T$ plots as a horizontal line. The $\Delta\theta_T$ and $\Delta\theta_o$ curves should and do intersect at range 11 km where the probability of detection is 50%.

A probability of visual discrimination vs the ratio $\Delta\theta_o/\Delta\theta_T$ is plotted in Fig. 6-7(c) using the second column of Table 5-1 with $\Delta\theta_o/\Delta\theta_T = 1$ corresponding to an angular resolution of $90 \mu\text{rad}$ and $\Delta\theta_o/\Delta\theta_T = 2$ corresponding to $180 \mu\text{rad}$. It can be seen that if the probability vs $\Delta\theta_o/\Delta\theta_T$ curve is centered at 0.50, $\Delta\theta_o/\Delta\theta_T = 1$ and by following the desired curve up to Fig. 6-7(b) and down to (c) the first point of the cumulative probability vs range curve becomes 0.5 at 11 km as it must by definition. Other points are found in a similar manner.

Where atmospheric transmittance is a factor, the sensor-augmented observer's ability to resolve a scene object at range R becomes a function of range as discussed in connection with Fig. 6-4 and as shown as curve 1 in Fig. 6-8. From this curve we can plot the ratio of $\Delta\theta_o/\Delta\theta_{T1}$ as shown in Fig. 6-9(b). With the cumulative probability curve of Fig. 6-9(c) we can obtain the cumulative probability vs range curve of Fig. 6-9(a). The curve 2 of Fig. 6-8 represents the case where the sensor augmented observer's ability to resolve the scene object is limited not only by the atmospheric transmittance but also by the falloff in video SNR as discussed previously. The effect of this further degradation on the cumulative probability vs range is shown as curve 2 on Fig. 6-9(a). For reference purposes we also show the probability curve for the case of Fig. 6-7 as curve 3 on Fig. 6-9(a). As can be seen, the effect of the atmospheric transmittance alone and the atmospheric transmittance plus the video SNR falloff (which is also due to atmospheric transmittance) is both to progressively shorten the threshold range at the 50% probability level and to cause the probability curves to become steeper. These trends have been experimentally observed and are in agreement with what one would intuitively expect.

F. A. ROSELL

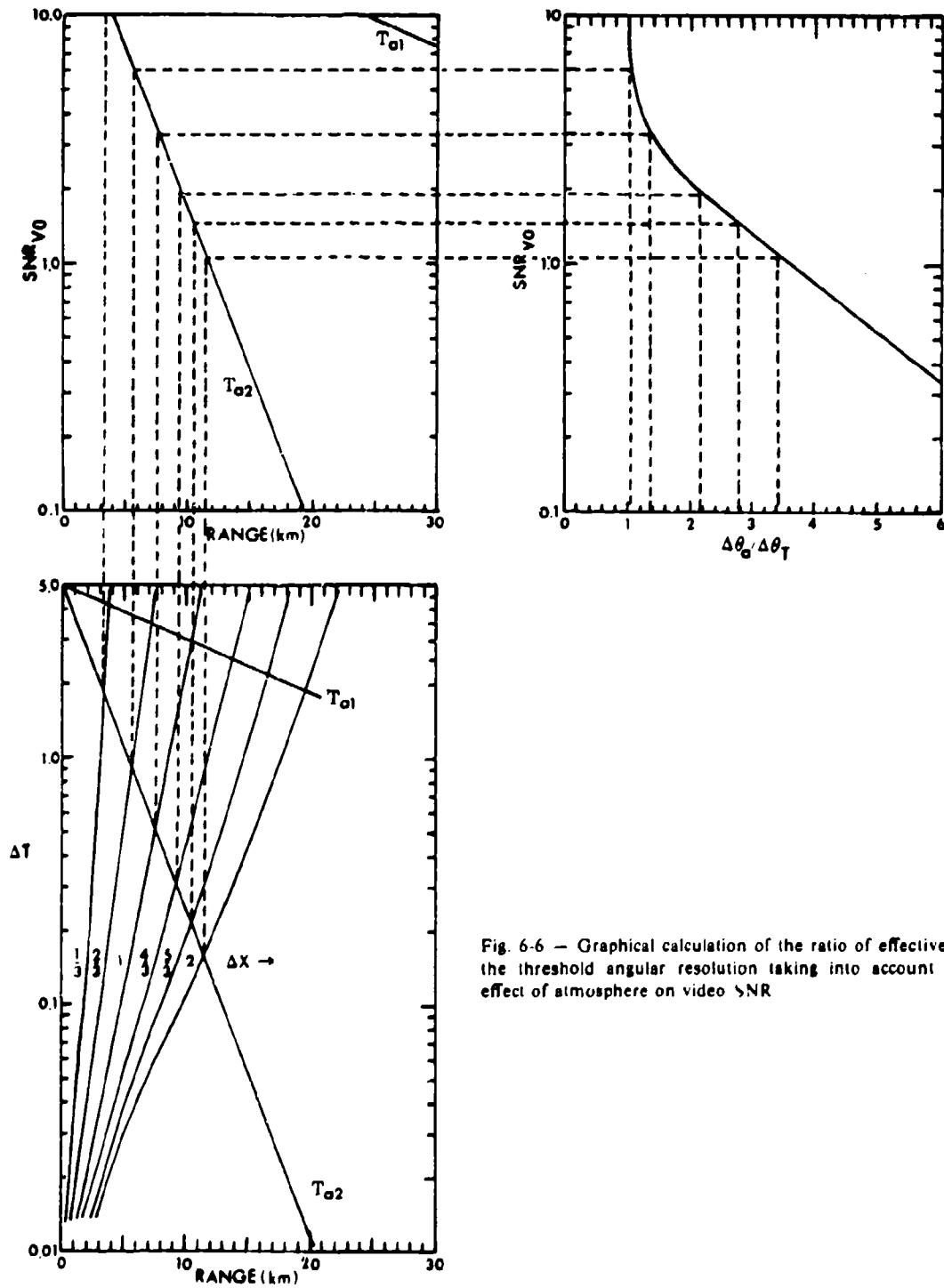


Fig. 6-6 — Graphical calculation of the ratio of effective to the threshold angular resolution taking into account the effect of atmosphere on video SNR

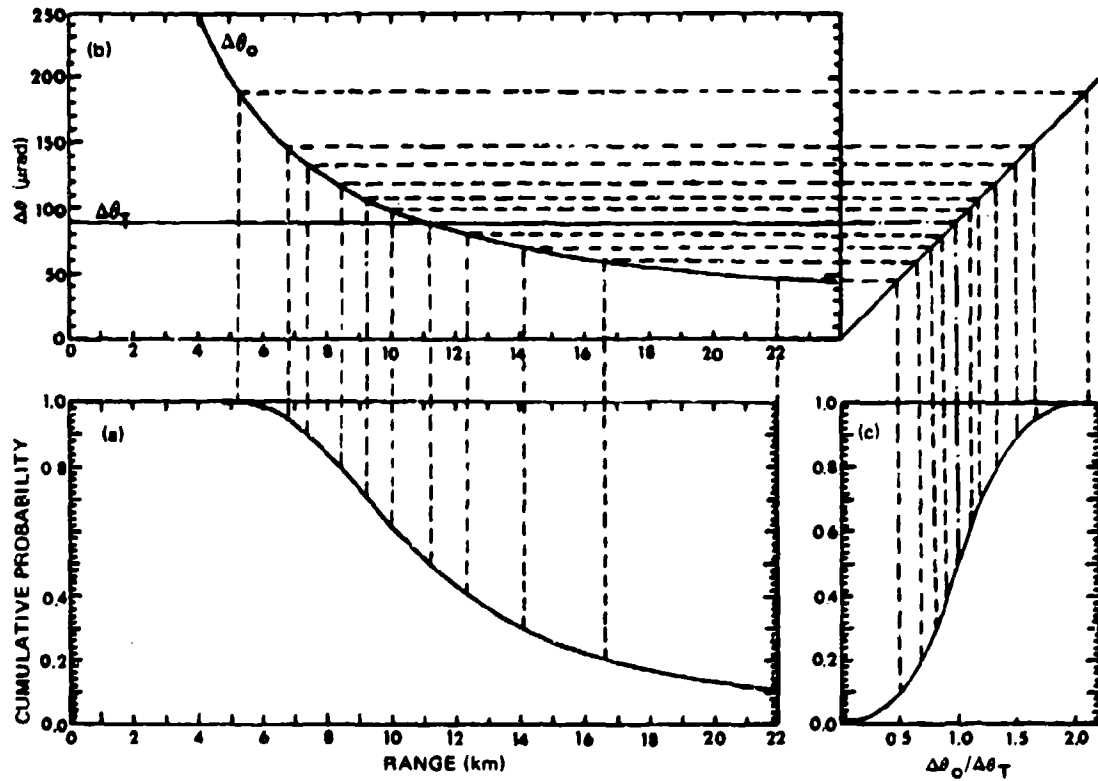


Fig. 6-7 — Graphical technique for determining the cumulative probability that a scene object will be visually discriminated at a range that is equal to or less than the range shown on the abscissa

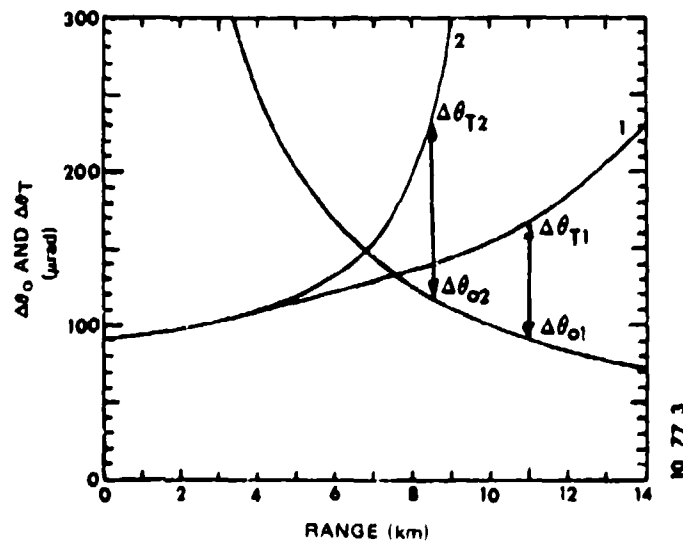


Fig. 6-8 — Angular subtense $\Delta\theta_0$ of a bar of an equivalent bar pattern and the threshold angular subtense $\Delta\theta_t$ for two cases; case 1, angular resolution is range dependent because of atmospheric transmittance only and case 2, angular resolution is range dependent because of a combination of atmospheric transmittance and the magnitude of the video SNR.

F. A. ROSELL

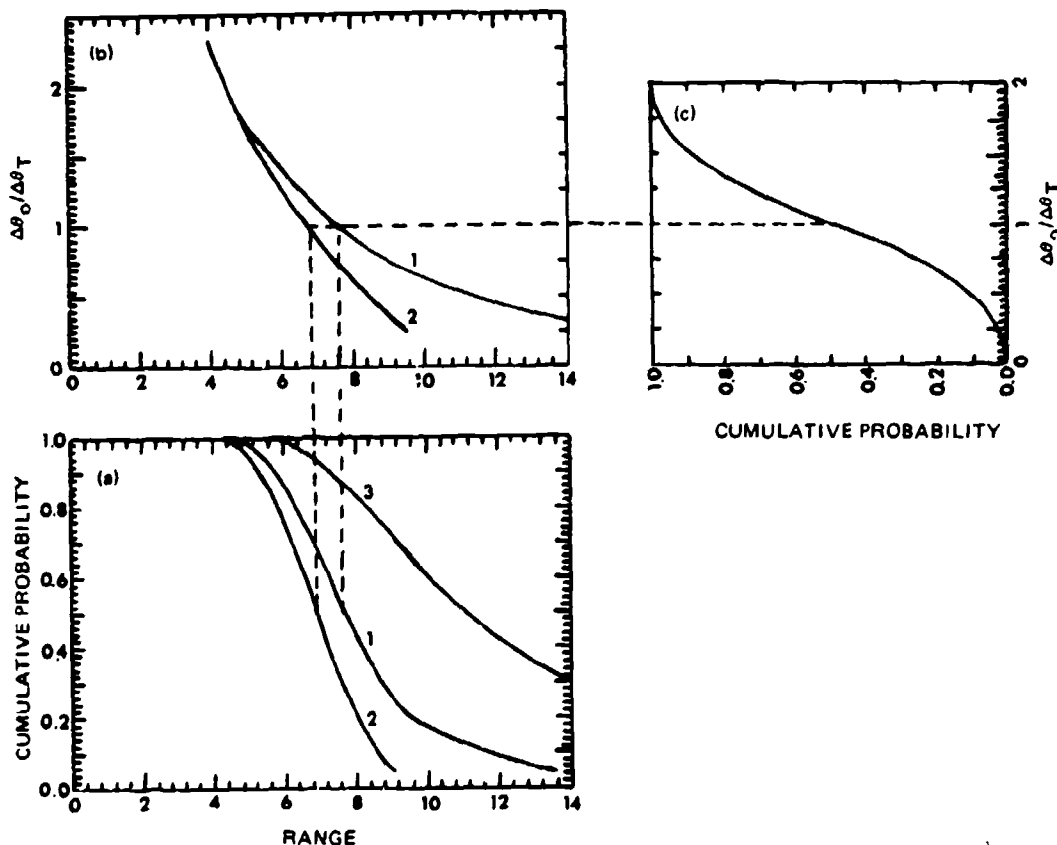


Fig. 6-9 — Graphical method of determining the cumulative probability that a scene object will be visually discriminated at a range that is equal to or less than the range shown on the abscissa

REFERENCES

- 6-1 Johnson, J. "Analysis of Image Forming System," Proc. of Image Intensifier Symposium, Oct. 6-7, 1958
- 6-2 Rosell, F.A., and Willson, R.H., Performance Synthesis (Electro-Optical Sensors), AFAL-TR-72-229, Air Force Avionics Laboratory, Ohio, August 1972, AD-905-2812
- 6-3 Rosell, F.A., Performance Synthesis of Electro-Optical sensors, Report No. EOTM No 575, Night Vision Laboratory, Ft. Belvoir Va., Contract No. DAAK-53-75-C-0225 Feb. 1977
- 6-4 O'Neill, G., Report No. NADC-202139: GJO, Naval Air Development Command, January 1974
- 6-5 Rosell, F.A. "Levels at Visual Discrimination for Real Scene Objects vs Bar Pattern Resolution for Aperture and Noise limited Imagery" Report 75CH0956-3 NAECON June 1975.

Chapter VII

THERMAL-IMAGING-SYSTEM (TIS) DYNAMIC FIELD PERFORMANCE

D. Shumaker

A. INTRODUCTION

1. Function of a Dynamic Model

Three major tasks must be accomplished to derive useful information from a thermal-imaging-system:

- Physical acquisition, which is the positioning of the field of view of the thermal-imaging-system about the target so that it is imaged on the display.
- Visual acquisition of the target on the display. This task contains both a visual search phase and a visual detection phase.
- Extraction of the required information from the previously detected target.

All of the tasks must often be accomplished in a limited amount of time.

The entire development of the last two chapters has been directed to predicting an observer's ability to visually detect, recognize, or identify a scene object given as much time as necessary to find the object of interest. The following sections are dedicated to considerations for incorporating this analysis into an overall characterization of thermal-imaging-system use in performing the above three functions. We will call this total thermal-imaging-system characterization a dynamic model, because addition of target acquisition (both physical and visual) requires considerable emphasis on the passing of time and the changing of geometry.

Dynamic modeling of imaging systems is presently in its infancy. Work on the subject is being pursued actively and thus the state of the art is evolving rapidly. The following material is presented in order that the reader may consider the implications of the truly dynamic conditions under which FLIR systems are often operated and the potential impact of these conditions on system analysis.

2. Justification for Constructing a Dynamic Model

Dynamic modeling may represent a considerable increase over static modeling in the complexity of analysis and bulk of computations required to reach meaningful conclusions. However, this increase is justified by the more thorough consideration of the thermal-imaging-system afforded. Static analysis cannot completely define all of the important parameters describing a thermal-imaging-system, since it does not include the important parameters of search and acquisition.

D. SCHUMAKER

Of the several hundred thousand resolution elements typically available in a thermal image, visual identification of real scene objects may require only 4 to 900 elements on the object's image. The function of the remaining 99% of the resolution elements in the thermal image is target acquisition, that is, making the field of view (FOV) of the system large enough to ensure that the target is imaged. Since system cost is highly dependent on the product of resolution and field of view, not considered in static analysis, if a thorough tradeoff of performance and cost is to be made, a dynamic analysis is appropriate.

3. Description of the Dynamic Environment

The treatment of dynamic performance is inherently statistical. This chapter will discuss statistical elements that could be used to describe various thermal-imaging-system applications. The synthesis of a performance model from these elements will vary, depending on the particular applications. The major effort of this chapter is to establish the proper temporal relationships between each of the statistical elements.

The general scenario which is used herein to describe thermal-imaging-system applications is as follows:

The target position is assumed to be known with some degree of certainty (meters, nautical miles, etc.). At the initiation of the mission the observer begins to look for the target on the system display while the system field of view itself is moved through some defined area of search, within which the target is expected to be located. The area within which the thermal-imaging-system field of view is moved is defined as the search field. The line of sight to the target may be blocked by terrain, foliage, etc., and the probability of a clear line of sight may change with time. The observer searches the system display visually. If an object is detected, it is retained in the field of view as the observer attempts to perform higher order visual processing of the image.

The above scenario is not all encompassing, but provides a convenient base for describing many thermal-imaging-system applications. The scenario can be conveniently described by using six probability functions listed below.

- P_{SF} , the probability that the object is within the search field;
- P_{FOV} , the probability that the object is within the sensor field of view given it is within the search field;
- P_{LOS} , the probability that a clear line of sight exists between the sensor and the object;
- $P_{L/D}$, the probability that a displayed object falls into the observer's area of visual attention or "glimpse";
- $P_{D/L}$, the probability that an object within the observer's glimpse is detectable, with ΔD being an incremental change in $P_{D/L}$; and
- $P_{I/D}$, the probability that an observer can identify (in the generic sense) a detected object, with ΔI being an incremental change in $P_{I/D}$ analogous to ΔD .

The three functions P_{SF} , P_{FOV} , and P_{LOS} are considered in Section B on physical target acquisition. Section B describes how P_{SF} can be calculated based on system and tactical factors. P_{SF} is assumed to be monotonically decreasing.

From the generalized scenario, it can be seen that the sensor field of view samples the search field. P_{FOV} might be thought of in simplest terms as the ratio of the area of the field of view to the area of the search field, although section B develops a more rigorous formulation for it and demonstrates the shortcomings of the simple area ratio concept.

The probability of having a clear line of sight to the target is assumed herein to be monotonically increasing. The elements that determine P_{LOS} include cloud cover and terrain and foliage masking. The effects of these elements on P_{LOS} are discussed in section B.

The function $P_{L,D}$, the probability that a displayed target is within the area of the observer's glimpse, describes visual search. It has been customary to describe the visual search process as the visual moving about of an aperture within which a target can be detected and outside of which a target cannot be detected. It is assumed that the aperture is moved rapidly and is then stationary for a relatively long period of time called the glimpse duration. Section C discusses $P_{L,D}$ for representative applications. The duration of the glimpse is usually the basic unit for stepping time in dynamic performance modeling.

$P_{D,L}$ is the probability of detecting an object that is being actively looked at by the observer. $P_{D,L}$ is related to the static probability of detection developed by the use of alternative approaches in Chapter VI. The function describes the fraction of the population that can detect the target. $P_{D,L}$ is assumed to be monotonically increasing. This is because in most applications range is either constant or decreasing and thus the signal to noise ratio (SNR) (upon which $P_{D,L}$ is dependent) is either constant or increasing.

The function $P_{I,D}$ is the probability that an observer can identify a detected target. The function behaves as does $P_{D,L}$. Methods for calculating $P_{I,D}$ were discussed in Chapter VI as the static probability of target identification (generically). In this chapter $P_{I,D}$ is assumed to change with time, being monotonically increasing.

4. Coordinate Systems

Many coordinate systems are used in describing overall sensor system performance. These include:

- Flat earth ground coordinates (X, Y), origin at the object.
- Platform coordinates (θ, ϕ), Az. El, origin in the platform.
- Display coordinates (x, y), origin at a display's center.
- Visual coordinates (Γ, Ψ), origin at the center of the fovea.

For general discussions in which we do not specify a coordinate system, we will use (γ, ψ).

B. PHYSICAL TARGET ACQUISITION

Physical acquisition is the act of getting an object displayed. An object may be physically acquired but not detectable; that is, if an object's location is displayed, it is physically acquired

whether it is detectable or not. Analysis of physical acquisition is broken down herein into three facets. The first facet is determining the probability, P_{SF} , that the object is within the field being searched. The second part is determining the probability, P_{FOV} , that the object is instantaneously within the field of view of the thermal imaging system. Lastly, the probability, P_{LOS} , that a clear line of sight exists between the object and the sensor must be determined. Each of these facets of the problem is examined below.

1. Probability that the Target is in the Search Field (P_{SF})

During the acquisition/detection phase of a thermal-imaging-system application, the sensor field of view may be moved about in an attempt to acquire an object whose actual position is uncertain. This search may be mechanized as a programmed search, may be totally manual, or may be partially or completely defined by platform motions. Irrespective of its mechanization, the search field is defined as that expanse throughout which the field of view may be moved to acquire the desired object. In many cases the limits are imposed by gimbal constraints or physical obscurations. In other cases tactics limit the usable area within which a mission can be prosecuted.

The probability that an object is in the search field (P_{SF}) represents the fraction of missions for which it will be in the search field. The probability is distributed over the ensemble of mission conditions but not over time within the mission itself. The search field may change size during a mission, changing the probability of the target being therein.

If $P_T(\gamma, \psi)$ is the probability distribution function for object position in pertinent coordinates, and the magnitude of the search field dimensions are defined to $\pm SF_\gamma/2$ by $\pm SF_\psi/2$ in the (γ, ψ) coordinate system, then the probability that the object is in the search field is simply:

$$P_{SF} = \int_{-SF_\gamma/2}^{SF_\gamma/2} \int_{-SF_\psi/2}^{SF_\psi/2} P_T(\gamma, \psi) d\gamma d\psi. \quad (7-1)$$

The following are examples of search fields found in typical scenarios and calculations of the probability of objects being therein.

a. Air-to-Ground Scenario with Handoff from a Radar to a Thermal-Imaging-System with Computer-Aided Tracking

In this type of mission it is assumed that the radar has acquired the desired object. At handoff ($t = t_o$) the operator directs the field of view of the thermal-imaging-system to search about the object position indicated by the radar. The reference frame is the coordinate system of the aircraft, and the object coordinates are typically in azimuth and elevation.

Systems such as radar are subject to inaccuracies in determining object location due to the noisy nature of both the electronic processing and the mechanical tolerances associated with position-signal generation.

These errors generally take the form of:

- equipment misalignment, such as boresite errors,
- resolver inaccuracies, and
- electronic signal detection uncertainty due to noise in the processed signal.

It is normally assumed that these errors can be approximated by a binormal distribution with a first standard deviation of σ_θ in azimuth and σ_ϕ in elevation. Since the noise in the radar signal might produce excessive focal-plane jitter if the thermal-imaging-system were simply slaved to the radar position information, it is customary to introduce the indicated object coordinates into an onboard computer and use inertial-navigation-system (INS) inputs to generate continuous positional information for the thermal-imaging-system.

Although cumulative errors in navigation inputs after handoff are also present and could be treated simultaneously, the largest source of uncertainty in the object position for this situation is the radar positional uncertainty. For many realistic situations using thermal-imaging-systems, one can expect the cumulative navigational errors from the time of handoff until thermal-imaging-system engagement to be small compared with radar-to-thermal-imaging-system handoff errors, and we assume this to be the case here. Airborne radar pointing errors typically range from less than 5 milliradians to one or more degrees depending on the type and vintage of the radar and the target conditions.

At handoff it is assumed that the search field is centered on the indicated object position. The probability that the search field is pointed away from the actual object position by angular extent (θ, ϕ) is

$$P_H(\theta, \phi) = (2\pi\sigma_\theta\sigma_\phi)^{-1} \exp(-\theta^2/2\sigma_\theta^2) \exp(-\phi^2/2\sigma_\phi^2), \quad (7-2)$$

which due to the symmetry of the function becomes $P_T(\theta, \phi)$. This is illustrated in Fig. 7-1.

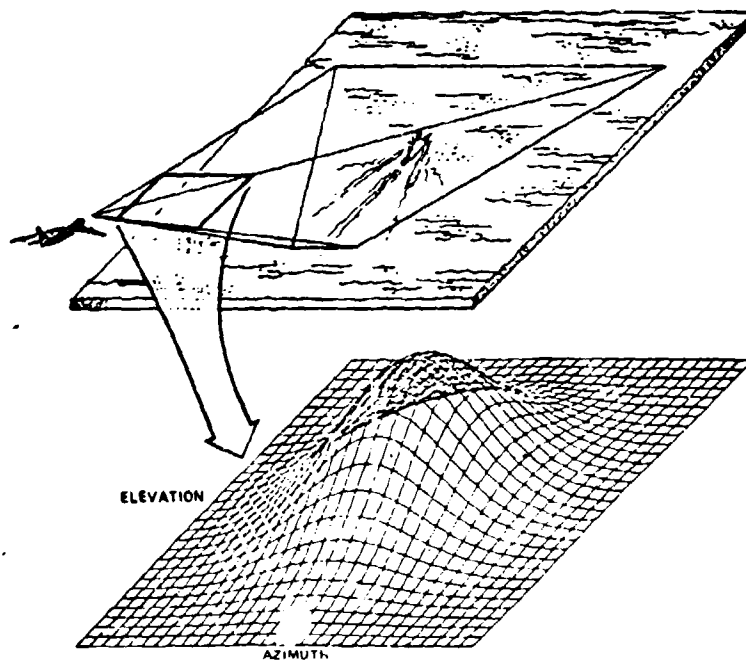


Fig. 7-1 — Radar-to-thermal-imaging-system handoff geometry

Integrating $P_T(\theta, \phi)$ over the search field of the thermal-imaging-system yields the probability that the object is in the search field at handoff.

Frequently in airborne systems using this mechanization no physical search with the field of view of the thermal-imaging-system is implemented, and the search field becomes the field of view itself. In this case Eq. (7-2) becomes

$$P_{SF} = \frac{1}{2\pi\sigma_\theta\sigma_\phi} \int_{FOV} \exp(-\theta^2/2\sigma_\theta^2) \exp(-\phi^2/2\sigma_\phi^2) d\theta d\phi. \quad (7-3)$$

If the field of view is set to $2\sigma_\theta$ by $2\sigma_\phi$ centered on the indicated object location, this integration yields a P_{SF} of 0.46. If this field of view is enlarged to $4\sigma_\theta$ by $4\sigma_\phi$, the probability becomes 0.91; and when the field of view is set to $6\sigma_\theta$ by $6\sigma_\phi$, the probability becomes 0.99. This illustrates the importance of sizing of the field of view in such cases, since if the field of view is set equal to the radar's 1σ accuracy, better than 50% of all missions are consigned to failure at handoff, because the object will not be in the field of view.

After handoff, the search-field footprint on the ground (the intersection of the search field with the ground plane) shrinks as range closes. However, the object distribution function on the ground $P_T(X, Y)$ is constant with time, as determined from $P_T(\theta, \phi)$ at the time of handoff. Therefore, the probability that the object is in the search field decreases with time, since it may be determined by integration of $P_T(X, Y)$ over the shrinking footprint.

To calculate the probability of the object being in the search field after handoff, the integration can continue to be accomplished in angular coordinates by applying appropriate coordinate transforms.

b. Ground-to-Air Scenario in Which Radar Is Used to Locate the Target and the Field of View of the Thermal-Imaging-System Is Permitted to Ride the Filtered (Low-Pass) Position Output of the Radar

For this case, the search field becomes the entire radar field of view, and the probability of the object being in the field approaches unity. However, if the freedom of the field of view to move is constrained to $\pm\Theta/2$ in azimuth and $\Phi/2$ in elevation, which is normally the case, the probability of the object being in the search field is given (assuming Θ and Φ are small) by:

$$P_{SF} = \frac{1}{2\pi\sigma_\theta\sigma_\phi} \int_{-\Theta/2}^{\Theta/2} \int_{-\Phi/2}^{\Phi/2} \exp(-\phi^2/2\sigma_\phi^2) \exp(-\theta^2/2\sigma_\theta^2) d\theta d\phi, \quad (7-4)$$

where σ_ϕ is the radar 1σ accuracy in elevation and σ_θ is the radar accuracy in azimuth. This formulation is also appropriate for radar designation for thermal-imaging-systems in air-to-surface and air-to-air applications.

c. Air-to-Ground Scenario in Which the Object Is Found Using a Navigation System to Get the Aircraft to the Known Coordinate of the Object

In this case it is assumed that the inertial navigation system (INS) of the aircraft is updated at a time $t = t_u$ and all navigation errors are set to zero. As the aircraft proceeds to the latitude and longitude of the object, the INS is subject to several sources of error, such as uncompensated wind gusting and INS drift, which accumulate in time to produce uncertainty in the true position of the aircraft. At handoff ($t = t_o$) the search field of the thermal-imaging-system is centered on the object's ground coordinates as best known to the aircraft.

Since the accumulation of errors is random, the uncertainty in the aircraft position, and therefore the object's position with respect to the aircraft, may be characterized by the probability distribution function (pdf) which is typically assumed to be a bivariate normal distribution in ground coordinates (X, Y) (Fig. 7-2):

$$P_T(X, Y) = (2\pi\sigma_X\sigma_Y)^{-1} \exp(-X^2/2\sigma_X^2) \exp(-Y^2/2\sigma_Y^2), \quad (7-5)$$

where σ_X^2 and σ_Y^2 , the variances of the object probability distribution functions in ground coordinates, are functions of time:

$$\sigma_X = K_X(t - t_u), \quad (7-6)$$

$$\sigma_Y = K_Y(t - t_u), \quad (7-7)$$

where K_X is the rate of error accumulation in X , K_Y is the rate of error accumulation in Y , and t_u is the time of the last navigation update. Typical values of K_X and K_Y are 1 to 5 nautical miles per hour.

The thermal-imaging-system is continually directed to the object after handoff using computer generated commands derived from the INS and known target coordinates.

The probability that the object will be in the search field at any time is given by the integral of the pdf given by Eq. (7-5) over the ground mapping of the search field:

$$P_{SF} = \frac{1}{2\pi\sigma_X\sigma_Y} \iint_{\text{Search Field}} \exp(-X^2/2\sigma_X^2) \exp(-Y^2/2\sigma_Y^2) dXdY. \quad (7-8)$$

This is shown schematically in Fig. 7-2.

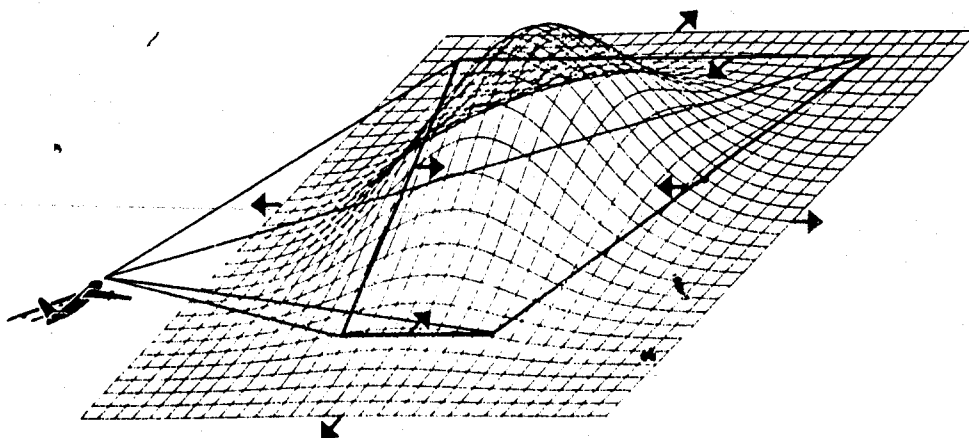


Fig. 7-2 — Navigation-to-thermal-imaging-system handoff geometry

2. Probability of the Target Being in the Field of View, Given It Is in the Search Field (P_{IOV})

The probability that an object is in the field of view of the thermal-imaging-system given that it is in the search field is a function of the object position probability distribution function due to the uncertainty of the object location within the search field (P_H), the distribution function describing the positioning of the field of view of the thermal-imaging-system within the

search field (P_{FF}), and the size of the field of view of the thermal-imaging-system (FOV). Since the FOV samples the search field during the mission, P_{FOV} is a probability that is distributed in time. The probability of the object being in the FOV at a particular moment can be expressed by calculating the probability that the effective area of the FOV envelops the point in the search field at which the object is positioned, given that the object is in the search field; that is:

The search field is subdivided into elemental areas ($\Delta\gamma, \Delta\psi$). If the FOV is assumed to be an area $VFOV$ high by $HFOV$ wide, the probability that it will envelop the object is the sum of a series of terms. The first term is the probability that the object falls in $(\Delta\gamma, \Delta\psi)_1$ multiplied by the probability that a FOV center falls somewhere in the area of dimension $VFOV$ by $HFOV$ centered at $(\Delta\gamma, \Delta\psi)_1$; the second term is the probability that the object falls in $(\Delta\gamma, \Delta\psi)_2$ multiplied by the probability that an FOV center falls somewhere in an area of dimension $VFOV$ by $HFOV$ centered by $(\Delta\gamma, \Delta\psi)_2$, and so on until the search field is covered. This process is illustrated in Fig. 7-3.

The integral representation of this sum is

$$P_{FOV} = \iint_{\text{Search field}} P_{TF}(\gamma, \psi) \int_{\gamma-HFOV/2}^{\gamma+HFOV/2} \int_{\psi-HFOV/2}^{\psi+HFOV/2} P_{FF}(\gamma', \psi') d\gamma' d\psi' d\gamma d\psi, \quad (7-9)$$

where $P_{TF}(\gamma, \psi)$ is the object-position probability distribution function (pdf) normalized to P_{SF} and $P_{FF}(\gamma, \psi)$ is the pdf describing the positioning of the FOV . Frequently P_{FOV} is assumed to be the ratio of the area of the FOV to the area of the search field. Tacit to this assumption is that P_{TF} and P_{FF} are uniformly distributed. While in many instances no better assumption may be possible regarding P_{TF} and P_{FF} , the value for P_{FOV} may be grossly incorrect if P_{TF} and P_{FF} are either correlated or anticorrelated. Such an example of this problem was given in paragraph B1b. In this case P_{TF} is the same as P_{FF} , maximizing the integral of Eq. (7-9) due to the correlation of the two functions and resulting in a very inaccurate calculation of P_{FOV} if it is set to the ratio of FOV /area of the search field.

In many air-to-ground, air-to-air, and ground-to-air scenarios, where searching with the field of view has proven fruitless, the search field is made equal to the FOV which is entered on the most likely target position. In this case $P_{FOV} = 1$.

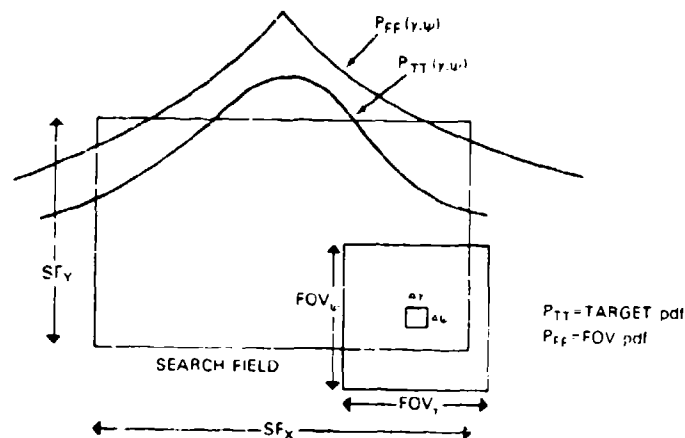


Fig. 7-3 — Search-field geometry used for the calculation P_{SF}

3. Probability of a Clear Line of Sight to the Target (P_{LOS})

The LOS to the target can be obscured for various reasons, including foliage masking, cloud cover, terrain masking, and occlusion by the horizon. In ground-to-ground applications and in many low-altitude air-to-ground and ground-to-air scenarios, cloud, foliage, and terrain masking may obscure the object to the point that detection may not be possible until range is below that appropriate to object identification.

The geometry of a mission and the local topography and foliage cover dictate at what point in a mission a terrain-and-foliage-free line of sight is obtained. In most cases, during range closure, it is expected that a single change of state from masked to unmasked will occur. Thus a statistical description of terrain-and-foliage-free line of sight reflects the statistics of mission profiles and topography. $P_{LOS}(r)$ due to terrain and foliage reflects the fraction of missions for which the line of sight will be unmasked at range R . P_{LOS} is, therefore, ensemble distributed. For a specific mission with known masking data, characterization of line-of-sight masking would simply include a change from a probability of zero to one at the range of unmasking.

Statistics of cloud cover for a few locations have been published including Ref. 7-1 for Hanover and Ref. 7-2 for Berlin/Tempelhof. The Hanover data exhibit little variation in probability of cloud-free line-of-sight with elevation angle. This indicates that in this area cloud decks dominate obscuration effects rather than partly cloudy conditions. Under these conditions the statistics of cloud-free line of sight refer to the fraction of missions for which no cloud decks will be between the target and the sensor platform operating at different altitudes. Table 7-1 provides summary material derived from the Ref. 7-1 data giving the probability of cloud-free line of sight from various altitudes to ground for various seasonal periods. In months where cloud cover is minimal, variation of P_{LOS} with elevation angle increases indicating the effects of partly cloudy skies. Under these conditions the assumption that P_{FOV} is distributed only over an ensemble of missions and not in time is compromised. That is, during this period, an aircraft flying at constant altitude may be visible from the ground one moment and not the next.

C. VISUAL SEARCH

1. Introduction

Visual display search is the most difficult portion of imaging system use to characterize and is not completely describable at this time, due to a lack of data. The following sections will, therefore, attempt to break down the display search problem into its contributing components, present treatments of those areas that have been analyzed, and discuss potential approaches in those areas as yet undefined.

2. Characterization of Scene Content

The ability of an observer to search a display scene is dependent on the scene content, which varies widely from uniform displays of sky or sea to highly complex displays of mixed landscapes or urban areas. For convenience, scene elements are broken down into competing target elements or clutter and major interest directing elements. The effect of clutter is to make more difficult the task of discriminating the target from background and to enlarge the set

D. SCHUMAKER

Table 7-1 — Probabilities (in percent) of a Cloud-Free Line-of-Sight from the Specified Altitude to the Ground at Hanover, W. Germany (Ref. 7-1)

Altitude (ft)	Time	Full Year	Apr - Sept	Oct - Mar	Clearest Month	Cloudiest Month
984	D	65.9	77.8	54.0	83.4	46.1
	N	66.4	78.4	54.4	82.3	44.4
	FD	66.1	78.05	54.15	82.7	45.3
3280	D	51.55	63.4	39.7	70.1	33.0
	N	55.8	70.2	41.45	73.9	32.3
	FD	53.7	66.75	40.6	71.9	32.7
4920	D	47.8	58.1	37.5	63.7	31.0
	N	51.35	65.0	37.7	68.8	28.7
	FD	49.5	61.5	37.5	66.2	29.7
35000 ^a	D	34.0	42.4	25.6	48.1	20.0
	N	37.0	46.8	27.2	51.4	19.3
	FD	35.5	44.6	26.4	49.7	25.5

D — Daytime (0630-1830)

N — Night (1830-0630)

FD — Full day (24 h)

^aInfinity for all practical purposes.

of possible nontargets that must be interrogated to find the desired one. Numerous researchers including Erickson (Ref. 7-3) and Smith (Ref. 7-4) have found that as the clutter is increased, search time is increased for any constant signal level.

Less investigated than clutter effects and perhaps more important to search time in many cases is the effect of scene complexity as dictated by the density and distribution of major interest-directing features. Figures 7-4 and 7-5 from Yarbus (Ref. 7-5) illustrate the effect of complexity on the visual search pattern. In the pictures relatively high amounts of search time are dedicated to small areas of the scene. In these scenes an object in a high-interest area is more likely to be looked at than the same object located in a low-interest area.

Displayed scenes might therefore be broken down orthogonally by levels of clutter and complexity. The simplest case would be a single object on a clear background: such as an aircraft against a clear sky or a ship on a calm ocean. A boat in a choppy sea, where waves might represent potential false targets represents the same complexity but increased clutter. A higher degree of clutter might be found in a desert scene, where isolated sparse foliage is easily confused with a military target.

The addition of the horizon in the scene represents a first level in increased complexity. The horizon does not represent a false target but does greatly influence where the observer



Fig. 7-4 — A visual search pattern. (Figure 117 from A. L. Yarbus, *Eye Movements and Vision*, Plenum Press (with permission).)



Fig. 7-5 — A visual search pattern. (Figure 118 from A. L. Yarbus, *Eye Movements and Vision*, Plenum Press (with permission).)

looks for targets. Air-to-ground scenes with large open areas bounded by roads and tree lines might be the next more complex type of scene.

Both clutter and complexity vary continuously from zero to some extremely high value typified by urban/industrial areas and mixed complex terrains as shown diagrammatically in Fig. 7-6.

A third dimension which influences the visual interrogation of a scene is the conspicuity of the desired object. The SNR has been used herein to describe the difficulty in detecting an object and as such represents a convenient description of conspicuity. Studies of the effects of SNR on search time indicate, as one would expect, that the higher the SNR the faster and more accurately objects can be located.

Little work has been done to define the effects of clutter, complexity, and SNR on search, detection, and identification in controlled experiments involving all three variables. As a result, little data exist upon which to formulate a model of this process. The following is therefore put forth as one possible means of approaching the problem.

D. SCHUMAKER

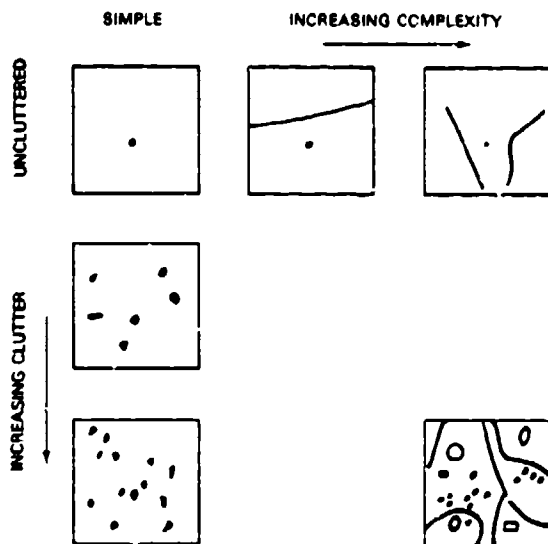


Fig. 7-6 — Breakdown of scenes by clutter and complexity

3. Definition of a Glimpse

Prior to formulating an equation for visual search time; it is convenient to define a unit of search in time and space. We will refer to this unit as a *glimpse* following traditional definition. The following explores the temporal and spatial characteristics of the glimpse.

Occulometer studies by Yarbus (Ref. 7-5) and Williams *et al.* (Ref. 7-6) indicate that the eye inspects a scene in a series of glimpses composed of a relatively long stationary period of *fixation* followed by a very short movement or *saccade*. The eye-brain is effectively blanked during the saccadic movement, so that the conscious effect is that of visual continuity. Fixations last for varying lengths of time, as indicated in Fig. 7-7 from Yarbus. The length of the fixation depends on the context of the visual scene and the task given the observer. Yarbus and Williams conclude that the mean fixation period is approximately 1/3 second.

The duration of the saccade is also variable depending on the distance moved between fixations. Yarbus indicates that the relationship between duration and amplitude of the saccade is

$$T_s = 0.121 \delta_s^{1/5}, \quad (7-10)$$

where T_s is the duration of the saccade in seconds and δ_s is its amplitude in degrees. The interfixation distance is itself a function of scene context, observer tasking, and scene subtense. Yarbus indicates that the fixation consumes 95% of the glimpse time, leaving only about 5% for the saccade.

The area of the glimpse, or that visual angle within which a target can be detected, is not sharply defined. The detection capability of the eye varies over the entire visual field and is a function of the type of detection problem. The fovea has the best color-detection capability, and the peripheral vision has excellent sensitivity to movement and excellent scotopic sensitivity. The probability of detecting an object of unknown location in the visual field can best be given, therefore, as an integral of detectability over the entire visual field:

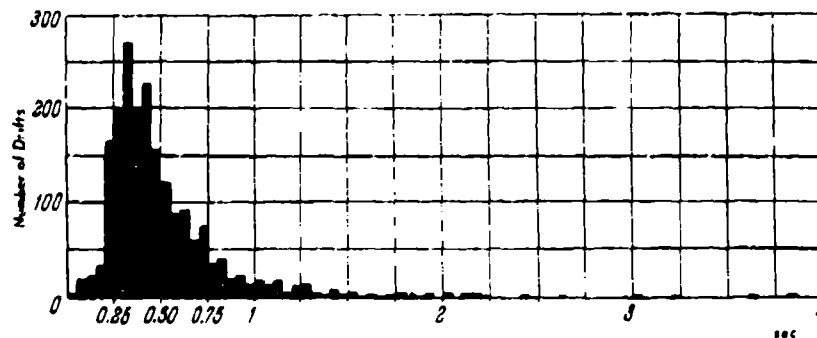


Fig. 7-7 - Distribution of glimpse duration. (Figure 58 from A. L. Yarbus, *Eye Movements and Vision*, Plenum Press (with permission))

$$P_{DV} = \iint_{\text{Visual Field}} P_T(\Gamma, \Psi) D_V(\Gamma, \Psi) dA, \quad (7-11)$$

where P_{DV} is the probability of visually detecting an object, P_T is the object's positional distribution function, and D_V is the visual detectability of the object in an incremental area of the visual field (dA) as a function of location within the visual field.

Since the integral is cumbersome to solve during computation of visual performance, and since P_T in visual coordinates is virtually never definable, it has been more convenient to spatially describe the glimpse as an area or visual lobe having constant $D_V(\Gamma, \Psi)$ equivalent to the total integral of D_V . Thus, assuming

$$P_T(\Gamma, \Psi) \equiv \text{CONST and } \iint_{\text{Visual Field}} P_T dA \equiv 1 \quad (7-12)$$

we have:

$$\iint_{A_0} D_V(\Gamma, \Psi) dA = \iint_{\text{Visual Field}} D_V(\Gamma, \Psi) dA \quad (7-13)$$

D. SCHUMAKER

and

$$A_G = 1/D_V \iint_{\text{Visual Field}} D_V(\Gamma, \Psi) dA, \quad (7-14)$$

where D_V is the detectability of the object within the area of the glimpse. For most applications, D_V is the best set equal to the detectability at the fovea, since most pertinent experiments in detection have been conducted in this portion of the visual field. When motion detection or detection under scotopic conditions is required, D_V might be set to a value of peripheral detectability.

Setting D_V equal to the object's detectability in the fovea and $D_V(\Gamma, \Psi)$ equal to the product of the object's detectability in the fovea and the ratio of detectability in the periphery to that in the fovea $R_{VD}(\Gamma, \Psi)$, we have

$$A_G = \iint_{\text{Visual Field}} R_{VD}(\Gamma, \Psi) dA. \quad (7-15)$$

Equation (7-15) gives the commonly assumed definition of the glimpse area.

Frequently the glimpse area is assumed to be some arbitrary constant such as the foveal area or a 5° cone. However search time is exceedingly dependent on the glimpse area, so that some attempt to approximate it as a function of signal level is warranted. For instance, the assumption that the glimpse area is equal to the fovea, which is approximately a 1° cone, yields a search time 25 times that required assuming a 5° cone for the same level of assurance. For a typical display of $14^\circ \times 18^\circ$ (13 by 18 cm viewed at 56 cm), random search times (assuming replacement) for 90% detection confidence require times as given below:

$$0.9 = 1 - \left[1 - \frac{A_G}{A_D} \right]^N \approx 1 - \exp(-A_G N / A_D), \quad (7-16)$$

$$\ln(0.1) \approx -(A_G N / A_D), \quad (7-17)$$

or

$$N = -(A_D / A_G) \ln(0.1), \quad (7-18)$$

where N is the number of glimpses required and A_D is the area of the display. Equation (7-18) indicates that N_{fovea} is 739 and N_{5° is 30. This result equates to a 246-second search interval for the fovea glimpse and 10 seconds for the 5° glimpse. While a 10-second time might be tactically acceptable, there are few applications in which a 4+ minute search is acceptable. Actual experience indicates search time varies from effectively zero ($A_G \geq A_D$), if the signal is sufficiently large and the picture simple, to infinity for very low signals and complex scenes. Thus, assumptions of a glimpse size can lead to staggeringly different calculations of search time and widely divergent conclusions regarding the tactical usefulness of a thermal-imaging system.

4. Visual-Lobe Models

Several visual-lobe models have been established as a means of calculating the size of the glimpse for unaided visual search. These models assume that the limitation to detectability is contrast. Although these models have applicability to infrared imaging systems, the basic

SNR_D limitation to visual perception assumed in previous chapters suggests a visual lobe based on SNR_D rather than contrast. Shumaker and Keller (Ref. 7-7) have developed a visual-lobe model for search in simple uncluttered displays based on the SNR_D concept of Worthy and Sendall (Ref. 7-8) which relates the visual lobe size to the falloff of visual acuity with increasing distance from the fovea. This is a theoretical rather than empirical model consistent with the integral definition of the glimpse area given in Eq. (7-15). In this model the size of the visual lobe is a function of system parameters as well as target size. The radius of the visual lobe in this model is

$$R_G = 0.14 - 0.63 \ln(\zeta) + 3.8[\ln(\zeta)]^2 + R_f, \quad (7-19)$$

where R_G is the radius of the glimpse in degrees, R_f is the radius of the fovea or about $1/2^\circ$, and ζ is a complex function of target and system parameters and SNR_D . Eq. (7-19) is based on the falloff of visual acuity with increasing peripheral angle. This model applies to aperiodic detection only. The model is qualitatively consistent with observed changes in the detectability of targets of unknown display coordinates with SNR_D but has not been verified experimentally. Fig. 7-8 gives the radius of the glimpse calculated using Eq. (7-19) for three systems. The graph illustrates why search in uncluttered displays is virtually instantaneous. As the object SNR_D exceeds threshold (2.8 in this case) the visual lobe grows rapidly to sizes comparable to that typical of display subtense.

Pearson (Ref. 7-9) developed a visual-lobe model similar to that of Shumaker and Keller but applicable to periodic object detection instead of aperiodic object detection. In this case ζ in Eq. (7-19) is given by

$$\zeta = [1 - 2 \ln(2.8/SNR_D) / \pi R_f^2 f_D^2]^{-1/2}, \quad (7-20)$$

where f_D is the spatial frequency characterizing detection and SNR_D sub f is the SNR_D calculated at target frequency f_D using the Rosell and Willson methodology for characterizing detection/identification.

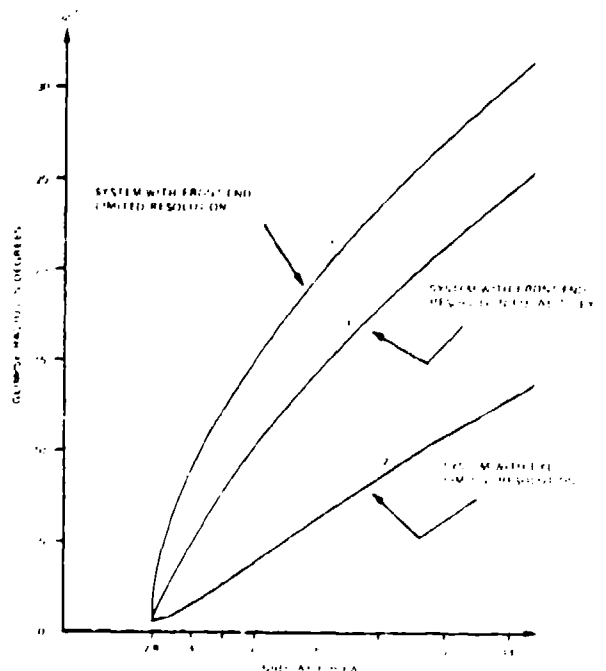


Fig. 7-8 — Radius of the visual lobe as a function of SNRP

D. SCHUMAKER

This model, like the foregoing aperiodic model, is unproven and is based purely on the falloff of visual acuity with increasing peripheral angle. Furthermore both of these models suffer from the additional problem of being derived from monocular vision data rather than from normal binocular vision.

Other visual-lobe models such as that of Lamar (Ref. 7-10) can be applied to thermal-imaging-system imagery, but care must be exercised in so doing to account for any potential differences between contrast-limited and SNR_D -limited conditions. Under contrast-limited conditions, Lamar found the radius of the glimpse to be related to contrast by the following relationships.

$$C_{T_F} = 1.55 + \frac{15.2}{\beta^2}, \text{ for } \theta < 0.8 \text{ (on axis)} \quad (7-21)$$

and

$$C_{T_u} = 1.75\theta^{1.2} + \frac{19\theta}{\beta^2}, \text{ for } \theta > 0.8, \quad (7-22)$$

where β is angular subtense of the desired object in minutes, θ is angle off the visual axis in degrees, and C_T is detectable contrast in percent.

The Lamar visual lobe model can be used in high-signal conditions if the signal transfer function of the system is known and display contrast is deducible. Under low-signal conditions its application may be somewhat compromised by potential differences between the Modulation Transfer Function (MTF) effects on noise-limited and contrast-limited performance. If second-order effects of noise filtering by the MTF are ignored and if both contrast-limited and noise-limited performance of the eye are assumed to fall off similarly with peripheral angle, Lamar's model can be applied to low-signal case. This model, like that of Shumaker and Keller, characterizes only aperiodic detection where there is no need for shape information.

5. Probability of Looking at a Displayed Target

Having defined in the previous section a unit of visual search (the glimpse), we can proceed to calculate the probability $P_{L,D}$ that a displayed object will be enclosed by the glimpse area during the display search process. Frequently $P_{L,D}$ (probability of being looked at given it is displayed) is assumed to be simply the ratio of the glimpse size to the display size. However, this assumption is seldom correct and is only a reasonable estimate under very specialized conditions to be discussed later. A general evaluation of $P_{L,D}$ is given below. The probability statement is formulated as follows:

The display of dimensions X_D by Y_D is subdivided into elemental areas $(\Delta X, \Delta Y)$. If the glimpse is assumed to be a square of area D^2 (recognizing that the assumption of a square is for simplicity of development only), the probability that it will envelope an object is the sum of a series of terms. The first term is the probability that the object falls in $(\Delta X, \Delta Y)_1$, multiplied by the probability that a glimpse falls in a square of dimension $D \times D$ centered at $(\Delta X, \Delta Y)_1$, the second term is the probability that the object falls in $(\Delta X, \Delta Y)_2$ multiplied by the probability that the glimpse center falls somewhere in an area $D \times D$ centered at $(\Delta X, \Delta Y)_2$, and so on until the display field is covered.

The process is identical to that used for calculation of P_{FOV} . Its integral representation is

$$P_{L/D} = \int_{-Y_D/2}^{Y_D/2} \int_{-X_D/2}^{X_D/2} P_{TD}(x, y) \int_{-Y_D/2}^{Y_D/2} \int_{-X_D/2}^{X_D/2} P_G(x', y') dx' dy' dx dy, \quad (7-23)$$

where $P_{L/D}$ is the probability of a displayed object falling within a glimpse. P_{TD} is the target position probability distribution function (pdf) normalized to the probability of being displayed, and P_G is the position pdf for glimpses.

a. Glimpse Distribution

Equation (7-23) describes the calculation of $P_{L/D}$ given a knowledge of the glimpse size, glimpse distribution, and displayed object pdf. Paragraph VII C(4) examined potential calculations of the glimpse size. The following subparagraphs will elaborate on formulations and assumptions with regard to determining the distribution of glimpses within (and beyond) the display. The problem can be broken down into structured and unstructured cases.

b. Unstructured Display Search

As indicated in VIII C(2), prominent scene features affect the order in which an observer inspects a display, especially if the features impart to the observer a higher or lower expectation of finding a target in their proximity. When no such structure is present on the display to otherwise direct search, a simpler search pattern should be expected. This pattern could still be influenced by expectations concerning the location of the desired object. Furthermore, the pattern could be influenced by the subtense and shape of the display and its immediate surround.

Enoch (Ref. 7-11) performed a study of the natural search patterns of observers using circularly apertured maps as the display to be searched. Equation 7-24 gives a glimpse distribution formulated for rectangular displays from the Enoch data (for 9° and larger displays) assuming that although structure was present on the display, the structure present was everywhere of equal interest to the observer.

$$P_T(x, y) = K \exp(-2|x|/X_D) \exp(-2|y|/Y_D), \quad (7-24)$$

where X_D is the display width (angular), Y_D is the display height (angular), and $K = 0.25/(X_D Y_D)$. This formulation is chosen largely to preserve the analytical integrability for Eq. (7-23) at the expense of more precise formulations that would not be as easily integrable. The equation indicates that the angular size of the display actually influences the radial distribution of glimpses.

If the target position pdf is known, Eq. (7-23) can be evaluated for $P_{L/D}$. Since in airborne and surface-to-air applications the target pdf is frequently known, because a radar or navigation handoff procedure is used to locate target, a good estimate of $P_{L/D}$ can be obtained. If the pdf describing either the distribution of glimpses or targets is unknown, then for unstructured displays the best estimate of $P_{L/D}$ is the ratio of the area of the glimpse to the area of the display.

c. Structured Display Search

In most cases any attempt to predict $P_{L/D}$ as a function of range is subject to considerable conjecture about the influence of displayed image structure. Unfortunately it is in these highly

D. SCHUMAKER

uncertain conditions that the $P_{L/D}$ term can be expected to dominate the overall probability of mission success. The figures from Yarbus (Figs. 7-4 and 7-5) seem to indicate that an observer spends 80 to 90% of his observation time focusing on interest attracting features which may constitute only a few percent of the area to be searched. Although Eq. (7-23) still predicts the probability of a displayed object falling within a glimpse in this complex case, the function P_G is difficult if not impossible to define. However, Eq. (7-23) does indicate why training is such an important factor in sensor use. Training and experience eventually lead to high correlation between the distribution of targets and that of glimpses, since observers eventually learn to look for objects where they have previously found them. This minimizes search time according to Eq. (7-23).

Fig. 7-8 from Ref. 7-12 shows the probability of target detection function of time in various degrees of background clutter. This is a composite set of curves comprising a large number of field trials involving various target-to-background contrasts. The interesting feature of the curves is that the time required to find a target is related to the final probability of ever finding it in the time allotted (45 s). It is clear that the easiest targets were not found by a systematic search with an angular aperture of foveal size. Table 7-2 gives values of $P_{L/D}$ for various values of probability of ever detecting the target (45 s) (which is not the same as the static probability of detection) as calculated from Fig. 7-9, assuming random sampling with replacement.

Pearson (Ref. 7-9) developed an alternative to formal application of Eq. (7-23), although it still is based on Eq. (7-23), that takes into account experimental work with slightly cluttered scenes. He breaks up the display into high-interest and low-interest areas and develops a probability ($P_{L/D}$) assuming simultaneous independent searches of the two areas.

There are several treatments (GRC model (Ref. 7-13) and Marsam II (Ref. 7-14)) of search in cluttered fields, based on the data of Boynton (Ref. 7-15), which assume that search is dominated by discrimination of the target from great numbers of similar false targets. However the Boynton work was done with synthetic scenes and does not allow for the effects of visual cues, therefore indicating that a truck on a road is as difficult to find as a truck in a field. Although the degree of similarity between the target and similar nontargets would appear to heavily affect search time, it would seem that in tactical scenes visual cues may dominate search.

Table 7-2 — $P_{L/D}$ as a Function of Probability of Detection.

Probability of Detecting in 45 s (%)	$P_{L/D}$
0	0
7.5	0.00058
25	0.036
42	0.008
69	0.031
86	0.021
97	0.198

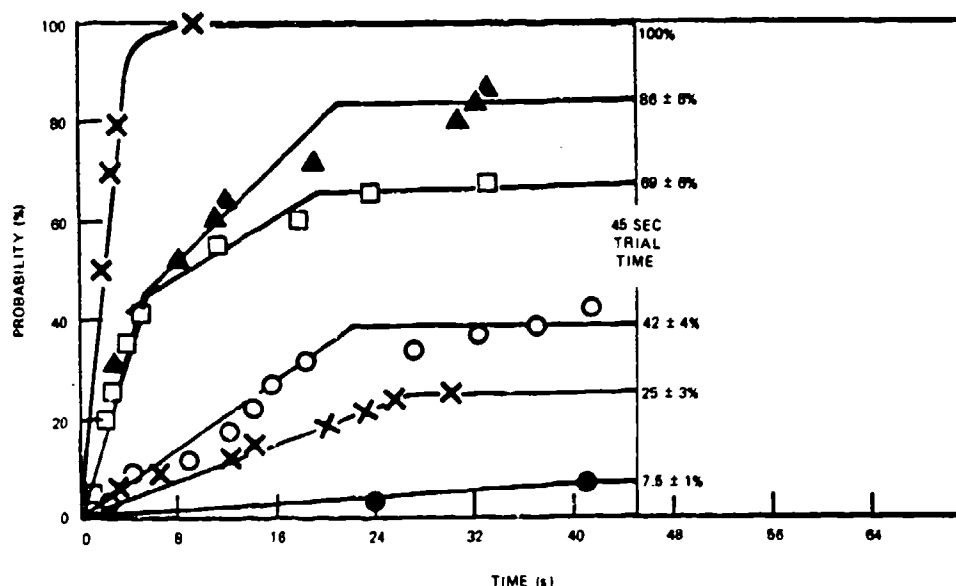


Fig. 7-9 — Field of view search composite data

6. Effects of Other Tasking

Enoch indicates that approximately 10% of all glimpses on tactically sized displays are lost to the immediate surroundings. Additionally, in the real world, the observer is tasked with performing functions other than monitoring a sensor display, such as piloting an aircraft, which decreases the probability of looking at a display target in any given time interval. If it is assumed that the distraction of the operator caused by monitoring nondisplay functions is independent of the display glimpse pattern, then the single-glimpse probability of looking at an object can be adjusted as follows to account for this additional tasking:

$$P_{L/D} = (1 - F_M) P_{L/D}(\text{display}), \quad (7-25)$$

where F_M is the fraction of the time the operator spends monitoring nondisplay functions during the detection phase of the scenario.

D. DYNAMIC MODEL FORMULATION

1. Introduction

The previous sections described the various elements that effect physical and visual acquisition. The following subparagraph will combine the classical calculations of static detection and identification with the elements of visual and physical acquisition to form a dynamic model of thermal imaging system performance.

a. Fundamental Concepts

Prior to synthesizing more general statistical models we will discuss some of the fundamental and elementary concepts for the purpose of gaining physical insight to the acquisition problem.

(1) Detection with a Changing Signal-to-Noise Ratio

In Chapter V, two alternative models were developed for detection of patterns; the aperiodic model which applies to the detection of rectangles on a uniform background and, the periodic model for the detection of bars within a pattern. In Chapter VI, methods of describing the visual discrimination of real scene objects in terms of these patterns were discussed. In the following we will assume that the methods devised are applicable. We will designate $P_{D/L}$ as the probability of detecting an object (given it is looked at) irrespective of the detection mechanism or prediction method. $P_{D/L}$ depends on some appropriate SNR irrespective of the detection mechanism. However, when predicting dynamic performance, the interpretation of $P_{D/L}$ is "the fraction of the observer population that can detect the target with the given signal level." This differs somewhat from the classical interpretation of probability of detection based on threshold conditions; however, it is believed representative of tactical decision making.

Let us now consider a SNR level that is changing in time such that $P_{D/L}(t)$ is monotonically increasing. At time t_1 , $P_{D/L}(t_1)$ is the fraction of observers that can detect an object with SNR(t_1). At time t_2 , $P_{D/L}(t_2)$ is the fraction of the observers that can detect the object with SNR(t_2). The fraction $P_{D/L}(t_2)$ contains all of the observers in the $P_{D/L}(t_1)$ fraction plus $P_{D/L}(t_2) - P_{D/L}(t_1)$ observers. The probability that an observer who failed to detect the object at time t_1 will be able to detect the target at time t_2 is given by $[P_{D/L}(t_2) - P_{D/L}(t_1)] / (1 - P_{D/L}(t_1))$, which is the probability that the observer's threshold, which could be anywhere above SNR(t_1), is actually between SNR(t_1) and SNR(t_2).

As time proceeds, a greater and greater fraction of observers can detect the object. With each step in time there is a distinct fraction of individuals added to the population of observers that can detect the object. Let us for convenience designate $\Delta D(t_i)$ as that fraction of the whole population that is added after the i th increase in SNR, and remember that prior to time t_i the group $\Delta D(t_i)$ could not detect the object, but that after time t_i they can with unity probability. Note that $\Delta D(t_1)$ is that fraction of the population that can detect the object with the signal at the first level attempted.

(2) Simple Search in a High SNR Environment

Suppose that the scene SNR as displayed is high enough so that there is no problem in discerning any target in the scene given that it is looked at. If a single fairly large target is present in the scene which is otherwise uniform, search will be quickly concluded as indicated in the preceding section. If, however, the scene is cluttered with objects that are close in size and contrast to the target, it may be reasonable to assume that the eye/brain performs a search which might be described as follows. Assume that the display is covered with a mask that covers all of its area with the exception of a small aperture. Finally, let the probability that the object is within the aperture and, therefore, visible to an observer be $P_{L/D}$ (the probability that it is looked at, given it is displayed). If we search the display by moving about this aperture, we can build up a probability function which describes cumulative probability of detection.

At time t_1 the first sample of the displayed imagery is made. The probability that the object is within the aperture is $P_{L/D}$. If the object is within the aperture, it is readily detected and the search is finished. However, the probability that the object is not found is $1 - P_{L/D} = \bar{P}_{L/D}$. Thus the probability that the mask will have to be moved to attempt detection again is $\bar{P}_{L/D}$. If detection does not occur, the aperture is rapidly moved to a new location.

If we assume the second position of the aperture is independent of its first position and if the aperture is small compared to the display area, then the probability that the object will be within the aperture on the second sample is also $P_{L/D}$. The probability of detecting the object after two possible (not necessarily required) samples is given by:

$$P_D(t_2) = P_{L/D} + \bar{P}_{L/D} P_{L/D} \quad (7-26)$$

which is the probability of detection on the first sample plus the product of the probability of not detecting on the first sample and the probability of detecting on a second sample.

After three glimpses the probability of detection becomes

$$P_D(t_3) = P_{L/D} + P_{L/D} \bar{P}_{L/D} + P_{L/D} \bar{P}_{L/D}^2 \quad (7-27)$$

From reasoning in a similar fashion, the cumulative probability of detection after N samples is:

$$P_D(t_N) = \sum_{i=1}^N P_{L/D} \bar{P}_{L/D}^{i-1} \quad (7-28)$$

If it had been assumed that the display was searched in a regular nonredundant pattern, a similar but more rapidly converging series would have resulted.

If we assume that $P_{L/D}$ may change its value with each new sample, Eq. (7-27) becomes

$$P_D(t_3) = P_{L/D}(t_1) + \bar{P}_{L/D}(t_1) P_{L/D}(t_2) + \bar{P}_{L/D}(t_1) \bar{P}_{L/D}(t_2) P_{L/D}(t_3) \quad (7-29)$$

where $P_{L/D}(t_i)$ refers to the probability of the object being located within the aperture on the i th sample period. In this case Eq. (7-28) must be generalized to

$$P_D(t_N) = \sum_{i=1}^N P_{L/D}(t_i) \prod_{j=1}^{i-1} \bar{P}_{L/D}(t_j) \quad (7-30)$$

Although the above formulation is comparatively simple and may actually describe certain visual search conditions, the search process may be much more complex.

(3) Search for an Object That May be Lost from the Display in a High SNR Environment

Assume that the object displayed in the previous example (simple search in a high SNR environment) is being observed by a TV camera that is pointed at some fixed point on the ground. The object of interest is located at some random location in the field of view. Assume further that the camera is steadily approaching the fixed ground point while the observer searches for the object on the TV display. With a fixed field of view, the "footprint" of the viewfield on the ground will constantly decrease and the probability, P_{FOV} , that the object will be in the field will decrease monotonically in turn.

Let us now consider the first sample taken as in the example of VIIDa(2) above. The probability that the object will be detected on the first sample is

$$P_D(t_1) = P_{FOV}(t_1) P_{L/D}(t_1) \quad (7-31)$$

which is the product of the probability that the object is within the camera field of view at time

t_1 and the probability that it is within the sampling aperture, if it is on the display. The probability that the object is not detected on the first sample is

$$\bar{P}_D(t_1) = P_{FOV}(t_1) \bar{P}_{L,D}(t_1) + \bar{P}_{FOV}(t_1), \quad (7-32)$$

which is the sum of the probability that the object was in the field of view but was not sampled, and the probability that the object was not in the field of view.

The probability of detecting the object on a second (possible) sample is

$$p_D(t_2) = P_{FOV}(t_1) \bar{P}_{L,D}(t_1) \frac{P_{FOV}(t_2)}{P_{FOV}(t_1)} P_{L,D}(t_2) + \bar{P}_{FOV}(t_1) P_{FOV}(t_2) P_{L,D}(t_2), \quad (7-33)$$

which is the product of probability that the object was within the field of view on the first sample but was not sampled and the probability that the object is still on the display at time t_2 and is sampled plus the probability that the target was not in the field of view on the first sample but is in it on the second sample and is sampled. However, this latter probability is zero due to the monotonically decreasing nature of $P_{FOV}(t)$. Thus the total probability of detecting the target on the second sample is

$$p_D(t_2) = P_{FOV}(t_1) \bar{P}_{L,D}(t_1) \frac{P_{FOV}(t_2)}{P_{FOV}(t_1)} P_{L,D}(t_2) = \bar{P}_{L,D}(t_1) P_{L,D}(t_2) P_{FOV}(t_2). \quad (7-34)$$

The cumulative probability of detecting the target by the second glimpse is:

$$P_D(t_2) = p_D(t_1) + p_D(t_2). \quad (7-35)$$

$$P_D(t_2) = P_{FOV}(t_1) P_{L,D}(t_1) + \bar{P}_{L,D}(t_1) P_{FOV}(t_2) P_{L,D}(t_2). \quad (7-36)$$

For the N th sample this can be given by the series

$$P_D(t_N) = \sum_{i=1}^N P_{FOV}(t_i) P_{L,D}(t_i) \prod_{j=1}^{i-1} \bar{P}_{L,D}(t_j). \quad (7-37)$$

Equation (7-37) illustrates that the function P_{FOV} does not accumulate but just limits the success that can be obtained during the sampling process. $P_{FOV}(t)$ is a function of the initial location of the target with respect to the center of the FOV and time. The function is ensemble distributed. The $P_{L,D}$ term does accumulate as it did in the example of VIIDa(2).

(4) Search for an Increasingly Detectable Object

Let us now combine the examples in VIIDa(1) and in VIIDa(2) to demonstrate search for an object which is more detectable as time goes by. We will assume that the display is searched with the aperture of VIIDa(2) and that the probability of the object being within the aperture is $P_{L,D}(t)$. However, if the object is within the aperture, it is detectable only by that fraction of the population, $P_{D,L}(t)$, determined by the SNR(t). (See VIIDa(2))

The probability of detecting the object on the first sample is

$$P_D(t_1) = \Delta D(t_1) P_{L,D}(t_1). \quad (7-38)$$

The probability of detection is the product of the probability that the object is within the sample aperture and the fraction of the population for which the object is detectable on the first sample.

Between the first and second samples the SNR increases to $\text{SNR}(t_2)$. On the second sample two potential sets of observers must be considered, those observers $\Delta D(t_1)$ who could have detected the object on the first sample but did not because the target was not in the aperture and those observers $\Delta D(t_2)$ for which the signal level was too low on the first sample for detection to occur whether or not the object was in the sample aperture.

For the fraction of the population $\Delta D(t_1)$, the probability on the second sample is

$$p_1(t_2) = \bar{P}_{L/D}(t_1) P_{L/D}(t_2) \quad (7-39)$$

just as indicated in VIIDa(2), since for this segment of the population the object was always "readily detectable."

For the fraction of the population represented by $\Delta D(t_2)$ the object could not be detected on the first sample whether the target was in the sample aperture or not. Therefore, the probability of detection on the second sample is

$$p_2(t_2) = P_{L/D}(t_2). \quad (7-40)$$

The total probability of detecting the object on the second sample is

$$p_D(t_2) = \Delta D(t_1) p_1(t_2) + \Delta D(t_2) p_2(t_2). \quad (7-41)$$

$$p_D(t_2) = \Delta D(t_1) \bar{P}_{L/D}(t_1) P_{L/D}(t_2) + \Delta D(t_2) P_{L/D}(t_2). \quad (7-42)$$

The cumulative probability of detection by the second sample is

$$P_D(t_2) = p_D(t_1) + p_D(t_2). \quad (7-43)$$

$$P_D(t_2) = \Delta D(t_1) [P_{L/D}(t_1) + \bar{P}_{L/D}(t_1) P_{L/D}(t_2)] + \Delta D(t_2) P_{L/D}(t_2). \quad (7-44)$$

From inspection it can be seen that with each additional sample a series exactly like that of VIIDa(2) is begun, prefixed by the ΔD term appropriate to the SNR on that sample. For sample 3, $p_D(t_3)$ is

$$p_D(t_3) = \Delta D(t_1) [\bar{P}_{L/D}(t_1) \bar{P}_{L/D}(t_2) P_{L/D}(t_3)] + \Delta D(t_2) [\bar{P}_{L/D}(t_2) P_{L/D}(t_3)] + \Delta D(t_3) P_{L/D}(t_3). \quad (7-45)$$

The series representation for the cumulative probability of detection is

$$P_D(t_N) = \sum_{i=1}^N \Delta D(t_i) \sum_{j=1}^N P_{L/D}(t_j) \prod_{k=1}^{j-1} \bar{P}_{L/D}(t_k). \quad (7-46)$$

We see in Eq. (7-46) that the ΔD portion of the probability of detection does not accumulate as does the $P_{L/D}$ portion. Also we see that the two contributors to the probability of detection cannot be separated into simple multiplicative functions, one describing detectability and one describing the probability of a successful search. This is an error frequently made in search models.

We can rapidly generalize from Eq. (7-46) the series representation of the search for an increasing detectable target which may be lost from the field of view (a generalization of example VIIDa(3)). The equation for this problem is:

$$P_D(t_N) = \sum_{i=1}^N \Delta D(t_i) \sum_{j=1}^N P_{FOV}(t_j) P_{L/D}(t_j) \prod_{k=1}^{j-1} \bar{P}_{L/D}(t_k). \quad (7-47)$$

(5) Conclusions Regarding Accumulation of Probabilities

In the foregoing examples, in particular example 4, we have described the interaction of three probability functions which were used to describe visual search and detection. All three functions behaved differently. All three probability functions *change value* during the experiments. However, the probability of detecting the object given it is looked at ($P_{D/L}$) monotonically increased, the probability that the object was in the viewfield footprint (P_{FOV}) monotonically decreased, and $P_{L/D}$, the probability that the object was in the aperture, was unconstrained. However, the significant difference between the three is their statistical interpretation. $P_{D/L}$ and thus ΔD describes the statistical behavior of an *ensemble of observers*. P_{FOV} describes the statistical fluctuation within an *ensemble of initial experimental conditions*; e.g., camera location with respect to target location. $P_{L/D}$ describes the *temporal statistics of random sampling*. In Section b that follows these three functions (and three others) are related to tactical performance using the statistical behavior of the functions that was explored above.

b. Dynamic Detection

Let us now look at the probability of detecting a target using the general scenario given in paragraph A3 and the principles developed in this chapter. In addition to the assumptions already stated regarding the behavior of each of the probability functions, we will assume that detection occurs in a single glimpse. This assumption is extremely questionable for it appears that in many detection problems, actual detection results from the building up of "confidence" that a potential target is actually the target through a series of successive glimpses. However, single-glimpse detection is widely assumed by the industry and will be assumed herein for its mathematical simplicity. The probability of detecting the target at the time (t_1) of the first visual sample or glimpse is given by:

$$P_D(t_1) = \Delta D(t_1) P_{LOS}(t_1) P_{VF}(t_1) P_{FOV}(t_1) P_{L/D}(t_1), \quad (7-48)$$

which is simply the product of all of the statistical elements affecting detection. The probability that the target will not be detected on the first glimpse by the $\Delta D(t_1)$ fraction of observers is a function of:

$\bar{P}_{LOS}(t_1)$ — the probability that the line of sight to the target is blocked;

$\bar{P}_{VF}(t_1)$ — the probability that the target is not in the search field;

$\bar{P}_{FOV}(t_1)$ — the probability that the field of view of the thermal imaging system was not directed at the target at time t ; and

$\bar{P}_{L/D}(t_1)$ — the probability that if the target was displayed, it was not within the observer's glimpse (or visual lobe).

Since, if the target is not in the search field at time t_1 it will not subsequently become so, the $P_{VF}(t_1)$ term does not contribute to future detections. The only way the set of observers $\Delta D(t_1)$ could fail to detect the target on the first glimpse and detect it later is if they do not physically or visually sample the target or the line of sight is blocked.

The combined miss-sampling of the target area consists of

$$\bar{P}_s(t_1) = \bar{P}_{LOS}(t_1) + P_{LOS}(t_1) \bar{P}_{L/D}(t_1), \quad (7-49)$$

that is, the target was not in the field of view or was in the field of view but was not visually sampled. Equation (7-49) can be rewritten

$$\bar{P}_S(t_1) = (\bar{P}_{FOV}(t_1) \bar{P}_{L/D}(t_1)). \quad (7-50)$$

The probability that the $\Delta D(t_1)$ fraction of the population will detect the object on a second glimpse is given by the sum of two terms. The first term is the probability that the object was in the search field and had a clear line of sight on the first glimpse, $P_{SF}(t_1) P_{LOS}(t_1)$, but the object location was not sampled ($\bar{P}_{FOV} \bar{P}_{L/D}$) times the probability that object is still in the search field $P_{SF}(t_2)/P_{SF}(t_1)$, still has a clear line of sight (probability of 1), and the observer (physically and visually) samples the object area on the second glimpse $P_{FOV}(t_2) P_{L/D}(t_2)$, with the product of these probabilities being:

$$P_{SF}(t_1) P_{LOS}(t_1) \left[\bar{P}_{FOV}(t_1) \bar{P}_{L/D}(t_1) \right] \frac{P_{SF}(t_2)}{P_{SF}(t_1)} (1) P_{FOV}(t_2) P_{L/D}(t_2).$$

The second term is the probability that the object was in the search field on the first glimpse $P_{SF}(t_1)$ but did not have a clear line of sight $\bar{P}_{LOS}(t_1)$, achieves a clear line of sight on the second glimpse, $[P_{LOS}(t_2) - P_{LOS}(t_1)]/P_{LOS}(t_1)$, (see VII Da(1), is still in the search field, $P_{SF}(t_2)/P_{SF}(t_1)$, and is sampled on the second glimpse, $P_{FOV}(t_2) P_{L/D}(t_2)$, with the product of these probabilities being

$$P_{SF}(t_1) \bar{P}_{LOS}(t_1) \frac{[P_{LOS}(t_2) - P_{LOS}(t_1)]}{\bar{P}_{LOS}(t_1)} \frac{P_{SF}(t_2)}{P_{SF}(t_1)} P_{FOV}(t_2) P_{L/D}(t_2).$$

The probability that the $D(t_1)$ fraction of observers will detect the object on a second glimpse is the sum of the two terms:

$$p_1(t_2) = P_{LOS}(t_1) \bar{P}_{FOV}(t_1) \bar{P}_{L/D}(t_1) P_{SF}(t_2) P_{FOV}(t_2) P_{L/D}(t_2) + [P_{LOS}(t_2) - P_{LOS}(t_1)] P_{SF}(t_2) P_{FOV}(t_2) P_{L/D}(t_2). \quad (7-51)$$

For the observers represented by $D(t_2)$, detection prior to the second glimpse was not possible because the SNR was too low. For this set of observers the probability of detecting the object on the second glimpse is

$$p_2(t_2) = P_{LOS}(t_2) P_{SF}(t_2) P_{FOV}(t_2) P_{L/D}(t_2). \quad (7-52)$$

The total probability of detecting the object on a second glimpse is

$$p_D(t_2) = \Delta D(t_1) p_1(t_2) + \Delta D(t_2) p_2(t_2). \quad (7-53)$$

The cumulative probability of detection by the second glimpse is

$$P_D(t_2) = \Delta D(t_1) [p_1(t_1) + p_1(t_2)] + \Delta D(t_2) p_2(t_2). \quad (7-54)$$

Although more complicated than the simple examples, it can be seen by inspection that the probabilities of detection form a series similar to that of Eq. 7-47.

The propagation of terms resulting from the passage of time is given for the first five glimpses in Table 7-3. Table 7-4 provides a reorganization of Table 7-3. The series representation of the probability of detection as derived from Table 7-4 is

$$P_D(t_N) = \sum_{i=1}^N \Delta D(t_i) \sum_{j=1}^N P_{SF}(t_j) P_{FOV}(t_j) P_{L/D}(t_j) \left[P_{LOS}(t_i) - \sum_{k=1}^{i-1} P_{LOS}(t_k) P_{FOV}(t_k) P_{L/D}(t_k) \prod_{L=k+1}^{i-1} \bar{P}_{FOV}(t_L) \bar{P}_{L/D}(t_L) \right]. \quad (7-55)$$

D. SCHUMAKER

Table 7-3 — Progression of Glimpses. The i th Element Is to Be Multiplied by $S_i P_i D(i)$, Where $S_i = P_{SF}(i)$ and $P_i = P_{L/D}(i) P_{LOV}(i)$. Further Element Notation Is $L_i = P_{LOS}(i)$ and $D_i = L(i_{-1})$.

Glimpse No.	Observer Category	1	2	3	4	5
		$\Delta D(i_1)$	$\Delta D(i_2)$	$\Delta D(i_3)$	$\Delta D(i_4)$	$\Delta D(i_5)$
1	$S_1 P_1$	L_1	0	0	0	0
2	$S_2 P_2$	$L_2 - L_1 P_1$	L_2	0	0	0
3	$S_3 P_3$	$L_3 - L_2 P_2 - L_1 P_2 P_1$	$L_3 - L_2 P_2$	L_3	0	0
4	$S_4 P_4$	$L_4 - L_3 P_3 - L_2 P_3 P_2 - L_1 P_3 P_2 P_1$	$L_4 - L_3 P_3 - L_2 P_3 P_2$	$L_4 - L_3 P_3$	L_4	0
5	$S_5 P_5$	$L_5 - L_4 P_4 - L_3 P_4 P_3 - L_2 P_4 P_3 P_2 - L_1 P_4 P_3 P_2 P_1$	$L_5 - L_4 P_4 - L_3 P_4 P_3 - L_2 P_4 P_3 P_2$	$L_5 - L_4 P_4 - L_3 P_4 P_3$	$L_5 - L_4 P_4$	L_5

Table 7-4 — Reorganized Glimpse Progression. The i th Element Is to Be Multiplied by $S_i P_i D(i)$; and S_i, P_i , and L_i Is the Same Notation as in Table 7-3.

Glimpse No.	Observer Category	1	2	3	4	5
		$\Delta D(i_1)$	$\Delta D(i_2)$	$\Delta D(i_3)$	$\Delta D(i_4)$	$\Delta D(i_5)$
1	$S_1 P_1$	L_1	0	0	0	0
2	$S_2 P_2$	$L_1 P_1 + D_2$	L_2	0	0	0
3	$S_3 P_3$	$L_1 P_1 P_2 + D_2 P_2 + D_3$	$L_2 P_2 + D_3$	L_3	0	0
4	$S_4 P_4$	$L_1 P_1 P_2 P_3 + D_2 P_2 P_3 + D_3 P_3 + D_4$	$L_2 P_2 P_3 + D_3 P_3 + D_4$	$L_3 P_3 + D_4$	L_4	0
5	$S_5 P_5$	$L_1 P_1 P_2 P_3 P_4 + D_2 P_2 P_3 P_4 + D_3 P_3 P_4 + D_4 P_4 + D_5$	$L_2 P_2 P_3 P_4 + D_3 P_3 P_4 + D_4 P_4 + D_5$	$L_3 P_3 P_4 + D_4 P_4 + D_5$	$L_4 P_4 + D_5$	L_5

Equation (7-55) is complicated due to a desire to make it adaptable to the widest possible range of applications. However it will simplify considerably under particular mission constraints.

c. Dynamic Identification

To calculate the probability of identifying a target, the following have been assumed:

- A target is identified on a single glimpse, which may be the glimpse on which it was detected.
- The distribution of identification thresholds among the population is independent of the distribution of detection thresholds (e.g., a person with a low threshold for detection may have a high threshold for identification).
- Prior to time $t = 0$ there is no possibility of identifying the target.

With these assumptions a development similar to that used to calculate the dynamic probability of detection can be used to calculate the dynamic probability of identification.

The probability of identifying the object on the first glimpse is

$$P_{ID}(t_1) = P_D(t_1) \Delta I(t_1), \quad (7-56)$$

which is the product of the probability that the object is detected on the first glimpse and the fraction of the population that can identify the object with the signal (calculated for the appropriate identification task) present at time t_1 . (Note that ΔI is analogous to ΔD , i.e., $\Delta I(t_i) = P_{ID}(t_i) - P_{ID}(t_{i-1})$).

For the $\Delta I(t_1)$ fraction of the population the probability that the target is not identified on the first glimpse is $\bar{P}_D(t_1)$, which is the probability that the object had not been detected by or on, as in this case, the first glimpse. The probability that the $\Delta I(t_1)$ population will identify the object on a second glimpse is

$${}^1P_{ID}(t_2) = \bar{P}_D(t_1) P_D(t_2) = p_D(t_2). \quad (7-57)$$

The probability that the $\Delta I(t_2)$ population can identify the object on the second glimpse is

$${}^2P_{ID}(t_2) = P_D(t_2). \quad (7-58)$$

which is the probability that the object has been detected by the second glimpse.

The total probability of identification on the second glimpse is

$$p_{ID}(t_2) = \Delta I(t_1) {}^1P_{ID}(t_2) + \Delta I(t_2) {}^2P_{ID}(t_2). \quad (7-59)$$

$$p_{ID}(t_2) = \Delta I(t_1) p_D(t_2) + \Delta I(t_2) P_D(t_2). \quad (7-60)$$

The cumulative probability of identification by the second glimpse is

$$P_{ID}(t_2) = \Delta I(t_1) [P_D(t_1) + p_D(t_2)] + \Delta I(t_2) P_D(t_2). \quad (7-61)$$

But

$$P_D(t_1) + p_D(t_2) = P_D(t_2). \quad (7-62)$$

Therefore, Eq. (7-61) can be rewritten

$$P_{ID}(t_2) = \Delta I(t_1)[P_D(t_2)] + \Delta I(t_2) P_D(t_2). \quad (7-63)$$

$$P_{ID}(t_2) = P_D(t_2)[\Delta I(t_1) + \Delta I(t_2)]. \quad (7-64)$$

$$P_{ID}(t_2) = P_D(t_2) P_{I/D}(t_2). \quad (7-65)$$

Thus we find that the probability of identification by the second glimpse is simply the product of the probability of having detected the object by the second glimpse and the fraction of the population for which the object is identifiable by the second glimpse.

Inspection of the third and subsequent glimpses shows that on the M th glimpse the cumulative probability of identification is

$$P_{ID}(t_N) = P_D(t_N) P_{I/D}(t_N). \quad (7-66)$$

Equations (7-55) and (7-66) give formulations for the probability of detection and identification, respectively, in the dynamic scenario given in Section A. The analysis has been generalized to accommodate most applications, but there are thermal-imaging-system applications, such as "snow plow" search, for which this analytical structure is not appropriate. When Eqs. (7-55) and (7-66) do not apply, the appropriate scenario can be synthesized from the six probability functions described or others, using the approaches developed in this section.

E. EXAMPLE OF A DYNAMIC MODEL

The following dynamic problem is analyzed for two systems to illustrate the effects of mission parameters on sensor system tradeoffs.

The first system (system A) is a nominal FLIR easily fabricated within current technology. The second, higher resolution, FLIR (system B) is obtained using the same focal plane and processing as the first by increasing the focal length by a factor of 2.5. In order not to compromise the sensitivity and resolution of the second FLIR, it is also assumed that aperture and stabilization are increased by a factor of 2.5 over system A. Since the focal plane was kept constant, system B has a *FOV* smaller than system A by a factor of 2.5. The penalties for high resolution in this case include increased aperture and stabilization which in turn increase cost, weight, drag, and complexity significantly while decreasing reliability and field of view.

The scenario for this example is an air-to-surface detection and identification of a target in clear weather, with the aircraft flying at 500 kt at a constant altitude of 900 m. The relative humidity is 80%, and the air temperature is 21°C (70°F). The target area is detected by radar initially and is handed off to the thermal-imaging-system at 24 km (80 000 ft) slant range with computer-aided tracking of the target area after handoff. No search with the field of view is used. A further assumption is that the system is not DC restored. The radar accuracy assumed in the problem is:

$$\text{Azimuth} - \sigma_{\theta} = 20 \text{ mrad.}$$

$$\text{Elevation} - \sigma_{\phi} = 14 \text{ mrad.}$$

The assumptions given above indicate that two of the six probability functions developed previously are not required in this problem. Since it is specified that the mission is flown at constant altitude, P_{LOS} can be removed from Eq. (7-55) and become a constant multiplier of the results. Furthermore, since no search with the field of view is permitted, the field of view and the search field are the same and P_{FOV} is therefore unity. The general probabilistic equation for detection is:

$$P_D(t_N) = P_{LOS} \left[\sum_{i=1}^N \Delta D(t_i) \sum_{j=1}^N P_{L/D}(t_j) P_{SF}(t_j) \prod_{k=1}^{i-1} \bar{P}_{L/D}(t_k) \right], \quad (7-67)$$

which is identical to Equation 7-47 for search for an increasingly detectable target which may be lost from display due to a shrinking FOV footprint.

The probability of identification is:

$$P_{ID}(t_N) = P_{I/D}(t_N) P_D(t_N). \quad (7-68)$$

The parameters in Table 7-5 define the two systems being analyzed.

Table 7-5 — Two Systems Being Analyzed

Parameter	Value	
	System A	System B
NET (°C)	0.25	0.25
Frame rate (Hz)	15	15
Overscan	2:1	2:1
Aperture (cm)	15	38
Stabilization (mrad rms)	0.1	0.04
Number of detectors	178	178
Field of view (mrad)	87 × 122	35 × 49
Display size (cm CRT)	20	20
Viewing distance (cm)	56	56
Visual-field brightness (cd/m ²)	3	3

The value of P_{LOS} can be derived from statistics of cloud cover and terrain masking for the area but will be assumed to be unity here for simplicity. The functions $P_{SF}(t_i)$ and $P_{L/D}(t_i)$ were calculated as indicated in this chapter.

The terms ΔD and ΔI are calculated using the aperiodic and periodic SNR_D equation of Chapter VI to calculate $P_{D/L}$ and $P_{I/D}$, respectively.

The NET of both systems is 0.25°C. Compared on this basis one would project equal performance from both systems. System B has a distinctly superior MRT (and MDT): scaled in frequency by 2.5:1 over system A. Based on MRT, system B is distinctly superior to system A.

D. SCHUMAKER

The results of a single dynamic mission characterization for systems A and B are given in Figs. 7-10 and 7-11, respectively. The static detection and identification ranges for the systems at 90% confidence read from the P_{DL} and P_{ID} curves of Fig. 7-10 and 7-11 are:

	System A	System B
Detection (km)	13	21
Identification (km)	1.2	3

Although the MRT values for the two systems are in a frequency ratio of 2.5:1, static detection range is in a ratio of only 1.6:1 due to atmospheric effects and the aperiodic nature of detection. Identification ranges, less affected by atmospheric attenuation, remain in a 2.5:1 ratio.

Dynamic performance is a more complex picture. Comparing the P_D curves, we find that system B can be used to detect the target at longer range than system A. However, system B fails to provide detection at all in better than 50% of all missions because the small field of view is insufficient to encompass the uncertainty of target location when the target becomes detectable. System A provides shorter range but does so on better than 75% of the missions rather than on 46% as does system B.

The cumulative probability of detection limits the probability of identification, so that although system B can provide identification ranges greater than system A by a factor of 2.5:1, 50% more missions are fruitless with system B than with system A. Limitations to the minimum acceptable ranges combined with these dynamic performance graphs determine which

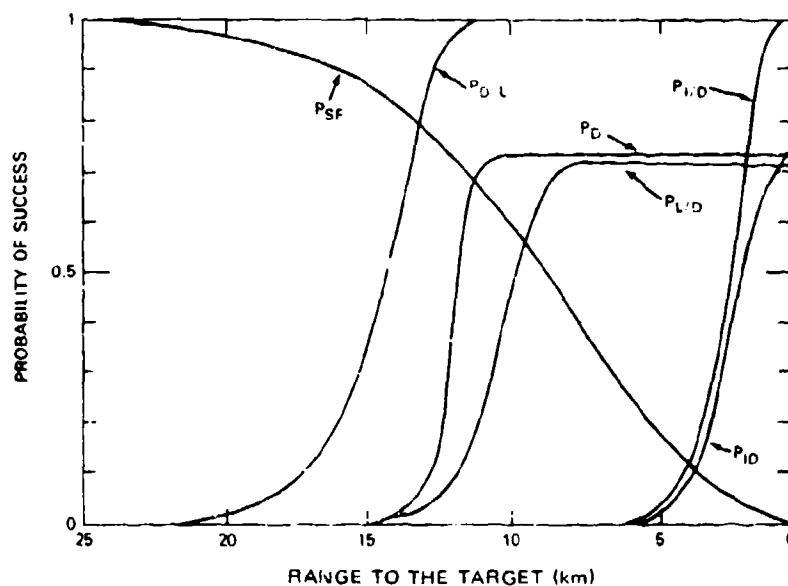


Fig. 7-10 - Dynamic performance system A

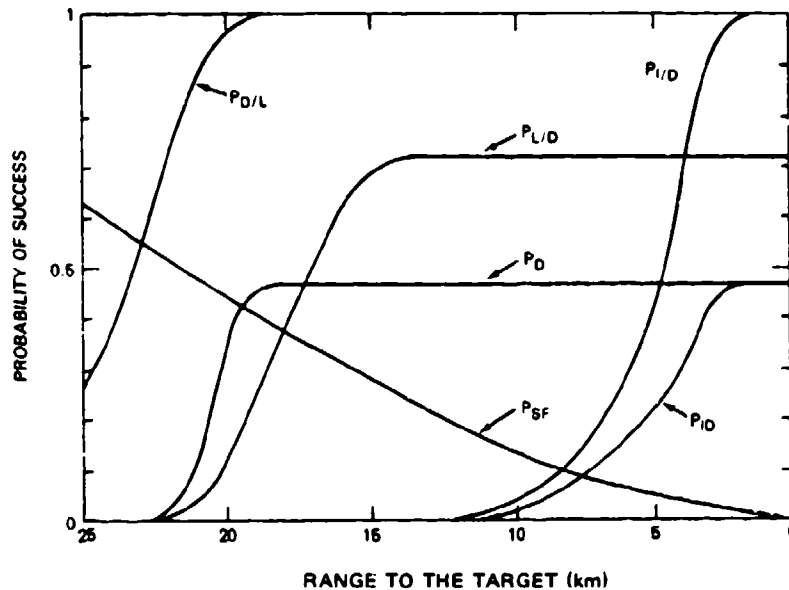


Fig. 7-11 — Dynamic performance system B

system is tactically superior. If no minimum range limitations exist, system A is superior to system B, since it will provide target identification on 50% more missions than will system B. In addition, if the line-of-sight were obscured by terrain or foliage until ranges on the order of 1 km as could easily happen in some locations, system A would provide superior performance.

REFERENCES

- 7-1 AASC Study Group No. 5, Final Report for the Hanover Area.
- 7-2 USAF Environmental Technical Application Center Project 7537, Cloud-Free Line-of-Sight Probabilities for 10384, Belin/Tempelhof, Airport, May 1974.
- 7-3 R. Eirckson, "Visual Search for Targets: Laboratory Experiments", Naval Ordnance Test Station Technical Publication 3328, October 1964.
- 7-4 S. W. Smith, "Time Required for Target Detection in Complex Abstract Visual Display", Project Michigan Memo 2900-235-R, Apr. 1961.
- 7-5 A. L. Yarbus, Eye Movements and Vision, Plenum Press, New York, 1967.
- 7-6 L. E. Williams, D. D. Fairchild, C. P. Graf, J. F. Joula, and G. A. Trumm, "Visual Search Effectiveness for Night Vision Devices", Report for Army Electronics Command Night Vision Laboratory, DAAK02-67-C-0472.

D. SCHUMAKER

- 7-7 D. L. Shumaker and R. B. Keller, "A Mathematical Model of FLIR System Performance in Target Detection and Identification", Final Report on Contract N00019-74-C-021, July 1974.
- 7-8 Discussions with N. Worthy and R. Sendall.
- 7-9 G. E. Pearson and D. L. Shumaker, "A Mathematical Model of FLIR System Performance in Target Detection and Interpretation, Mod I", Final Report on Contract N00019-75-C-0261, December 1975.
- 7-10 E. S. Lamar et al, from C. P. Greening, "Acquisition Model Evaluation", Final Summary Report, NWC Report TP 5536, June 1973.
- 7-11 J. M. Enoch, "Effect of the Size of a Complex Display on Visual Search" J. Opt. Soc. Am., 49 (No. 3), 208, (March 1959).
- 7-12 Remotely Piloted Aerial Observation/Designation System (RPAODS) Field Experiment—Phase I: Philco Ford Praeire Daylight Television Sensor R and D Tech. Dept ECM 7040, Ft. Monmouth, N. J., February 1975.
- 7-13 Personal discussions with A. D. Stathaopoulos, June 1974; also see Ref. 7-12.
- 7-14 See Ref. 7-9.
- 7-15 R. M. Boynton and W. R. Bush, "Laboratory Studies Pertaining to Visual Air Reconnaissance", AD 118 250, April 1957.

Appendix A

NOMENCLATURE, UNITS, AND SYMBOLS

A1. Radiometric and Photometric Nomenclature

FLIR technology involves two sets of nomenclature, one for radiometric terms and one for photometric terms. Unfortunately, workers in various fields have adopted certain terms that are often foreign to workers in another field. For example, astronomers use star magnitude, and probably will always do so, therefore someone using astronomical data must convert it to illuminance, radiance, or some other unit befitting the problem at hand. For performance modeling and for thermal imaging systems in general, the CIE nomenclature of the International Commission on Illumination is recommended as being the least controversial and the most widely used in publications on radiometry and photometry. The CIE nomenclature and symbols of radiometric and photometric terms are given in Tables A-1 and A-2.

One of the problems encountered in making photometric measurements results from the fact that they are supposed to be representative of what the human eye would observe. Since everyone's eye is a little different, a standard response curve called the spectral luminous efficiency for the CIE Standard Photometric Observer has been established and is shown in Fig. A-1. Note that the spectral response of the eye varies with the adaptation and therefore curves are shown for photopic response or cone vision which occurs when the eye is adapted to "room light" and scotopic or rod vision which occurs when the eye is dark-adapted. The numerical values of Fig. A-1 are tabulated in Table A-3 (Ref. A3).

A2. International System of Units

The base units of the International System (SI) are given in Table A-4. Their magnitudes and names are well known except perhaps the candela. The candela is officially defined as "the luminous intensity, in the perpendicular direction, of a surface $1/600,000$ square meter of a blackbody at the temperature of freezing platinum under pressure of 101325 newtons per square meter." Prefixes for the SI units are given at the bottom of the table.

Unfortunately, one frequently encounters photometric units in the literature which do not appear in Table A-2; for example, nearly all the units given in Table A-5 are fairly common. For this reason the non-SI photometric units in Table A-2, together with the factors for converting to SI units, are listed in Table A-5.

Fig. A-1 — Spectral luminous efficiency for the CIE standard photometric observer



APPENDIX A

Table A-1 — International Commission on Illumination Comparison Chart of Nomenclature Units and Symbols for Radiometry and Photometry

Type of Quantity	Name	Symbol (Notes 1, 2)	Definition	SI Units (Note 3)	Abbreviation (Note 3)	Other Units (Note 3)
Radiometry						
Energy	Radiant Energy	Q_e, Q	Energy emitted, transferred, or received in the form of radiation	Joule	J	-
Power	Radiant Flux Radiant Power	Φ_e, Φ P	$\Phi_e = dQ_e/dt$	Watt	W	-
Source (Point)	Radiant Intensity	I_e, I	$I_e = d\Phi_e/d\Omega$ Radiant power per unit solid angle	Watt/steradian	W sr ⁻¹	-
Source (Area)	Radiant Exitance	M_e, M	$M_e = d\Phi_e/dA$ The flux leaving a surface per unit area	Watt/(meter) ²	W m ⁻²	-
Receiver (Power)	Irradiance	E_e, E	$E_e = d\Phi_e/dA$ The flux incident on a surface per unit area	Watt/(meter) ²	W m ⁻²	-
Receiver (Energy)	Radiant Exposure	H_e, H	$H_e = dQ_e/dA = \int E_e dt$ Surface density of the radiant energy received	Joule/(meter) ²	J m ⁻²	-
Universal (Source, transmitting, or received)	Radiance	L_e, L	$L_e = \frac{d^2 Q_e}{d\Omega dA \cos \theta}$ The radiant flux per unit projected area per unit solid angle in a given direction from a source in transit or at a receiver	Watt/(meter) ² steradian	W (m ² sr) ⁻¹	-
Photometry						
Energy	Quantity of Light	Q_v, Q	$Q_v = \int \Phi_v dt$	Lumen second (talbot)	lm s	Lumen-hour (lm·h)
Power	Luminous Flux	Φ_v, Φ	$\Phi_v = K_m \int [\Phi_e(\lambda) \cdot V(\lambda)] \lambda d\lambda$	Lumen	lm	-
Source (Point)	Luminous Intensity	I_v, I	$I_v = d\Phi_v/d\Omega$ The luminous intensity normal to the surface of 1.60 (cm) ² of a black body at the temperature of freezing platinum (2042K) is candela	Candela $\equiv 1 \frac{\text{lumen}}{\text{steradian}}$	cd lm sr ⁻¹	Candipower designates a luminous intensity expressed in candelas
Source (Area)	Luminous Exitance	M_v, M	$M_v = d\Phi_v/dA$ Luminous flux leaving a surface per unit area	lumen/(meter) ²	lm m ⁻²	-
Receiver (Power)	Illuminance	E_v, E	$E_v = d\Phi_v/dA$ The luminous flux incident on a surface per unit area	Lux = $1 \frac{\text{lumen}}{(\text{meter})^2}$	lx	1 phot (ph) = 10 ⁴ lx 1 lumen/m ² = 1 foot-candle (fc) 1 foot-candle (fc) = 10 ⁻⁴ lx
Receiver (Energy)	Light Exposure	H_v, H	$H_v = dQ_v/dA = \int E_v dt$ The quantity of light received per unit area	Lux seconds	lx s (lm s m ⁻²)	-
Universal (Source, transmitting, or received)	Luminance	L_v, L	$L_v = \frac{d^2 \Phi_v}{d\Omega dA \cos \theta}$ The luminous flux per unit projected area per unit solid angle in a given direction from a source in transit or arriving at a surface	Candela (meter) ⁻² $\equiv 1 \text{ nit}$	cd m ⁻² nit	1 stilb (sb) = 10 ⁴ cd m ⁻² 1 apostilb (asb) = (1 π × 10 ⁻⁴) cd m ⁻² 1 lambert (l) = (10 ⁴ π × 10 ⁻⁴) cd m ⁻² 1 foot-lambert (FL) = 3.426 cd m ⁻²

- Note 1: Symbol subscripts (*e* for radiant energy and *v* for photometry) may be dropped if no confusion is likely to arise.
- Note 2: Symbols may be further subscripted with the symbols λ, ν , or σ (i.e., $Q_e(\lambda)$) to indicate the quantity per unit wavelength, frequency, or wave number interval respectively.
- Note 3: When the subscripts λ, ν , or σ are employed, the units given in the table are to be divided by the units for wavelength, frequency, or wave number respectively.
- Note 4: K_m is the spectral luminous efficacy for radiation at the wavelength of peak eye response in photopic vision. Its value for photopic vision is 680 lumens/watt. $V(\lambda)$ is the spectral luminous efficiency for photopic vision scaled so that for λ_m , the wavelength of maximum response, $V(\lambda_m) = 1$. Photopic vision refers to reception by the cone receptors. Eye adaptation requires luminance levels of at least several candelas/(meter)².

Table A-2 - International Commission on Illumination International Lighting Vocabulary and Other Radiometric and Photometric Quantities

Name	Symbol	Definition	Units
Spectral luminous efficiency	$V(\lambda)$, photopic vision	Adopted by CIE in 1924	Dimensionless
	$V'(\lambda)$, scotopic vision	Provisionally adopted by CIE for young observers in 1951	Dimensionless
Luminous efficacy of radiation	K for complex radiation; $K(\lambda)$ for monochromatic radiation	Ratio of the luminous flux to the corresponding radiant flux: $K = \Phi_v / \Phi_e$ $K(\lambda) = \Phi_{v\lambda} / \Phi_{e\lambda}$	lumen/W
Luminous efficacy of a source	η_v, η	Ratio of the luminous flux emitted to the power consumed	lumen/W
Maximum spectral luminous efficacy	K_m	The maximum value of $K(\lambda)$. Its value is $K_m \approx 680$ lm/W at about 555 nm for the CIE standard photometric observer in photopic vision	lumen/W
Luminous efficiency	$V(^*)$	Ratio of the luminous efficacy for complex radiation to that for the same radiant power at the wavelength of maximum photopic response: $V(^*) = [\int \Phi_{e\lambda} V(\lambda) d\lambda] / [\int \Phi_{e\lambda} d\lambda] = K / K_m$	—
Emissivity of a thermal radiator	ϵ	Ratio of the thermal radiant exitance to that of a blackbody at the same temperature: $\epsilon = [M_{e, \text{thermal}}] / [M_{e, \text{black body}}]$	—
Directional emissivity of a thermal radiator	$\epsilon(\theta, \Phi)$	Ratio of the thermal radiance to that of a blackbody at the same temperature: $\epsilon(\theta, \Phi) = [L_{e, \text{thermal}}] / [L_{e, \text{black body}}]$	—
Geometric extent	G	$dG = dA \cos \theta d\Omega$	Meter ²
Optical extent		ndG , where n is refractive index	Meter ²
Basic radiance or basic luminance		L_e/n^2 and L_v/n^2 , a constant in a medium with no losses or scattering	

APPENDIX A

**Table A-3 – Relative Spectral Luminous Efficiency
Values of the Human Eye**

Wavelength (nm)	Photopic V(λ) $L > 3 \text{ nt (cd m}^{-2}\text{)}$	Scotopic V'(λ) $(L < 3 \times 10^{-5} \text{ nt (cd m}^{-2}\text{)})$
380	0.00004	0.00059
390	0.00012	0.00221
400	0.0004	0.00929
410	0.0012	0.03484
420	0.0040	0.0966
430	0.0116	0.1998
440	0.0230	0.3281
450	0.0380	0.4550
460	0.0600	0.5672
470	0.0910	0.6756
480	0.1390	0.7930
490	0.2080	0.9043
500	0.3230	0.9817
510	0.5030	0.9966
520	0.7100	0.9352
530	0.8620	0.8110
540	0.9540	0.6497
550	0.9950	0.4808
560	0.9950	0.3288
570	0.9520	0.2076
580	0.8700	0.1212
590	0.7570	0.0655
600	0.6310	0.03325
610	0.5030	0.01593
620	0.3810	0.00737
630	0.2650	0.003335
640	0.1750	0.001497
650	0.1070	0.000677
660	0.0610	0.0003129
670	0.0320	0.0001480
680	0.0170	0.0000716
690	0.0082	0.00003533
700	0.0041	0.00001780
710	0.0021	0.00000914
720	0.00105	0.00000478
730	0.00052	0.000002546
740	0.00025	0.000001379
750	0.00012	0.000000740
760	0.00006	0.000000425
770	0.00000	0.000000241
780	0.00000	0.000000139

Table A-4 — Systeme International (SI), The International System of Units

	Type of Unit	Name of Unit	Symbol	Basis for Definition
SI basic units	Length	meter	m	1,650,763.73 wavelengths of the orange-red line of krypton 86
	Mass	kilogram	kg	Mass of a platinum-iridium cylinder at the International Bureau of Weights and Measures
	Time	second	s	Duration of 9,192,631,770 cycles of oscillation of the hyperfine structure transition in cesium 133
	Current	ampere	A	That current which will produce a force of 2×10^{-7} newtons per meter of length between two long parallel wires 1 meter apart
	Temperature	kelvin	K	$1/273.16$ of the thermodynamic temperature of the triple point of water
	Amount of substance	mole	mol	Number of atoms in 0.012 kg of carbon 12
	Luminous intensity	candela	cd	Radiation from $1/60 \text{ (cm)}^2$ of a blackbody at the temperature of freezing platinum (2045 K)
SI supplementary units	Plane Angle Solid Angle	radian Steradian	rad sr	
SI derived units	Force	newton	N	1 newton = force to accelerate 1 kg mass 1 meter/(s) ²
	Pressure	pascal	Pa	1 Pa = 1 N/m ²
	Work, energy	joule	J	1 J = 1 Nm
	Power	watt	W	1 W = 1 J/s
	Frequency	hertz	Hz	1 Hz = 1 cycle/s
	Voltage	volt	V	1 V = 1 W/A
	Resistance	ohm	Ω	1 Ω = 1 V/A
	Concentration	moles per cubic meter	mol/(m) ³	
	Light flux	lumen	lm	A light source having an intensity of 1 candela in all directions radiates a flux of 4π lumens

Multiples and Prefixes

Multiple Prefix Symbol	10 ⁻¹⁸	10 ⁻¹⁵	10 ⁻¹²	10 ⁻⁹	10 ⁻⁶	10 ⁻³	10 ⁻²	10 ³	10 ⁶	10 ⁹	10 ¹²
	atto	femto	pico	nano	micro	milli	centi	kilo	mega	giga	tera
	a	f	p	n	μ	m	c	k	M	G	T

APPENDIX A

Table A-5 — Some Additional non-SI Photometric Units (Ref. A-4)

Unit	Symbol	SI Equivalent	Quantity
apostilb	[asb]	$= \pi^{-1} [\text{cd} \cdot \text{m}^{-2}]$	luminance
candela-second	[cd · s]	$= 1 [\text{cd} \cdot \text{s}]$	ergolumic intensity*
footcandle	[fc] = [lm · ft ⁻²]	$= 10.764 [\text{lm} \cdot \text{m}^{-2}]$	illuminance
footlambert	[fL] = $\pi^{-1} [\text{cd} \cdot \text{ft}^{-2}]$	$= 3.426 [\text{cd} \cdot \text{m}^{-2}]$	luminance
lambert	[L] = $\pi^{-1} [\text{cd} \cdot \text{cm}^{-2}]$	$= 10^4 \cdot \pi^{-1} [\text{cd} \cdot \text{m}^{-2}]$	luminance
light-watt†	[lW] = $[K_m^{-1}] \cdot [\text{lm}]$	$= 680^{-1} [\text{lm}]$	luminous flux
phot	[ph] = $1 [\text{lm} \cdot \text{cm}^{-2}]$	$= 10^4 [\text{lm} \cdot \text{m}^{-2}]$	illuminance
stilb	[sb] = $1 [\text{cd} \cdot \text{cm}^{-2}]$	$= 10^4 [\text{cd} \cdot \text{m}^{-2}]$	luminance

*The CIE [5] seems not to have any term for this quantity, nor does there seem to be any in general use other than the term for the units, although "beam-candlepower-second" is also used at times. This term for the quantity is taken from Jones' "photometry" proposal.

†The light-watt [lW] is related to the unit of radiant flux, the watt (W), by

$$\phi_v = \int_{380}^{760} V(\lambda) \cdot \phi_{e,\lambda}(\lambda) \cdot d\lambda \text{ [lW]},$$

where

$V(\lambda)$ [dimensionless] is the photopic spectral luminous efficiency,

λ [nm] is the wavelength,

$\phi_{e,\lambda}(\lambda)$ [W · nm⁻¹] is a distribution of spectral radiant flux as a function of wavelength, and

ϕ_v [lW] is the luminous flux in light-watts of the radiation described by the spectral distribution $\phi_{e,\lambda}(\lambda)$.

The luminous flux, in lumens, in this same beam of radiation is given by

$$\phi_v = [K_m] \cdot \phi_l \approx 680 \cdot \phi_l [\text{lm}],$$

where

$K_m \approx 680 [\text{lm} \cdot \text{W}^{-1}]$ at $\lambda \approx 555$ [nm] is the maximum spectral luminous efficacy (of radiation).

Note that both the lumen and the light-watt are units of luminous flux. They have the same dimensionality and differ only by the numerical scale factor $[K_m] \approx 680$. There are approximately 680 lumens per light-watt at all wavelengths in the visible region of the spectrum where $380 \leq \lambda \leq 760$ [nm].

REFERENCES

- A.1 "International Lighting Vocabulary," Third Edition, Publication CIE No. 17 (E-1.1) 1970 of the International Commission on Illumination, Bureau Central de la CIE, 4 Av. du Recteur Poincaré, 75 Paris 16^e, France. c/o L. E. Barbrow, National Bureau of Standards Washington, D.C. 20234.
- A.2 NBS Special Publications 330 and 304A (Revised October 1972).
- A.3 Kingslake, R. Applied Optics and Optical Engineering Vol. 1 "Light; Generation and Modification" Academic Press, New York, N.Y., 1965.
- A.4 "Self-Study Manual on Optical Radiation Measurements" Part 1 — Concepts Chapter 1-3, NBS Technical Note 910-1, Fred E. Nicodemus, Editor, March 1976.

Appendix B SYMBOLS

a	Image area (cm^2)
A	Image plane area (cm^2)
a_d	Detector area (cm^2)
A_D	Area of the display
A_G	Area of the glimpse
A_i	Areas of constant temperature (cm^2)
A_H	Absolute humidity
BLIP	Designation for background noise limited detector
C_T	Contrast threshold for visual detection, from reference 7.10
C_1	Radiation constant, $3.7413 \times 10^4 \text{ W cm}^2 \mu\text{m}^4$
C_2	Radiation constant, $14\,388 \mu\text{m K}$
D	Dimension of a square glimpse
D_n	Lens diameter (cm^2)
$D_V(\Gamma, \Psi)$	Visual target detectability as a function of location in the visual field
D'_V	Visual target detectability within the glimpse area
$D^*(\Omega_c)$	Detectivity for a solid viewing angle of Ω_c sr ($\text{cm Hz}^{1/2} \text{ W}^{-1}$)
$D^*(2\pi)$	Detectivity for a solid viewing angle of 2π sr ($\text{cm Hz}^{1/2} \text{ W}^{-1}$)
$D^{**}(2\pi)$	D^* of a perfect detector of unit quantum efficiency viewing 2π sr of background ($\text{cm Hz}^{1/2} \text{ W}^{-1}$)
ΔD	An incremental change in $P_{D/L}$
$\Delta D(i)$	The change in $P_{D/L}$ between the $(i-1)$ th and i th glimpse
e	Charge of an electron (coul)
E	Irradiance (W cm^{-2})

APPENDIX B

E_{av}	Average photosurface irradiance (W cm^{-2})
E_h	Photosurface highlight irradiance (W cm^{-2})
$e_s(T)$	Saturation vapor pressure of water surface (dynes cm^{-2})
f	Lens focal ratio (F_L/D_o)
f_D	The spatial frequency characterizing detection of a specific target
F_L	Lens focal length (cm)
F_M	Fraction of time an observer spends monitoring nondisplay functions
F_R	Frame rate (s^{-1})
Δf_c	Detector channel bandwidth (Hz)
Δf_v	Video bandwidth (Hz)
Δf_{cr}	Reference channel bandwidth (Hz)
Δf_v	Video bandwidth (Hz)
Δf_{vr}	$n_p \Delta f_{cr}$ = reference video bandwidth (Hz)
g	Grams
G	Gain of signal processor
G_v	Display (or video) gain
HFOV	Horizontal field of view (deg, rad, mrad)
i	Signal current (A)
i_{av}	Average of current due to object and background (A)
i_{n_i}	rms noise current (A)
$i_{p_{ID}}(i_j)$	The probability that the segment of the population whose threshold for identification was passed on the i th glimpse will be able to identify the target on the j th glimpse
Δi	Incremental signal current (A)
ΔI	An incremental change in P_{ID}
K	Temperature in Kelvins
K	Constant $[2.25/(X_D Y_D)]$ used to calculate distribution of glimpses on a uniform display

NRL REPORT 8311

K_d	Display conversion gain
K_I	Interlace ratio
K_M	ΔL (radiance) to ΔT (temperature) conversion factor ($\text{W cm}^{-2} \text{sr}^{-1} \text{K}^{-1}$)
k_θ	Spatial frequency (cycles/mrad)
k_d	Number of lines required per minimum object dimension for a given level of visual discrimination of a displayed image
$k_{\theta 0}$	Spatial cut off frequency for a diffraction limited lens (cycles/mrad)
km	kilometers
K_p	Phosphor gain (lumens/electron)
K_X	Rate of navigational error accumulation in direction X
K_Y	Rate of navigational error accumulation in direction Y
L_{av}	Average display luminance ($\text{lumens sr}^{-1} \text{cm}^{-2}$)
LED	Light emitting diode
$l/p.h.$	Lines per picture height
L_y	Luminance distribution in the vertical direction ($\text{lumens sr}^{-1} \text{cm}^{-2}$)
ΔL	Incremental scene radiance ($\text{W sr}^{-1} \text{cm}^{-2}$)
ΔL_H	Incremental luminance swing (high) ($\text{W sr}^{-1} \text{cm}^{-2}$)
ΔL_L	Incremental luminance swing (low) ($\text{W sr}^{-1} \text{cm}^{-2}$)
mb	Pressure (mbar)
MDT	Minimum detectable temperature (K)
MRT	Minimum resolvable temperature ($^{\circ}\text{C}$)
MRT'	Minimum resolvable temperature for a bar aspect ratio \neq other than 7
MTF	Modulation transfer function
$M_\lambda(T)$	Spectral radiant exitance (W cm^{-2})
n_{av}	$(n_o + n_b)/2$

APPENDIX B

\dot{n}'_{av}	Derivatives of the above quantities with respect to space and time (photoelectrons/cm ² - s)
n_b	Number of photoelectrons in image area a and sampling time T_s due to background
\dot{n}'_b	Derivatives of the above quantity with respect to space and time (photoelectrons/cm ² - s)
n_l	Number of detectors in series
n_o	Number of photoelectrons in image area a and sampling time T_s due to object (photoelectrons)
\dot{n}'_o	Derivatives of the above quantity with respect to space and time (photoelectrons/cm ² - s)
n_p	Number of detectors in parallel
N	Number of glimpses taken (Chapter 7)
N	Spatial frequency (lines/pict. ht.)
N_e	Noise equivalent bandwidth (l/p.h.)
$N_{e0}(i)$	Noise equivalent bandwidth of specific sensor components or groups of components as identified by the appropriate subscript (l/p.h.)
N_s	Sampling frequency
NEP^*	Specific noise equivalent power of detector (W/cm Hz ^{1/2})
$NE\Delta T$	Noise equivalent temperature difference (°C)
N_y	Number of active scan lines
Δn	$n_o - n_b$
$\Delta \dot{n}'$	Derivatives of the above quantity with respect to space and time (photoelectrons/cm ² - s)
O_s	Overscan ratio = ratio of detector dimension in the cross scan direction to the scan line pitch
P	Vapor pressure of water (mm of Hg)
P	Scan line or detector pitch (cm)
$P_{D/L}$	Probability that a target is detectable given it is looked at
$P_D(t_i)$	Cumulative probability of detection by the time of the i th glimpse
$p_D(t_i)$	Probability of detection on the i th glimpse

NRL REPORT 8311

pdf	Probability distribution function
P_{DV}	Probability of visual detection integrated over the visual field
P_{FF}	Probability distribution function (pdf) describing the positioning of the field of view within the search field
P_{FOV}	Probability that the target is in the sensor field of view
P_G	Pdf for glimpse position on the system display
$P_H(\theta, \phi)$	Probability that the search field is centered on a position that is θ, ϕ distant from the actual target location
P_{IID}	Probability that a target is identifiable given it is detected
$P_{ID}(t_i)$	The probability of identification <i>by</i> the i th glimpse
$p_{ID}(t_i)$	The probability of identification <i>on</i> the i th glimpse
$p_i(t_j)$	The probability that the segment of the population whose detection threshold was surpassed on the i th glimpse will detect the target <i>on</i> the j th glimpse
$P_{L/D}$	Probability that a displayed target is looked at (in the observers glimpse area)
P_{LOS}	Probability that the clear-line-of-sight exists between sensor and target
P_{SF}	Probability that the target is in the search field
$P_T(\gamma, \psi)$	Probability distribution function describing the uncertainty in the target location in coordinates (γ, ψ)
P_{TD}	Pdf for target location on the system display
P_{TF}	Probability distribution function describing the uncertainty of target location within the search field (normalized to P_{SF})
$\overline{(\text{Quantity})}$	One minus (Quantity) or not (Quantity)
R	Range (m or km)
R_f	Radius of the fovea (deg)
$R_F(\nu)$	Frequency response of a filter
R_G	Radius of the glimpse (deg)
R_H	Relative humidity
$R_o()$	Optical transfer function or complex steady state spatial frequency response

APPENDIX B

$R_{oi}()$	Same as above but added subscript identifies specific or groups of specific sensor components
$R_{sf}(N)$	Square wave flux response
$R_{sp}(N)$	Spurious response
$R_{SQ}(N)$	Square wave amplitude response
$R_{VD}(\Gamma, \Psi)$	Ratio of target detectability at visual coordinate (Γ, Ψ) to that in the fovea
S	Specific detector spectral responsivity (A/W)
s	Time (s)
SF_{γ}	Dimension of the search field in direction γ
SF_{ψ}	Dimension of the search field in direction ψ
SNR	Signal-to-noise ratio
SNR_D	Display signal-to-noise ratio
$SNRD_f$	SNR_D calculated using the MTF of the fovea
SNR_{co}	Detector channel SNR for broad area images
SNR_{DT}	Threshold SNR_D
SNR_I	SNR of the electron image
SNR_p	Perceived SNR
SNR_v	Video SNR
SNR_{vo}	Video SNR for broad area images
t	Time (s)
T	Temperature (K)
T_a	Temperature of air (K)
T_d	Dwell time (s)
T_e	Eye integration time (s)
TDI	Time delay integration
T_{dp}	Dew point temperature
T_f	Frame time

NRL REPORT 8311

t_i	Time of the i th sample, usually time of the i th visual glimpse
t_o	Time of target handoff from a cueing sensor to the thermal-imaging-system
t_d	Dead time
T_S	Duration of a visual saccade
t_u	Time of the last inertial navigation system update
T_w	Temperature of water (K)
ΔT	Incremental temperature ($^{\circ}\text{C}$)
ΔT_o	Incremental temperature at zero range ($^{\circ}\text{C}$)
$\Delta T(R)$	Incremental Temperature at range R ($^{\circ}\text{C}$)
V	Visual meteorological range (km)
VFOV	Vertical field of view (deg, rad, mrad)
W	Watts
X	Effective focal plane width (cm)
X_o	Size of the scene object in the x direction (cm)
Δx	Size of the equivalent bar pattern for bar width in the x direction of the image (cm)
ΔX	Incremental horizontal element of the display (cm)
X_D	Display width (cm)
Y	Effective height of the image plane (cm)
Y_D	Display height (cm)
Y_o	Size of the scene object in the y direction (cm)
Δy	Size of the equivalent bar pattern bar width in the y direction of the image (cm)
ΔY	Incremental vertical element of the display (cm)
Z	Random variable
α	Picture aspect ratio, width-to-height = ϕ_H/ϕ_V
β	Target sublense used in reference 7.10

APPENDIX B

β_{CONT}	Extinction coefficient for continental aerosol model (km^{-1})
$\beta ()$	Noise filtering function (periodic patterns)
$\Gamma ()$	Noise filtering function (aperiodic patterns)
δ_e	Noise equivalent aperture (cm, mrad or pict. hts.)
$\delta_{e(i)}$	Noise equivalent aperture of specific sensor or groups of sensor components as identified by the appropriate subscript (cm, mrad, or pict. hts.)
δ_S	Amplitude of a visual saccade (deg)
δ_s	Amplitude of a saccade
δ_x, δ_y	Detector dimensions in x and y (cm)
e	Bar aspect ratio (length-to-width)
η_c	Cold shield efficiency
η_o	Lens transmittance
η_s	Scan efficiency
η_λ	Detector spectral quantum efficiency (electrons/photons)
θ	Instantaneous field of view (rad or mrad)
θ	Visual angle from the fovea to a target in the visual field, used by Lamar (reference 7.10)
λ	Spectral wavelength (μm)
ν	Spatial frequency
ζ	Complex function of system and target parameters used in reference 7.7 to calculate target size
$\xi ()$	Noise increase factor
σ	Atmospheric extinction coefficient (km^{-1})
σ_θ	First standard deviation of pdf for target location in direction θ
σ_ϕ	First standard deviation of pdf for target location in direction ϕ
τ	Transmittance

NRL REPORT 8311

Ψ, ϕ_H	Vertical and horizontal fields of view (deg, rad, mrad)
Ω	ϕ, ϕ_H (deg, rad, mrad)
ω_i	Instantaneous solid angle of view (sr)
$\Delta\psi$	An incremental element of the search field in direction ψ
$\Delta\gamma$	An incremental element of the search field in direction γ

Appendix C

**THE NIGHT VISION LABORATORY STATIC PERFORMANCE
MODEL BASED ON THE MATCHED FILTER CONCEPT**

*W.R. Lawson
J.A. Raiches*

A. INTRODUCTION

The NVL model for thermal imaging systems is based on a model originally proposed by Barnard [Ref. C.1] and is conceptually different from the synchronous integrator concept originally formulated by Otto Schade, Sr. The latter model, as refined by Sendall and Rosell is discussed in detail in Appendix D. In the synchronous filter concept, it is assumed that the eye/brain combination will integrate over the entire area of an image even though the image has been smeared out over a large distance by finite sensor apertures. In the formulation for signal, the integration limits are plus or minus infinity although as a practical matter the effective distance is usually much smaller because signal integrated in the low-amplitude tails of a blurred image in a real imaging system increases only very slowly with increase in integration distance from the image center or core. It is felt that the eye/brain only integrates in space for so long as image SNR increases in turn but that this more complex consideration would unduly complicate the analysis and would result in only minor changes in the final result for most cases of practical interest. In the synchronous integrator concept a perfect integrating filter is hypothesized and used to bound and compute the noise.

The matched filter concept stems from communications theory [Ref. C.2]. In* a video channel "a matched filter is a delayed (time shifted), time reversed (spatially reversed) version of the signal. Thus if $i(t)$ is the signal function, the response function of the matched filter is proportional to $i(t_1 - t)$. (In discussing time functions causality becomes a problem; however the discussion here will not be complicated by this). The matched filter is the filter which maximizes the signal-to-noise ratio (signal being the magnitude of the output from the matched filter and noise being the standard deviation of the noise fluctuations) at a time t_1 for the case that the noise is additive (independent of signal) and white (the power spectrum equals a constant at all frequencies). Note that for the case of a symmetrical signal and for t_1 equal to zero, the matched filter has precisely the same shape as the signal. (In general, the matched filter is the mirror image of the signal.)"

So far as is known, neither the synchronous-integrator nor the matched filter concepts have any proven basis in psychophysical fact. The eye's ability to spatially integrate over images which are not too large in two dimensions simultaneously is beyond question, but the precise method of image processing that takes place in the eye-brain is probably much more complex than either model would indicate. Efforts have been made to validate, or, at least determine the limits to the applicability of the synchronous filter concept. Over a fairly wide

*Ref C-2

APPENDIX C

range of conditions, the experimental results are generally in satisfactory, if not perfect agreement with the model predictions as is shown in part in Appendix D. However, no efforts have been made to determine whether the matched filter or the synchronous filter approach gives a better fit to the data, and to provide definitive results, specific experiments of high precision will be required.

A model is required in order to take into account the effects of finite sensor apertures. The matched filter equations have been formulated in a manner so as to agree with the synchronous filter equations for periodic images and will also agree for aperiodic images when the image being viewed is rectangular in intensity distribution, i.e., constant amplitude. However, with blurred images, the matched filter concept will result in a somewhat smaller image signal level prediction for aperiodic images. However, the difference between the signal levels predicted using either model will be trivial until the image dimensions become of the order of the dimensions of the overall sensory systems noise equivalent aperture or smaller. In general, the statistical variance in making threshold resolution measurements will be larger than any error which may result from using one larger or the other model, and the selection of the model to be used is largely one of personal preference.

B. NEAT, MRT, AND MDT DERIVATIONS

The noise equivalent temperature (NEAT), the minimum resolvable temperature (MRT), and the minimum detectable temperature (MDT) will be derived in the following. Complete and simplified expressions are given for each quantity; the complete expressions provide a basis for rigorous analyses, and the simplified expressions provide a means for obtaining reasonable estimates through use of hand calculations.

Neither the concepts nor the final relationships contained herein are new. The NEAT derivation is similar to an analysis in Jamieson [C.3]. The MRT and MDT derivations are slightly different from others of which the author is aware. The techniques employed to derive MRT and MDT are equally applicable to the derivation of subjective resolution relationships for intensifier and LLLTV viewers.

Terminology

NEAT	— Noise equivalent temperature
MRT	— Minimum resolvable temperature
MDT	— Minimum detectable temperature
t	— time
$i_o(t)$	— an output signal
$i_i(t)$	— an input signal
$*$	— convolution
$h(t)$	— temporal response function
f	— frequency
$I_o(f)$	— Fourier transform of $i_o(t)$
$I_i(f)$	— Fourier transform of $i_i(t)$
$H(f)$	— transfer function (fourier transform of $h(t)$)
OTF	— optical transfer function
MTF	— modulation transfer function
$R(\tau)$	— auto-correlation function

NRL REPORT 8311

$S(f)$	— power spectrum
$\langle \rangle$	— ensemble average
τ	— time difference
σ	— rms value of a random process
r	— detector response function
$v_s(t)$	— a (voltage) signal
$\phi(\lambda)$	— watts/micron on the detector
$D_{f_n}^*(\lambda)$	— detector detectivity
$D_{f_o}^{**}(\lambda)$	— detector detectivity (no cold shielding)
l	— focal length
$\eta_o(\lambda)$	— optical transmission
T	— temperature
L	— radiance from source (target)
HFOV	— horizontal field of view
VFOV	— vertical field of view
t_E	— eye integration time
η_{OVSC}	— overscan ratio
F_R	— frame rate
n_s	— number of detectors in series
n_P	— number of detectors in parallel
η_{CS}	— cold shield efficiency
τ_D	— picture element delay time
η_{SC}	— scan efficiency
θ	— cold shield angle
W	— an integral Eq. (C-24)
$i(x,y)$	— spatial signal
A	— area (signal)
k	— a constant
M	— watts/area from display
Δy_i	— distance between scan lines
v	— scan velocity
f_o	— frequency of MRT bar pattern
L	— bar length in MRT bar pattern
b	— noise function along a line of the display
f_x	— spatial frequency (x or horizontal direction)
f_y	— spatial frequency (y or vertical direction)
S	— a threshold signal-to-noise ratio
q_i	— an integral (defined below equation, Eq. (C-45))
p_i	— an integral (defined below equation, Eq. (C-45))
p_i	— an integral (defined below equation, Eq. (C-45))
q_4	— an integral (defined below equation, Eq. (C-51))
p_{y4}	— an integral (defined below equation, Eq. (C-51))
p_{y4}	— an integral (defined below equation, Eq. (C-51))

Preliminaries

Throughout this section, elementary concepts and analysis techniques employed in electrical communication theory are used. The necessary relationships are presented below; the

APPENDIX C

reader unfamiliar with these relationships could profitably read the first three or four chapters of Wozencraft and Jacobs [C.4]. (It is possible to derive NEAT, MRT, *etc.*, without employing these concepts.)

An output signal from a linear system (circuit, optical device) is equal to the input signal convolved with the response function of that system, *i.e.*,

$$i_o(t) = i_i(t) * h(t) = \int_{-\infty}^{\infty} i_i(t') h(t-t') dt' \quad (C-1)$$

where $i_o(t)$, $i_i(t)$, and $h(t)$ equal the output signal, the input signal, and the system response function, respectively. The response function $h(t)$ is simply the system output for an input pulse approximating a Dirac delta function. If both sides of Eq. (C-1) are Fourier transformed, the expression

$$I_o(f) = I_i(f) H(f) \quad (C-2)$$

is obtained. Here $I_o(f)$, $I_i(f)$, and $H(f)$ are the Fourier transforms of $i_o(t)$, $i_i(t)$, and $h(t)$, respectively. The quantity $H(f)$ is referred to as the transfer function of the system. The one-dimensional (spatial) version of $H(f)$ (*i.e.*, the Fourier transform of the line spread function) for an optical system corresponds to the system's optical transfer function (OTF) whose absolute value equals the modulation transfer function (MTF) of the systems. In Eq. (C-2), the quantity $H(f)$ is said to "filter" the signal $I_i(f)$. Note that if a signal is passed through two systems in series the output from the first system equals the input to the second; therefore, if $i_i(t)$ is the input signal and $h_1(t)$ and $h_2(t)$ are the response functions of the two systems, the output is given by

$$i_o(t) = i_i(t) * h_1(t) * h_2(t). \quad (C-3)$$

Correspondingly, the transform of $i_o(t)$ is given by

$$I_o(f) = I_i(f) H_1(f) H_2(f). \quad (C-4)$$

Thus the "two-system" response and transfer functions equal $h_1(t) * h_2(t)$ and $H_1(f) H_2(f)$, respectively; *e.g.*, the OTF of a complex optical system equals the product of the component OTFs (ignoring component interactions).

A wide-sense stationary random process (*e.g.*, noise in most electrooptical viewers) can be characterized by its autocorrelation function

$$R(\tau) = R(t, t+\tau) = \langle n(t) n(t+\tau) \rangle, \quad (C-5)$$

where $n(t)$ designates the random process and τ represents a time difference. The Fourier transform of this function, called the power spectrum of the process, is given by

$$S(f) = \int_{-\infty}^{\infty} R(\tau) e^{-2\pi i f \tau} d\tau. \quad (C-6)$$

The brackets in Eq. (C-5) indicate an average over an ensemble of $n(t)$ functions. The output power spectrum of noise processes passed through (filtered by) a linear system is given by

$$S_o(f) = S(f) H^2(f). \quad (C-7)$$

where S_o and S_i are the output and input power spectra, respectively. An extremely important relationship between the power spectrum and the variance (at a point) of the random process is

$$\sigma^2 = \int_{-\infty}^{\infty} S(f) df. \quad (C-8)$$

Since engineers are reluctant to employ negative frequencies and since $S(f)$ is an even function of frequency, it is common practice to redefine the power spectrum such that

$$\sigma^2 = 2 \int_0^{\infty} S(f) df. \quad (C-9)$$

This latter power spectrum is just twice the one used in Eq. (C-8); this power spectrum is used for the temporal voltage noise and the corresponding (horizontal) spatial noise since it is the one commonly employed by thermal viewer engineers. In the vertical direction, however, the power spectrum in Eq. (C-8) is used.

A matched filter is a filter whose response function is a delayed (shifted), time-reversed (spatially reversed) version of the signal. Thus, if $i(t)$ is the signal function, the response function of the matched filter is proportional to $i(t_1 - t)$. (In discussing time functions, causality becomes a problem; however, the discussion here will not be complicated by this.) The matched filter is the filter which maximizes the signal-to-noise ratio (signal being the magnitude of the output from the matched filter and noise being the standard deviation of the noise fluctuations) at a time t_1 for the case that the noise is additive (independent of the signal) and white (the power spectrum equals a constant at all frequencies). Note that for the case of a symmetrical signal and for t_1 equal to zero the matched filter has precisely the same shape as the signal. (In general, the matched filter is the mirror image of the signal.) Also note that if

$$I(f) = \int_{-\infty}^{\infty} i(t) e^{-2\pi i f t} dt, \quad (C-10)$$

then the frequency response of the matched filter is proportional to $I^*(f)$, i.e.,

$$H_m(f) \sim \int_{-\infty}^{\infty} i(-t) e^{-2\pi i f t} dt = I^*(f). \quad (C-11)$$

NEAT Derivation

The noise equivalent temperature is defined as that input temperature difference for a "large" target (a large target being one whose size is large relative to the system response function) which is required to generate a signal (voltage amplitude) just prior to the display (or after the detector preamplifier) which is just equal to the rms noise (voltage) at that point, assuming that the filtering action of the electronics prior to the measurement point corresponds to that of a "standard" filter. The ambiguities in this NEAT definition provide at least part of the reason NEAT is viewed with disfavor in some circles; the precise point of measurement and the "standard" filter are not necessarily identical from one measurement to the next. A second reason NEAT is viewed with disfavor is that it does not relate directly to the signal-to-noise ratios which are fundamental for perception of targets on the device display; it is not a display signal-to-noise ratio and it is a point signal-to-noise rather than one "averaged" over the target. Nevertheless, NEAT can be a useful indication of system sensitivity, and (although not necessary) it can be used to simplify the MRT and MDT relations; therefore, its derivation follows.

APPENDIX C

The detector plus its associated preamplifier is assumed to be a linear system with a response function $r(\lambda, t) * h_{ELECT}(t)$, where $r(\lambda, t)$ is the response function of the detector in volts per watt and h_{ELECT} is the amplifier (and other circuitry) response function. Therefore, if the signal onto the detector equals $\Delta\phi(\lambda) i(t)$ watts per micron, where $i(t)$ is a normalized time function, the response of (i.e., the signal from) the detector-amplifier system is given by

$$v_s(t) = \int_0^\infty \Delta\phi(\lambda) i(t) * r(\lambda, t) * h_{ELECT}(t) d\lambda \quad (C-12)$$

$$= \int_{-\infty}^\infty e^{2\pi i f t} I(f) H_{ELECT}(f) \int_0^\infty \Delta\phi r(\lambda, f) d\lambda df,$$

where $I(f)$, $H_{ELECT}(f)$, and $r(\lambda, f)$ are the Fourier transforms of $i(t)$, $h_{ELECT}(t)$, and $r(\lambda, t)$, respectively. Assume that $r(\lambda, f)$ (or $r(\lambda, t)$) is separable into a frequency and a wavelength-dependent part; then

$$r(\lambda, f) = r(\lambda, f_0) \frac{r(\lambda, f)}{r(\lambda, f_0)}, \quad (C-13)$$

where $r(\lambda, f_0) \neq$ function of f and $\frac{r(\lambda, f)}{r(\lambda, f_0)} \neq$ function of λ . Equation (C-12) giving the signal v_s can now be simplified to

$$v_s = \int_{-\infty}^\infty e^{2\pi i f t} I(f) H_{ELECT}(f) \frac{r(\lambda, f)}{r(\lambda, f_0)} df \int_0^\infty \Delta\phi(\lambda) r(\lambda, f_0) d\lambda \quad (C-14)$$

$$= i'(t) \int_0^\infty \Delta\phi r(\lambda, f_0) d\lambda,$$

where $i'(t)$ is defined in an obvious manner.

The rms noise voltage corresponding to $v_s(t)$ must now be determined. Let $S(f)$ equal the power spectrum of the noise from the detector. Then the power spectrum beyond the preamplifier (i.e., system with transfer function $H_{ELECT}(f)$) equals $S(f) H_{ELECT}^2(f)$ and therefore the desired rms noise is given by

$$\sigma^2 = \int_0^\infty S(f) H_{ELECT}^2(f) df. \quad (C-15)$$

Combining Eq. (C-14) and (C-15), the signal-to-noise beyond the preamplifier is given by

$$S/N = \frac{v_s(t)}{\sigma} = \frac{i'(t) \int_0^\infty \Delta\phi r(\lambda, f_0) d\lambda}{\left[\int_0^\infty S(f) H_{ELECT}^2(f) df \right]^{1/2}}. \quad (C-16)$$

Equation (C-16) yields the NEAT once the various variables are recast into more useful forms, the S/N is set equal to 1 (note that the NEAT definition can be recast to "that temperature difference such that $S/N = 1$ "), and $i'(t)$ is set equal to 1. The quantity $i'(t)$ can be set equal to 1 because the signal is measured (determined) at approximately the midpoint of an extended (large) signal; if $i(t) = 1$ at its midpoint then $i'(t)$ will also equal one since the signal is of much greater duration than the response function of the detector-amplifier system.

To recast the variables, first note that the detector detectivity D_λ^* is given by

$$D_\lambda^*(f_o) = \frac{A_d^{1/2} r(\lambda, f_o)}{(S(f_o))^{1/2}} \quad (C-17)$$

where A_d equals the area of the detector [C.3]. Those familiar with the expression

$$D^* = \frac{(A_d \Delta f_n)^{1/2}}{\text{NEP}},$$

where Δf_n is the bandwidth and NEP is the noise-equivalent power, should note the following heuristic derivation:

$$\text{Detector signal-to-noise ratio } (S/N)_D = \frac{\Delta \phi r}{\left(\int_0^\infty S(f) df \right)^{1/2}}.$$

$$\text{For a small bandwidth around } f_o, (S/N)_D = \frac{\Delta \phi r(f_o)}{(S(f_o) \Delta f_o)^{1/2}}.$$

Now, $\text{NEP} = \Delta \phi$ for $(S/N)_D = 1$; therefore, $\text{NEP} = \frac{(S(f_o) \Delta f_o)^{1/2}}{r(f_o)}$ and, therefore,

$D^* = \frac{A_d^{1/2} r(f_o)}{(S(f_o))^{1/2}}$ Q.E.D.]. Solving Eq. (C-17) for $r(\lambda, f_o)$ and inserting into Eq. (A16), the signal-to-noise ratio is given by

$$S/N = \frac{\int_0^\infty \Delta \phi_\lambda D_\lambda^*(\lambda) d\lambda}{\left[A_d \int_0^\infty \frac{S(f)}{S(f_o)} H_{ELECT}^2 df \right]^{1/2}} \quad (C-18)$$

where $i'(r)$ has been set equal to 1. Next, note that for a simple imaging system

$$\Delta \phi_\lambda = \frac{\pi A_d}{4 F^2} \eta_o(\lambda) \frac{\partial L_\lambda}{\partial T} \Delta T, \quad (C-19)$$

where

- $\eta_o(\lambda)$ = the optical efficiency of the viewer
- F = the f /number
- T = temperature
- L_λ = watts/cm²/steradian/micron from the source.

Finally, using Eq. (C-19) for $\Delta \phi_\lambda$ and defining Δf_n by

$$\Delta f_n = \int_0^\infty \frac{S(f)}{S(f_o)} H_{ELECT}^2 df, \quad (C-20)$$

Eq. (C-18) becomes

$$S/N = \frac{\pi A_d^{1/2} \Delta T \int_0^\infty \eta_o(\lambda) \frac{\partial L_\lambda}{\partial T} D_\lambda^*(\lambda) d\lambda}{4 F^2 (\Delta f_n)^{1/2}} \quad (C-21)$$

The ΔT in Eq. (C-21) is the desired NE ΔT provided the S/N is set equal to 1 and provided the bandwidth equals the appropriate reference bandwidth.

APPENDIX C

The bandwidth to which NEAT is commonly referenced is given by

$$\Delta f_n = \pi/2 f_o = \frac{\pi}{2} \left[\frac{(HFOV) (VFOV) F_R \eta_{OVSC}}{2n_p \Delta x \Delta y \eta_{SC}} \right], \quad (C-22)$$

where HFOV = device horizontal field of view (mrad)

VFOV = device vertical field of view (mrad)

F_R = frame rate

η_{OVSC} = overscan ratio for the device

n_p = number of detectors in parallel

Δx = horizontal detector size (mrad)

Δy = vertical detector size (mrad)

η_{SC} = scan efficiency (fraction of time spent in actually scanning the field).

The initial form for Δf_n in Eq. (C-22) is obtained from Eq. (C-20), first, by setting the power spectrum ratio equal to 1 (i.e., ignoring any low-frequency $1/f$ component and high-frequency roll off) and, second, by equating H_{ELECT}^2 to $1/(1 + (f/f_o)^2)$ corresponding to an exponential response function for the electronic circuitry. The expression for f_o is simply derived by setting f_o equal to $1/(2\tau_D)$, where τ_D is the delay time for a picture element of size $\Delta x \times \Delta y$ (essentially the time the detector element spends on each picture element). The $1/(2\tau_D)$ corresponds to

$$\int_0^\infty \left[\frac{\sin(\pi f \tau_D)}{\pi f \tau_D} \right]^2 df,$$

which is the bandwidth associated with a rect function of duration τ_D .

The use of the "standard" bandwidth given in Eq. (C-22) in place of the bandwidth given in Eq. (C-20) yields the NEAT values commonly used. Recognize, however, that the bandwidth given by Eq. (C-20) is the true system noise bandwidth; and, therefore, a measurement of the S/N will yield the value given by Eq. (C-21) using this bandwidth (assuming H_{ELECT} includes any filtering by the measuring device); the S/N calculated using the "standard" bandwidth of Eq. (C-22) would be measured only if H_{ELECT} in Eq. (C-20) were so adjusted (e.g., by the measuring device) so as to make the true bandwidth of Eq. (C-20) equal to the "standard" bandwidth of Eq. (C-22).

The S/N (and the NEAT) obtained from Eq. (C-21) is that for a single detector; this S/N is appropriate for parallel scanning thermal viewers; however, for discoid systems, the S/N obtained by summing the signals and noises from the number of detectors in series is more useful. In this latter case, a reasonable approximation to the S/N is the S/N given in Eq. (C-21) divided by $(n_s)^{1/2}$, where n_s equals the number of detectors in series (assuming uniform

D_λ^* 's). In general, blind application of Eq. (C-21) (as well as the MRT and MDT equations) to unconventional systems can lead to difficulties and incorrect conclusions: this problem is usually easily circumvented by simple adjustments to the equation which can be made by anyone having an understanding of the material presented herein. (More often than not, one only needs to recognize the fact that the noise variances add directly.)

Prior to summarizing the results, several additional expressions and definitions are useful. First, D_λ^* is given by

$$D_\lambda^* = \eta_q^{1/2} \frac{D_\lambda^{**}}{\sin \theta/2} = \eta_q^{1/2} \eta_{CS} D_\lambda^{**} (2F). \quad (C-23)$$

where D_λ^{**} is D_λ^* for no cold shielding and 100% quantum efficiency;

η_q = quantum efficiency

η_{CS} = the cold shield efficiency

θ = the cold shield angle.

Second, the quantity W is defined by

$$W = \int_0^\infty \frac{\eta_o(\lambda)}{\eta_o(\lambda_p)} \frac{D_{fo}^*(\lambda)}{D_{fo}^*(\lambda_p)} \frac{\partial L_\lambda}{\partial T} d\lambda, \quad (C-24)$$

where λ_p is the wavelength for maximum $D_{fo}^*(\lambda)$. For hand calculations, Hudson notes that $\int_{3.2}^{4.8} \frac{\partial L_\lambda}{\partial T} d\lambda$ equals 5.2×10^{-6} while $\int_8^{13} \frac{\partial L_\lambda}{\partial T} d\lambda$ equals 7.4×10^{-5} [C.6]; these quantities are obviously useful approximations to W .

To summarize, then, the NE Δ T using Eq. (A-24) is given by

$$NE\Delta T = \frac{4F^2(\Delta f_n)^{1/2}}{\pi A_d^{1/2} \eta_o(\lambda_p) D_{fo}^*(\lambda_p) W}, \quad (C-25)$$

where Eqs. (C-22), (C-23), and (C-24) provide useful expressions for Δf_n , $D_{fo}^*(\lambda)$, and W . Also, note that A_d can be expressed in terms of focal length and nominal system resolution in milliradians, i.e.,

$$A_d^{1/2} = (\text{focal length}) \cdot (\text{resolution in mrad}) / (1000). \quad (C-26)$$

(If we included atmospheric transmission over the short path length in the NE Δ T laboratory experiment, then Eq. (C-24) becomes

$$W = \int_0^\infty \frac{\eta_o(\lambda)}{\eta_o(\lambda_p)} \frac{\eta_a(\lambda)}{\eta_a(\lambda_p)} \frac{\Gamma_{fo}^*(\lambda)}{D_{fo}^*(\lambda_p)} \frac{\partial L_\lambda}{\partial T} d\lambda$$

and Eq. (C-25) becomes

$$NE\Delta T = \frac{4F^2 \sqrt{\Delta f_n}}{\pi A_d^{1/2} \eta_o(\lambda_p) \eta_a(\lambda_p) D_{fo}^*(\lambda_p) W}$$

APPENDIX C

MRT and MDT Derivations

Basic Concepts

The minimum resolvable temperature (MRT) of a system is defined as the temperature difference relative to a background which the bars of a bar pattern must possess in order for a human observer to detect the individual bars when viewing the pattern through the system. The minimum detectable temperature (MDT) is the temperature difference a square object must possess in order to be detectable. Obviously, the MRT is a function of the bar pattern spatial frequency while the MDT is a function of the object size.

Historically, the MRT bar pattern has been a 4-bar pattern whose bars had lengths equal to their width; also, the pattern has been oriented such that the bars are perpendicular to the detector scan direction. The derivation presented here assumes that both the pattern and the detector orientation correspond to these historical precedents. The derivation also assumes that there is no sampling in the direction (horizontal) along which the detectors are scanned. This latter assumption is not valid for all systems; specifically, the signals from the detectors of a parallel scanning system are sometimes multiplexed in a manner which provides a sampling effect in the scan direction. This sampling can introduce noise fold-over and signal aliasing effects; however, if the system is well designed these effects will not be severe and the equations derived herein can be applied to these systems.

The basic hypothesis underlying the theory of MRT and MDT is that visual thresholds correspond to a critical value of "matched filter" signal-to-noise ratios; *i.e.*, the ratio formed from the maximum amplitude of the target and the rms value of the noise obtained by passing the signal (target) and noise which are actually observed by an individual through a filter matched to the observed signal. (Note that the signal and noise are not actually physically filtered by a matched filter; it is just hypothesized that the relevant signal-to-noise ratio for perceptual purposes is the signal-to-noise ratio obtained assuming that the signal and noise are filtered by the matched filter.) Thus, if the viewed object is characterized by the spatial function $i(x,y)$, the signal will be proportional to $i(x,y) * i(-x,-y)$ for x and y equal to zero which equals

$$\int_{-\infty}^{\infty} I(f_x, f_y) d^2 f,$$

where $I(f_x, f_y)$ is the transform of $i(x,y)$. Correspondingly, the noise will be proportional to

$$\left[\int S(f_x, f_y) I(f_x, f_y) d^2 f \right]^{1/2},$$

where $S(f_x, f_y)$ is the power spectrum of the observed noise. (Throughout this section, the quantity $i_0(x,y)$ representing the undegraded target will be normalized such that its maximum value is 1 while the (matched) filter corresponding to this quantity, $H^*(f_x, f_y)$, will be normalized such that $H^*(0,0) = 1$. Thus, for a uniform target,

$$I_0(f_x, f_y) = A_T H^*(f_x, f_y),$$

where A_T equals the area of the target.)

Although the determination of MDT is straightforward using the above hypothesis, an extension is required to determine MRT, *i.e.*, the perception threshold for a periodic pattern. Specifically, the nature of the matched filter (and the signal) must be established for the (potentially) infinite periodic pattern. The assumption is made that the filter in the periodic

direction is a rect function whose width is equal to the width of the bar while in the other direction the filter is simply the device degraded rect function corresponding to the length of the bar. (Note that a degraded periodic pattern retains its periodicity with unchanged spatial frequency.) Furthermore, the "signal" is assumed to be the difference between the "signal energy" coming through the filter centered over the bar and a filter centered over the neighboring trough. (Note that in some sense this corresponds to taking the signal for an aperiodic pattern as the difference between the "signal energy" passed through the matched filter centered over the target and the "energy" passed through a filter centered over the background.) With these assumptions, calculation of the MRT becomes very straightforward.

In the above, the implication is made that the object and noise observed are the object and noise existing on the device display. More fundamentally, they are the object and noise projected on the retina of the eye or, still better, the object and noise interpreted by the observer, *i.e.*, after degradation by the retina and nervous system. Given a transfer function for the eye, an effective power spectrum for the internal noise in the eye, and a knowledge of the actual extent of eye signal (and noise) summation, it is possible to extend the calculations to the retina and beyond. This extension will not be pursued here; rather, the assumption will be made that the eye transfer function and noise do not significantly alter the signal-to-noise ratio calculated using the displayed quantities. (In actual calculations, however, an eyeball term is included.)

A few comments concerning the (matched) filter formulation are possibly useful. The matched filter can be thought of as a window over which the signal and noise "energies" are summed to formulate a signal-to-noise ratio. This summation is similar to that performed by Rose in formulating S/N ratios which correlate with Blackwell's visual thresholds [C.5]; in Rose's case, MTF type degradations were not considered and, consequently, the matched filter was just the target itself. Thus, a matched filter signal and noise are just slightly sophisticated versions of a signal and noise summed over the target; the matched filter procedure merely provides a consistent technique for handling degraded (blurred) targets. An equivalent (but, to this author's thinking, more cumbersome) formulation uses the total signal energy as the signal (*i.e.*, sums all the signal energy) and then sums the noise over a equivalent target area which is larger than the original target as a result of MTF degradations.

The Derivations

The MRT and MDT equations can now be formulated rather easily, the only complication being that introduced by sampling.

To perform a reasonably rigorous derivation, a consistent set of units must be used. Let k be defined such that $k \Delta T$ equals the watts emitted by a display element (spot, etc.) for a large target with a temperature difference ΔT . Then, the signal energy per unit area from the display for a single frame will be equal to

$$M(x, y) = \frac{k \Delta T i(x, y)}{\Delta y, v} \quad (C-27)$$

where

$\Delta y,$ is the distance between scan lines $= \Delta y / \eta_{OVS}$.

v is the scan velocity of the display element.

$i(x, y)$ is the spatial distribution function of the degraded target.

APPENDIX C

The quantity $i(x,y)$ will equal (ignoring sampling effects, a procedure completely legitimate only if Δy_i is very small) the convolution of the original target with the system response function, i.e.,

$$i(x,y) = i_T(x,y) * h_D(x,y) \quad (C-28)$$

or, taking transforms,

$$I(f_x, f_y) = I_T(f_x, f_y) H_D(f_x, f_y),$$

where i_T is the target distribution and h_D is the system response function. (Note that for constant $i(x,y)$ the formulation above will yield a uniform display brightness; thus, this formulation uses an average display radiance across scan lines.)

The aperiodic matched filter signal, using Eq. (C-27), is given by

$$\begin{aligned} \text{Signal} &= \text{MAX} \left[\frac{k \Delta T}{\Delta y_i v} i(x,y) * h_m \right] \\ &= \frac{k \Delta T}{\Delta y_i v} \int_{-\infty}^{\infty} I(f_x, f_y) H_m d^2 f, \end{aligned} \quad (C-29)$$

where h_m and H_m are, respectively, the real space and the frequency space representations of the matched filter. (Note that "MAX" refers to the maximum value of the convolution over x and y .) As indicated previously, H_m is simply the normalized version of $I(f_x, f_y)$ (the degraded target); therefore, the signal for the aperiodic target is

$$(\text{SIGNAL})_a = \frac{k \Delta T}{\Delta y_i v} A_T \int_{-\infty}^{\infty} H_T^2(f_x, f_y) H_D^2 d^2 f, \quad (C-30)$$

where A_T is the area and H_T is the transfer function corresponding to the undegraded target.

The periodic matched filter signal, using Eq. (C-27) is given by

$$\text{SIGNAL} = \text{MAX} \left[\frac{k \Delta T}{\Delta y_i v} i(x,y) * h_m \right] - \text{MIN} \left[\frac{k \Delta T}{\Delta y_i v} i(x,y) * h_m \right], \quad (C-31)$$

where $i(x,y)$ is the degraded bar pattern and h_m is the undegraded rect function horizontally and the degraded rect function vertically. The quantity $i(x,y)$ is approximated (horizontally) by the first harmonic of the square wave; therefore, since the amplitude of this harmonic is $4/\pi$ times the amplitude of the square wave,

$$\begin{aligned} i(x,y) &= \left[\left(\text{square wave with} \right) + .5 \right] * h_D(x,y) \\ &\quad \left(\text{amplitude } .5 \right) \\ &\approx \text{MTF}(f_o) \frac{4}{\pi} (.5) \sin(2\pi f_o x) i_v(y) + .5, \end{aligned} \quad (C-32)$$

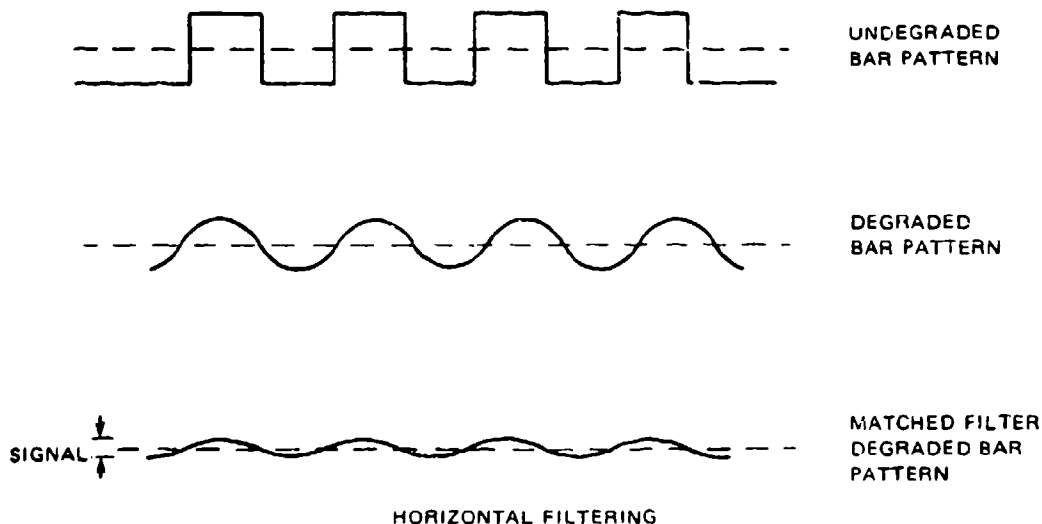
where f_o is the frequency of the bar pattern and $i_v(y)$ is the degraded vertical rect function corresponding to the length of the bar. (The fact that $i(x,y)$ will be negative at some points

when $MTF(f_0)$ equals approximately unity is an unimportant consequence of using the first harmonic approximation.) Substitution of $i(x,y)$ from Eq. (C-32) into Eq. (C-32) yields (evaluating the horizontal integrals in real space and the vertical integrals in frequency space):

$$(\text{SIGNAL})_p = \frac{k}{\Delta y, v} MTF(f_0) \frac{4}{\pi} \Delta T \int_0^{1/(2f_0)} \sin(2\pi f_0 x) (2f_0) dx \int_{-\infty}^{\infty} I_y H_y df_y. \quad (\text{C-33})$$

In Eq. (C-33), the factor $2f_0$ in the first integral comes about because the horizontal filter (rect function) of width $1/(2f_0)$ has an amplitude of $2f_0$ under the normalization convention that $H(f_x) = 1$ for $f_x = 0$. Since the first integral in Eq. (C-33) equals $2/\pi$ and since L equals $L H_L H_D$, where H_D is the transfer function of the device in the y direction and L is the length of the bars, Eq. (C-33) can be simplified to

$$(\text{SIGNAL})_p = \frac{k}{\Delta y, v} MTF(f_0) \frac{8}{\pi^2} \Delta T L \int_{-\infty}^{\infty} H_L^2 H_D^2 df_y. \quad (\text{C-34})$$



The noise expressions for MRT and MDT must now be determined; this requires establishing the power spectrum of the noise displayed to the observer. The function describing the noise on the display is given by

$$n(x,y) = \sum_i b_i(x) \delta(y - y_i) * h_d(y) = \sum_i b(x) h_d(y - y_i). \quad (\text{C-35})$$

APPENDIX C

where $h_d(y)$ is the impulse response of the display in the y direction and $b_i(x)$ is the function describing the horizontal noise function along the i th scan line. The form of Eq. (C-34) arises as an obvious result of the sampled nature of the thermal image which consists of independent scan lines; the convolution is merely a manifestation of the fact that each line is "spread out" by the display element. The autocorrelation of the noise is given by

$$\begin{aligned} & \langle n(x, y) n(x', y') \rangle \\ &= \sum_i \sum_j b_i(x) b_j(x') h_d(y - y_i) h_d(y' - y_j) \\ &= \sum_i \sum_j \langle b_i(x) b_j(x') \rangle h_d(y - y_i) h_d(y' - y_j). \end{aligned} \quad (C-36)$$

Assuming that $\langle b_i(x) \rangle$ equals zero, note that $\langle b_i(x) b_j(x') \rangle$ will equal zero unless $i = j$ since b_i and b_j are, otherwise, independent random processes. Thus

$$R(xx'yy') \triangleq \langle n(x, y) n(x', y') \rangle = \sum_i \langle b_i(x) b_i(x') \rangle h_d(y - y_i) h_d(y' - y_i). \quad (C-37)$$

Now $\langle b_i(x) b_i(x') \rangle$ is independent of i since all lines are (supposedly) the same and, therefore,

$$R(xx'yy') = \langle b(x) b(x') \rangle \sum_i h_d(y - y_i) h_d(y' - y_i). \quad (C-38)$$

Approximating the summation by an integral, we have

$$\begin{aligned} R(xx'yy') &\approx \langle b(x) b(x') \rangle \frac{1}{\Delta y_i} \int_{-\infty}^{\infty} h_d(y - y_i) h_d(y' - y_i) dy_i \\ &= \frac{\langle b(x) b(x') \rangle}{\Delta y_i} \int_{-\infty}^{\infty} h_d(p) h_d(Y + p) dp \triangleq R(XY), \end{aligned} \quad (C-39)$$

where $Y = y - y'$ and $X = x - x'$. (The quantity $\langle b(x) b(x') \rangle$ is assumed to be a function only of $x - x'$ which is true if the random process is wide-sense stationary.)

The power spectrum of the noise is just the Fourier transform of $R(X, Y)$, i.e.,

$$S(f_x, f_y) = \int_{-\infty}^{\infty} \langle b(x) b(x') \rangle e^{-2\pi i f_x X} dX \frac{1}{\Delta y_i} H_d(f_y) H_d^*(f_y). \quad (C-40)$$

Now $b(x)$ corresponds to the "voltage" noise function which is transformed from a "voltage" to a one-dimensional radiant energy function by the display elements; therefore, the Fourier transform of $\langle b(x) b(x') \rangle$ equals the "voltage" noise power spectrum provided the units are

properly transformed from "voltage" and "voltage" space to radiant energy and display space. (This conversion, itemized below, is based upon the implicit assumption that voltage is linearly related to radiant energy.) As discussed prior to Eq. (C-15), the "voltage" noise power spectrum equals

$$S(f) H_{\text{ELECT}}^2(f)$$

or

$$(\text{constant}) \frac{S(f)}{S(f_0)} H_{\text{ELECT}}^2(f).$$

In the latter expression above, the constant obviously equals $S(f_0)$ if the units of this expression are the same as those of the first expression (i.e., (volts) (second)); since the signal is given in terms of temperature units, the noise must also be and, therefore, the value of the constant is desired which references the power spectrum to temperature units, i.e., (temperature difference) (second). To establish the value of this constant, note that by definition the square of the $NE\Delta T$ equals the variance of the voltage noise in temperature units. Therefore we have,

$$(NE\Delta T)^2 = \sigma = \int_0^\infty (\text{constant}) \frac{S(f)}{S(f_0)} H_{\text{ELECT}}^2 df = (\text{constant}) \Delta f_n,$$

where Δf_n is defined by Eq. (C-20), and therefore,

$$\text{constant} = \frac{(NE\Delta T)^2}{\Delta f_n}.$$

(The quantity $(NE\Delta T)^2/\Delta f_n$ can be expressed in terms of detector sensitivity and device parameters using Eq. (C-25). Note that although the above discussion uses the true $NE\Delta T$ and Δf_n , i.e., not the standardized ones, the last equation is valid regardless of which Δf_n is used provided the Δf_n in the denominator is the same as the Δf_n used to calculate the $NE\Delta T$.) Consequently, the voltage noise power spectrum referenced to temperature units equals

$$\frac{NE\Delta T^2}{\Delta f_n} \frac{S(f)}{S(f_0)} H_{\text{ELECT}}^2(f).$$

Now, converting from temperature to radiant energy through use of the correspondence (see reasoning prior to Eq. (C-27),

$$NE\Delta T \leftrightarrow \frac{kNE\Delta T}{v} \text{ (energy/cm)},$$

using the relation (valid since $f = v/\lambda$)

$$\frac{S(f)}{S(f_n)} H_{\text{ELECT}}^2(f) = v \frac{S(f_\lambda)}{S(f_{\lambda n})} H_{\text{ELECT}}^2(f_\lambda).$$

where $S(f_\lambda) = S(v/\lambda)$, etc., and, using the fact that the Fourier transform of $\langle b(x) b(x') \rangle$ corresponds to the voltage power spectrum, the relation

APPENDIX C

$$\int_{-\infty}^{\infty} \langle b(x) b(x') \rangle e^{-2\pi i f_x X} dX = \frac{k^2 NE \Delta T^2}{v^2} \frac{1}{\Delta f_n} v \frac{S(f_x)}{S(f_{ox})} H_{ELECT}^2(f_x) \quad (C-41)$$

is obtained (assuming that the display transfer function equals 1). A careful examination of Eq. (C-40) shows that the units are energy²/cm which are those desired of the one-dimensional "display" power spectrum. Combining Eqs. (C-41) and (C-40) including the display transfer function, $H_d(f_x)$, the desired (two-dimensional) noise power spectrum is given by

$$S(f_x, f_y) = \frac{k^2 (NE \Delta T)^2}{\Delta y_i v \Delta f_n} \frac{S(f_x)}{S(f_{ox})} H_{ELECT}^2 H_d^2(f_x, f_y). \quad (C-42)$$

(The critical step in the derivation of $S(f_x, f_y)$ is Eq. (C-39) where the sampling characteristic of the display is in a sense approximated away. Strictly speaking, the sampled noise process cannot be characterized by a power spectrum.)

Given the power spectrum $S(f_x, f_y)$, the (matched, filtered) noises required to establish MRT and MDT are easily determined. As previously indicated, the matched filter for the MRT calculation is

$$H_W(f_x) H_L(f_y) H_D(f_y),$$

where H_W , H_L , and H_D are the transfer functions corresponding to the width of the bar, the length of the bar, and the system impulse function in the y direction, respectively. Therefore, the MRT noise is given by

$$(\text{Noise})_n = \left[\frac{k^2 (NE \Delta T)^2}{\Delta y_i \Delta f_n v} \int_{-\infty}^{\infty} \int_0^{\infty} \frac{S(f_x)}{S(f_{ox})} H_{ELECT}^2(f_x) H_d^2(f_x, f_y) H_W^2(f_x) H_L^2(f_y) H_D^2(f_y) df_x df_y \right]^{1/2} \quad (C-43)$$

The filter for the MDT is

$$H_T(f_x, f_y) H_D(f_x, f_y),$$

where H_T and H_D are the target and device transfer functions; therefore, the MDT noise is

$$(\text{Noise})_a = \left[\frac{k^2 (NE \Delta T)^2}{\Delta y_i \Delta f_n v} \int_{-\infty}^{\infty} \int_0^{\infty} \frac{S(f_x)}{S(f_{ox})} H_{ELECT}^2 H_d^2 H_T^2 H_D^2 df_x df_y \right]^{1/2} \quad (C-44)$$

The ratio of the signal given in Eq. (C-34) and the noise given in Eq. (C-43) yields the fundamental signal-to-noise ratio for periodic patterns for a single frame. The MRT is simply the ΔT found by summing the signal and noise over the frames in an eye integration time and setting the signal-to-noise ratio equal to a threshold value S . Thus, the MRT is given by (from Eqs. (C-34) and (C-43)).

MRT =

$$\begin{aligned} & \frac{\Delta y_i v \frac{\pi^2}{8} S}{MTF(f_o) L \int_{-\infty}^{\infty} H_T^2 H_D^2 df_x} \left[\frac{(NE \Delta T)^2}{\Delta y_i \Delta f_n v} \int_{-\infty}^{\infty} \int_0^{\infty} \frac{S(f_x)}{S(f_{ox})} H_{ELECT}^2 H_d^2 H_W^2 H_L^2 H_D^2 df_x df_y \frac{1}{F_{RTE}} \right]^{1/2} \\ & = \frac{\pi^2}{8} \frac{S}{MTF(f_o) L \int_{-\infty}^{\infty} H_T^2 H_D^2 df_x} \frac{NE \Delta T}{F_{RTE} \Delta f_n} \left[\frac{\Delta y_i v}{F_{RTE} \Delta f_n} \int_{-\infty}^{\infty} \int_0^{\infty} \dots df_x df_y \right]^{1/2} \quad (C-45) \end{aligned}$$

where F_R is the frame rate of the system and t_E is the eye integration time. Similarly, the MDT is given by (using Eqs. (C-30) and (C-44))

$$\text{MDT} = \frac{\text{NEATS}}{A_T \int_{-\infty}^{\infty} H_L^2 H_B^2 df} \left(\frac{\Delta y, v}{F_R t_E \Delta f_n} \int_{-\infty}^{\infty} \int_0^{\infty} \frac{S(f_x)}{S(f_{ox})} H_{\text{ELECT}}^2 H_d^2 H_f^2 H_b^2 df_x df_y \right)^{1/2} \quad (\text{C-46})$$

The somewhat formidable Eq. (C-45) can be expressed in a much more useful form through use of the following definitions and relations:

$$q_y \triangleq L \int_{-\infty}^{\infty} H_L^2 H_B^2 df_y$$

$$\rho_x \triangleq 2W \int_0^{\infty} \frac{S(f_x)}{S(f_{ox})} H_{\text{ELECT}}^2 H_d^2(f_x) H_w^2 df_x$$

$$\rho_y \triangleq L \int_{-\infty}^{\infty} H_L^2 H_B^2 H_d^2(f_y) df_y$$

$$L = \frac{7}{2f_o} \quad (\text{assuming bar length equals 7 times its width})$$

$$W = \frac{1}{2f_o}$$

Employing these last relations, the MRT reduces to

$$\text{MRT} = \frac{\pi^2}{8} \frac{S}{\text{MTF}(f_o)} \frac{\text{NEAT}}{q_y} \left(\frac{\Delta y, v}{F_R t_E \Delta f_n} \frac{2}{7} f_o^2 \rho_x \rho_y \right)^{1/2} \quad (\text{C-47})$$

This expression is further simplified by noting that q_y and ρ_y will equal approximately 1 for essentially all applications since the bar length will almost always be large compared to the system response function (for any reasonable f_o) in the y direction; therefore, the MRT is finally given by

$$\text{MRT} = \frac{\pi^2}{4(14)^{1/2}} \frac{S \text{NEAT} f_o}{\text{MTF}(f_o)} \left(\frac{\Delta y, v \rho_x}{F_R t_E \Delta f_n p} \right)^{1/2} \quad (\text{C-48})$$

which is the recommended equation for calculating MRT. (This last approximate expression can be arrived at by a somewhat simpler argument which is perhaps useful. Calculate the one-dimensional matched filter signal and noise for a single scan line assuming that the bar length is greater than the height of a scan line. This calculation, as easily seen from the above analysis, yields a signal

$$(\text{Signal}) = \frac{\lambda \Delta I}{v} \text{MTF}(f_o) \frac{8}{\pi^2} \Delta I \text{ energy/cm}$$

and a noise

$$(\text{Noise})_r = \left[\frac{\lambda^2 (\text{NEAT})^2}{\Delta f_n v} \int_0^{\infty} \frac{S(f_x)}{S(f_{ox})} H_{\text{ELECT}}^2(f_x) H_d^2(f_x) H_b^2(f_x) df_x \right]^{1/2}$$

APPENDIX C

Since the "matched" filtering in the y direction corresponds to summing the signal and noise over the length of a bar, since signals add directly and noises add quadratically, and since the bar extends over $(L/\Delta y)$ independent lines, the desired MRT signal-to-noise ratio is given by

$$(S/N)_p = \frac{\frac{L}{\Delta y} \frac{K \Delta T}{V} MTF(f_o) \frac{8}{\pi^2} \Delta T}{\left(\frac{L}{\Delta y} \frac{k^2 (NE \Delta T)^2}{\Delta f_n v} \int_0^\infty \dots df_x \right)^{1/2}}$$

which directly yields the MRT given in Eq. (C-48).

Each individual concerned with MRT has his own favorite form for the MRT equation derived by using different definitions and different approximations than those used above. For example, a quantity Q is used by some individuals where

$$Q = \rho_x f_o;$$

others approximate the integrals such as

$$\int_{-\infty}^{\infty} H_L^2 H_B^2 df$$

by

$$\left(\frac{f_L^2 f_B^2}{f_L^2 + f_B^2} \right)^{1/2}$$

where

$$f_L = \int_{-\infty}^{\infty} H_L^2 df$$

and

$$f_D = \int_{-\infty}^{\infty} H_D^2 df; \text{ etc.}$$

To the author's knowledge, however, all the expressions follow directly from Eq. (C-45) using the appropriate definitions and approximations. (In one instance, an equation is used which is derived on the assumption that the "matched filter" for the bar pattern is a square whose side is equal to the width of the bar. Even in this case, the final equation reduces to Eq. (C-48) except for a different constant.)

The use of Eq. (C-48) requires establishing the values of S and t_k ; again, unfortunately, universal values for these constants do not exist. The values recommended at this time are

$$S = 2.25, \quad (C-49)$$

$$t_k = 0.2.$$

Several approximations and facts are useful for using Eq. (C-48) to make quick calculations. First, from Eq. (C-22) (and the material following Eq. (C-22))

$$\frac{v}{\Delta f} = \frac{2}{\pi} \Delta x \approx \frac{4}{\pi} \Delta x,$$

where Δx is the detector width. Also Δy is given by

$$\Delta y = \frac{\Delta y}{\eta_{OVSC}}$$

where Δy is the detector height and η_{OVSC} is the overscan ratio. Finally, ρ_x will equal approximately 1 for small f_o while for any f_o a respectable approximation, assuming $S(f_o)/S(f_{ox})$ equals 1, is

$$\rho_x = \frac{1}{(4f_o^2(\Delta x)^2 + 1)^{1/2}} / p. \quad (C-50)$$

Therefore, a useful form of Eq. (C-48) for hand calculations is

$$\text{MRT} = 0.66 S \frac{NE \Delta T f_o}{\text{MTF}(f_o)} \left[\frac{4}{\pi} \frac{\Delta x \Delta y}{\eta_{OVSC} F_R t_E} \right]^{1/2} \left[4f_o^2(\Delta x)^2 + 1 \right]^{-1/4}, \quad (C-51)$$

where the last factor can be set equal to a 1 for many values of f_o .

The MDT given in Eq. (C-46) can be simplified to

$$\text{MDT} = \frac{SNE \Delta T}{q_A} \left[\frac{\Delta y}{F_R t_E \Delta f_n} \frac{1}{2W^2} \rho_{xA} \rho_{yA} \right]^{1/2}. \quad (C-52)$$

through use of the definitions

$$q_A = A_T \int_{-\infty}^{\infty} H_f^2 H_b^2 df$$

$$\rho_{xA} = 2W \int_0^{\infty} \frac{S(f_x)}{S(f_{ox})} H_{\text{ELECT}}^2 H_d^2 H_W^2 H_b^2 df_x$$

$$\rho_{yA} = W \int_{-\infty}^{\infty} H_W^2 H_f^2 H_b^2 df_y$$

where H_W is the transfer function corresponding to the side of the test square. Approximations to q_A , ρ_{xA} , and ρ_{yA} can be formulated similar to those used to simplify the MTF; these will not be pursued here.

VERTICAL MRT

If sampling effects are assumed to be negligible, then a vertical MTF and MRT can be defined and an expression for them derived. A system's performance can then be a function of some combination of horizontal and vertical MRT. As an example, the MRTs in the two directions can be assumed to form an average MRT whose value is

$$\text{MRT}_a = [\text{MRT}^2(f_x) + \text{MRT}^2(f_y)]^{1/2} / \sqrt{2}$$

A vertical MRT (f_y) similar to the horizontal MRT (f_x) can be derived in the same manner utilized in A. The only difference is that the target bar pattern is now oriented with the long dimension parallel to the scan direction. Then returning to Eq. (C-32), we get

$$i(x, y) = \text{MTF}(f_y) \frac{4}{\pi} (.5) \sin(2\pi f_y y) i_x(x) + .5. \quad (C-53)$$

where $i_x(x)$ is the degraded rect function in the x direction. Eq. (C-33) becomes

APPENDIX C

$$(\text{SIGNAL})_p = \frac{k}{\Delta y_i v} \text{MTF}(f_{oy}) \frac{4}{\pi} \Delta T \int_0^{1/2 f_{oy}} \sin(2\pi f_{oy} y) (2f_{oy}) dy \int_{-\infty}^{\infty} I_x H_x df_x, \quad (\text{C-54})$$

where now $I_x = L H_L(f_x) H_D(f_x)$. Hence, the signal for the case of horizontal bars is

$$(\text{SIGNAL})_p = \frac{k}{\Delta y_i v} \text{MTF}(f_{oy}) \frac{8}{\pi^2} \Delta T L \int_{-\infty}^{\infty} H_L^2(f_x) H_D^2(f_x) df_x. \quad (\text{C-55})$$

In deriving the noise power spectrum, we still get the result

$$S(f_x, f_y) = \frac{k^2 \text{NE} \Delta T^2}{\Delta y_i v \Delta f_n} \frac{S(f_x)}{S(f_{ox})} H_{\text{ELECT}}^2(f_x) H_d^2(f_x, f_y), \quad (\text{C-56})$$

since the target plays no roll in the noise at this point. The matched filter for the horizontal case is

$$H_w(f_y) H_L(f_x) H_D(f_x).$$

Hence, the noise is

$$(\text{NOISE})_p = \left[\frac{k^2 (\text{NE} \Delta T)^2}{\Delta y_i v \Delta f_n} \int_{-\infty}^{\infty} \int_0^{\infty} \frac{S(f_x)}{S(f_{ox})} H_{\text{ELECT}}^2 H_d^2(f_x, f_y) H_w^2(f_y) H_L^2(f_x) H_D^2(f_x) df_x df_y \right]^{1/2}. \quad (\text{C-57})$$

Taking the ratio of Eqs. (C-55) to (C-57), integrating over frames, and solving for MRT yields

$$\text{MRT}(f_o) = \frac{\Delta y_i v \frac{\pi^2}{8} S}{\text{MTF}(f_o) L \int_{-\infty}^{\infty} H_L^2 H_D^2 df_x} \quad (\text{C-58})$$

$$\left[\frac{\text{NE} \Delta T^2}{\Delta y_i \Delta f_n v} - \left(\frac{1}{F_R I_E} \right) \int_{-\infty}^{\infty} \int_0^{\infty} \frac{S(f_x)}{S(f_{ox})} H_{\text{ELECT}}^2 H_d^2(f_x, f_y) H_w^2(f_y) H_L^2(f_x) H_D^2(f_x) df_x df_y \right]^{1/2}$$

Defining the quantities

$$R_x \equiv L \int_{-\infty}^{\infty} H_L^2 H_D^2 df_x,$$

$$\rho_x \equiv 2L \int_0^{\infty} \frac{S(f_x)}{S(f_{ox})} H_{\text{ELECT}}^2 H_d^2 H_L^2 H_D^2 df_x$$

$$\rho_y \equiv W \int_{-\infty}^{\infty} H_w^2 H_d^2 df_y,$$

where $L = \frac{7}{2f_o}$ and $W = \frac{1}{2f_n}$, then Eq (C-58) becomes

$$\text{MRT}(f_o) = \frac{\pi^2}{8} \frac{S}{\text{MTF}(f_o)} \frac{\text{NE} \Delta T}{k} \left[\frac{\Delta y_i v}{F_R I_E \Delta f_n} \frac{2}{7} f_o^2 \rho_x \rho_y \right]^{1/2}. \quad (\text{C-59})$$

As in Appendix A, g_x approaches 1, however ρ_x will not asymptote as fast as before because of the additional electronic filtering H_{ELECT}^2 . Using this relation, we get

$$\text{MRT}(f_o) = \frac{\pi^2}{4(14)^{1/2}} \frac{SNE\Delta T f_o}{\text{MTF}(f_o)} \left(\frac{\Delta y_i \nu \rho_x \rho_y}{F_R t_E \Delta f_n} \right)^{1/2} \quad (\text{C-60})$$

REFERENCES

- C.1 Perkin-Elmer Corporation, "A Symposium on Sampled Images", Report No. IS10763, 1971.
- C.2 Ratches, J.A., *et al.*, "Night Vision Laboratory Static Performance Model for Thermal Viewing Systems", U.S. Army Electronics Command, Report No. ECOM 7043, April 1975.
- C.3 J. A. Jamieson *et al.*, *Infrared Physics and Engineering*, McGraw-Hill, New York, 1963.
- C.4 J. W. Wozencraft and I. M. Jacobs. *Principles of Communication Engineering*, Wiley, New York, 1965.
- C.5 J. A. Jamieson *et al.*, *Infrared Physics and Engineering*, McGraw-Hill, New York, 1963.
- C.6 R. D. Hudson, Jr., *Infrared System Engineering*, Wiley, New York, 1969.
- C.7 Albert Rose, "The Sensitivity Performance of the Human Eye on an Absolute Scale," *J. Opt. Soc. Am.* 35, 196 (1948).

Appendix D

STATIC PERFORMANCE MODEL BASED ON THE PERFECT SYNCHRONOUS INTEGRATOR MODEL

R.L. Sendall and F.A. Rosell

The perfect synchronous integrator model was originally developed by Otto Shade, Sr. and predates the matched filter concept by 15 to 20 years. Its utility is in predicting sensor resolution-irradiance characteristics with excellent precision. The model presented in this appendix is the result of a collaboration by R.L. Sendall and F.A. Rosell based on an earlier TV/IR comparison study (Ref. D.1) and previous independent efforts. Numerous approximations have been developed in order to make rapid computations on hand calculators possible and to give physical insight to the physical processes involved.

D1. THE ELEMENTARY MODEL

Consider a scene consisting of a uniformly radiant object of area "a" upon a uniformly radiant background. This scene is focused onto a photosurface of an imaging sensor and the sensor output is used to generate a displayed image which is viewed by an observer. The observer detection theory to be discussed here considers the observer to function as a spatial and temporal integrator and therefore image signal-to-noise ratios, SNR, will be defined in terms of area and time integrations. The photosurface of the sensor linearly converts a portion of the impinging photons to photoelectrons. The photoconverted image signal is therefore defined as an area and time integration of the photoelectrons derived from the object and is

$$\text{Signal} = \Delta n = (\dot{n}_o - \dot{n}_b) a T_e \quad (\text{D-1})$$

where \dot{n}_o and \dot{n}_b are the per unit area and time rates of photoelectron generation due to object and background images, respectively, and T_e is the time over which photoelectrons are integrated. The signal generated by this photoconversion process is noisy with the photoelectrons being generated with a Poisson distribution which results in white noise with an rms value equal to the square root of the average number of photoelectrons generated. That is

$$\text{Noise} = (n_{av})^{1/2} = [a T_e (\dot{n}_o + \dot{n}_b)/2]^{1/2} \quad (\text{D-2})$$

The image SNR at the output of the photosurface therefore becomes

$$\text{SNR} = \Delta \dot{n}' [a T_e (\dot{n}_o + \dot{n}_b)/2]^{1/2} = \Delta \dot{n}' [a T_e / \dot{n}_{av}]^{1/2} \quad (\text{D-3})$$

The image SNR defined in Eq. (D-3) is essentially that proposed by Barnes and Czerny in 1932, and by de Vries in 1943 but has been formulated to agree with Shade. In the early efforts, it was postulated that an image, to be detectable must have a SNR exceeding some threshold value and that this threshold value is a constant. This has been found to be a reasonable approximation for small images but as Rosell and Willson (D.2) have shown, the apparent thresholds increase for images which subtend more than about $1/2^\circ$ in two directions simultaneously at the observer's eye.

APPENDIX D

D2. FOURIER ANALYSIS OF IMAGE SIGNALS

If an imaging system were perfect, point source images would appear as points on the display and all images would be displayed with perfect fidelity. In reality, displayed images differ from the original scene in amplitude, shape, and/or phase due to finite sensor apertures which may include optical and electrooptical lenses, phosphor particles, electron scanning beams, and the like. Whatever their form, the effect of finite apertures is to blur image detail in a manner analogous to electrical filters in communications systems. Being analogous, the mathematical transform methods of Heavside, LaPlace, and Fourier originally developed for communications systems are directly applicable. Since images are two-dimensional, two-dimensional transforms may be required. However, many images are primarily one-dimensional or functionally independent and separable in two orthogonal dimensions so that one-dimensional analysis applies. One-dimensional analysis will be employed for the discussion below for the sake of brevity and clarity.

Following standard television practice, the fundamental measure of spatial frequency will be N lines or half cycles per picture height. For a repetitive bar pattern of period $2\Delta x$, as shown in Fig. D-1, the spatial frequency

$$N = Y/\Delta x, \quad (D-4)$$

where Y is the height of the picture. The virtue of N is that it is dimensionless and eliminates the need for scale changes when multiple imaging and reimaging processes are involved. The applicable Fourier transform pair is

$$F(N) = \int_{-\infty}^{\infty} f(x) \exp(-j\pi Nx) dx, \quad (D-5)$$

$$f(x) = \int_0^{\infty} F(N) \exp(j\pi Nx) dN. \quad (D-6)$$

The response of a one-dimensional linear system to a unit area impulse $\delta_o(x)$ is known as the impulse response $r_o(x)$ or alternatively, as the line spread function for imaging systems. The Fourier transform of $r_o(x)$ is $R_o(N)$ which, for imaging systems, is known as the Optical Transfer Function or OTF. In general,

$$R_o(N) = |R_o(N)| \exp[j\phi(N)]. \quad (D-7)$$

The modulus $|R_o(N)|$ is the Modulation Transfer Function or MTF, and the argument $\phi(N)$ is the Phase Transfer Function or PTF. The conjugate $R_o^*(N) = R_o(-N)$ and $R_o(0) = 1.0$. Furthermore, $R_o(N)$ is always smaller than 1.0 at all $N > 0$ (Ref. D.3).

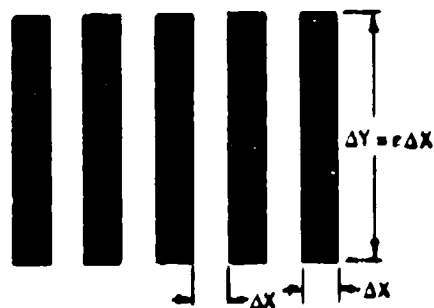


Fig. D-1 - Bar pattern geometry

In optical systems, the transmission losses or gains are always separated from the MTF. Hence, when a unit area impulse is used as the input, the integral of the output waveform must equal unity. This places a normalization on the OTF that causes it to have a value of unity at $N = 0$. It has become common practice to maintain this normalization when analyzing imaging systems, i.e., if the image intensity distribution is $r_o(x)$ for a unit area impulse input, then

$$\int_{-\infty}^{\infty} r_o(x) dx = 1 = R_o(0) \quad (D-8)$$

as can be seen by setting $N = 0$ in Eq. (D-5).

In the space domain, the input to any component aperture in a linear system will be $kf(x)$, the aperture response will be $r_o(x)$, and the output will be $kg(x)$, where $g(x)$ is the convolution of $r_o(x)$ and $f(x)$, i.e.,

$$g(x) = r_o(x) \cdot f(x) \quad (D-9)$$

and k is an arbitrary constant. In the spatial frequency domain,

$$G(N) = R_o(N) \cdot F(N), \quad (D-10)$$

where $G(N)$, $R_o(N)$, and $F(N)$ are the Fourier transforms of $g(x)$, $r_o(x)$, and $f(x)$, respectively.

D3. THE EFFECT OF APERTURES ON APERIODIC IMAGES

An aperiodic image, as the term is used here, is defined to be an isolated object viewed against a uniform background of large extent relative to the object. Suppose that an input image is a rectangular pulse of amplitude k and duration x_o . After passing through a linear system with finite apertures, the output image waveform will be $kg(x)$. This output image will be of greater duration and its amplitude may be altered. It is customary to assume that the observer is able to integrate all of the image signal under the waveform of the output image. This assumption is obviously optimistic, but it is a good approximation for most waveforms. For images with a strong central core but with a long low-amplitude skirt, it would be expected that the eye-brain combination will truncate the integration when the signal-to-noise ratio no longer improves by increasing the integration distance. Using these criteria for limiting the integration distance would be more accurate, but the calculation would be difficult and time consuming.

If we accept an infinite integration distance or duration for the signal on the basis that the signal would not change considerably and even though a different duration is used for the noise, we have that the signal will be equal to

$$\text{Signal} = k \int_{-\infty}^{\infty} g(x) dx. \quad (D-11)$$

Observe that

$$G(N) = \int_{-\infty}^{\infty} g(x) \exp(-j\pi Nx) dx, \quad (D-12)$$

and

$$G(0) = \int_{-\infty}^{\infty} g(x) dx. \quad (D-13)$$

APPENDIX D

That is, the integral over the output image area is equal to the value of the Fourier transform of the output image at zero frequency. From Eq. (D-10), we can infer that $G(0) = R_o(0)$, $F(0)$ and since $R_o(0) = 1.0$, $G(0) = F(0)$. Thus,

$$\text{Signal} = kG(0) = kF(0). \quad (\text{D-14})$$

By the same argument then,

$$kF(0) = k \int_{-\infty}^{\infty} f(x) dx \quad (\text{D-15})$$

or the

$$\text{Signal} = k \int_{-\infty}^{\infty} f(x) dx, \quad (\text{D-16})$$

which is equal to kx_o when $kf(x)$ is a pulse of amplitude k and duration x_o . The implication of the above result is that the area under the output pulse is identical to the area under the input pulse. If the observer is able to integrate all of the image signal under the output waveform, as we have assumed, then the sensor's apertures have no effect on signal. Note that to conform with the elementary imaging model, the value of k for our one-dimensional image of constant amplitude and of duration x_o will be $\Delta \dot{n}' T_e$ and

$$\text{Signal} = \Delta \dot{n}' T_e x_o. \quad (\text{D-17})$$

While an imaging sensor's aperture may not affect the image signal, we would expect the blurring of an image by sensor apertures to adversely affect the image's detectability. On the premise that the important parameter with respect to image detectability is its SNR, we are led to hypothesize that noise discerned must then be increased by the apertures.

Before continuing, it is worthwhile to review the effects of an integrator. A perfect integrator continuously sums the value of a function for a set period of time or space. For the theory being presented here, it is assumed that the observer's eye-brain combination processes images in this manner with the duration being synchronous with the image anomalously being detected. There are two effects of interest. The low-frequency gain is proportional to the integration duration, and the response to high frequencies, relative to low frequencies, decreases as the image duration increases. Specifically, the normalized frequency response of an integrator is given by

$$R(\nu)/R(0) = [\sin \pi \nu x_i / 2] / (\pi \nu x_i / 2), \quad (\text{D-18})$$

where ν is the dummy frequency variable in lines per unit distance and x_i is the duration variable. The low-frequency response $R(0)$ is equal to x_i .

If noise is being integrated, then the rms value of the variations, I_n , in the output of the integrator from integration period to integration period, which is the integrator output noise, is predicted by integrating the product of the spectral density of the noise and the response function of the integrator, i.e.,

$$I_n^2 = \int_0^\infty \sigma^2(\nu) R^2(\nu) d\nu. \quad (\text{D-19})$$

For white noise, $\sigma^2(\nu) = \sigma^2$, a constant and

$$I_n = x_i \sigma (N_{ei})^{1/2} = \sigma x_i^{1/2}. \quad (\text{D-20})$$

since the noise bandwidth of the integrator N_{ei} is

$$N_{ei} = \int_0^\infty \left[\frac{\sin(\pi \nu x_i/2)}{(\pi \nu x_i/2)} \right]^2 d\nu = \frac{1}{x_i}. \quad (D-21)$$

When the input signal is of constant amplitude, the signal output of the integrator is proportional to x_i and therefore the integrator SNR is proportional to $x_i^{1/2}$.

It should be noted that the definition of $\sigma(\nu)$ as noise spectral density implies an integration for the duration of one cycle. Therefore our integrator is summing up independent samples of one cycle duration and as is commonly noted when the signal is coherent and the noise is random, the SNR improves as the square root of the number of samples summed, i.e., the square root of the integration duration. If the noise is not broadband, then the noise bandwidth is not determined solely by the integration duration but also by the spectral characteristics of the noise being integrated. Consider the case of bandlimited white noise which is flat from approximately DC until rolled off by a filter of frequency response $R_f(\nu)$ and noise bandwidth N_{ef} . For this case, the integrated noise is

$$\begin{aligned} I_N &= \left[\int_0^\infty \sigma^2 R_f^2(\nu) R_i^2(\nu) d\nu \right]^{1/2} \\ &= \sigma x_i [(1/N_{ei})^2 + (1/N_{ef})^2]^{1/4} \\ &= \sigma x_i [x_i^2 + (1/N_{ef})^2]^{-1/4}. \end{aligned} \quad (D-22)$$

Considering the total noise bandwidth out of the integrator to be that due to the filter and the integrator, we have

$$(N_{ef})^{-2} = (N_{ei})^{-2} + (N_{ef})^{-2} \quad (D-23)$$

and for this case

$$I_N = \sigma x_i [N_{ef}]^{1/2}. \quad (D-24)$$

The signal should be the result of integrating over the same x_i duration as the noise. However, as was discussed above it is easier to assume that the signal integration over x_i is essentially the total integrated signal and therefore is the same as the integral over the total image and, in turn, equal to the integral over the total object x_o . The image SNR for this case becomes proportional to $(x_o/x_i) (1/N_{ef})^{1/2}$.

All photoconversion processes are noisy. The principal noises may be added either prior to or subsequent to a sensor aperture. To begin, let the noise be added after the image has passed through an aperture. Suppose the input pulse is rectangular of duration x_o as shown in Fig. D-2(a) and then let noise be added with the result shown in Fig. D-2(b). Assuming a unity OTF, the noise integration distance will then be x_o . If, however, the input image is blurred by apertures as shown in Fig. D-2(c), the effective noise integration distance will be increased as shown in Fig. D-2(d). While the exact size of this integration will involve further assumptions and will be less than that presumed for the signal, it is clear that it can be increased beyond the size of the input object. It is also apparent that an optimum integration distance will exist which is less than the duration we assume for the signal but which would not significantly change the value of the integrated signals and noises. While the optimization of integrator area to maximize SNR may be important in some applications, it is ignored here in favor of a more direct solution.

APPENDIX D

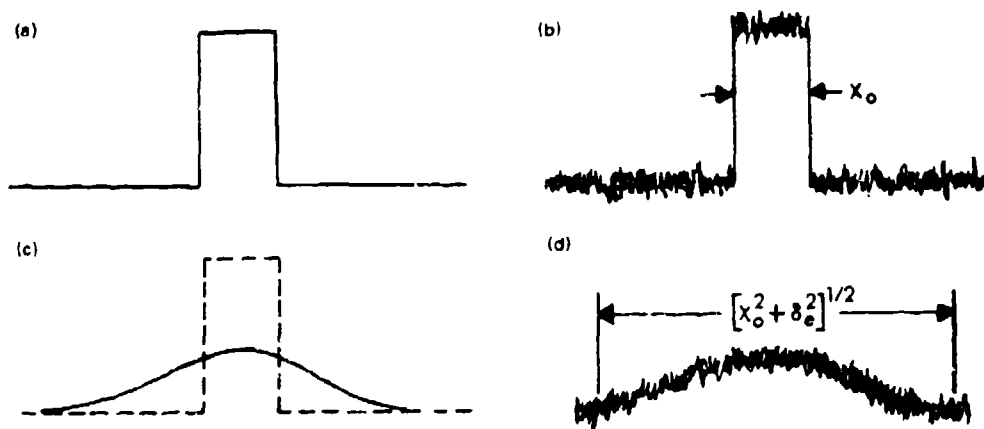


Fig. D-2 — Noise integration distances with unity MTF (case b) and after passing through a real aperture (case d)

If the input image is of unit amplitude and long duration x_o , relative to the sensor's line spread function, the sensor apertures should have little effect and the rms noise would simply be proportional to the square root of x_o (or image area in the case of a two-dimensional image). As x_o is made small, approaching an impulse in dimensions, the noise integration distance becomes the effective dimensions of the line spread function.

We will first consider the case where the sensor apertures precede the point of noise insertion as shown in Fig. D-3. Assume the input image to be a unit amplitude rectangular pulse of width x_o and the output pulse is a function $g(x)$ of amplitude $g(o)$. Noise is then linearly added. The noise to be integrated is broadband and independent of the sensor apertures, but the integration duration is determined by the object size and the sensor apertures. The preferred image size approximation can be obtained from

$$x_i \approx [x_o^2 + (1/N_e)^2]^{1/2} = [x_o^2 + \delta_e^2]^{1/2}, \quad (D-25)$$

where N_e is the sensor's equivalent bandwidth, i.e.,

$$N_e = \int_0^\infty R_g^2(N) dN \text{ and } \delta_e = 1/N_e. \quad (D-26)$$

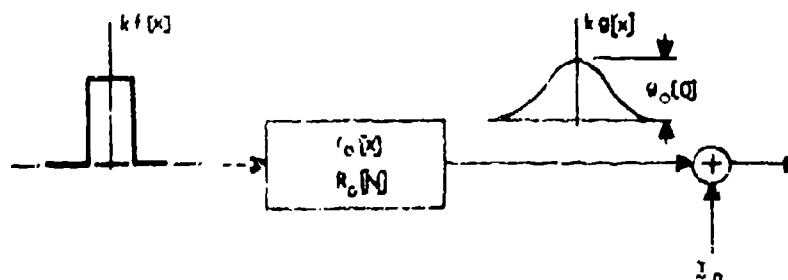


Fig. D-3 — Input-output relationships for the case where the point of noise insertion follows the apertures

An alternative approximation that has been investigated is to use the equivalent signal duration, x_a , which is defined as the width of a rectangle of height equal to the maximum amplitude of the output signal waveform $g(o)$ and of area equal to the area under the waveform $g(x)$. This duration x_a can be approximated in a manner similar to that used for x , by

$$x_a = [x_o^2 + \delta_a^2]^{1/2}, \quad (D-27)$$

where δ_a is the equivalent duration as x_o approaches zero and can be exactly determined from this limiting process by having $kx_o = 1$. Then,

$$\begin{aligned} g(o)\delta_a &= kx_o = 1, \\ \delta_a &= 1/g(o) \\ &= \left[\int_0^\infty G(N) dN \right]^{-1}, \end{aligned} \quad (D-28)$$

and since as $x_o \rightarrow 0$, $F(N) \rightarrow 1$ for all N , $G(N) \rightarrow R_o(N)$ and

$$\delta_a = \left[\int_0^\infty R_o(N) dN \right]^{-1}. \quad (D-29)$$

This particular integration duration (area) is less than or equal to δ_e and is of interest not only because it puts a lower bound on the noise integration distance but because it is determined by a limiting case of the area under the MTF curve which has been described by Snyder (D-4). The use of δ_a , rather than δ_e , as the noise integration duration in conjunction with the total signal integration assumption will result in a higher SNR_D value but has not proved to be as accurate experimentally as the δ_e choice and therefore is only presented as alternate and a limiting case. For images that are much larger than the sensor line spread function, the choice is immaterial and even for small images, the differences will be comparatively small.

Using the δ_a assumption, the mean-square-noise for a rectangular image of unit amplitude is

$$\begin{aligned} \text{M.S. Noise} &= \sigma^2 x \\ &= \sigma^2 [x_o^2 + (\delta_a)^2]^{1/2}. \end{aligned} \quad (D-30)$$

In two dimensions

$$\begin{aligned} \text{M.S. Noise} &= \sigma^2 x_y \\ &= \sigma^2 [x_o^2 + (1/N_{ex})^2]^{1/2} \cdot [y_o^2 + (1/N_{ey})^2]^{1/2} \\ &= \sigma^2 [x_o^2 + \delta_{ex}^2]^{1/2} \cdot [y_o^2 + \delta_{ey}^2]^{1/2}, \end{aligned} \quad (D-31)$$

where

- x_o is the input image width,
- y_o is the output image height,
- N_{ex} is the sensor noise equivalent bandwidth in x , and
- N_{ey} is the sensor noise equivalent bandwidth in y .

The image signal for the two-dimensional object is $kx_o y_o = \Delta n' t_p x_o y_o$ and $\sigma^2 = n_o' t_p$. Therefore, for the case of white noise

APPENDIX D

$$\begin{aligned} \text{SNR}_D &= \frac{\dot{n}' T_c x_o y_o}{(\dot{n}_{av} t_p)^{1/2} [x_o^2 + (1/N_{cx}^2)]^{1/4} [(y_o^2 + (1/N_{cy}^2)]^{1/4}} \\ &= \frac{(x_o y_o)^{1/2}}{[1 + (1/x_o N_{cx})^2]^{1/4} \cdot [1 + (1/y_o N_{cy})^2]^{1/4}} \cdot \frac{\Delta \dot{n}' T_c^{1/2}}{(\dot{n}_{av})^{1/2}}. \end{aligned} \quad (\text{D-32})$$

For the case where the system MTF = 1.0 at all spatial frequencies of interest or where the input image is of large extent, $N_{cx} = N_{cy} = \infty$ and we have agreement with Eq. (D-3) of the elementary model since

$$\text{SNR}_D = [T_c x_o y_o]^{1/2} \cdot \Delta \dot{n}' / [n_{av}]^{1/2}. \quad (\text{D-33})$$

On the other hand, when the object is very small such that $x_o = y_o \rightarrow 0$,

$$\text{SNR}_D = [x_o y_o / (\delta_{cx} \delta_{cy})^{1/2}] \cdot \Delta \dot{n}' T_c^{1/2} / (n_{av})^{1/2}, \quad (\text{D-34})$$

showing that sensor apertures degrade the SNR_D . These two expressions show that for large objects, SNR_D is proportional to $(x_o y_o)^{1/2}$ while for objects which are smaller than the sensors equivalent aperture ($\delta_c = N_c^{-1}$), the SNR_D is proportional to $x_o y_o$. As a result, it is possible to introduce a noise increase factor, ξ , which is a measure of the noise power increase due to integration over the blurred image. These factors are

$$\begin{aligned} \xi_x &= [1 + (1/x_o N_{cx})^2]^{1/2} \\ \xi_y &= [1 + (1/y_o N_{cy})^2]^{1/2}. \end{aligned} \quad (\text{D-35})$$

ξ_x is therefore a factor for comparing the system with finite apertures to a perfect system and for any given system is a function of the input image size having a minimum value of unity when $x_o \gg \delta_{cx}$ and a value $\xi_x = \delta_{cx}/x_o$ which is greater than unity as $x_o \rightarrow 0$. The SNR_D for a sensor with an aperture which does not filter the noise becomes

$$\text{SNR}_D = \frac{(x_o y_o)^{1/2}}{\xi_x^{1/2} \xi_y^{1/2}} \cdot \frac{\Delta \dot{n}' T_c^{1/2}}{n_{av}^{1/2}}. \quad (\text{D-36})$$

We next consider the case where the aperture follows the point of noise insertion as shown in Fig. D-4(a). In this case, the aperture function, $r_p(x)$, can both increase the perceived noise by increasing the noise integration distance and decrease it by virtue of a filtering action. In the previous case (noise added after the aperture), the noise in the image is white in character (though spatially band-limited). In the case now under consideration, the displayed noise will have a finite spectrum due to passing through the aperture.

Conceptually, the processes will be assumed to be of the following nature. The input is first passed through the aperture so as to increase the noise integration distance. Next, the noise is bandpass limited and added to the output signal as shown in the functional noise diagram of Fig. D-4(b).

For this case, the noise to be integrated is band-limited to the transfer function $R_o(N)$ and the integration duration is determined by the object size and the sensor aperture. The noise integration duration as determined by the sensor and object can be approximated by

$$x = (x_o^2 + \delta_{cx}^2)^{1/2}. \quad (\text{D-37})$$

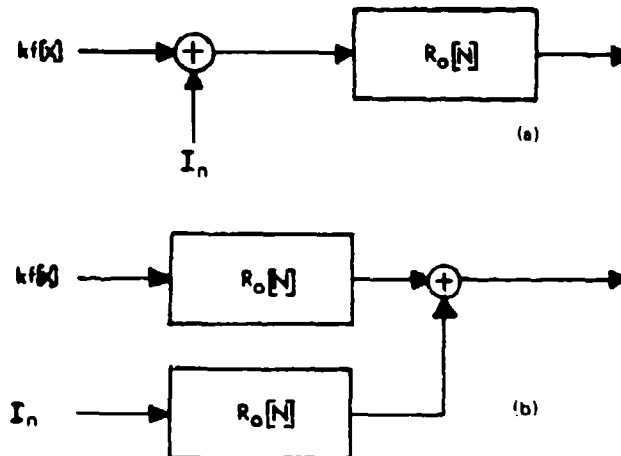


Fig. D-4 - (a) Aperture following a point of noise insertion and (b) functional diagram for analysis of (a)

The noise to be integrated has already been band-limited by the sensor to $N_{ex} = 1/\delta_{ex}$. This M.S. noise out of the integrator can then be approximated by

$$\begin{aligned} \text{M.S. Noise} &= \sigma^2 x_i^2 \int_0^\infty R_o^2(N) \left(\frac{\sin \pi N x_i}{\pi N x_i} \right)^2 dN \\ &= \sigma^2 x_i^2 [\delta_{ex}^2 + x_i^2]^{-1/2} \\ &= \frac{\sigma^2 [x_o^2 + \delta_{ex}^2]}{[x_o^2 + 2\delta_{ex}^2]^{1/2}} \end{aligned} \quad (D-38)$$

The signal is as was presented previously. Consequently, the two-dimensional SNR_D may be written as

$$\begin{aligned} \text{SNR}_D &= \frac{x_o y_o}{[(x_o^2 + \delta_{ex}^2)^{1/2} / (x_o^2 + 2\delta_{ex}^2)^{1/4}] \cdot [(y_o^2 + \delta_{ey}^2)^{1/2} / (y_o^2 + 2\delta_{ey}^2)^{1/4}]} \cdot \frac{\Delta \dot{n}' T_e}{(\dot{n}'_{av} T_e)^{1/2}} \\ &= \frac{(x_o y_o)^{1/2}}{\left[\left(1 + \frac{\delta_{ex}^2}{x_o^2} \right)^{1/2} + \left(1 + \frac{2\delta_{ex}^2}{x_o^2} \right)^{1/4} \right] \cdot \left[\left(1 + \frac{\delta_{ey}^2}{y_o^2} \right)^{1/2} + \left(1 + \frac{2\delta_{ey}^2}{y_o^2} \right)^{1/4} \right]} \cdot \frac{\Delta \dot{n}' T_e^{1/2}}{(\dot{n}'_{av})^{1/2}} \end{aligned} \quad (D-39)$$

Since this expression is cumbersome, it is convenient, as in the previous case, to compare the above SNR_D to the case where the displayed noise is white and to introduce factors to quantify the differences. Therefore, we define a bandwidth reduction factor Γ to quantify the SNR_D improvement occurring due to filtering of white noise by the sensor apertures. These factors are

$$\begin{aligned} \Gamma_x &= [(1 + \delta_{ex}^2/x_o^2)/(1 + 2\delta_{ex}^2/x_o^2)]^{1/2} \\ \Gamma_y &= [(1 + \delta_{ey}^2/y_o^2)/(1 + 2\delta_{ey}^2/y_o^2)]^{1/2} \end{aligned} \quad (D-40)$$

APPENDIX D

Using these factors and the noise increase factors of Eq. (D-35) the SNR_D becomes

$$SNR_D = \frac{(x_o y_o)^{1/2}}{(\xi_x \xi_y \Gamma_x \Gamma_y)^{1/2}} \frac{\Delta \dot{n}'(T_e)^{1/2}}{(\dot{n}'_{av})^{1/2}}. \quad (D-41)$$

Γ is a function of x_o and has a maximum value of 1 when $x_o \gg \delta_{ex}$. When $x_o \ll \delta_{ex}$, Γ in the limit becomes $\sqrt{1/2}$. Thus Γ can often be ignored in first-order calculations. It should be noted that while ξ , the noise increase factor is always ≥ 1 , Γ , the noise bandwidth reduction factor is always ≤ 1 but the product $\Gamma\xi$ is always ≥ 1 . Hence, the effect of an aperture following a point of noise insertion is to increase the noise but by an amount that is smaller than if the aperture preceded the point of noise insertion.

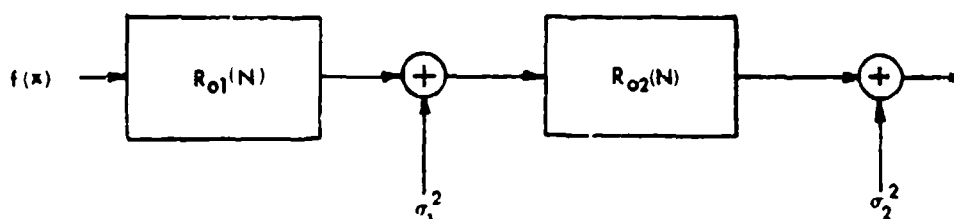


Fig. D-5 — Aperture $R_{01}(N)$ precedes noise source 1 and aperture $R_{02}(N)$ which follows noise source 1 and precedes noise source 2

To complete the discussion of aperiodic object discussion, we consider the case of two system apertures; one preceding a point of noise insertion followed by a second aperture which is followed in turn by a second point of noise insertion as shown schematically in Fig. D-5. When multiple noise sources are involved, they are not usually related to \dot{n}_{av} alone. Hence, the following will be presented in terms of two noise spectral densities σ_1 and σ_2 referred to the input so that sensor gain parameters can be ignored. If the two apertures of Fig. D-5 did not exist, the two noise sources would add in quadrature and

$$\sigma = [\sigma_1^2 + \sigma_2^2]^{1/2}. \quad (D-42)$$

If the constant amplitude input signal with duration x_o were used and both noise sources were white, then the perceived mean square noise would be simply

$$\text{M.S. Noise} = [\sigma_1^2 + \sigma_2^2] T_e x_o. \quad (D-43)$$

but both apertures increase the noise integration distance. Since the apertures are in series and are independent, the noise increase factor can be calculated from the combined transfer function and

$$\xi_r = \left[1 + \left(\frac{\delta_{e1}}{x_o} \right)^2 + \left(\frac{\delta_{e2}}{x_o} \right)^2 \right]^{1/2}. \quad (D-44)$$

where δ_{e1} and δ_{e2} are the noise equivalent apertures of $R_{01}(N)$ and $R_{02}(N)$, respectively. Since the first noise source precedes the second aperture, it must be corrected for noise bandwidth reduction due to the second aperture. Γ can be determined by considering the image at the input to $R_{02}(N)$ to be of width $(\delta_{e1}^2 + x_o^2)^{1/2}$ and by use of Eq. D-41,

$$\Gamma_x = \left\{ \left[\frac{1 + \delta_{e2x}^2 / (\delta_{e1x}^2 + x_o^2)}{1 + 2\delta_{e2x}^2 / (\delta_{e1x}^2 + x_o^2)} \right] \right\}^{1/2} \\ = \left[\left(1 + \frac{\delta_{e1x}^2}{x_o^2} + \frac{\delta_{e2x}^2}{x_o^2} \right) \cdot \left(1 + \frac{\delta_{e1x}^2}{x_o^2} + 2 \frac{\delta_{e2x}^2}{x_o^2} \right) \right]^{1/2} \quad (D-45)$$

and the noise becomes

$$\text{M.S. Noise} = [\sigma_x^2 \Gamma_x \Gamma_y + \sigma_y^2] t_p x_o y_o \xi_x \xi_y \quad (D-46)$$

and the SNR_D is written as

$$\text{SNR}_D = \frac{(x_o y_o)^{1/2} \Delta \dot{n}' T_e^{1/2}}{[\xi_x \xi_y]^{1/2} [\sigma_x^2 \Gamma_x \Gamma_y + \sigma_y^2]^{1/2}} \quad (D-47)$$

Before proceeding, initial experimental efforts to confirm the theory will be presented.

D4. PSYCHOPHYSICAL EXPERIMENTATION – APERIODIC IMAGES

The theory for the elementary case where the input image is large with respect to the sensor's noise equivalent aperture has been experimentally verified and the equations presented herein are consistent with the elementary theory. The psychophysical experiments reported herein are concerned with the case where the input image width becomes small with respect to the sensory systems noise equivalent aperture, δ_e . The results obtained are in general consonance with the theory but some differences are noted which are probably due to secondary observer effects which have not yet been included in the overall model. The primary parameter tested was the noise increase factor ξ since the bandwidth increase factor Γ has a weak dependence which would be difficult to test at best and has been bounded by the analysis.

The experimental setup for the television camera generated images is shown in Fig. D-6. The test images consisted of a series of a well spaced, vertically oriented white bars against a black background. The individual bars were of constant height but of varying widths and their widths are described in terms of their line number N , equal to Y (the picture height) divided by Δx (the bar width). These bars were projected onto the faceplate of a high resolution 1.5-in. vidicon operated at 25 frames/s with 875 scan lines (825 active) interlaced 2:1 and at abroad area video SNR of 50:1 or more. The display brightness was 1 ft-Lambert and the displayed picture height was 8 in. located 28 in. from the observer's eye. Both signals and noises were passed through identical low pass filters of 12.5 MHz bandwidth which have negligible effect on the results reported here. White noise of Gaussian distribution was linearly added to the signals prior to display.

The overall sensor MTF was varied by defocusing the lens with the results shown in Fig. D-7. Since neither of these curves approach a Gaussian (for which the approximations for the theory hold), some experimental deviations from the theory could be expected. The noise equivalent passbands of the lens and camera are indicated in Table D-1. In the measurement, the camera N_{eC} was calculated from a measured MTF curve as was that of the overall sensory system (N_{eT}). The lens N_{eL} was calculated from the relation $N_{eL} = [N_{eC}^2 N_{eT}^2 / (N_{eC}^2 - N_{eT}^2)]^{1/2}$ to show the degree of defocus necessary. The quantity $\Delta \theta_T$ is the angular subtense of δ_{eT} relative to the observer's eye.

APPENDIX D

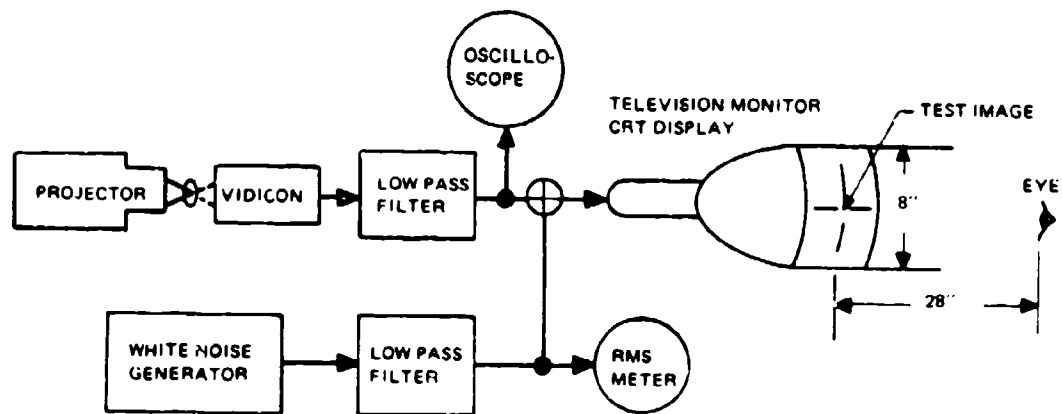


Fig D-6 — Experimental setup for the television camera generated imagery

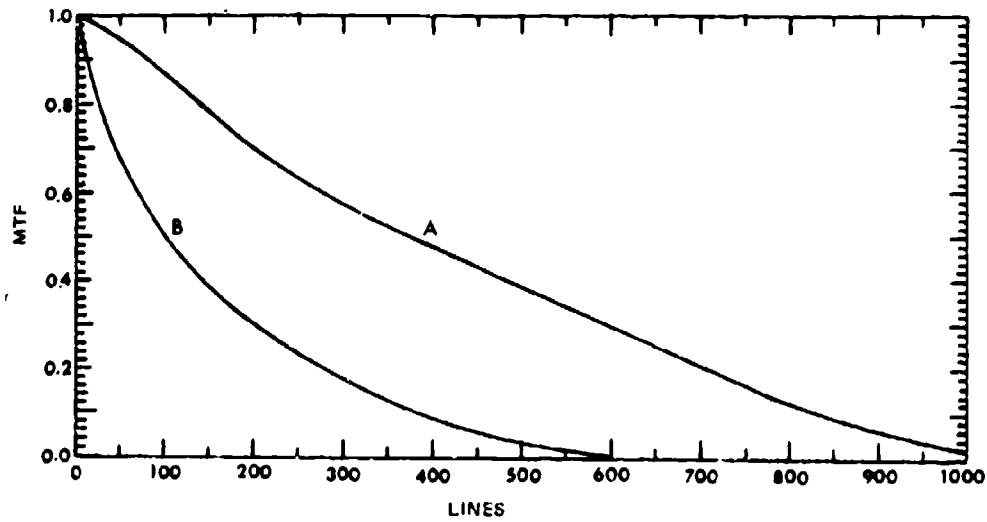


Fig. D-7 — Modulation transfer functions for Cases A and B

Table D-1 — Sensory System Characteristics

Case	Lens N_{eL} (Lines/Pt Ht)	Camera N_{eC} (Lines/Pt Ht)	System N_{eT} (Lines/Pt Ht)	$\Delta\theta_T$ (mrad)
A	1266	261	256	1.11
B	123	261	69	4.14

The line numbers of the bars used are summarized in Table D-2. The angular subtense of each bar was 20.6 mrad in the vertical and variable in the horizontal (relative to the observer's eye). $\Delta\theta_b$ represents the angular subtense which would be observed with a unity MTF, while $\Delta\theta_e$ represents the noise effective width including the sensor's noise equivalent aperture.* When the display luminance is about 1 ft-Lambert, the noise equivalent aperture of the eye is about 1 mrad (D-5) and therefore should be included as a filter but would have very little effect on Case B and an almost uniform effect on Case A since it increases every $\Delta\theta$ except the largest by less than $\sqrt{2}$. Observe that in Case B, $\Delta\theta_e$ is very nearly a constant over the entire range of bar line numbers.

Table D-2 - Bar Number Summary

Bar Line No. (L/PH)	$\Delta\theta_b$ (mrad)	Case A $\Delta\theta_e$ (mrad)	Case B $\Delta\theta_e$ (mrad)	Bar Line No. (L/PH)	$\Delta\theta_b$ (mrad)	Case A $\Delta\theta_e$ (mrad)	Case B $\Delta\theta_e$ (mrad)
74	3.86	4.02	5.60	900	0.32	1.15	4.15
261	1.10	1.56	4.28	1090	0.26	1.14	4.15
357	0.80	1.37	4.22	1205	0.24	1.14	4.15
494	0.58	1.25	4.18	1605	0.18	1.12	4.14
625	0.46	1.20	4.17	1780	0.16	1.12	4.14
760	0.38	1.17	4.16				

In the experiment all of the bars were simultaneously imaged. The observer's task was to select the bar of highest line number which he could just barely discern as the bar image's SNR were randomly varied through increase or decrease of noise. For Case A, 6 observers were used to make 1730 trials while 5 observers made 1400 observations for Case B. To calculate the threshold SNR_D, we note that the photoelectron rate \dot{n}' is related to the signal current as measured in the video channel by

$$\dot{n}' = i/eA, \quad (D-48)$$

where e is the charge of an electron and A is the effective area of the photosurface. Using this equation, the elementary Eq. (D-3) may be written as

$$\text{SNR}_P = \left[T_c \frac{a}{A} \right]^{1/2} \frac{\Delta i}{[ei_{av}]^{1/2}}. \quad (D-49)$$

Next, we note that mean square shot noise has the form $I_n^2 = 2ei\Delta f_v$, where Δf_v is the video bandwidth. Then the above equation can be written as

$$\begin{aligned} \text{SNR}_P &= \left[T_c \frac{a}{A} \right]^{1/2} \frac{\Delta i}{I_n/(2\Delta f_v)^{1/2}} \\ &= \left[2T_c \Delta f_v \frac{a}{A} \right]^{1/2} \frac{\Delta i}{I_n} \\ &= \left[2T_c \Delta f_v \frac{a}{A} \right]^{1/2} \text{SNR}_{VD}. \end{aligned} \quad (D-50)$$

* $\Delta\theta_e = [\Delta\theta_b^2 + \Delta\theta_f^2]^{1/2}$

APPENDIX D

In the above equation, $\Delta i/I_n$ is the peak-to-peak signal to rms noise measured for a broad area image when the noise is white and SNR_{VO} is therefore the video signal-to-noise ratio. For convenience, we will let $A = \alpha Y^2$, where α is the picture aspect ratio ($H:V$) and Y is the picture height. We will also describe the bar dimensions in the forms $\Delta x \Delta y = \epsilon \Delta x^2$, where Δx is the bar width and ϵ is the ratio of bar length-to-width. Finally, we will note that

$$\frac{a}{A} = \frac{\Delta x \cdot \Delta y}{\alpha Y^2} = \frac{\epsilon \Delta x^2}{\alpha Y^2} = \frac{\epsilon}{\alpha N^2}, \quad (\text{D-51})$$

where $N = Y/\Delta x$. Now, Eq. (D-50) may be written as

$$\text{SNR}_D = \left[\frac{2T_e \epsilon \Delta f_v}{\alpha} \right]^{1/2} \frac{1}{N} \text{SNR}_{VO}. \quad (\text{D-52})$$

The effect of an aperture is to increase the noise. Using the formulation of Eq. (D-37), we note this fact by modifying the above equation to read

$$\text{SNR}_D = \left[\frac{2T_e \epsilon \Delta f_v}{\alpha} \right]^{1/2} \frac{1}{N \xi_x(N)^{1/2}} \text{SNR}_{VO}. \quad (\text{D-53})$$

We observe that the aperture also increases perceived noise along the length of the bar, but this effect is negligible compared to the increase across the bar widths. The noise increase factor is given by

$$\xi_x(N) = [1 + (N/N_{eT})^2]^{1/2}. \quad (\text{D-54})$$

Since ξ is the primary new parameter in this experiment, its value is presented in Fig. D-8. It is a significant factor for both cases and in Case A, adding the effect of the eye MTF would have small effect.

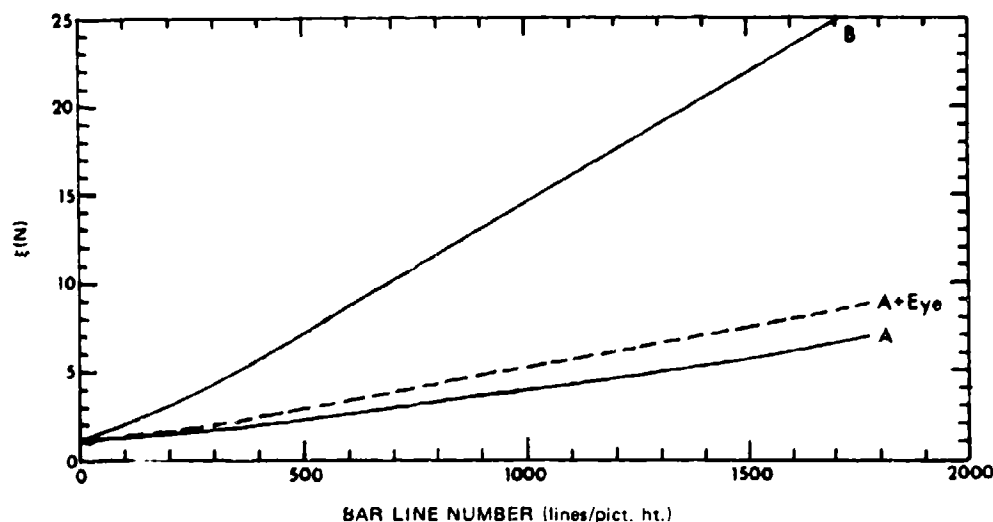


Fig. D-8 — Noise increase factor for Cases A and B. Dashed curves for Case A includes the noise increase due to the eye MTF

The results of the experiment are shown in Fig. D-9. According to the theory, the SNR_{DT} , as calculated using Eq. (D-53) and the measured SNR_{VO} , should be a constant over all line numbers. This is nearly true for Case A except at the lowest line number. For Case B, the SNR_{DT} appears consistent with that of Case A up to about bar line numbers of 500 to 700 lines/picture height, but linearly increases with bar number thereafter. The increase at very low line numbers has been previously noted and while the cause is unknown, the result was not unexpected. The theory appears valid for Case A over a wide range of line numbers but does not completely account for Case B. One possible explanation is the difference in displayed image amplitude which is plotted in Fig. D-10 for the two cases. The noise equivalent pulse

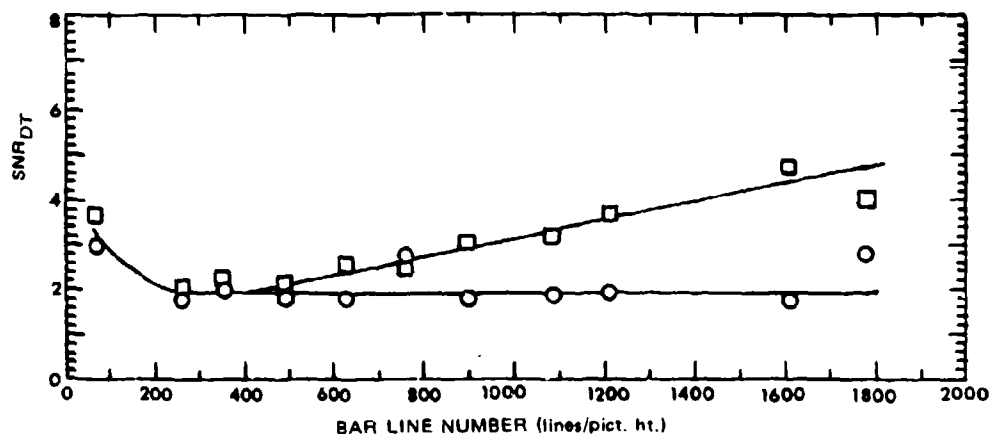


Fig. D-9 — Threshold perceived signal-to-noise ratio vs spatial frequency for \circ Case A and \square Case B MTFs

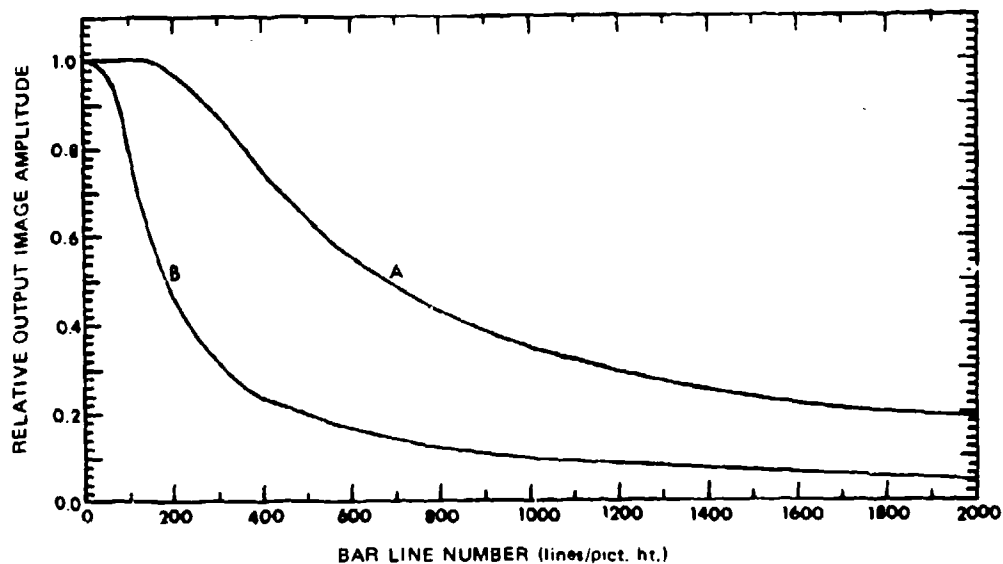


Fig. D-10 — Relative output image amplitude vs bar line number for Case A and B MTFs

APPENDIX D

shapes at $N = 2000$ is shown in Fig. D-11. In Case B, the image amplitude, and hence the image contrast is a factor of 3.65 lower. In the sensor system model, we have ignored the possibility of a photoconversion noise in the observer's retina which surely must exist. When video gain is insufficient, images of small amplitude (or incremental luminance) may become perception limited by retinal photoconversion noise component and this effect may account for the departure from theory noted in Case B. In summary, the theory appears to be valid but the range of validity needs further investigation and other effects apparently must be taken into account.

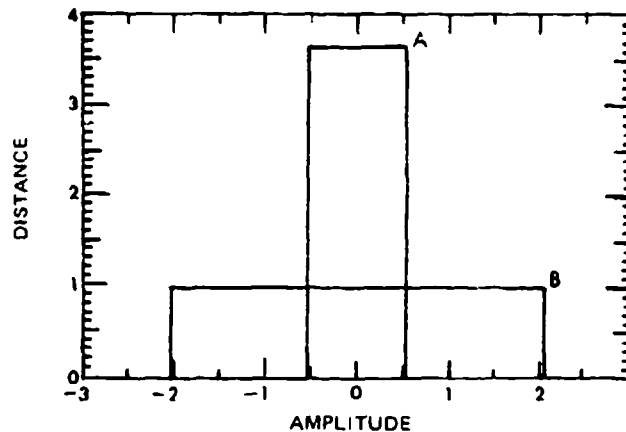


Fig. D-11 -- Noise equivalent output pulse amplitude vs distance for Case A and B MTFs at bar line number 2000

D5. THE EFFECT OF APERTURES ON PERIODIC BAR PATTERN PERCEPTION

A periodic bar pattern consists of an alternating series of black and white bars as shown in Fig. D-1. In practice, the number of black and white bars used is usually 5 to 11 but the number should be much larger to approach true periodicity. It is well known that if the input image to a linear system is periodic, the displayed image will also be periodic. It is postulated that to perceive the presence of a bar pattern that the observer must make the decision on the basis of resolving a single bar. Thus the problem becomes one of calculating the perceived SNR based upon a single bar. Again, it is assumed that the observer functions as a spatial and temporal integrator and makes a detection decision when the SNR_p exceeds a threshold value. The effect of a sensor aperture is to smear periodic images as in the aperiodic case, but one noticeable difference is that adjacent bars may become blurred into one another. At very low spatial frequencies, the effect of an aperture may be only one of slightly rounding the edges of the input square wave train while at high spatial frequencies, the displayed waveform will be sinusoidal as shown in Fig. D-12.

There are at least two plausible methods of calculating the SNR_p . One method is to assume the image runs from trough-to-trough of the periodic image in which case the width will vary from $1/N$ to $2/N$ as the spatial frequency of the pattern increases. Alternatively, it can be considered to be the 50% width which is equal to $1/N$. The second method is suggested by O. Schade and will be used herein but the first method will be discussed for the purpose of giving perspective.

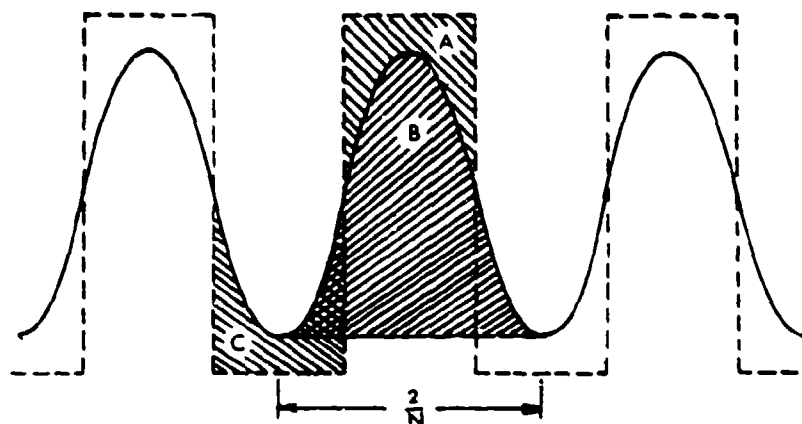


Fig. D-12 — Waveform diagram for periodic waves. Dashed line is input waveform; solid line is output waveform

In the first case, the signal is the integral from trough-to-trough and will be the Area B in Fig. D-12. Observe that Area A = Area C, and Area B equals the output peak-to-peak value, or $g(x)_{p-p}$, times the duration $1/N$. That is,

$$\text{Integrated Signal} = \text{Area B} = \frac{g(x)_{p-p}}{N} \quad (\text{D-55})$$

$g(x)_{p-p}$ is often referred to as the square wave amplitude response $R_{SQ}(N)$ and is related to the MTF or $R_o(N)$ by

$$R_{SQ}(N) = \frac{4}{\pi} \sum_{k=1}^{\infty} \frac{(-1)^{k-1}}{2k-1} R_o[(2k-1)N] \quad (\text{D-56})$$

which is equal to $(4/\pi)R_o(N)$ when $N \geq N_c/3$. Here, N_c is the "cutoff" frequency where $R_o(N)$ becomes zero. The noise integration distance will vary from $1/N$ at very low spatial frequencies to $2/N$ when $N \geq N_c/3$. Actually the very low spatial frequencies are not usually of much interest, and $2/N$ is a useful approximation for the integration distance. The above method is of interest because it is a straightforward extension of the aperiodic theory and it relates directly to the square wave amplitude response (which is most often measured). The answers obtained will not be far different than will be obtained using the preferred method below particularly if the thresholds are measured and specified using the parameters of the square wave train.

The accepted method considers the signal and noise duration to remain constant and equal to a bar width, $1/N$. The integrated signal then becomes the difference between the flux integrated over the area of the bar and that obtained by integrating an immediately adjacent area (background) of equal duration. This assumption leads directly to the concept of the square wave flux response function $R_{sf}(N)$ which represents the peak-to-peak amplitude of an equivalent square wave function which would have the same integral difference as the actual signal. To derive $R_{sf}(N)$, each term of the square wave transfer function is integrated for a duration $1/N$. Since the square wave transfer function has only odd harmonics of the input spatial frequency, each odd harmonic adds twice the integral of $1/2$ cycle to the total integral difference. The value of twice the integral of $1/2$ cycle of frequency ν in lines is $2/\pi$ times the

APPENDIX D

peak-to-peak value times the half period $(\nu)^{-1}$. As a result, the square wave flux transfer function can be written as

$$R_{sf}(N) = \frac{8}{\pi^2} \sum_{k=1}^{\infty} \frac{R_o[(2k-1)N]}{(2k-1)^2} \quad (D-57)$$

and $R_{sf}(N) = (8/\pi^2) R_o(N)$ for $N \geq N_c/3$. The above function can then be used to predict the integrated signal compared to an equal neighboring area over a duration of $1/N$. If the peak-to-peak signal is $\Delta \dot{n}'$, the perceived signal for the one-dimensional case with bars of constant height is given by

$$\text{Signal} = \frac{R_{sf}(N)}{N} \Delta \dot{n}' T_e \quad (D-58)$$

The noise integration distance used in this method is constant and equal to N^{-1} . If the noise is white at the input to the integrator, which is the observer, we can refer to the aperiodic image discussion of an integrator and write the noise expression as

$$\text{M.S. Noise} = \frac{\sigma^2}{N} = \frac{\dot{n}_{av}' T_e}{N} \quad (D-59)$$

Consequently, the SNR_D for the simplest one-dimensional case becomes

$$\text{SNR}_D = \frac{R_{sf}(N)}{N^{1/2}} \frac{\Delta \dot{n}' (T_e)^{1/2}}{\dot{n}_{av}'^{1/2}} \quad (D-60)$$

Extending this expression to the two-dimensional case with bars of length y_o , we find that

$$\text{SNR}_D = R_{sf}(N) \left(\frac{y_o}{\xi_y N} \right)^{1/2} \frac{\Delta \dot{n}' T_e^{1/2}}{\dot{n}_{av}'^{1/2}} \quad (D-61)$$

The bars are aperiodic in the y direction and therefore we introduce the noise increase factor ξ_y as previously discussed. The bar length y_o can be written as ϵ/N as described in connection with Eq. (D-51) and then

$$\text{SNR}_D = \frac{R_{sf}(N)}{N \xi_y^{1/2}} \frac{\Delta \dot{n}' (\epsilon T_e)^{1/2}}{(\dot{n}_{av}')^{1/2}} \quad (D-62)$$

and as can be seen, SNR_D is proportional to N^{-1} at low spatial frequencies for bar charts when ϵ is a constant.

In the aperiodic case, the sensor apertures have no effect on the perceived signal but the perceived noise does increase due to image blurring and the resulting increase in the observer's integration distance. Also, the apertures can band-limit and, therefore, reduce the effect of the noise. In the periodic image case, the image size does not increase due to apertures so there is no noise increase factor ξ . Instead, the integrated signal is reduced rather than being maintained at a constant level. While the sensor apertures do not increase noise in the periodic case, the apertures can band-limit the noise so there will be a factor similar to Γ .

When white noise is filtered by the sensor apertures as in Fig. D-4, the mean square noise is

$$\text{M.S. Noise} = \sigma^2 \int_0^{\infty} R_o^2(\nu) R_f^2(\nu/N) d\nu \quad (D-63)$$

where ν is introduced as a dummy spatial frequency variable since the integration is keyed to the duration which is now N . There is no generality lost in assuming white noise as an input since an equivalent system model can be constructed for any colored noise by adding dummy transfer functions to shape the noise spectrum. As before $R_o(\nu)$ is the sensor MTF and $R_I(\nu/N)$ represents the integrator. When the aperture has very little effect on the noise, $R_o(N) \approx 1$ and $\int_0^\infty R_I^2(\nu) dN = 1/N$ which agrees with Eq. (D-59). It is convenient to separate $R_I(\nu/N)$ into gain and bandwidth terms as was done originally, i.e.,

$$R_I(\nu/N) = \frac{1}{N} \cdot \frac{\sin(\pi\nu/2N)}{(\pi\nu/2N)} \quad (D-64)$$

Then,

$$\text{M.S. Noise} = \frac{\dot{n}_{av}' T_c}{N^2} \int_0^\infty R_o^2(\nu) \left[\frac{\sin(\pi\nu/2N)}{(\pi\nu/2N)} \right]^2 d\nu \quad (D-65)$$

and for the general two-dimensional case

$$\text{SNR}_P = \frac{R_{sf}(N)}{N(\Gamma, \xi_v)^{1/2}} \cdot \frac{\epsilon^{1/2}}{\left[\int_0^\infty R_o^2(\nu) \left[\frac{\sin(\pi\nu/2N)}{(\pi\nu/2N)} \right]^2 d\nu \right]^{1/2}} \frac{\Delta \dot{n}' T_c^{1/2}}{(\dot{n}_{av}')^{1/2}} \quad (D-66)$$

in analogy with Eq. (D-62). As in the aperiodic case, it is convenient to introduce a *bandwidth reduction term* $\beta(N)$ which relates the decrease in integrated noise that occurs due to filtering. For the unfiltered case, the noise bandwidth is N and for the filtered cases it is as given by Eq. (D-63) and

$$\beta(N) = \frac{\int_0^\infty R_o^2(\nu) \left[\frac{\sin(\pi\nu/2N)}{(\pi\nu/2N)} \right]^2 d\nu}{N} \quad (D-67)$$

whence Eq. (D-66) becomes

$$\text{SNR}_D = \frac{R_{sf}(N)}{N(\Gamma, \xi, \beta_r)^{1/2}} \frac{\Delta \dot{n}' (\epsilon T_c)^{1/2}}{(\dot{n}_{av}')^{1/2}} \quad (D-68)$$

A Gaussian approximation for $\beta(N)$ is given by

$$\beta(N) = 1/[1 + (N/N_c)^2]^{1/2}, \quad (D-69)$$

and an alternative approximation which is often used (D-6) is based on the notion that the integrator limits the region of integration to N so that

$$\beta(N) = \frac{\int_0^N R_o^2(N) dN}{N} \quad (D-70)$$

In general, $\beta(N)$ has a stronger effect than $\Gamma(N)$, the bandwidth reduction factor for the aperiodic case but even so, the effect is not large except at high line numbers.

D6. PSYCHOPHYSICAL EXPERIMENTATION - PERIODIC IMAGES

The mathematical model developed herein has been extensively used to predict the threshold resolution vs input image irradiance level or input photocurrent characteristic of a wide variety of imaging sensors. As will be seen, the predicted performance closely correlates with

APPENDIX D

that measured. To show the prediction method, we start with Eqs. (D-49) and (D-51) of the aperiodic case which give

$$\text{SNR}_D = \left[\frac{T_e \epsilon}{\alpha} \right]^{1/2} \frac{1}{N} \frac{\Delta i}{[e i_{av}]^{1/2}}. \quad (\text{D-71})$$

Following the discussion of section D5, we modify the above equation for the periodic case as follows:

$$\text{SNR}_D = \left[\frac{T_e \epsilon}{\alpha} \right]^{1/2} \frac{R_{sf}(N)}{N} \frac{\Delta i}{[e \beta_x(N) \xi_v(N) \Gamma_v(N) i_{av}]^{1/2}}. \quad (\text{D-72})$$

If the bars are long with respect to their width, ξ_v and Γ_v can be neglected and by use of the contrast definition $C_l = \Delta i / i_h = (i_h - i_o) / i_h$, we may write

$$\text{SNR}_D = \left[\frac{T_e \epsilon}{\alpha} \right]^{1/2} \frac{R_{sf}(N)}{N} \frac{C_l i_h^{1/2}}{\left[\left(\frac{2 - C_l}{2} \right) e \beta_x(N) \right]^{1/2}}. \quad (\text{D-73})$$

where note is made of the fact that $i_{ave} = [(2 - C_l)/2] i_h$, where i_h is the input photocurrent due to the "bright" bars in the bar pattern. Sensor gains and other sources of noise such as preamp noise can also be included in the above expression (D-72) but with low-light-level television cameras with very high prestorage gain, the above equation applies to a very good approximation.

In a particular LLLTV camera design the square wave flux factor $R_{sf}(N)$ and noise bandwidth reduction terms were estimated to be as shown in Fig. D-13. These were obtained by measuring the square wave amplitude response, and by mathematically calculating the MTF, $R_{sf}(N)$, and $\beta(N)$. Note that two sets of curves are shown. The TV camera in use employs horizontal aperture correction which is an electronic boost of midfrequency spatial frequencies. The boost has a peak response of about 2.5 at 400 lines/picture height and is unity at 0 and 800 lines. The square wave amplitude response with boost is shown in Fig. D-14. The effect of the aperture correction is to both improve the sensor MTF and to decrease the noise bandwidth reduction, i.e., the noise increases. The preamp noise which precedes the aperture corrector is also increased by a considerable amount but when the sensor is operated at maximum gain, it can still be neglected except at the lowest light levels. In Fig. D-15, we show the SNR_D calculation normalized to the contrast function noted for the uncompensated case. Also shown is the threshold SNR_{DT} for an input image of unity contrast. The decrease in threshold with increase in spatial frequency is an experimentally noted effect (D-4). The intersection of the SNR_D with the SNR_{DT} curves give the threshold resolution vs highlight input photocurrent characteristic shown in Fig. D-16 as the dot-dash curve.

The predicted curve with aperture correction is shown as the dashed line and the measured curve with correction is shown as the solid line and is seen to agree quite closely with the predicted curve except at the lowest and the highest photocurrents. At low photocurrents, the departure is due to the neglect of preamp noise while at high photocurrents, the difference is attributed to a lack of precision in measuring the sensor's square wave amplitude response at the higher line numbers.

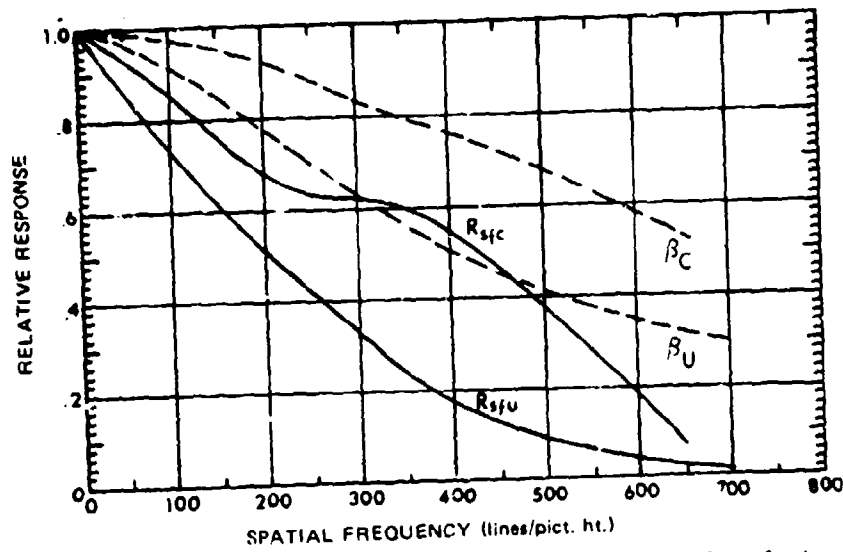


Fig. D-13 — Square wave flux response and noise bandwidth reduction factor for the (U) Uncompensated and (C) Compensated 25/25/27 mm I-Zoom ERSICON

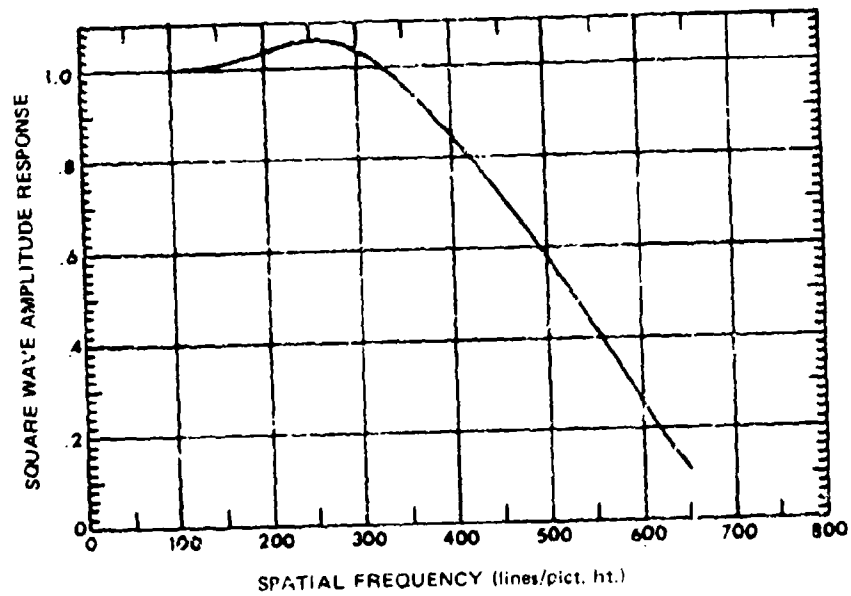


Fig. D-14 — Square wave amplitude response for the I-Zoom BSICON with horizontal aperture compensation

APPENDIX D

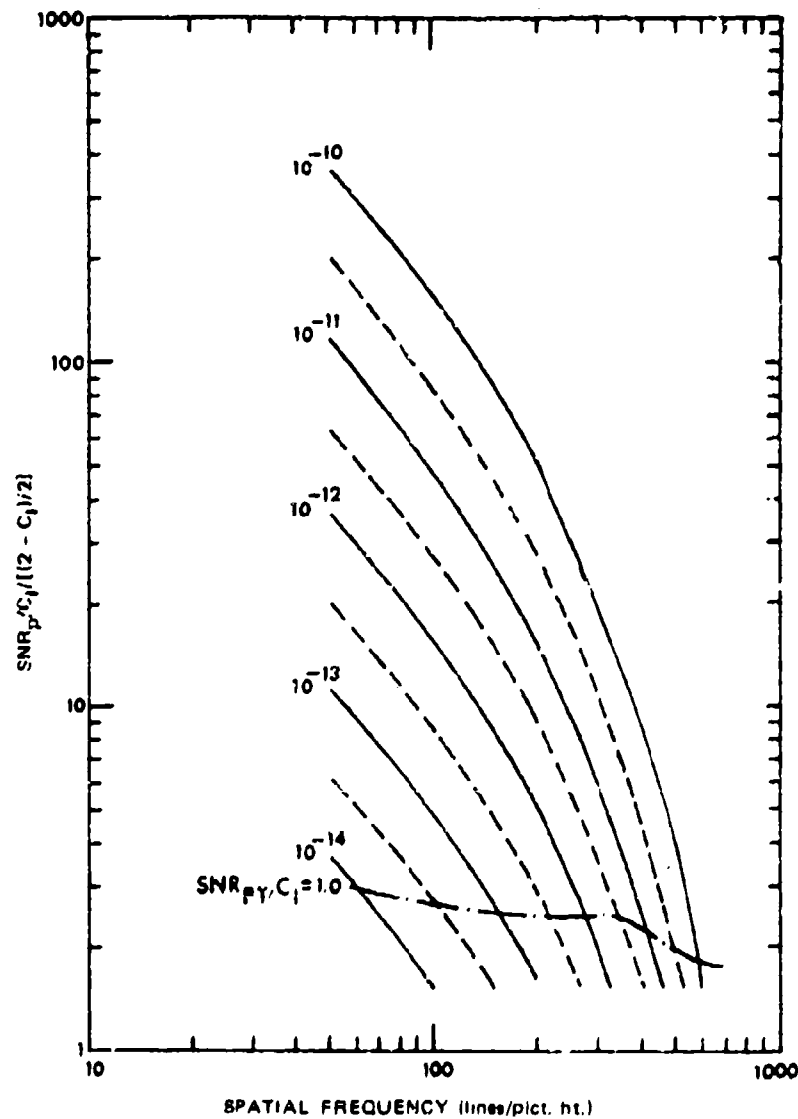


Fig. D-15 — SNR_p vs spatial frequency for the uncompensated 1-Zoom EBSICON. Also shown is the observer's threshold SNR_{PT} for $C_i = 1.0$. Dashed lines are 10 lower in photocurrent than solid curve directly above

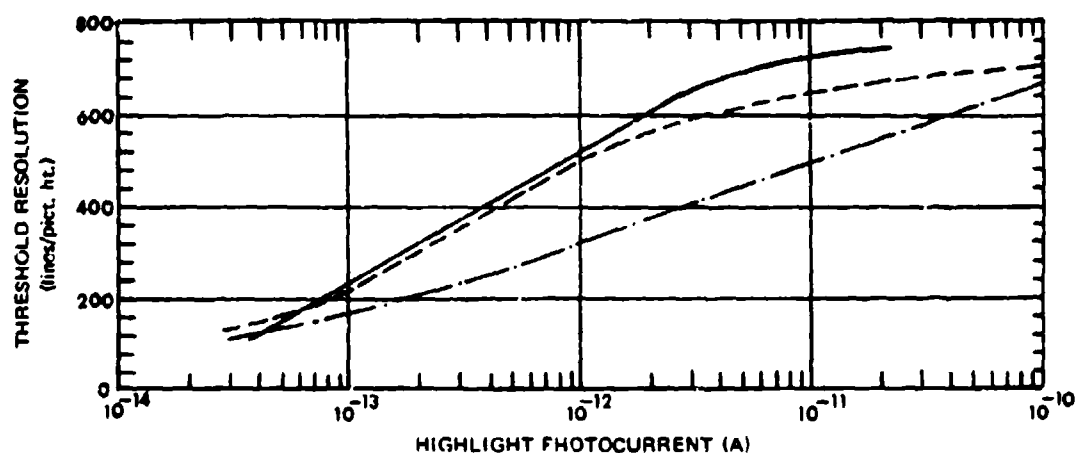


Fig. D-16 — Threshold resolution vs highlight photocurrent for the I-Zoom EBSICON, (—) measured, (---) calculated with aperture correction, and (- · -) calculated without aperture correction

REFERENCES

- D-1 R.L. Sendall and F.A. Rosell, E/O Sensor Performance Analysis and Synthesis (TV/IR Comparison Study), Air Force Avionics Laboratory Report No. AFAL-TR-72-374, April 1973.
- D-2 F.A. Rosell and R.H. Willson, Psychophysical Experiments and the Display — SNK Concept, Chapt. 5, Perception of Displayed Information, Edited by L. M. Biberman, Plenum Press (1973): 167-232.
- D-3 J.W. Goodman, Introduction to Fourier Optics, Chapt. 1, McGraw Hill (1968).
- D-4 H.L. Snyder, Image Quality and Observer Performance, Chapt. 3, Perception of Displayed Information (Edited by L. M. Biberman), Plenum Press (1973): 87-118.
- D-5 O.H. Schade, Sr., Optical and Photoelectric Analog of the Eye, *J. Opt. Soc. Am.* **46**(9): 726.
- D-6 O.H. Schade, Sr., The Resolving Power Functions and Quantum Processes of Television Cameras, *RCA Review* **28**(3): 460-535.
- D-7 F.A. Rosell, E.L. Svensson, and R.H. Willson, Performance of the Intensified Electron-Bombarded Silicon Camera Tube in Low-Light-Level Television Systems, *Applied Optics*, **2**, May 1972: 1058-1067.

Appendix E

THE COLTMAN AND ANDERSON EXPERIMENT

F.A. Rosell

The Coltman and Anderson experiment (Ref. E-1) is often cited to prove that the eye uses up to 14 lines in the process of detecting a bar pattern. This conclusion is believed to be an error in interpretation as will be discussed. It is our view that the eye integrates along the length of the bar and that only one bar is used by the observer in discerning the bar pattern. Coltman and Anderson derived Eq. (E-1) below through a thought argument combined with a psychophysical experiment in order to obtain a necessary constant. Their equation is

$$N_w = 615 \sqrt{\Delta f_v} \text{ SNR}_{\text{vrms}} \quad (\text{E-1})$$

where N_w is the threshold resolution in line pairs per picture width, Δf_v is the video bandwidth in MHz, and SNR_{vrms} is the rms threshold video SNR.

In our formulation,

$$N = \left[\frac{T_e \epsilon \Delta f_v}{\alpha} \right]^{1/2} \frac{\text{SNR}_{\text{VO}}}{\text{SNR}_{\text{DT}}} \quad (\text{E-2})$$

where N is the threshold resolution in lines per picture height, T_e is the observers integration time, ϵ is the picture aspect ratio, Δf_v is the video bandwidth in Hz, SNR_{VO} is the broad area image peak-to-peak to rms noise ratio, and SNR_{DT} is the threshold SNR_D. The purpose of the following analysis is to determine whether Eq. (E-2) matches that of the Coltman and Anderson equation, Eq. (E-1). To do this, it is necessary to convert units. Since Coltman and Andersons bandwidth is in MHz rather than Hertz,

$$\Delta f_v = \Delta f_v \cdot 10^6 \quad (\text{E-3})$$

and they use rms signal to rms noise rather than peak-to-peak signal to rms noise,

$$\text{SNR}_{\text{VO}} = \sqrt{8} \text{ SNR}_{\text{vrms}} \quad (\text{E-4})$$

and then spatial frequency is in line pairs per picture width rather than lines per picture height, so that

$$N_w = \frac{\alpha N}{2} \quad (\text{E-5})$$

Inserting these changes into Eq. (E-2),

$$N_w = \frac{1}{2} [8 \cdot 10^6 \alpha T_e \epsilon \Delta f_v]^{1/2} \frac{\text{SNR}_{\text{vrms}}}{\text{SNR}_{\text{DT}}} \quad (\text{E-6})$$

With $\alpha = 4/3$, $T_e = 0.1$ s, $\epsilon = 14$, and $\text{SNR}_{\text{DT}} = 3.0$,

$$N_w = 644 \sqrt{\Delta f_v} \text{ SNR} \quad (\text{E-7})$$

which is only 5% different from Coltman and Anderson's experimentally derived value. The length-to-width ratio of 14 used is an approximation since the actual value used is unknown. However, it is not critical as can be inferred from the discussion below.

APPENDIX E

Coltman and Anderson did not take the bar aspect ratio into account but only stipulated that bar length should be large relative to its width.

To show the impact of reducing the number of bars available to the observer, Coltman and Anderson devised the experiment shown in Fig. E-1. The displayed pattern "was left fixed and a series of cardboard apertures were employed to vary the number of lines seen by the observer." The mask was presumably of square aspect ratio. The results, as shown in Fig. E-1, "show that the observer probably uses no more than seven line pairs in making an identification. As the number which he is permitted to see is decreased, the signal required rises rapidly being greater by a factor of four when only one line pair is presented."

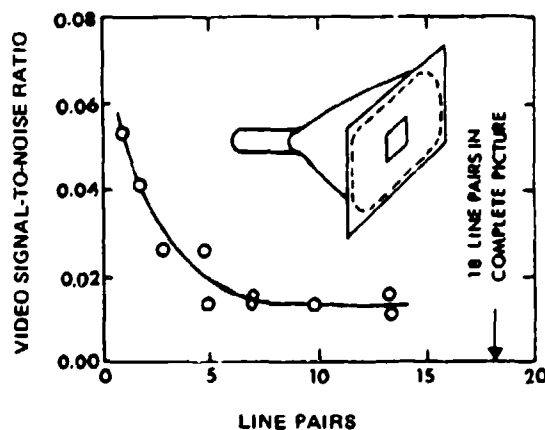


Fig. E-1 — Video SNR required to detect pattern as a function of the number of line pairs visible through mask

Suppose that instead of the main effect of the cardboard aperture being one of reducing the number of bars, that the main effect was really one of reducing the bar length, or aspect ratio. If this latter interpretation were correct, then the SNR_v should decrease with increase in bar length as

$$SNR_v = \frac{N_w}{615 \sqrt{\Delta f_v} \times \epsilon/14} \quad (E-8)$$

With a mask of square aspect ratio, $\epsilon = 2$ times the number of line pairs seen through the mask. The $\epsilon/14$ term under the radical in Eq. (E-8) results from an assumption that the SNR_v thresholds were measured with bars of 14:1 aspect ratio. Using Eq. (E-7), we plot the threshold SNR_v in Fig. E-2 as a dashed curve. Also shown on this curve are the experimentally measured data points from Fig. E-1. It appears clear that the change in aspect ratio hypothesis is a reasonable interpretation of the measured results rather than the number of lines that are visible through the mask.

For the past two decades or more, threshold resolution measurements have been made by various television camera manufacturers. The number of bars used in the experiments are not reported showing a lack of concern for bar number. On the other hand, bar aspect ratio is not reported either. As is evident from Fig. E-2, the bar aspect ratio is not particularly significant

NRL REPORT 8311

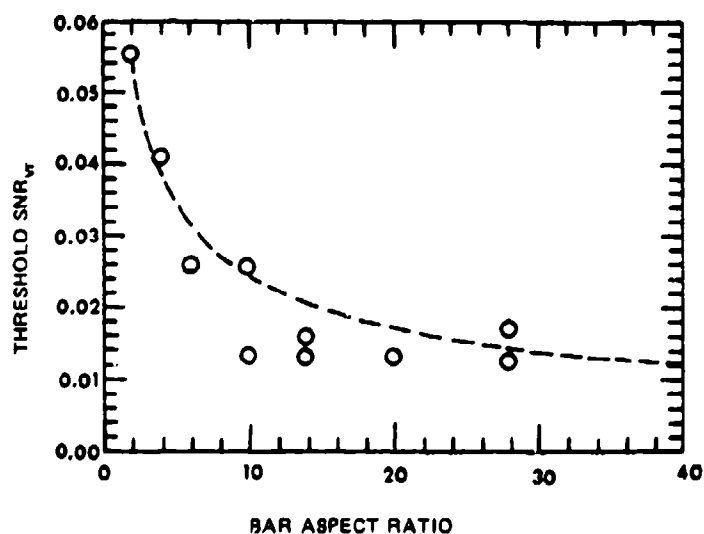


Fig. E-2 — Video SNR required to detect bar patterns interpreted as being a function of bar aspect ratio

if the ratio is above about 10:1. In the particular case of TIS, the bar pattern to be used has been specified to consist of four bars with each bar being of 7:1 aspect. In general, more bars would be desired in order to avoid transient end effects but the temperature variant bar patterns are difficult to construct at best.

REFERENCE

- E-1 Coltman, J.W., and Anderson, A.E., Noise Limitations to Resolving Power in Electronic Imaging, *Proc. IRE*, 48(5), 1960.

Appendix F BASIC SNR AND DETECTIVITY RELATIONS

F. A. Rosell

A. INTRODUCTION

In this appendix, a number of basic relations will be derived and discussed. These include the relation between the display SNR_D and the video SNR_{VO} , the channel SNR_{CO} and the detector's detectivity, the detectors responsivity and detectivity, and various detector parameters such as cold shielding. This appendix is written in part to increase the reader's understanding of the basic sensor parameters, but certain equations such as those relating detector responsivity and detectivity are required when multiple noise sources must be considered.

B. RELATIONSHIP BETWEEN SNR_D AND SNR_{VO} FOR TIS

In Chapter IV-B, it was stated that Eq. (4-8) which is repeated below

$$SNR_D = \left[2\Delta f_v T_r \left(\frac{a}{A} \right) \right]^{1/2} SNR_{VO} \quad (F-1)$$

holds for thermal imaging and television systems if A is interpreted as the total effective image plane area regardless of the total area of the detectors within that area. To find this result observe that the signal current from an array of $n_l n_p$ detectors of size $\delta_x \delta_y$ will be

$$i = n' e n_l n_p \delta_x \delta_y \quad (F-2)$$

regardless of the total scan area. By analogy to Eqs. (4-3), (4-7), and (4-8)

$$\begin{aligned} SNR_D &= \frac{[2\Delta f_v T_r a]^{1/2}}{[n_l n_p \delta_x \delta_y]^{1/2}} \frac{\Delta i}{[2eI_{dv} \Delta f_v]^{1/2}} \\ &= \frac{[2\Delta f_v T_r a]^{1/2}}{[n_l n_p \delta_x \delta_y]^{1/2}} SNR_{VO} \end{aligned} \quad (F-3)$$

The quantity in the denominator represents the total sensitive area of the detectors. However, this equation does not take into account the fact that the image plane area A is larger than the total detector area. The scanning required to image the entire area results in a loss of spatial integration by a factor of exactly $[(n_l n_p \delta_x \delta_y)/A]^{1/2}$ because scene photons are "raining" on portions of the image plane where the detectors are not always present at any instant of time. By including this spatial integration factor in Eq. (F-3), Eq. (F-1) results. If desired the above result can be interpreted as a loss of temporal integration within the sensor (but not in the eye which is unaware of the source the displayed imagery).

C. DETECTOR CHANNEL SNR_{CO}

The incremental signal current out of any given detector channel (which may contain n_l TDI elements) is equal to

APPENDIX F

$$\Delta i = S n_f \delta_x \delta_y \Delta E \eta_{sc}, \quad (F-4)$$

where S is the specific responsivity* of the detector(s) to the specific irradiance ΔE falling on the detector(s), n_f is the number of detectors in the scan direction, $\delta_x \delta_y$ are the detector dimensions, and η_{sc} is the scan efficiency defined as the ratio $(T_f - T_R)/T_f$, where T_f is the frame time and T_R is the time during each frame that the detectors are not viewing the scene. The rms noise current, I_{nc} is equal to

$$I_{nc} = (2e \Delta f_c i_{nc})^{1/2}, \quad (F-5)$$

where e is the charge of an electron, Δf_c is the bandwidth of each detector channel, and i_{nc} , for detectors sensitive to the longer infrared bandwidths, is primarily photoelectron noise and is usually of near constant magnitude. Numerically,

$$i_{nc} = S n_f \delta_x \delta_y E_B \eta_{sc}, \quad (F-6)$$

where E_B is taken to be the average value of the background irradiance which the detector views and to which it is sensitive. By use of Eqs. (F-4), (F-5), and (F-6), the channel signal-to-noise ratio for broad area objects which are unattenuated by sensor apertures is given by†

$$SNR_{CO} = \frac{S n_f \delta_x \delta_y \Delta E \eta_{sc}}{[2e S n_f \delta_x \delta_y E_B \eta_{sc} \Delta f_c]^{1/2}}. \quad (F-7)$$

If we set $SNR_{CO} = 1$ and solve for ΔE , the value of ΔE becomes ΔE_{min} , the minimum detectable irradiance which is equal to

$$\Delta E_{min} = \left[\frac{2e E_B \Delta f_c}{S n_f \delta_x \delta_y \eta_{sc}} \right]^{1/2}. \quad (F-8)$$

When the detector area, channel bandwidth, and scan efficiency are set equal to 1 cm^2 , 1 Hz , and 1 , respectively, ΔE_{min} is defined as the detector's noise equivalent power or NEP^* . Thus,

$$NEP^* = \left[\frac{2e E_B}{S} \right]^{1/2}. \quad (F-9)$$

Now, Eq. (F-7) may be written as

$$SNR_{CO} = \frac{(n_f \delta_x \delta_y \eta_{sc})^{1/2} \Delta E}{(\Delta f_c)^{1/2} NEP^*}. \quad (F-10)$$

Detector sensitivity is usually specified in terms of its specific detectivity which is the inverse of NEP^* or

$$D^* = \frac{1}{NEP^*}. \quad (F-11)$$

*The specific responsivity is defined as: $S = \frac{\int_0^\infty S_\lambda E_\lambda d\lambda}{\int_0^\infty E_\lambda d\lambda}$, where S_λ is the spectral responsivity of the detector ($A/W - \mu m$) and E_λ is the detector irradiance ($W/cm^2 - \mu m$) due to a specific source such as a 300 K blackbody. Detectivity, to be defined, is most often given as an integrated value over wavelength for a specific source and to be precise, it should be designated as a specific detectivity when so given.

†Again, the subscript 0 used in connection with SNR_{CO} is used to indicate a broad area image which is unaffected by sensor apertures as in the case of the SNR_{FO} discussed in connection with Eq. (4-8).

with which, Eq. (F-10) becomes

$$\text{SNR}_{CO} = \frac{(\eta_l \delta_x \delta_y \eta_{sc})^{1/2} D^* \Delta E}{[\Delta f_c]^{1/2}} \quad (\text{F-12})$$

The incremental irradiance level ΔE can be related to the incremental scene radiance ΔL by the relation

$$\Delta E = \frac{\pi \eta_0 \Delta L}{4 f^2} \quad (\text{F-13})$$

where η_0 is the light gathering efficiency of the objective lens. For a Lambertian, or diffusely, emitting scene, we can write

$$\Delta L = \frac{1}{\pi} \frac{\delta}{\delta T} \left[\int_{\lambda_1}^{\lambda_2} M_\lambda(T) d\lambda \right] \Delta T \quad (\text{F-14})$$

which relates the incremental scene radiance to the incremental scene temperature differences ΔT . $M_\lambda(T)$ is the spectral radiant exitance of the scene. For a blackbody,

$$M_\lambda(T) = \frac{C_1}{\lambda^5} \frac{10^8}{(e^{C_2/\lambda T} - 1)} \quad (\text{F-15})$$

where $C_1 = 3.7412 \cdot 10^{-4} \text{ W} \mu^2$ and $C_2 = 14.388 \mu\text{K}$. For $\lambda T < 6200 \mu\text{K}$, the error will be less than 10% if we assume that

$$M_\lambda(T) = \frac{C_1 \cdot 10^8}{\lambda^5} e^{-(C_2/\lambda T)} \frac{W}{\text{cm}^2 \cdot \text{sr} \cdot \text{K}} \quad (\text{F-16})$$

For $\lambda T < 3100 \mu\text{K}$, the error in using Eq. (F-16) will be less than 1%. Integrating M_λ with respect to wavelength, we have

$$\int_{\lambda_1}^{\lambda_2} M_\lambda(T) d\lambda = \frac{C_1 \times 10^8 e^{-C_2/\lambda T}}{\lambda^4} \left[\frac{\lambda T}{C_2} + \frac{3(\lambda T)^2}{C_2^2} + \frac{6(\lambda T)^3}{C_2^3} + \frac{6(\lambda T)^4}{C_2^4} \right]_{\lambda_1}^{\lambda_2} \quad (\text{F-17})$$

and by inserting Eq. (F-17) in Eq. (4-28) and by performing the indicated integration we obtain

$$\begin{aligned} \Delta L &= \frac{\Delta T}{\pi} \left[\frac{C_1 \cdot 10^8 T^3 e^{-C_2/\lambda T} [C_2^4 + 4C_2^3 \lambda T + 12C_2^2 (\lambda T)^2 + 24C_2 (\lambda T)^3 + 24(\lambda T)^4]}{C_2^4 (\lambda T)^4} \right]_{\lambda_1}^{\lambda_2} \\ &= K_M \Delta T \end{aligned} \quad (\text{F-18})$$

Calculated values for K_M are provided in Table 4-1 of Chapter IV.

By combining Eqs. (F-12), (F-13), and (F-18), we have that

$$\text{SNR}_{CO} = \frac{\pi \eta_0}{4 f^2} \frac{(\eta_l \delta_x \delta_y \eta_{sc})^{1/2} D^* K_M \Delta T}{[\Delta f_c]^{1/2}} \quad (\text{F-19})$$

which is the Eq. (4-9) desired when a_j is substituted for $\delta_x \delta_y$.

APPENDIX F

D. DETECTIVITY

The fundamental measure of infrared detector sensitivity is detectivity as previously discussed. Detectivity is actually a signal-to-noise measure rather than a pure sensitivity measure as in the case of responsivity as discussed in connection with Eq. (F-4). When normalized to unit area and bandwidth, detectivity is primarily a function of the quantum efficiency of the detector material, the noise which may be generated either in the primary photon-to-electron conversion process, in the mechanics of the semiconductor process, or in external circuits such as the preamplifier. In the simplest case, the detector is primarily limited by fluctuation noise due to its photoconversion of background photons. When this is the case, the detector is said to be background limited and the detectivity is then sometimes written as D^*_{BLIP} .

The spectral detectivity of a BLIP photoconductive detector is given by

$$D^*_\lambda = \frac{\lambda}{2hc} \left[\frac{\eta_\lambda}{p_\lambda} \right]^{1/2} \quad (\text{photoconductive}), \quad (\text{F-20})$$

where h is Planck's constant, c is the velocity of light, λ is the radiation wavelength, η is the detector's spectral quantum efficiency, and p_λ is the rate at which scene image photons fall on the detector. For a photovoltaic detector, the detectivity is greater by $\sqrt{2}$ so that

$$D^*_\lambda = \frac{\lambda}{hc} \left[\frac{\eta_\lambda}{2p_\lambda} \right]^{1/2} \quad (\text{photovoltaic}). \quad (\text{F-21})$$

Observe that the quantum efficiency is given by

$$\eta_\lambda = S_\lambda \frac{hc}{\lambda}, \quad (\text{F-22})$$

and the photon arrival rate due to background is equal to

$$p_\lambda = E_{B\lambda} \cdot \frac{\lambda}{hc}. \quad (\text{F-23})$$

By insertion of Eqs. (F-22) and F-23) in Eq. (F-21), we see that

$$D^*_\lambda = \left[\frac{S_\lambda}{2eE_{B\lambda}} \right]^{1/2} \quad (\text{photovoltaic}), \quad (\text{F-24})$$

which is analogous to the inverse of Eq. (F-9).

The radiation to which a BLIP detector responds may come in part from outside the field of view such as from the objective lens housing. These photons from outside the field of view introduce an additive fluctuation noise in the detector but, this noise can be reduced considerably by cold shielding the detector. With optimum cold shielding, the field of view of a detector will include only the objective lens and the number of background photons detected will be proportional to $\sin^2 \theta$ where $\theta = D_o/2F_L$; the lens diameter, D_o , divided by its focal length, F_L . Since the lens focal ratio is F_L/D_o , the number of background photons detected is proportional to $(1/2f)^2$ and consequently, a detector with a cold shield limiting the field of view to a solid angle of Ω_{sr} will have a detectivity equal to

$$D^*_\lambda (\Omega_{sr}) = 2f D^*_\lambda (2\pi). \quad (\text{F-25})$$

where $D^*_\lambda(2\pi)$ implies the detectivity of a detector viewing a solid angle of background of 2π sr. The detectivity of a perfect detector viewing 2π sr of background is defined as $D^{**}(2\pi)$ and in this case,

$$D^*(\Omega_c) = 2f\eta_\lambda^{1/2} D^{**}(2\pi), \quad (F-26)$$

where η_λ is the detector's quantum efficiency. If the cold shielding is not optimum, it is common practice to define a cold shield efficiency η_c which is equal to

$$\eta_c = \frac{\Omega_p}{\Omega_c}, \quad (F-27)$$

where Ω_p is the solid angle which the detector would view with perfect cold shielding and Ω_c is the actual solid angle being viewed. With Eq. (F-27), Eq. (F-25) becomes

$$D^*_\lambda(\Omega_c)' = 2f\eta_c D^*_\lambda(2\pi). \quad (F-28)$$

In the case where system-generated noise is a factor, an effective D^* which includes the added noise is sometimes reported. As an example, consider the case where preamp noise is comparable or larger than the photoelectron noise. Let $D^*(f)$ be the detector detectivity as a function of frequency and note that

$$\text{NEP}(f) = \frac{\sqrt{a_d}}{D^*(f)}, \quad (F-29)$$

where A_d is the area of the detector. The noise voltage can be calculated from

$$V_d = \frac{\sqrt{a_d}}{D^*(f)} R(f), \quad (F-30)$$

where $R(f)$ is the detector responsivity in volts/watt. Let the preamp noise spectral density be white and referred to the preamp input (or detector output), the noise voltage is

$$V_p^2 = F_N V_f^2, \quad (F-31)$$

where F_N is the preamp noise figure, and V_f^2 is the mean square noise spectral density. The overall system mean square noise voltage V_s^2 is then

$$V_s^2(f) = \frac{a_d R^2(f)}{[D^*(f)]^2} + F_N V_f^2, \quad (F-32)$$

and since

$$\text{NEP}_s(f) = \frac{V_s}{R(f)}, \quad (F-33)$$

it is found that

$$[\text{NEP}_s(f)]^2 = \frac{a_d}{[D^*(f)]^2} + \frac{F_N V_f^2}{R^2(f)}, \quad (F-34)$$

and by use of Eq. (F-19),

$$[D^*(f)]^2 = \frac{1}{\left[\left(\frac{1}{D^*(f)} \right)^2 + \frac{F_N V_f^2}{R^2(f)} \right]^{1/2}}. \quad (F-35)$$

APPENDIX F

The noise terms must of course be appropriately integrated to find D^* , the *effective overall "system" detectivity*. The above example is primarily for the purpose of illustrating a method of handling multiple noise sources.

Finally, it is noted that D^* is usually quoted in terms of a specific test source background such as a 300 K background, *i.e.*,

$$D^*(300 \text{ K}) = \frac{\int_{\lambda_1}^{\lambda_2} D^*_{\lambda} E_{\lambda} (300 \text{ K}) d\lambda}{\int_{\lambda_1}^{\lambda_2} E_{\lambda} (300 \text{ K}) d\lambda} \quad (\text{F-36})$$

where $E_{\lambda} (300 \text{ K})$ is the detector irradiance due to a 300 K blackbody.

Appendix G

EFFECTS OF IMAGE SAMPLING

F. A. Rosell

Commercial television broadcast systems form images by a line raster process and thus fall in the category of sampled data systems. The effects of sampling in the television process has been quite thoroughly analyzed and discussed by Schade (Ref. G-1). While the sampling process can have a noticeable effect on televised pictures, the effects are not as objectionable as they are in either FLIRs or some of the newer solid state imagers which may be sampled in two directions instead of one and because the amount of prefiltering of input spatial frequencies is generally less for systems using discrete detectors. It is noted that the so-called bad effects of sampling, *i.e.*, moiré, spurious responses, and information loss are felt by some to be over-emphasized in military and industrial applications. However, this view has not been quantitatively supported and it can be shown that image quality improvements can be obtained by proper pre- and postfiltering of the sampled images in many cases.

A high sensor MTF is generally desired. Detector MTF can be improved by reducing the detector dimensions, but if the detectors are made smaller than the interline spacing, for example, losses in information and in sensitivity will result. Even further, it is clearly evident that continuity in the displayed image requires that the display aperture fill the interline spaces. The inference which can be drawn is that picture quality and overall resolution may be improved by purposely degrading certain system component apertures.

It is common experience that the majority of FLIR and television monitors have a pronounced visible line structure. Images with line structure may actually appear to be sharper while, in fact, more image detail will be perceived when the line structure is removed by aperture overlap. An alternative, most commonly employed method of eliminating line structure is simply to increase the observer-to-display viewing distance whereupon the blur circle of the eye smears out the line structure to the point of bare perceptibility.

The ideal sampled data system is shown schematically in Fig. G-1. An ideal low pass filter prefilters the *input image function* $f_1(y)$ prior to sampling. The high-frequency cutoff should be numerically equal to the *sampling frequency* N_s and thus the image to be sampled will contain no frequencies higher than N_s . The sampling frequency results in a line spacing $\Delta y_s = 1/N_s$. Each sample duration should be infinitesimally short so that only the signal amplitude is preserved. The output of the sampler is then passed through an ideal low pass filter which will then perfectly construct the function $f_1(y)$ to within a constant multiplier.

As we noted, the highest spatial frequency which can be reproduced is equal to half the sampling frequency. Stated differently the sample frequency must be equal to or greater than twice the highest spatial frequency of interest and this means that at least two samples per cycle (or one sample per half-cycle) must be taken. This may be visualized by reference to Fig. G-2. If every other cycle were eliminated, the output of the sampler would be indistinguishable from that which one would obtain from a uniform background. A frequency corresponding to half the sampling frequency is sometimes called the *Nyquist frequency limit*.

APPENDIX G

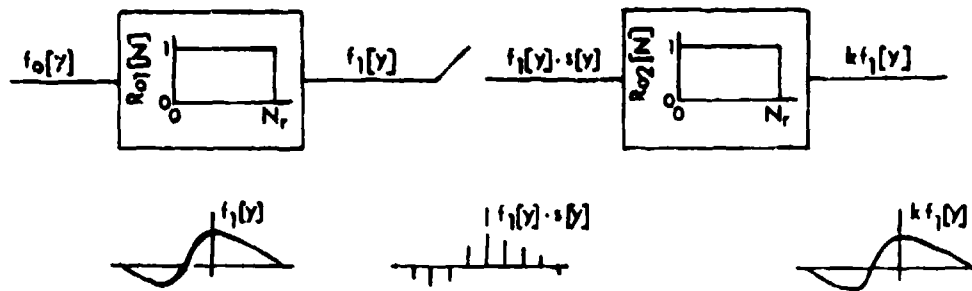


Fig. G-1 — Block diagram of the ideal sampling and reconstruction process

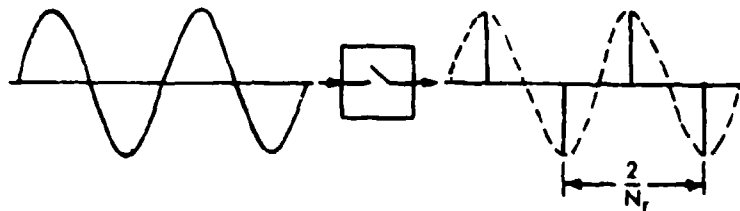


Fig. G-2 — The highest spatial frequency of interest must be sampled at least twice per cycle

The ideal sampled data system of Fig. G-1 is typified by the electronically multiplexed system of Fig. 4-4. In the basic FLIR configuration of Fig. 4-8, the detectors themselves perform the sampling process. In Fig. G-3, we show three line array detector configurations. In all cases, the detector widths are identical. Also, the Nyquist frequency is the same for all three because the *scan line pitch* (or center-to-center detector spacing), P , is the same. However, the sensitivities which are proportional to the square root of detector area are clearly different and, the MTFs in the vertical direction are widely different as shown in Fig. G-4. With $\delta_y = P/2$, the MTF is 0.90 at the Nyquist limit while with $\delta_y = P$ and $2P$, the corresponding MTFs are 0.64 and 0, respectively.

The combination of the lens and the detectors form the prefilter of the sampled data system. The $\delta_y = P/2$ provides the least prefiltering and will be the most subject to spurious responses and aliasing. Furthermore scene information will be lost since only half of the area of the vertical field is scanned. The eye can of course perform an image reconstruction process provided that details such as horizontal edges are not completely lost.

The detector MTFs shown in Fig. G-4 represent the maximum MTF obtainable in the sampling direction. Actually, the word MTF not really appropriate after a sampling process has taken place since sampling is not a linear operation but we shall ignore this distinction for the present discussion purposes. By maximum MTF obtainable, it is meant that this "MTF" is obtained only when the sine wave pattern is aligned for maximum response. At the Nyquist frequency, this occurs when the positive swing of a half cycle of the pattern falls exactly on one detector and the negative half cycle falls exactly on the adjacent detector. On the other hand, if this same pattern is shifted one-quarter cycle or 90° , the measured "MTF" will be zero. In general, the "MTF" is given by

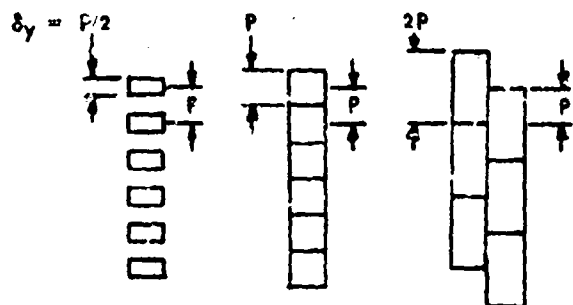


Fig. G-3 — Three line array detector configurations with the same Nyquist spatial frequency limit and the same resolution in the horizontal scan direction

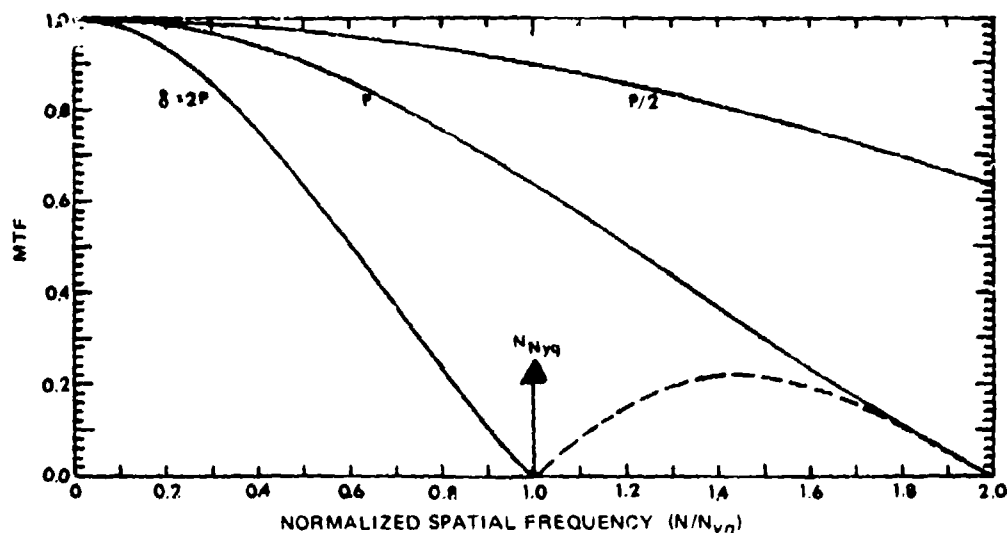


Fig. G-4 — Geometrical MTF of detector elements as a function of spatial frequency normalized to the Nyquist limit for detectors of size equal to $2P$, P , and $P/2$

$$MTF = R_{0d}(N) \cos \theta. \quad (G-1)$$

The angle θ will have a maximum value which is different for each spatial frequency. At the Nyquist limit $\theta_{max} = 90^\circ$; and at half the Nyquist limit, $\theta_{max} = 45^\circ$. In Fig. G-5, we plot Eq. (4-58) as modified by Eq. (G-1) as Curve 1 with $\theta = 0$, as Curve 2 with $\theta = \theta_{max}/2$, and as Curve 4 with $\theta = \theta_{max}$. If any value of θ between $\theta = 0$ and $\theta = \theta_{max}/2$ is equally probable, then the apparent "MTF" will be greater than that of Curve 3 half the time and less, the other half of the time. It has also been suggested that the "average" detector "MTF" in a cross scan direction be given by

$$MTF = R_{0d}^2(N) = \frac{\sin^2(\pi N/2Nyq)}{(\pi N/2Nyq)^2}. \quad (G-2)$$

which is plotted as Curve 3 and is seen to be only slightly less than that given by Curve 2. Because of its simplicity, this latter approach is suggested as a reasonable approximation.

APPENDIX G

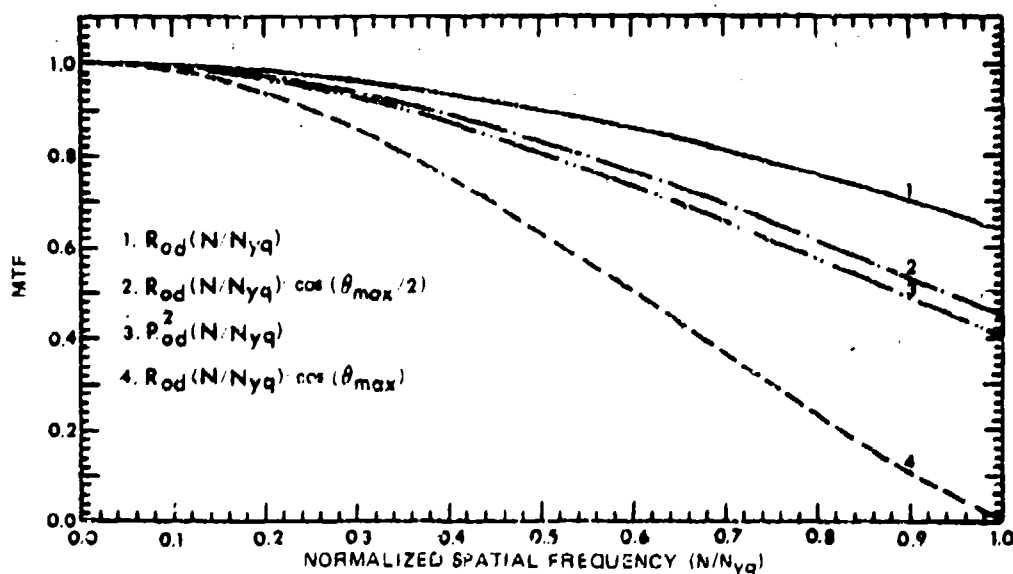


Fig. G-5 — Detector MTF in the across scan direction for various phase angles and for the detector MTF squared

In the particular case where the detector array performs the sampling function, the input signal $f_1(y)$ may be considered to be sampled by a function $f_2(y)$, where

$$f_2(y) = r_{od}(x) * f_1(y). \quad (G-3)$$

In the above $r_{od}(x)$ is the impulse response of the detector and

$$f_2(y) = \sum_{n=-\infty}^{\infty} \mu_0(y - n\Delta y), \quad (G-4)$$

where μ_0 are impulses occurring at $y = 0$ and Δy is the sampling period. The Fourier transform of $f_2(y)$ are unit amplitude impulses in the spatial frequency domain which repeat at spatial frequencies $2nN_{yq}$. The output of the sampler is $f'(y) = f_1(y) \cdot f_2(y)$ and it will be found that the amplitude spectrum $F(N_{yq})$ will consist of a band about zero frequency and identical bands about $\pm 2nN_{yq}$ as shown in Fig. G-6 (a) and (b). In case (a), it is assumed that the input signal $f_1(y)$ has been bandpass limited to N_{yq} and thus none of the spectra overlap. In case (b), there is considerable overlap due to the sidebands which will result in spurious responses and aliasing.

The detectors are designated the analyzing aperture by Schade (Ref. G-1) while the electron beam of the display along with the phosphor is designated the synthesizing aperture. The function of the display is of course to reconstruct the image but it also serves a postfiltering function. Consider a CRT display operated in a conventional manner. A Fourier analysis of the luminance distribution L_v in the vertical direction (across the scan) shows that L_v contains the dc level \bar{L} and a series of harmonic cosine waves given by

$$L_v = \bar{L} [1 + 2 \sum_k R_{od}(kN_{yq}) \cos(2k\pi N_{yq}y)] \quad (G-5)$$

$k = 1, 3, 5, \dots$

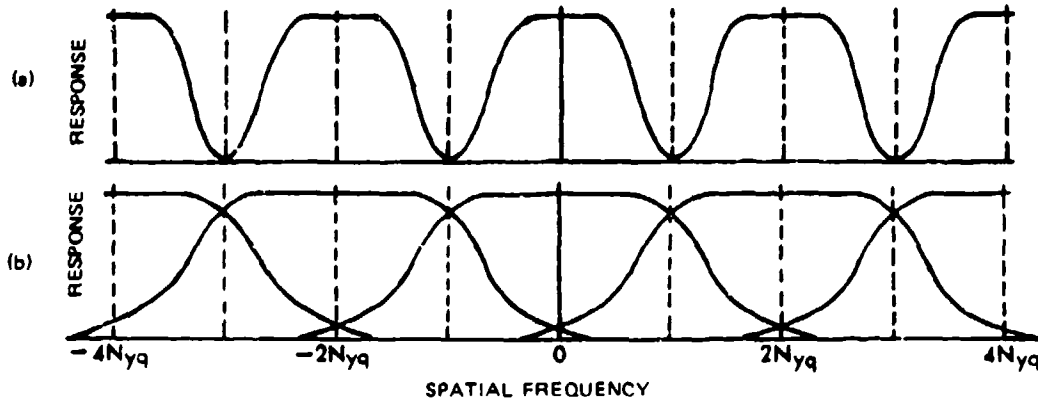


Fig. G-6 — Repetitive amplitude spectra due to sampling. Case (a) — Spectra bandpass limited to the Nyquist frequency, and Case (b) — Overlapping spectra due to inadequate prefiltering

where $|R_{0d}(kN_r)|$ represents the "MTF" of the display at integral multiples of the raster frequency N_r . This luminance distribution exists without any added signal and thus is independent of the sensor MTF. The cosine waves are in place on the center of a raster when the display's aperture has axial symmetry and its response decreases asymptotically to zero. A line structure in the vertical direction, without signal being present, is undesirable. Perfect continuity, i.e., a flat field, is restored when none of the carrier wave components are reproduced by the displays aperture. For this to be true, the display MTF must be equal to zero at line numbers above $2N_r$. A substantially flat field condition is obtained when

$$R_{0d}(2N_r) \leq 0.005, \quad (\text{G-6})$$

which as can be seen from Eq. (G-5) gives a ripple amplitude of 1% and a peak-to-peak luminance amplitude of 2%. Most television monitors show a pronounced line structure. A flat field condition can still be achieved by moving away from the screen until the lines can no longer be resolved by the observer's eye.

Suppose next that we modulate the display with a periodic signal of frequency N_m in the vertical direction. The display luminance terms will then be given by

$$\begin{aligned} L_y = \bar{L} [1 + 2 \sum_k R_{0d}(kN_r) \cos(2k\pi N_r y)] & \quad (\text{carrier}) \\ & + L_m R_{0F}(N_m) R_{0d}(N_m) \cos(\pi N_m y + \theta) \quad (\text{signal}) \\ & + L_m R_{0F}(N_m) \sum_k R_{0d}(2kN_r - N_m) \cos[\pi(2N_r - N_m) + \theta], \quad (\text{sum}) \\ & + L_m R_{0F}(N_m) \sum_k R_{0d}(2kN_r + N_m) \cos[\pi(2N_r + N_m) + \theta] \quad (\text{difference}) \\ & k = 1, 2, 3, 4, \dots \quad (\text{G-7}) \end{aligned}$$

where \bar{L} is the average luminance of the test signal waveform, L_m is the crest luminance of the signal waveform, and θ is the displacement between the peak of the L_m waveform and the raster lines.

APPENDIX G

The first term is the carrier waveform discussed in connection with Eq. (G-5) while the second, the signal term, is recognized as nearly equal to the normal term expected without a raster process, *i.e.*, the displayed image waveform amplitude is proportional to the amplitude of the test image times the product of the camera and display MTFs. Note, however, that the output amplitude can be modified by the phase angle between the input waveform and the raster which is a consequence of the sampling process.

The third and fourth terms are sum and difference modulation products of the carrier frequencies with the test object signal. In communications theory, these sum and difference products are called sidebands while in imaging practice their effects are more often referred to as *aliasing*. Patterns generated by the sum and difference frequencies when periodic patterns are being viewed are called moiré patterns. The difference term is more likely to present problems. Consider the case where $N_m = 1.5 N_r$ and $k = 1$. The crest amplitude of spurious response is then equal to the crest amplitude of the original test image amplitude multiplied by the MTF of the sensor at $1.5 N_r$ and the MTF of the display at $0.5 N_r$. It is clearly evident that with perfect prefiltering, no aliasing results but a perfect postfilter would not attenuate the alias frequency at all. Postfiltering cannot eliminate the effects of imperfect prefiltering with respect to the first difference, low-frequency terms.

The various terms of Eq. (G-7) are depicted in graphical form in Fig. G-7. The sensor MTF, or $R_{0F}(N)$, is the product of all the MTFs in the y direction which precede the raster process including the scanning detectors which are part of the prefiltering process. The display MTF, or $R_{0d}(N)$, includes all of the MTFs following the raster process including $R_{0d1}(N)$ and $R_{0d2}(N)$, but $R_{0d2}(N)$ has essentially zero response for the *difference frequency* D_2 .

The higher MTF of $R_{0d1}(N)$ reproduces the carrier, C , with a modulation amplitude of 36% which corresponds to a 72% peak-to-peak luminance variation on a uniform field. The $R_{0d2}(N)$ provides a nearly flat field but the MTF is reduced at line numbers less than N_r . As a compromise, a display MTF of 0.025 at $2N_r$ is often selected. This gives a peak-to-peak luminance variation of 10% and still provides a reasonable MTF at the lower spatial frequencies.

In Fig. G-8, the MTFs for five sensors are shown together with the display MTF referenced to the first carrier frequency (the display MTF repeats at each carrier frequency). The second difference terms (D_2) can be neglected. The MTF diagram is used to evaluate the $R_{0F}(N) \cdot R_{0d}(N)$ products which are shown in Fig. G-8. Note that the zero frequency of the cross products occurs when $N_m = 2N_r$ and that the spurious modulation frequencies are higher than N_m for $N_m < N_r$. A *spurious response* of $R_{0F}(N)$ equal to 15% is considered to be an upper limit for good system design according to Schade. The value is a worst case and occurs occasionally for periodic image inputs of 100% contrast. A maximum spurious response of 15% is obtained with the $R_{0F3}(N)$ curve in combination with the assumed display. The sensors with higher MTFs would exceed the 15% criterion, and thus it follows that the number of raster lines should be equal to or greater than

$$N_r \geq N_{m(0.4)} \quad (4-89)$$

where $N_{m(0.4)}$ is the spatial frequency where the sensor MTF is equal to 0.4. An overall system response $R_{0c}(N) \cdot R_{0d}(N) \approx 0.15$ is then obtained with a flat-field display having a sine wave response of 0.38 at the theoretical limit $N_m = N_r$.

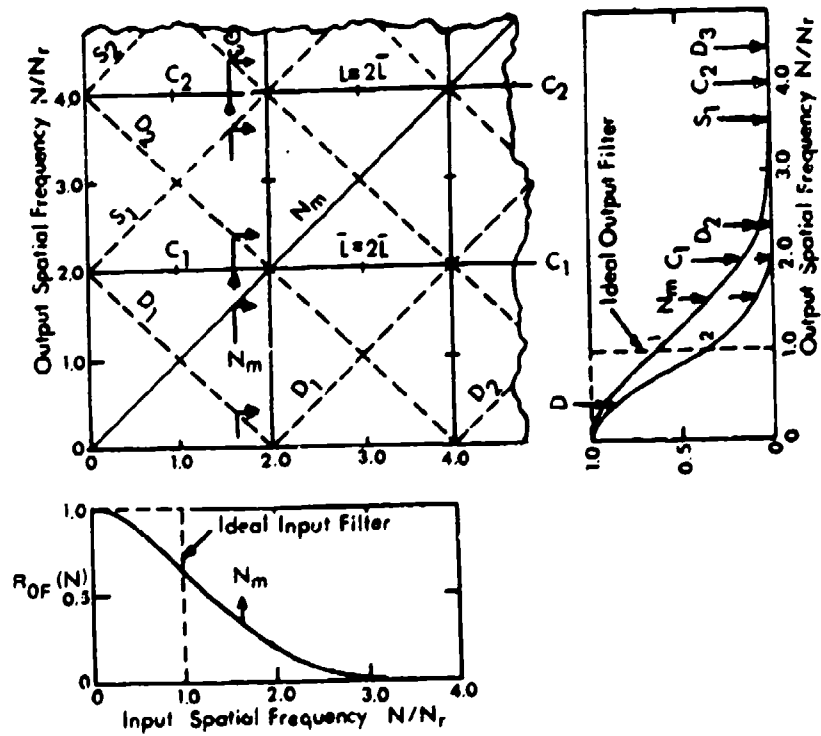


Fig G-7 — Graphical representation of the carrier and sideband terms of Eq. (4-88)

APPENDIX G

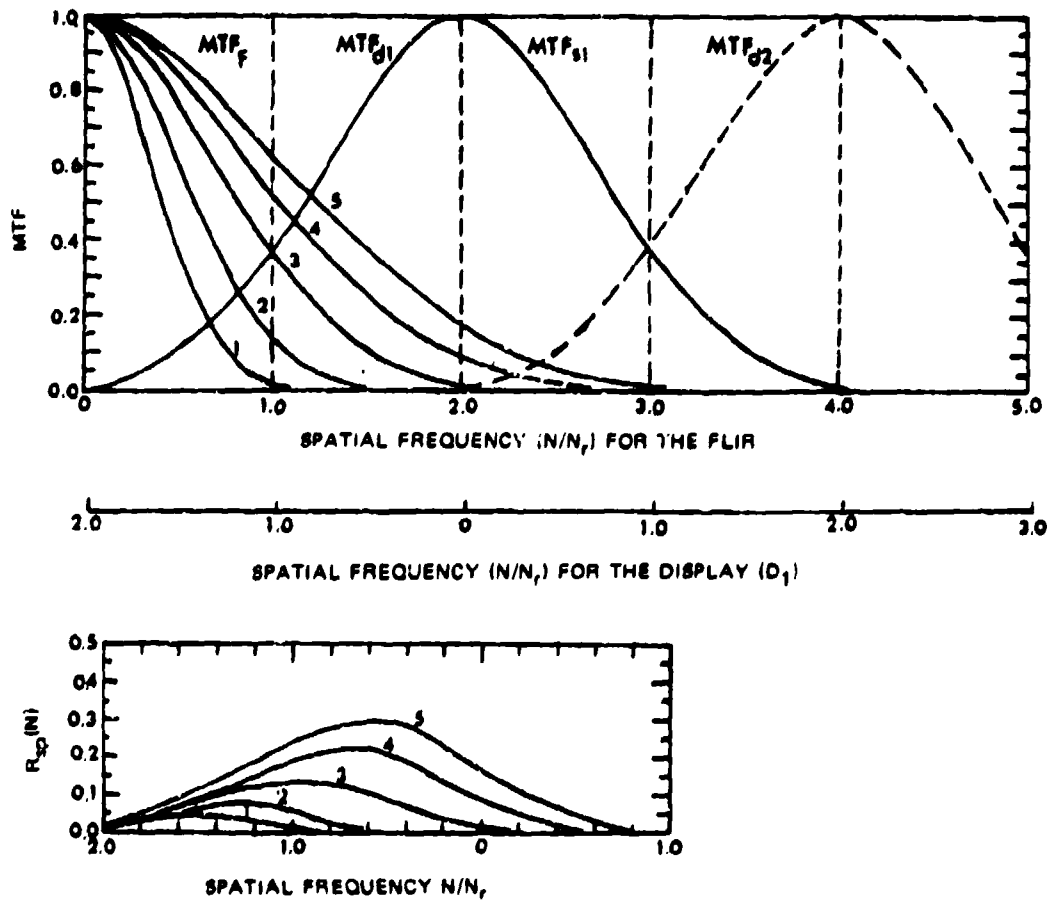


Fig. G-5 - Evaluation of spurious cross products for display MTF giving a flat field

REFERENCE

- G-1 Schade, Otto H. Sr., Image Reproduction by a Line Raster Process Chapter 6, Perception of Displayed Information, Plenum Press, May 1973.

Appendix H PSYCHOPHYSICAL EXPERIMENTATION

F.A. Rosell

A. INTRODUCTION

A number of psychophysical experiments performed for the purpose of determining observer thresholds are summarized in this appendix. The test objects include both rectangles and bar patterns. The observer effects studied include the limits to the eye's ability to spatially integrate, the effects of observer, to display viewing distance, and retinal fluctuation noise considerations.

B. THRESHOLD SIGNAL-TO-NOISE RATIOS FOR APERIODIC IMAGES

Aperiodic images are defined here as rectangles imaged against a uniform background. To perform psychophysical experimentation to determine observer thresholds, use is made of Eq. 4-8, which is repeated below

$$\text{SNR}_D = \left[2T_r \Delta f_{10} \left(\frac{a}{A} \right) \right]^{1.2} \text{SNR}_{10}, \quad (\text{H-1})$$

which holds for band-limited white noise and for the case where the observer is not limited by image magnification or retinal fluctuation noise. The experimental setup used is shown in Fig. H-1. In the experiment, a single pulse of rectangular waveshape but variable duration is electronically generated and mixed with band-limited white noise of Gaussian distribution. The spatial image displayed on the screen is a rectangle which can appear in any of four quadrants (but always in the same position in the quadrant selected). The observer is asked to specify the quadrant in which the image is located as the video signal-to-noise ratio and the image locations are randomly located. The observer is asked to specify the image location whether he could see it or not. The probability of detection, determined in this manner, was then corrected for chance. The observation times were usually 10 seconds. For a complete description and discussion of this experiment and the other experiments discussed below, the reader is referred to Ref. (5-1).

For the rectangle experiments, it was found to be convenient to define the image size in terms of the dimensions of a single scan line. Thus, we define the quantities A_x and A_y as

$$A_x = \frac{490 \Delta x}{Y}, \quad A_y = \frac{490 \Delta y}{Y},$$

where $\Delta x \cdot \Delta y$ equals the image area a , 490 is the number of active lines in a conventional 525 line television display, and Y is the image plane height. Since the image plane area A can be written as αY^2 , where α is the width-to-height picture aspect ratio,

$$A_x, A_y = (490)^2 \alpha \frac{a}{A}, \quad (\text{H-2})$$

and Eq. (H-1) may be written as

$$\text{SNR}_D = (1/490) (2A_x A_y T_r \Delta f_{10} / \alpha)^{1.2} \text{SNR}_{10}, \quad (\text{H-3})$$

APPENDIX H

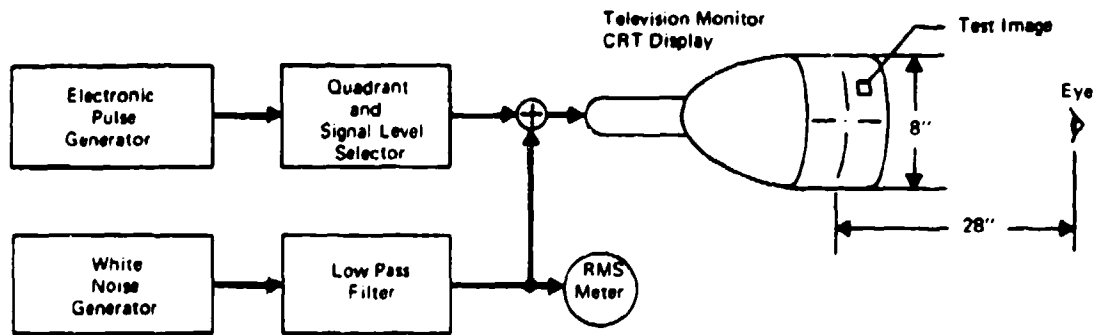


Fig. H-1 — The display signal-to-noise ratio experiment. Display background luminance was 0.2-0.3 or 1 ft-L. TV camera operated at 30 frames/s with a 525 line raster scan.

This equation is used to calculate the SNR_D for the rectangular images used in the experimental program reported below. The numerical values used for α were 0.1 s and 4/3, respectively.

It is generally true that the probability of detecting a signal in the presence of noise is related to the signal-to-noise ratio and the purpose of the first experiment was to determine the form of the probability function when the signal is a visually observed image. We hypothesize that the probability of detection would be a constant for any given value of SNR when the image SNR is as quantitatively described by Eq. (H-1), as opposed to being described by the video signal-to-noise ratio associated with the image. To test this concept, the probability of detection, corrected for chance, was measured as a function of the video SNR, or SNR_V , with the results shown in Fig. H-2 for images of size 4×4 , 4×64 , 4×128 , and 4×180 scan lines. It is seen that the larger the image length (and therefore the image area), the smaller the SNR_V required for a given value of detection probability. Thus, a given value of probability cannot be associated with a given value of SNR_V because the SNR_V required at the given probability level is image area dependent. However, when the probability is plotted vs SNR_D , which includes image area in its definition, the dependence of detection probability on area disappears as shown in Fig. H-3 where we have plotted Eq. (H-1) using the probabilities and SNR_V values of Fig. H-2. This is interpreted as a confirmation of the original hypothesis.

The angular extent of the test images relative to the observer's eye varied from $0.13^\circ \times 0.13^\circ$ for the smallest rectangle to $0.13^\circ \times 6.02^\circ$ for the largest rectangle. This experiment infers that the eye can integrate over very large angles in space; angles which are much larger than were previously thought to be the case.

The most probable explanation for this effect is that the eye, through a differentiating action, is more sensitive to edges and the test images of large angular extent in one dimension were nearly all edge, being long thin rectangles. To test this hypothesis, a second experiment was performed using a rectangle of length 96 scan lines (or angular subtense 3.2°) and of variable widths of 4, 8, 16, and 32 scan lines corresponding to angular subtenses of 0.13° , 0.267° , 0.534° , and 1.07° relative to the observer. The corrected probability of detection for this case is shown for the various rectangles in Fig. H-4 and a plot of the thresholds as a function of image

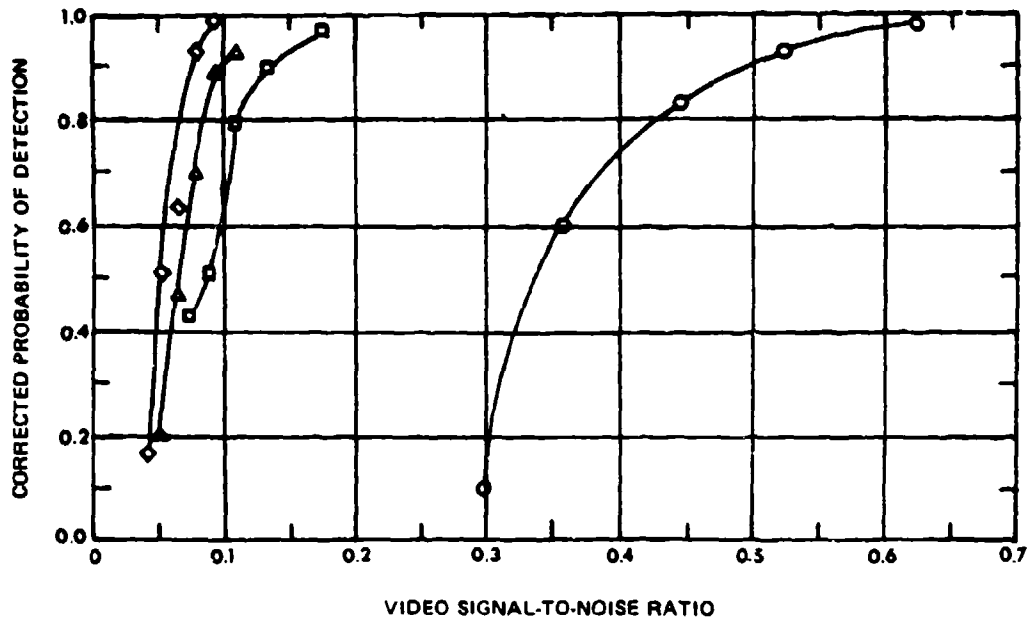


Fig. H-2 — Probability of detection vs video signal-to-noise ratio required for rectangular images of size $\circ 4 \times 4$, $\square 4 \times 64$, $\triangle 4 \times 128$, and $\diamond 4 \times 180$ scan lines

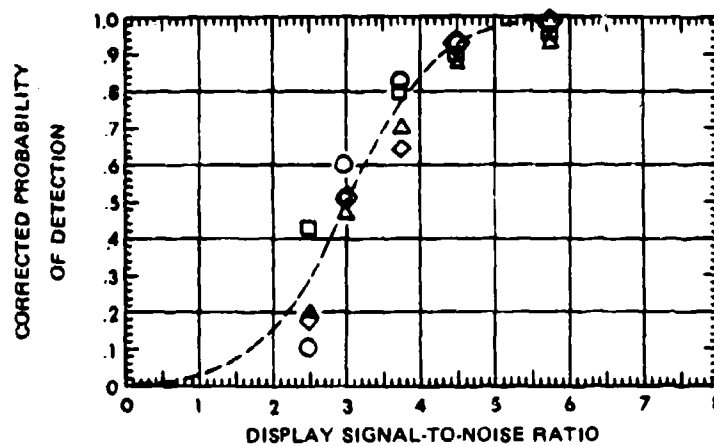


Fig. H-3 — Corrected probability of detection vs SNR_D required for rectangular images of size $\circ 4 \times 4$, $\square 4 \times 64$, $\triangle 4 \times 128$, and $\diamond 4 \times 180$ scan lines

size is shown in Fig. H-5. For long narrow rectangles, the same threshold value of SNR_D is obtained as was obtained for narrow rectangles of various lengths (Fig. H-4) and we conclude that for narrow widths (angular subtense of up to 0.5°) that the eye fully integrates the whole area of the rectangle, but for wider rectangles of angular subtense larger than 0.5° , the eye is apparently less efficient in utilizing image area.

APPENDIX H

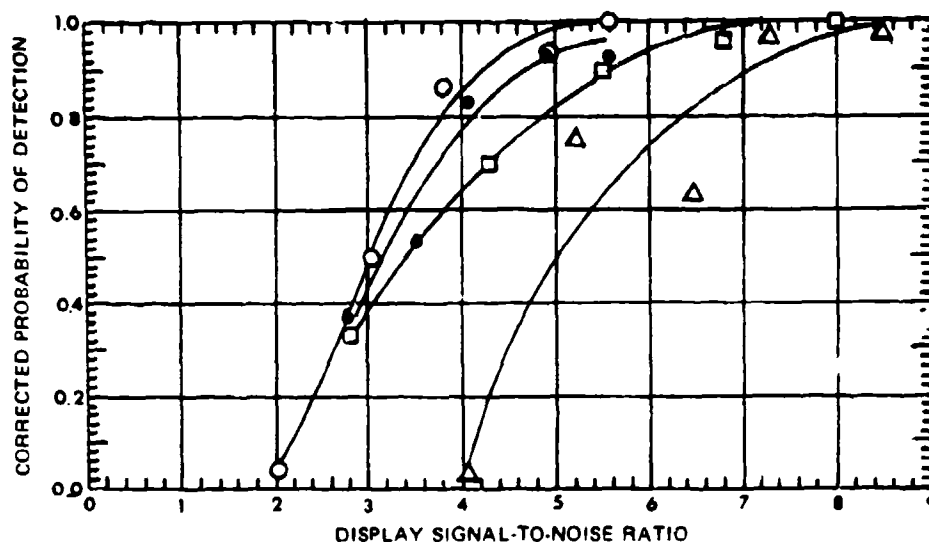


Fig. H-4 — Probability of detection vs display signal-to-noise ratio for a rectangle of height 96 scan lines and widths • 4, ○ 8, □ 16, and △ 32 scan lines

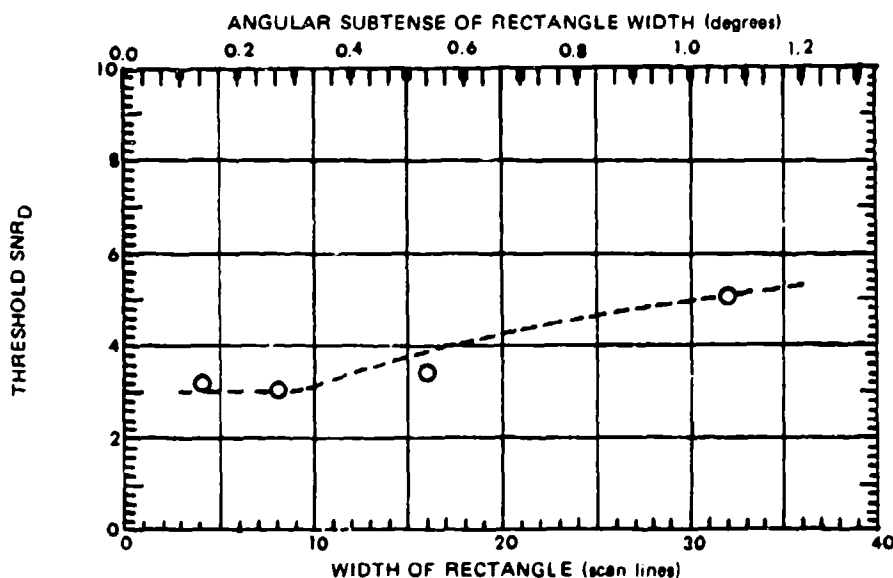


Fig. H-5 — Threshold SNR_D as a function of linear and angular extent of rectangle of height 96 scan lines (3.2°) and variable width 4, 8, 16, and 32 scan lines (0.13°, 0.267°, 0.534°, and 1.07°). Dashed curve is theoretical.

To further verify the area effect, square images of size 2×2, 4×4, 8×8, and 16×16 scan lines were used. The measured threshold SNR_{DT} values, calculated on the assumption that the eye integrates over the total image area, are shown in Fig. H-6. The increase noted for the 2×2

line image is thought to be due to the aperture response of the eye while the apparent threshold increases for the 16×16 , 32×32 , and 64×64 line squares is thought to be due to the edge differentiation effect.

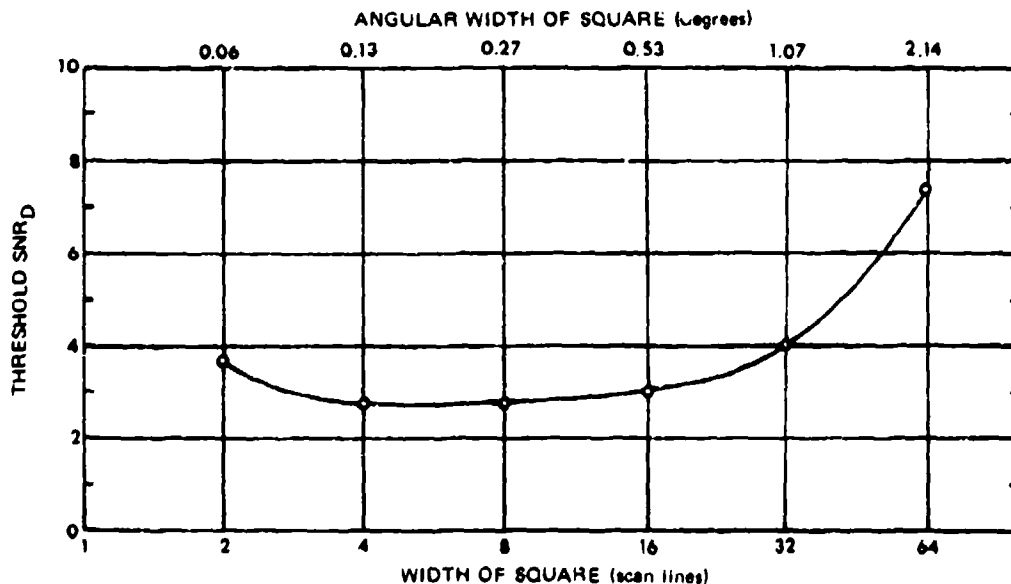


Fig. H-6 — Threshold SNR_D required to detect square images of various size and angular extent

C. THRESHOLD SIGNAL-TO-NOISE RATIOS FOR PERIODIC BAR PATTERNS

The relationship between the video signal-to-noise ratio and the detectability of bar patterns was investigated and reported by Coltman and Anderson in 1960 (Ref. H-1). A review of the Coltman and Anderson experiment has historical merit and lends credence to the current approaches being used. In addition, the Coltman and Anderson experiment is often cited to prove that the eye uses up to 14 lines in the process of detecting a bar pattern. This result is believed to be an error in interpretation as was discussed in Appendix E. Rather than integrating over a number of bars, it is hypothesized that the observer, to detect the presence of a bar pattern, must detect the presence of a single bar.

Psychophysical threshold SNR experiments using bar pattern test images were performed using the experimental setup of Fig. H-7. The periodic test images were bar patterns of various height-to-width ratios and spatial frequencies and were projected on the faceplate of a high-resolution 1-1/2-inch vidicon operated at highlight video signal-to-noise ratios of 50:1 or better. Band-limited white noise of Gaussian distribution was mixed with the camera-generated signal.

In the experiment, the observer was required to state whether or not the pattern displayed was resolvable as the image SNR_D was randomly varied. Chance was not involved since the patterns were always present on the display. The experimental constants for the various experiments are given in Ref. S-1. The purpose of the experiment was to determine the effect of bar

APPENDIX H

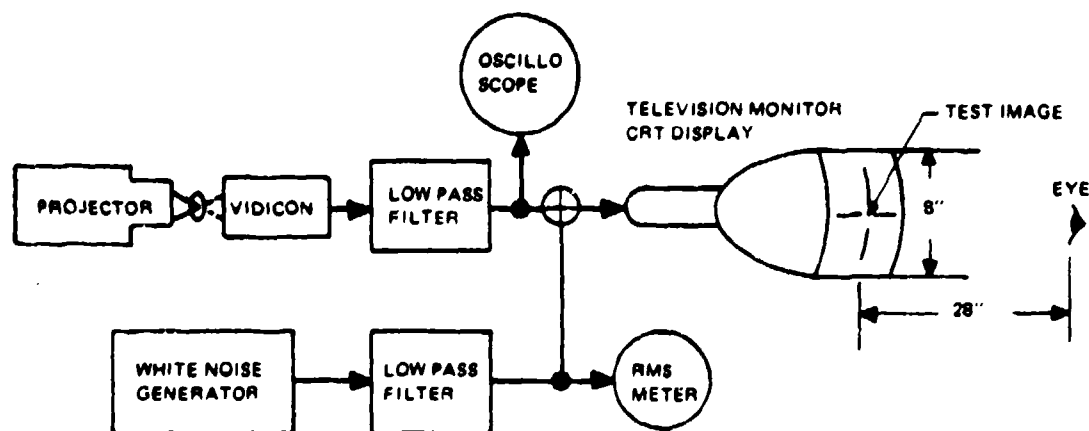


Fig. H-7 — Experimental setup for the television-camera-generated imagery. TV camera was operated at 25 frames/s and 875 scan lines (825 active) display luminances with 1 ft-L.

height-to-width ratio on the bar pattern detectability, with the results shown in Figs. H-8 through H-10. At a low spatial frequency of 104 lines/picture height, the threshold SNR_{DT} is seen to increase slightly with bar height-to-width ratio (Fig. H-8), while at the highest spatial frequency of 396 lines/picture height the SNR_{DT} required is very nearly independent of bar height-to-width ratio, as shown in Fig. H-10. By threshold SNR_{DT} it is implied that the observer discerned the pattern 50% of the time when the image SNR was at the threshold value.

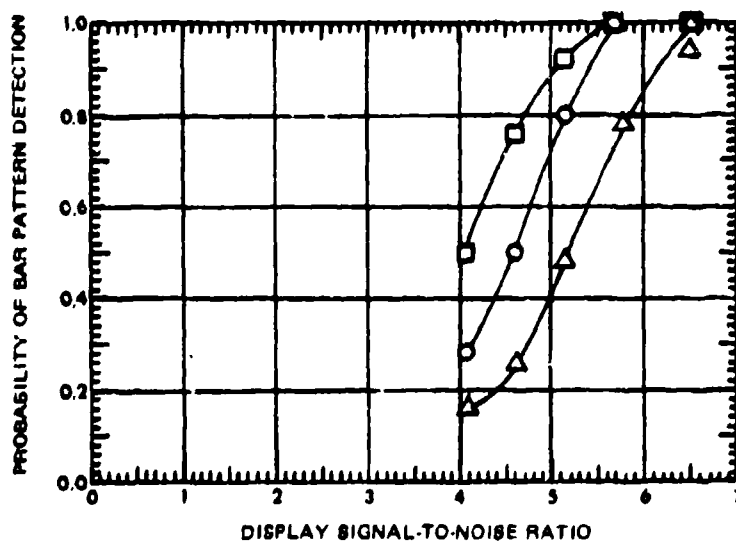


Fig. H-8 — Probability of bar pattern detection vs SNR_D for a 104-line bar pattern of bar height-to-width ratio (□) 5:1, (○) 10:1, and (Δ) 20:1

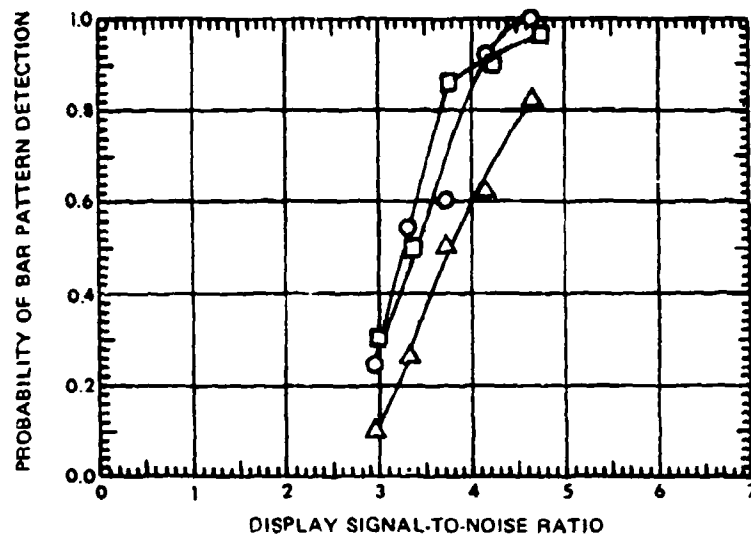


Fig. H-9 - Probability of bar pattern detection vs. SNR_D for a 200-line bar pattern of bar height-to-width ratio (□) 5:1, (○) 10:1, and (Δ) 20:1

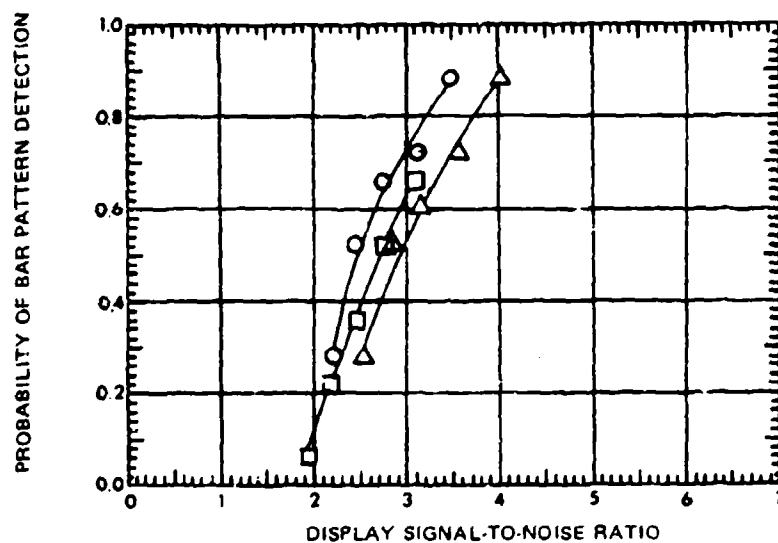


Fig. H-10 - Probability of bar pattern detection vs. SNR_D for a 396-line bar pattern of bar height-to-width ratio (□) 5:1, (○) 10:1, and (Δ) 20:1

The SNR_{DT} values are summarized in Fig. H-11 as a function of spatial frequency and are seen to decrease slowly with line number for all the patterns.

The angular subtenses of the bars used in the experiment, relative to the observer's eye, are given in Table H-1. It is seen that a bar of the 104 line pattern with 20:1 aspect subtended

APPENDIX H

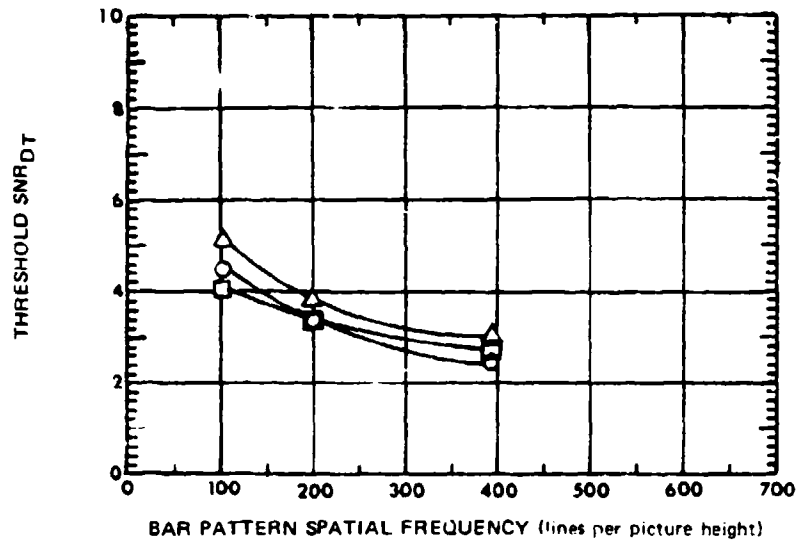


Fig. H-11 — Threshold SNR_{DT} vs bar pattern spatial frequency for three bar height-to-width ratios of (□) 5:1, (○) 10:1, and (Δ) 20:1

Table H-1 — Angular Subtense (degrees) of a Bar in Each Experiment Relative to the Observer as a Function of the Bar Height-to-Width Ratio.

Bar Pattern Spatial Frequency Lines/P.H.	Angular Subtense in the Horizontal	Angular Subtense in the Vertical for Bar Height-to-Width Ratios of		
		5	10	20
104	0.157	0.785	1.57	3.14
200	0.0818	0.409	0.818	1.636
396	0.0413	0.2065	0.413	0.826

3.14°. Apparently the observer was not able to fully integrate over the entire bar length as evidenced by the higher SNR_{DT} required. For an isolated bar, the observer was able to spatially integrate over at least an angle of 6° as was discussed previously. This marks at least one difference between the detection of isolated bars and bar patterns.

The probability of bar pattern detection is plotted in Fig. H-12 vs SNR_D for spatial frequencies equal to 104, 200, 329, 396, 482, and 635 l/p.h. Bar length-to-width was 5:1 in all cases. The corresponding threshold SNR_{DT} values are plotted in Fig. H-13. Again the fall off in SNR_{DT} with increase in spatial frequency is noted. The effect of observer-to-display viewing

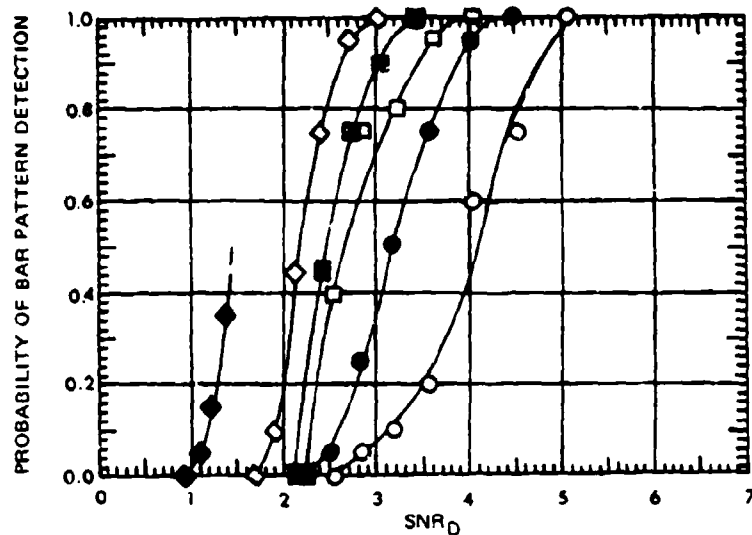


Fig. H-12 — Probability of bar pattern detection vs SNR_D for spatial frequencies of \circ 104, \bullet 200, \square 329, \blacksquare 396, \blacktriangledown 482, and ∇ 635 lines/pict. ht. Bar length to width = 5, televised images at 25 frames/s

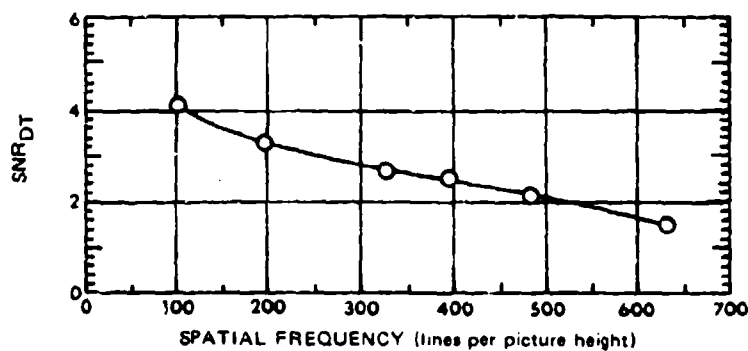


Fig. H-13 — Threshold SNR_{DT} vs bar pattern spatial frequency for the data of Fig. H-12

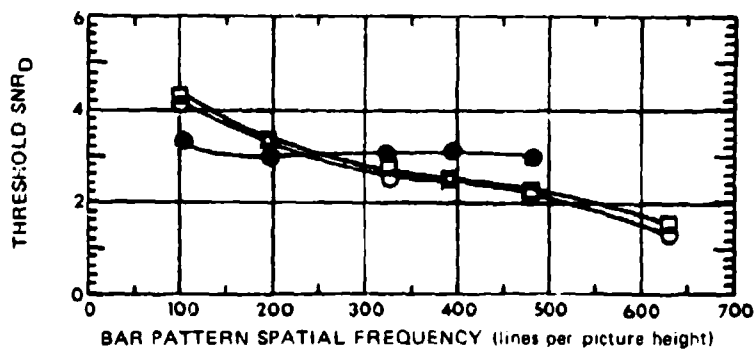


Fig. H-14 — Threshold display signal-to-noise ratio vs bar pattern spatial frequency for display to observer viewing distance of \circ 14", \square 28", and \bullet 56". Televised images at 25 frames/s and 875 scan lines

APPENDIX H

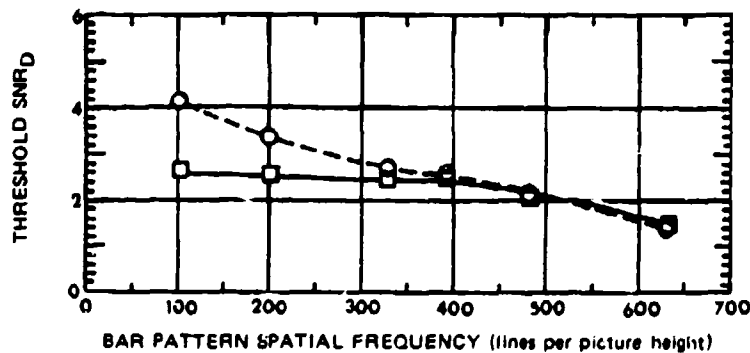


Fig. H-15 — Threshold display signal-to-noise ratio vs bar pattern spatial frequency for □ optimum viewing distances and ○ 28" viewing distance from one observer

distance is shown in Figs. H-14 and H-15. In Fig. H-14, the thresholds were measured for viewing distances of 14", 28", and 56" from an 8" high display. As can be seen, low frequency patterns are discerned, with the lowest SNR_D at the largest viewing distances while the higher spatial frequencies are discerned with the lowest SNR_D at shorter viewing distances. In Fig. H-15, we compare the thresholds measured with a viewing distance of 28" to that measured at an optimum distance, i.e., the observer was permitted to choose the viewing distance at will during the experiment.

D. RETINAL FLUCTUATION NOISE LIMITATIONS

Both the MRT and MDT are measured under optimum laboratory conditions. In general, the dynamic temperature range of the test patterns is small and the display gain (contrast) control can be set at a very high value. When viewing a real scene with a wide dynamic temperature range the ability to adjust display gain may become limited. In Case 1 of Fig. H-16, the incremental luminance swing ΔL_H is not far different from that of ΔL_L . The average display luminance L_{av} can be set at some low comfortable level just high enough to prevent clipping the scene blacks. If desired, both L_{av} and G_v , the display (or video) gain can be increased to improve the contrast of the displayed images but the exact values, so long as they are high enough is not critical. In Case 2, we assume that the incremental luminance swing ΔL_H required to image large scene temperature swings has become so large that the observer must both increase L_{av} and decrease gain to stay within the display's dynamic range.

It is postulated that a retinal fluctuation noise exists due to photoconversion of display photons to sensor impulses within the observer's retina. The effect of increasing display luminance is to increase the retinal fluctuation noise and the decrease in gain decreases the incremental signal ΔL_L and therefore, ΔL_L may become imperceptible because of the overall decrease in signal-to-noise ratio.

A number of psychophysical experiments were performed to determine the effect of display luminance on the detection of square images and the interaction of display luminance with image detection and video gain. The result of one such experiment is shown in Fig. H-17. As can be seen, an increase in display gain must accompany an increase in display luminance when operating in the retinal fluctuation noise limited region. From the experiments it was found to be possible to estimate the individual contributions of the system and retinal fluctuation noise to the total noise as shown in Fig. H-18.

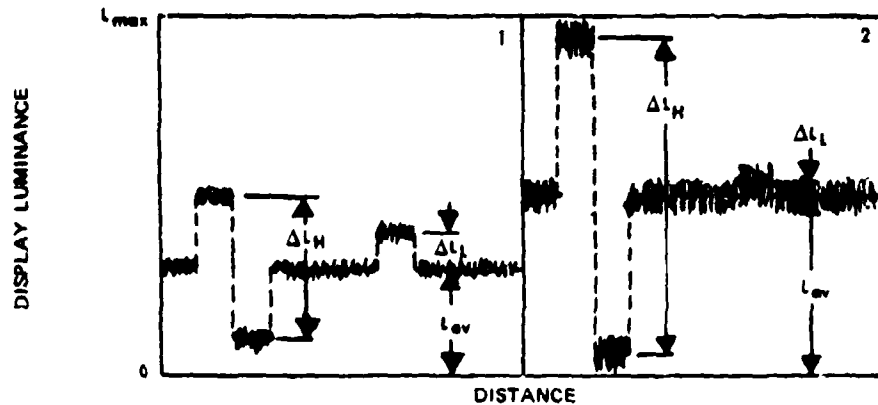


Fig. H-16 — Case 1. Displayed image has small dynamic range, moderately low brightness and adequate video gain. Case 2. Large input signal, L_H , requires an increase in display brightness and a reduction of video gain. L_L/L_{av} is reduced in turn.

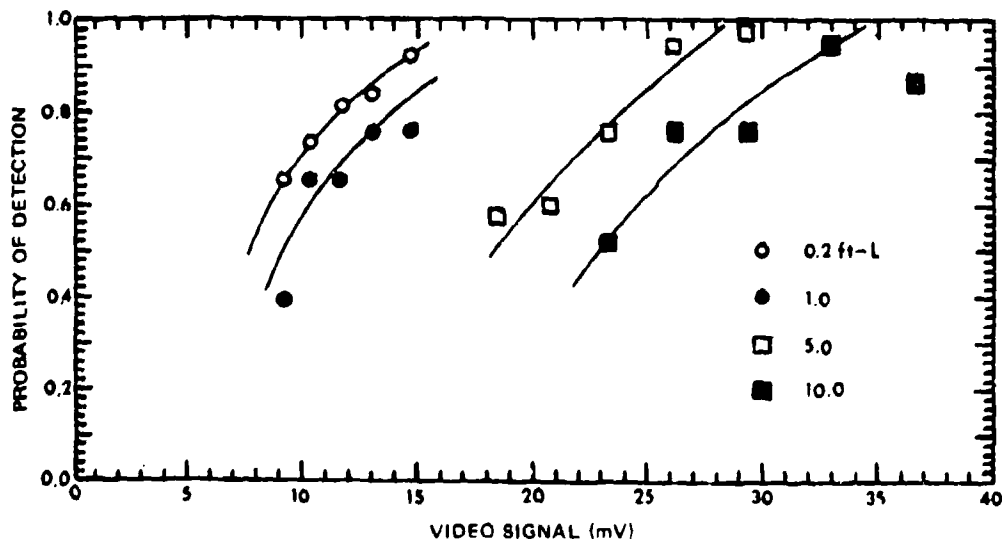


Fig. H-17 — Probability of detection corrected for chance vs video signal, α , for the 8×8 scan line square. Display gain = 5.5. Televised images, 30 frames/s. ≤ 25 scan lines.

The conclusion drawn from the experimental program is that a retinal fluctuation noise exists, and the implication is that the MRT and MDT values obtained will not always be achieved in imaging real scenes.

The SNR_p equation, including retinal fluctuation noise, will take the form (Ref. H-2)

$$SNR_p = \left[\frac{e T_e}{\alpha} \right]^{1/2} \frac{R_f(N)}{N} \frac{[(\eta_e/K_p)/4T^2](A_r/A_d)G_v K_d \Delta i}{\left[\left(\frac{\eta_e K_p}{4T^2} \frac{A_r}{A_d} G_v K_d \right)^2 \beta(N) + \frac{\eta_e K_d}{4T^2} \frac{A_r}{A_d} e \phi_{av} \right]^{1/2}} \quad (H-4)$$

APPENDIX H

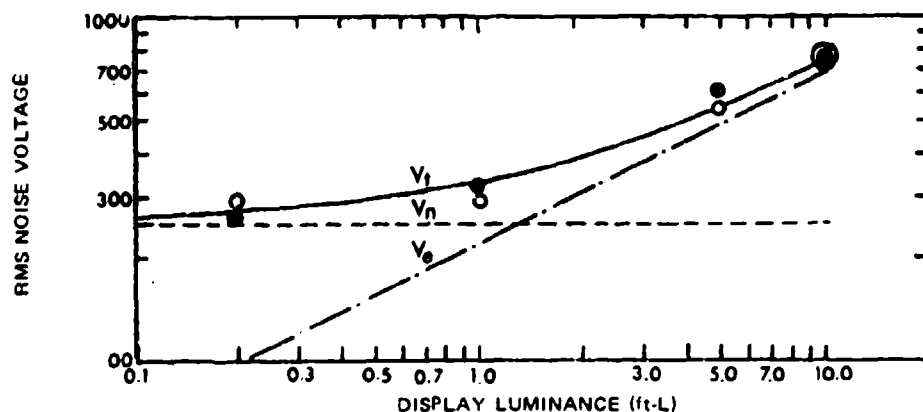


Fig. H-18 — (---) Estimated fixed system noise, (---) estimated retinal photoconversion noise, and (—) total noise. Measured noise data for a (○) 4 × 4 and a (●) 8 × 8 scan line square image.

where the terms are as before except that

- η_e is the quantum efficiency of the observer's eye,
- K_p is the conversion constant (photons/lumen),
- T is T_{stop} of the observer's eye,
- (A_r/A_d) is the ratio of picture area on retina to that on the display,
- G_v is video gain,
- K_d is the phosphor conversion constant (lumens/ampere),
- ϕ_{av} is the average luminous flux received from the display (lumens),
- Δi is the incremental signal current (A), and
- i_{nb} is rms noise current due to scene background photons.

The ϕ_{av} term above can be converted to current in the video channel by dividing by K_d the display conversion gain. It is therefore clear that we can refer the eye noise term to an equivalent noise current in the video channel. When the perceived SNR is sensory system noise limited, Eq. (H-4) reduces to

$$\text{SNR}_p = \left[\frac{\epsilon T_e}{\alpha} \right]^{1/2} \frac{R_{sf}(N)}{N} \frac{\Delta i}{i_{nb} [\beta(N)]^{1/2}}, \quad (\text{H-5})$$

which is seen to be independent of operator-to-display viewing distance (except to the extent that the eye MTF effects are included in $R_{sf}(N)$).

When the SNR is primarily retinal fluctuation noise limited, Eq. (H-5) becomes

$$\text{SNR}_p = \left[\frac{\epsilon T_e}{\alpha} \right]^{1/2} \frac{R_{sf}(N)}{N} \frac{[(\eta_e K_p)^{1/2} / 2 T] (F_L / D_v) \Delta \phi_r}{(e \phi_{av})^{1/2}}, \quad (\text{H-6})$$

where $F_L / D_v = (A_r / A_d)^{1/2}$ where F_L is the air equivalent focal length of the eye and D_v is the display viewing distance. As can be seen, the SNR_p is now inversely proportional to viewing distance.

NRL REPORT 8311

In addition to retinal fluctuation noise, there are generally other image defects which may cause the MRT to be higher than predicted. Some causes are unbalance between adjacent detector channels due to either image cell detectivity differences or preamp channel gain variations, and extraneous noise such as switching transients resulting from the sampling processes.

REFERENCES

- H-1 Coltman, J.W., and Anderson, A.E., Noise Limitations to Resolving Power in Electronic Imaging, *Proc. IRE* 48(5), 1960.
- H-2 Rosell, F.A., Performance Synthesis of Electro-Optical Sensors, EOTM No. 575. Final Technical Report, Contract No. DAAK-53-75-c-0225, Night Vision Laboratory, Ft. Belvoir, Va., Feb. 1977.

Appendix I

OBSERVER RESOLUTION REQUIREMENTS

F. A. Rosell

A. INTRODUCTION

In this appendix, it is shown that the equivalent bar pattern approach which has seen long use in predicting the range at which scene objects can be visually discriminated on a sensor's display has restricted validity. It was formerly assumed that the number of resolution lines required per minimum object discussion was relatively a constant for a given object. More recently it has been found that the number is variable with signal level and that the variability is considerable. It is also shown that the resolution required can be a strong function of scene object viewing aspect angle.

B. HISTORICAL APPROACHES

One of the earliest attempts to functionally relate threshold resolution with the visual discrimination of images of real scenes is attributed to John Johnson (Ref. 6.1). The levels of visual discrimination were arbitrarily divided into four categories: detection, orientation, recognition, and identification, with detection being the lowest and identification being the highest discrimination level. The basic experimental scheme was to move a real scene object such as a vehicle out in range until it could be just barely discerned on a sensor's display at a given discrimination level. Then the real scene object was replaced by a bar pattern of contrast similar to that of the scene object. The number of bars in the pattern per minimum object dimension was then increased until the bars could just barely be individually resolved. In this way the detectability, recognizability, *etc.* of the scene object can presumably be correlated with the sensor's threshold bar pattern resolution. The basic idea makes sense—the better the sensor's resolution, the higher the level of visual discrimination should be.

In addition to sufficient resolution, Johnson noted that image SNR had to be sufficient but the definition of image SNR was not clear.

By use of the methods of Chapters IV and V, image SNR values can be defined for bar patterns and other simple geometric shapes. By 1970, it appeared appropriate to test the Johnson criteria further by using improved image SNR concepts. For analysis purposes, an equivalent bar pattern was defined. This bar pattern concept is essentially the same as proposed by Johnson except that the bar lengths are made equal to the length of the scene object whereas in the Johnson criteria the lengths are unspecified. The justification for this approach is that many objects will be more easily detected, recognized, or identified when viewed broadside as opposed to head-on, and this notion can be quantitatively noted by including the maximum object dimension in the image SNR definition. The Navy, as will be discussed, has used a pixel approach in an attempt to realize the same objective. To test the Johnson concept by using the equivalent bar pattern, images of four different vehicles were televised against a uniform background. Additive white noise was added to the displayed image and background to

APPENDIX I

vary the SNR. The probabilities of correct recognition were measured as the type of vehicle and the image SNR_D was randomly varied. The result is shown in Fig. I-1. The SNR for the real object was calculated on the basis of the peak-to-peak signal excursion within the vehicle outline, the area of a bar of width equal to 1/8 the object's minimum dimension, of length equal to the object's longest dimension, and the rms noise. The vehicles were then replaced by a bar pattern of the appropriate spatial frequency for recognition, and the probability of discerning the bar pattern was determined and plotted in Fig. I-2. The results appear to confirm the Johnson hypothesis. However, when the same vehicles were imaged against a more complex background (though not so complex as to obscure the vehicle outline), the SNR_D needed at a given probability and the spread in the data increased as shown in Fig. I-3. The increase in SNR_D required could alternatively be treated as a need for an increase in resolution. Note also, that it is difficult to define the signal excursion and average contrast for real scene objects.

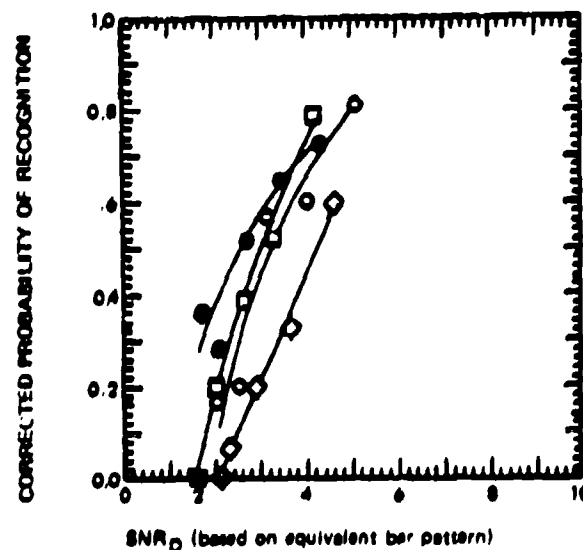


Fig. I-1 — Probability of recognition vs SNR_D for a ○ tank, ◇ radar half track, □ van track, and ● derrick bulldozer. Background was uniform.

In the concepts discussed above, resolution is not defined by the number of scan lines or detectors but rather, by the threshold resolution as defined by an MRT curve. For an ideal sensor, which is defined as one with a unity MTF, the SNR_D can be written as

$$\text{SNR}_D = \left[\frac{T_s}{\alpha} \right]^{1/2} \frac{1}{N} \frac{\Delta I}{I_n}, \quad (I-1)$$

where the terms are as defined in Chapter IV and I_n is the rms noise.

Two SNR_D curves for an ideal sensor are plotted in Fig. I-4. Also shown is the observer's threshold SNR_{DT} which is very nearly a constant at optimum viewing distance. The intersection of the SNR_D and SNR_{DT} curves gives the threshold resolution for the sensor aided observer. Note that doubling the SNR_D by increasing the incremental signal current from level 1 to level 2, doubles the threshold resolution from N_1 to N_2 .

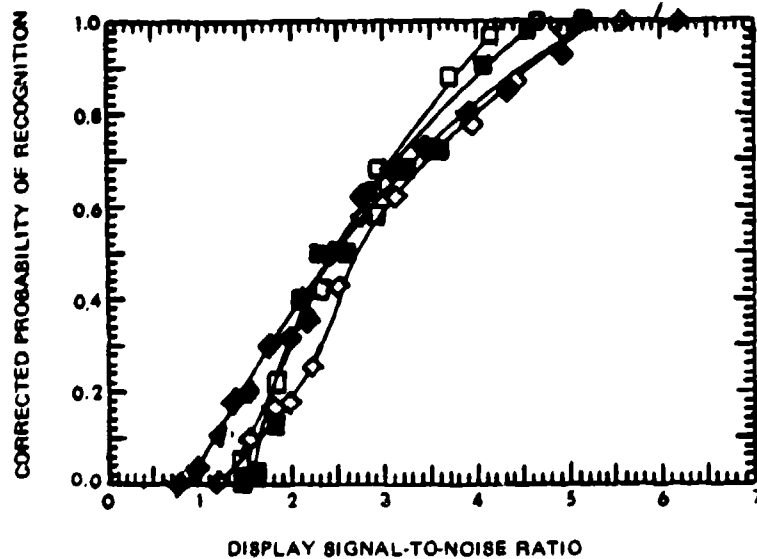


Fig. 1-2 - Probability of bar pattern detection vs SNR_{D1} for pattern of area equal to average real object area of $N = \blacksquare$ 329, \square 396, \diamond 482, \blacklozenge 635 lines/picture height

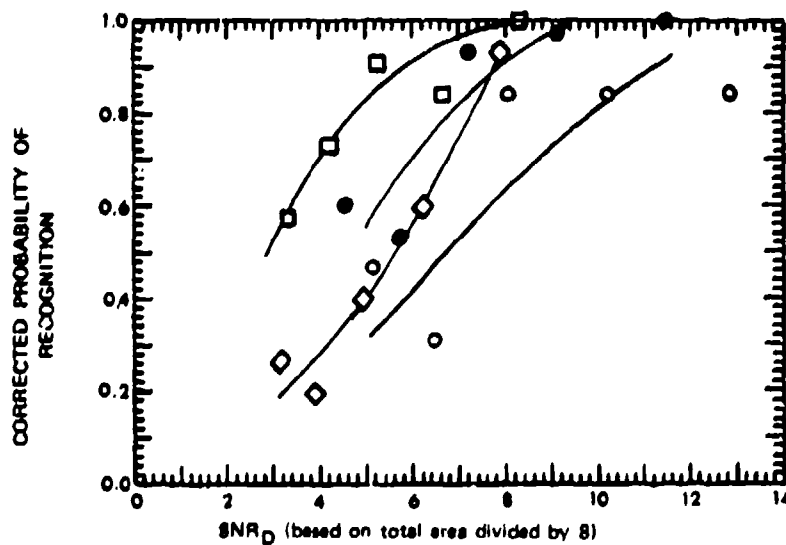


Fig. 1-3 - Probability of recognition vs SNR_D for a \circ tank, \diamond radar half track, \square van truck, and \bullet derrick bulldozer, grass-trees background, televised imagery at 875 lines, 25 frames/s

APPENDIX I

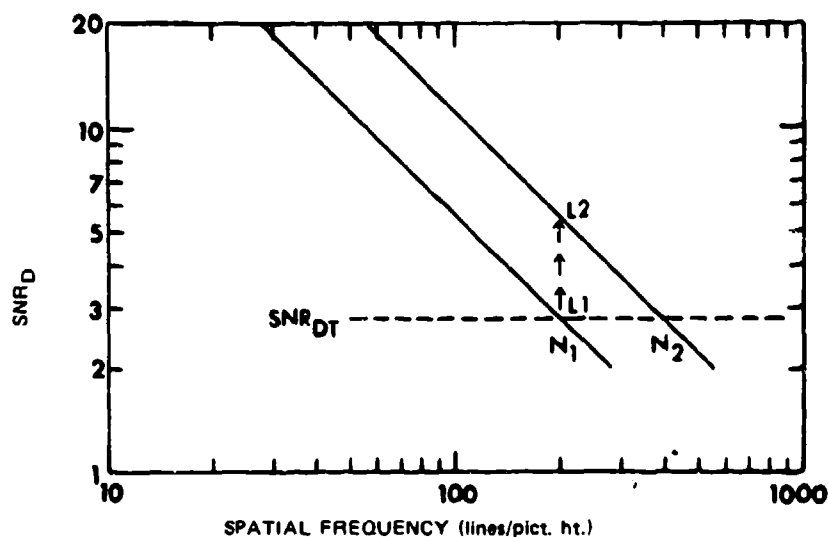


Fig. I-4 — SNR_D vs spatial frequency for an ideal sensor. Doubling SNR_D from L_1 to L_2 doubles threshold resolution from N_1 to N_2 .

In Fig. I-5, we plot three SNR_D curves for a real nonideal sensor at three different light levels. At some low-light level assume that the threshold resolution is N_1 . Doubling the SNR_D increases the threshold resolution from N_1 to N_2 . For Case 1, the resolution increases from 80 to 140 lines/picture height; not quite 2 times. For Case 2, the increase is from 190 to 290; about 1.5 times. For Case 3, the increase is only about 1.15 times. Thus, for a system including finite apertures, it would appear that an increase in SNR_D at low spatial frequencies would be much more effective than a similar increase at high spatial frequencies since at low spatial frequencies, an increase in SNR_D results in a greater increase in threshold resolution. An increase in SNR_D at high spatial frequency may result in no improvement in threshold resolution at all. However, an improvement in overall image quality will result because of the increase in SNR_D at all of the spatial frequencies below the threshold.

The probability of detecting simple geometric shapes such as bar patterns generally follows a normal cumulative probability curve with unit variance as shown in Fig. I-6(a). It has been assumed that the probability of recognizing real scene objects will follow the same functional relationship. In Fig. I-6(a) we see that increasing the SNR_D by about 2 increases the probability of discerning a given bar pattern from 50% to near 100%. Also, as discussed above an increase in SNR_D of 2 at line number N , will increase the system's limiting resolution to $2 N_1$. It can therefore be argued that the increase in probability of detecting the bar pattern of frequency N_1 is due to the increase in limiting resolution. Since limiting resolution and SNR_D are linearly related in 1:1 correspondence for the ideal sensor, we could alternatively plot the cumulative probability curve as a function of threshold resolution as shown in Fig. I-6(b).

The Night Vision Laboratory hypothesized that the probability of correct recognition vs threshold resolution was the correct approach (Ref. 6-3) and attempted, through field tests, to prove its validity. Although the results were somewhat subject to interpretation and not entirely conclusive, the probability vs threshold resolution approach appeared to be superior to the probability vs SNR_D approach. It was stated, however, that both approaches give the same result at the 50% level of probability.

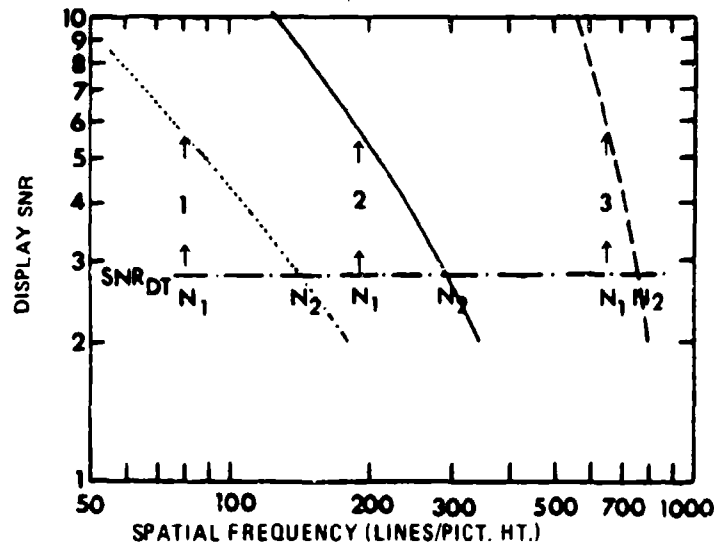


Fig. 1-5 — SNR_D vs spatial frequency for a typical LLLTV sensor for three values of input photocurrent. (...) Case 1, (—) Case 2, (---) Case 3. If N_1 is the threshold frequency at one level, N_2 is the new threshold frequency when SNR_D at N_1 is doubled.

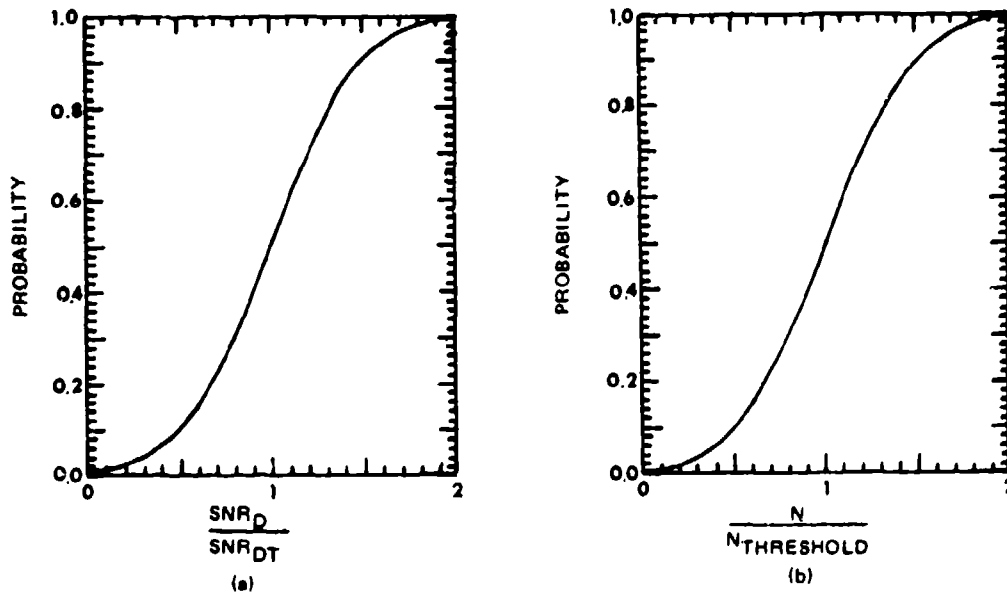


Fig. 1-6 — Probability of discerning bar pattern vs (a) SNR_D normalized to the threshold SNR_{DT} and (b) spatial frequency N normalized to the threshold resolution

APPENDIX I

The work of Johnson and the previously described work of Rosell did not broadly range over the methods of limiting image quality, *i.e.*, aperture effects (MTF limitations) versus noise limitations. Discrepancies were noted between crisp image quality of broadcast images aperture limited to 340 TV lines per picture height, and the poor image quality limited to 340 TV lines per picture height by noise in low-light-level imagery.

In an effort to understand the difference in image quality, when both images yielded the identical values of limiting resolution, O'Neill and Rosell in independent experiments, showed that neither approach is valid Refs (6-4 and 6-5). Even further, it was shown that the original Johnson criteria and the equivalent bar pattern approaches are also untenable because the number of lines required per minimum object dimensions is a variable depending on some function of the video signal-to-noise ratio. This result should have been foreseen. Its reasonableness can be inferred from the following simple illustration. The maximum resolution of a standard television broadcast camera is bandwidth or aperture limited, to approximately 340 lines per picture height. Picture quality can be very high indeed, with good gray shade rendition, and the picture may be near noise-free. Contrast this with the picture obtainable from a low-light-level television sensor which is irradiance level limited to 340 lines per picture height. The picture observed is very noisy, and only a few shades of gray can be differentiated. Clearly, the picture obtained from the aperture limited broadcast camera is substantially superior to that obtained from the noise limited LLLTV sensor. Thus, the threshold resolution observable is not necessarily a reliable guide to a sensory systems performance.

Rosell's experiments were conducted to determine the resolution required to identify televised human faces under two extremes: the case where scene light level is more than adequate as in sunlight and where the scene light level is very low as at night. Under high light level conditions the sensor resolution is primarily aperture response limited while under low light level conditions the sensor resolution was primarily noise limited. It was found that when the resolution was primarily aperture response limited, 5.8 lines per face width were needed for a 50% probability of correct identification while when the resolution was primarily noise limited 12.4 lines were required for the same probability. About 1.8 to 2.0 times more resolution, measured in the threshold sense was required for 100% identification probability in both cases *i.e.*, about 11 lines per face width in the aperture limited case and 23 lines per face width in the noise limited case.

O'Neill performed extensive experiments by using televised ship silhouette images. The televised images were photographed and later sorted according to the level of visual discrimination each photograph provided. Seven discrimination tasks are defined as shown in Table I-1. In Naval Air Development Center models, pixels are used to describe resolution requirements. The number of pixels required to perform a given task is found by creating two equivalent bar patterns: one with horizontal and the other with vertical bars. The product of horizontal and vertical resolutions represents the number of pixels. For example, if 3-foot resolution is needed to achieve a given level of discrimination and the ship is 30 x 300 feet in size, the number of pixels is 10 x 100 or 1,000. However, pixels are converted to equivalent bar pattern resolution at the ship for discussion purposes.

To continue, O'Neill's results were evaluated in terms of the resolution required in the vertical or ship height direction with the results shown in Table I-1. The ship was 46 ft high and 520 ft long. The data in Table I-1 are the results obtained when the light level was very

Table I-1 -- Resolution Required for the Various Levels of Ship Classification

Discrimination Task	Pixels Required	Resolution at Ship		No. of Lines per Ship (height)
		(feet)	(meters)	
0 Detect object on horizon sky	36	25.78	7.86	1.78
1 Recognize as vessel	100	15.47	4.72	2.97
2 Recognize ship structure	500	6.9	2.10	6.65
3 Recognize ship type	1,000	4.89	1.49	9.4
4 Classify king posts	2,000	3.46	1.05	13.3
5 Discern radar detail	4,300	2.36	0.72	19.5
6 Detect 40 mm gun barrel	12,000	1.41	0.43	32.6

high so that the sensor was primarily aperture response rather than noise limited. For initial analytical purposes, it is assumed that the resolution required by the observer at the ship is a constant independent of light level. O'Neill provides data showing the range at which the observer visually discriminated the targets at various light levels which we can use to calculate the angular subtense of the assumed required resolution. Then, knowing the camera field of view (2.1° in the vertical), we can calculate the apparent TV camera angular resolution as the ratio of the resolution required (from Table I-1) for any given visual discrimination-level to the threshold detection range which is shown in Table I-2. Also shown are the spatial frequencies corresponding to a bar pattern with bar of angular extent equal to the apparent angular resolution. We plot these spatial frequencies on Fig. I-7 along with the threshold TV camera resolution measured using bar patterns. As can be seen the apparent resolution is much less than the threshold camera resolution at the lower light levels. It should be noted that the TV camera had to be quite highly aperture corrected in order to achieve the measured curve shown. It is possible that aperture correction is not very effective in improving the visual discrimination of real scene objects (as opposed to bar patterns). In Fig. I-8, we plot the ratio of apparent to measured threshold resolution.

In the above discussion it was assumed that the resolution required for a given visual discrimination level is a constant independent of light level which leads to the conclusion that the apparent resolution is less than measured. Alternatively it could be assumed that more lines are required per ship height at the 50% probability level to discriminate an object at low light level (noise limited) conditions.

As the level of visual discrimination increases at a given light level, the resolution measured in feet or meters at the scene object must decrease as can be seen from column 2 of Table I-2. Observe that at 10^{-6} f.t.c., the apparent angular resolution corresponding to the assumed resolution required divided by the range, is approximately the same for all the discrimination levels. As the light level increases to 3×10^{-6} f.t.c., the apparent angular resolution required for any given discrimination level decreases but again, the apparent angular resolution required is approximately a constant independent of the discrimination level. This same result is observed as the light level increases to 10^{-5} f.t.c. In Fig. I-9, the apparent angular resolution required is plotted as a function of the visual discrimination levels to emphasize these results.

APPENDIX I

Table 1-2 - Apparent Threshold TV Resolution vs Visual Discrimination Level at Various Photosurface Light Levels

1 Visual Discrimination Level	2 Assumed ^a Resolution at Ship (meters)	3 Threshold Range (km)	4 Apparent ^b Angular Resolution (μrad)	5 Apparent TV Resolution (Lines/ Picture height)
Photosurface Illuminance = 10^{-6} ft-candles				
0	7.86	45.0	175	197
1	4.71	23.5	201	172
2	2.10	14.0	151	229
3	1.45	6.8	219	157
				Avg = 189
Photosurface Illuminance = 3×10^{-6} ft-candles				
0	7.86	78.0	100	342
1	4.72	44.0	107	322
2	2.10	26.5	80	433
3	1.49	20.0	75	462
4	1.05	8.2	128	269
5	0.71	5.4	132	262
6	0.43	3.0	143	241
				Avg = 333
Photosurface Illuminance = 10^{-5} ft-candles				
0	7.86	120.0	65.5	526
1	4.72	68.0	69.3	498
2	2.10	33.0	63.9	539
3	1.49	20.0	74.5	463
4	1.05	13.0	80.7	423
5	0.71	9.4	75.7	455
6	0.43	5.6	76.7	449
				Avg = 479

^aFrom Table 1-1

^b 10^3 times column 2 divided by column 3

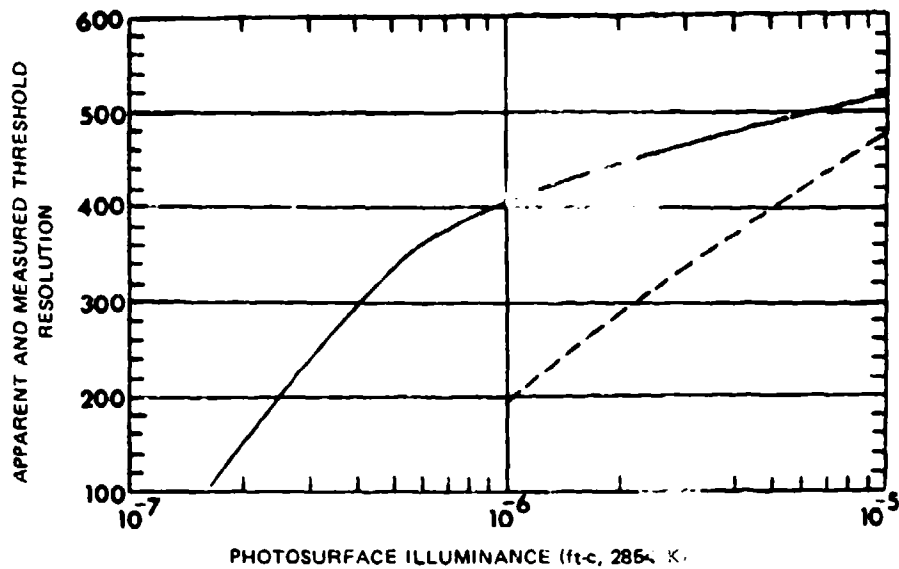


Fig. 1-7 — Threshold resolution vs photosurface illuminance. (—) measured using bar patterns and (---) inferred from real object discrimination measurements assuming a resolution requirement which is independent of light level.

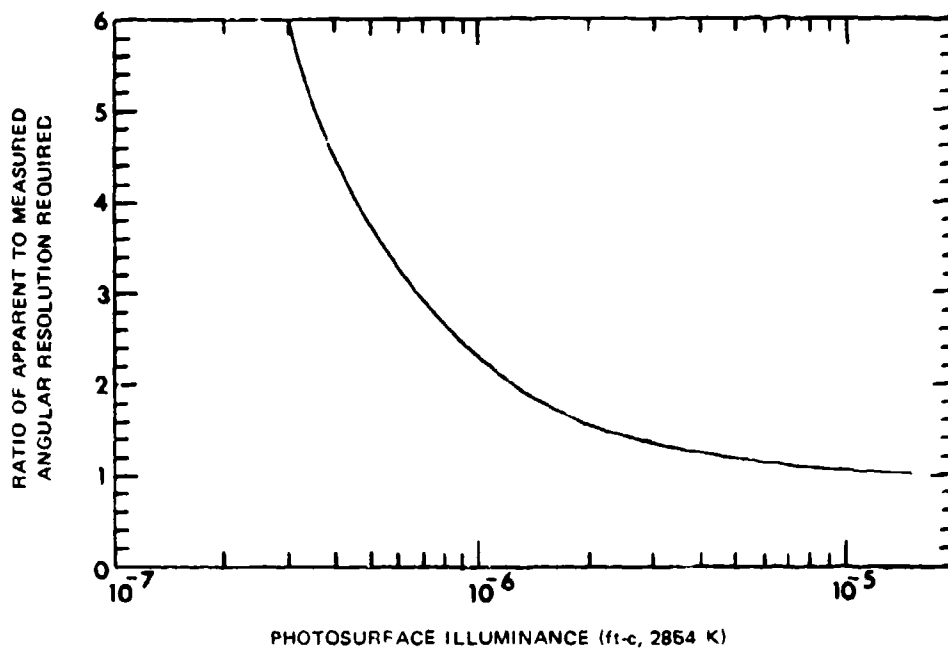


Fig. 1-8 — Ratio of apparent to measured angular resolution required to visually discriminate the ship silhouette as a function of photosurface illuminance

APPENDIX I

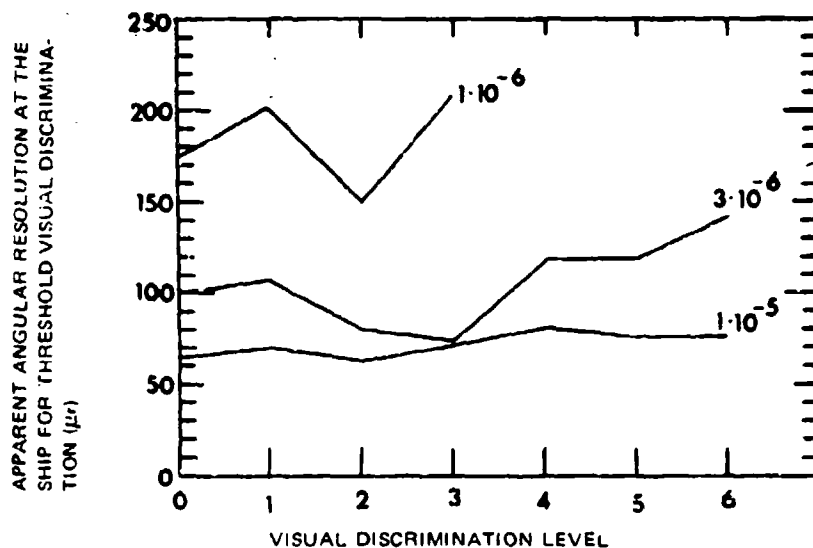


Fig. 1-9 — Angular subtense of the apparent spatial resolution at the ship for threshold visual discrimination vs the visual discrimination level

The tentative conclusion is that as the signal levels decrease, the number of lines required per minimum object dimension to perform a specified visual discrimination task must increase but the relative increase is nearly the same for all the discrimination levels.

A third set of data is shown in Fig. 1-10 which represents data measured at the Night Vision Laboratory by R. Flaherty which again shows that the number of resolvable lines per target height required to recognize a real scene object increases with decreasing light level. The recognition task in this experiment consisted of discriminating front and side views of a tank, an APC, and a truck (9 signatures in all).

The above data conclusively show that an equivalent bar pattern approach cannot employ a fixed line number criterion for any given level of visual discrimination but will vary depending on the degree to which the sensor's resolution is noise or aperture response limited.

To make use of the O'Neill data, the broad area video SNR_{VO} was estimated by using the relation

$$\text{SNR}_{VO} = \frac{SAE_h/e_v e_h}{[2eSAE_{av} \Delta f_c/e_v e_h]^{1/2}} \quad (1-2)$$

where for the case under consideration S is the photosurface response to 2854K light, A is the effective photosurface area, E_h is the highlight and E_{av} is the average photosurface irradiance, $e_v e_h$ is the scan-efficiency, e is the charge of an electron, and Δf_c is the video bandwidth defined by

$$\Delta f_c = \frac{\alpha N_c N_f}{2 t_f \cdot e_v e_h} \quad (1-3)$$

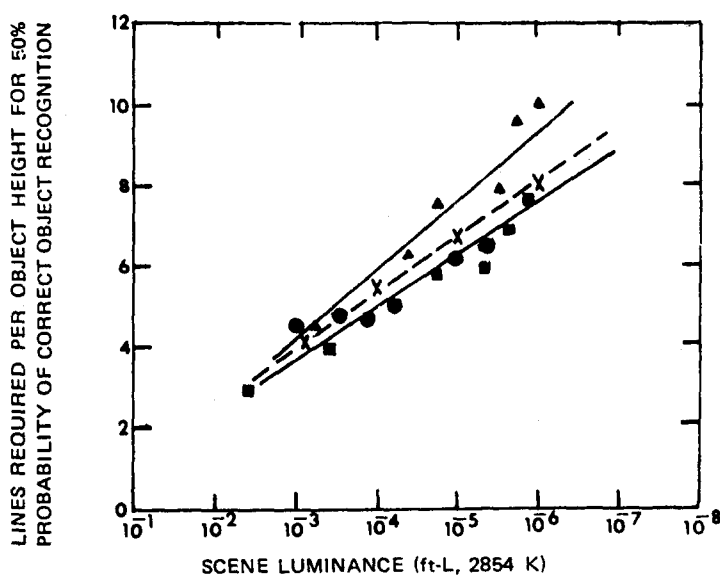


Fig. I-10 — Lines required per object height for 50% probability of correct object recognition vs scene luminance level

where α is the picture aspect ratio (H/V), N_e is the noise equivalent bandwidth, N_v is the number of active scan lines, and t_f is the frame time. In the above, we have assumed that the sensor is photoelectron noise limited. The ratio of apparent to measured angular resolution is plotted vs the SNR_{VO} calculated using Eqs. (I-2) and (I-3) and the available data in Fig. I-1. It can be seen that with broad area video signal-to-noise ratios below about 3 to 5, substantial increases in the number of lines per minimum scene object dimension may be required for any visual discrimination task.

It is seen that the equivalent bar pattern approach as used in the past is not valid. However there is no proven alternative at present. One possible near term solution is to adjust the number of lines required per minimum object dimension at the 50% probability level on the basis of the broad area SNR in accord with the curve of Fig. I-11. It should be emphasized that the curve of Fig. I-11 is based on very little data derived from an experiment which was not specifically designed to determine a correlation between video SNR and resolution criteria. However, it is believed that the curve is of the correct form if not of precise values. A method of using the data will be developed and discussed in Chapter 6 including methods of estimating higher levels of probability.

C. SCENE OBJECT VIEWING ASPECT VS RESOLUTION REQUIRED

The results of an NVL aspect angle experiment are partially shown in Figs. I-12 through I-15. These experiments were performed using scale models viewed through an image intensifier. The resolution of the intensifier was varied through light level control and was measured by viewing a repetitive square wave pattern of 7:1 aspect and contrast equal to that of the object to be recognized or identified. The resolution was set to zero at the beginning of each set of trials and increased until the object was correctly recognized at the 80% probability

APPENDIX I

level. As noted in the previous section, the number of lines needed per minimum object dimension may be light level dependent but this aspect of the problem was not investigated in the experiment.

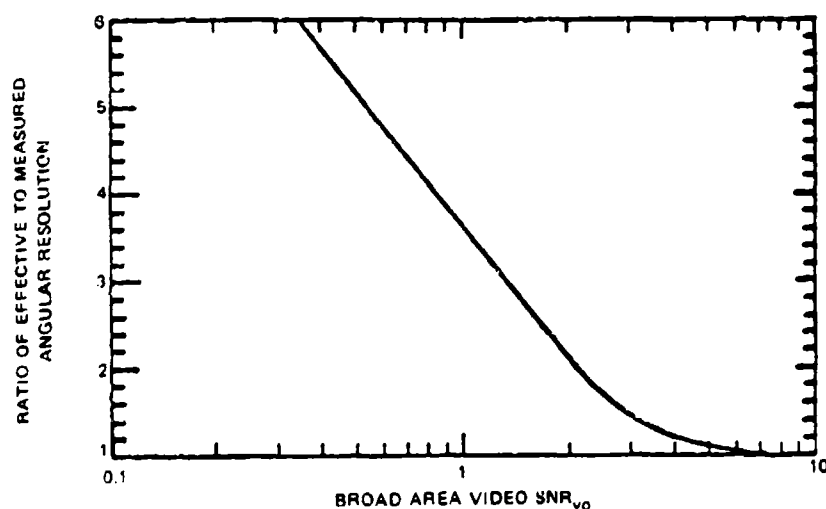


Fig. I-11 — Ratio of effective to measured angular resolution required to visually discriminate the ship silhouette as a function of the broad area video SNR

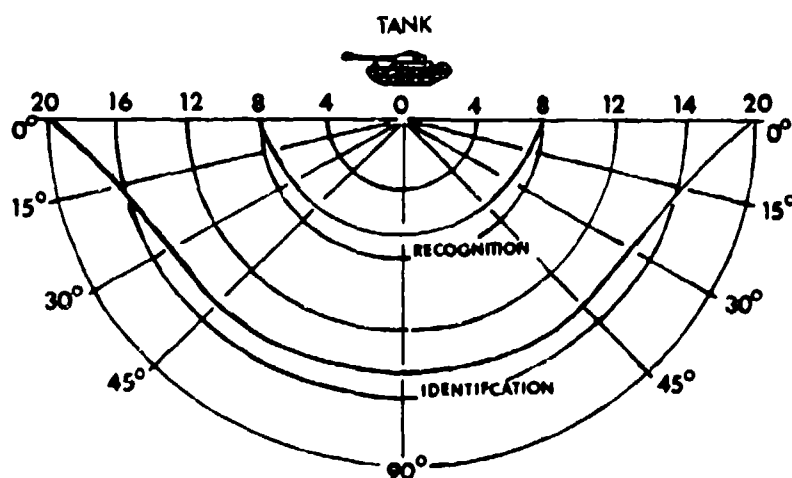


Fig. I-12 — Number of lines on half cycles per minimum dimension required for recognition and identification of a tank as a function of viewing aspect angle

NRL REPORT 8311

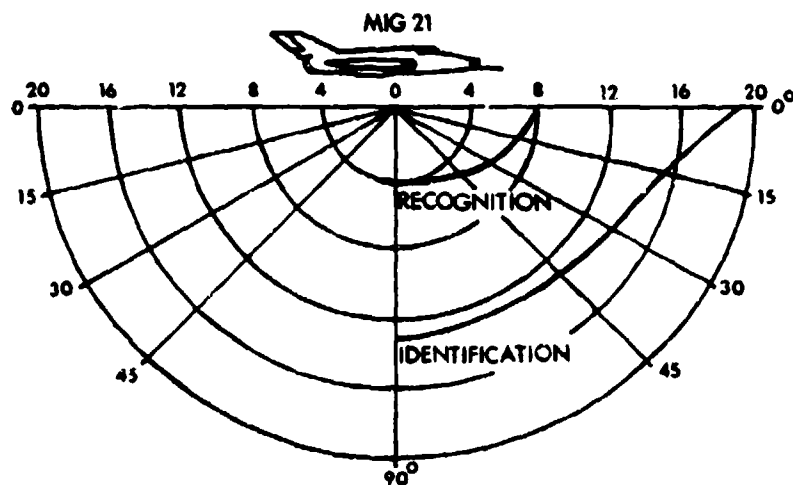


Fig. 1-13 -- Number of lines or half cycles per minimum dimension required for recognition and identification of a MIG 21 as a function of viewing aspect angle

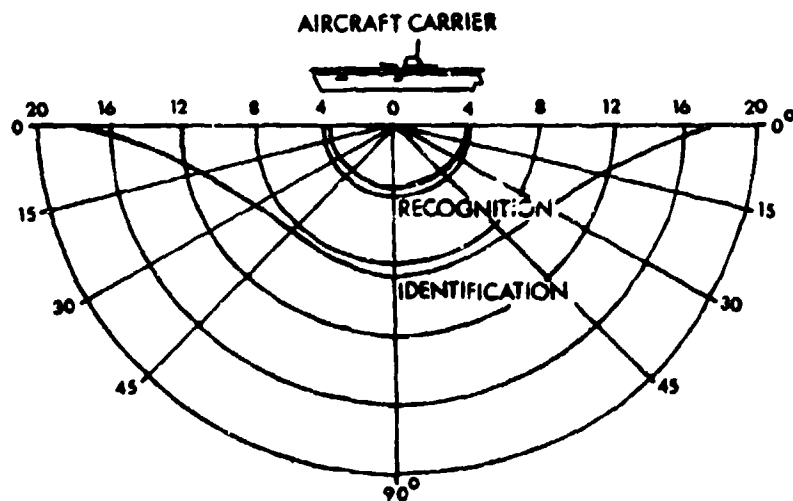


Fig. 1-14 -- Number of lines or half cycles required the minimum dimension required for recognition and identification of an aircraft carrier as a function of viewing aspect angle

APPENDIX I

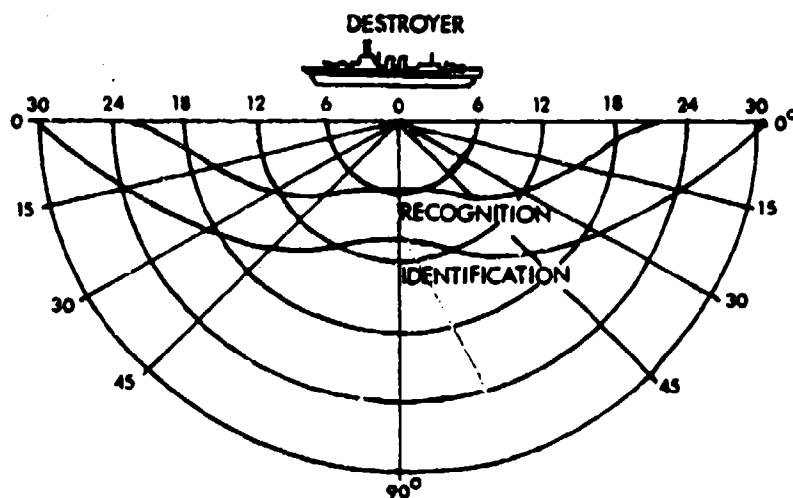


Fig. I-15 — Number of lines on half cycles required per minimum dimension required for recognition and identification of a destroyer as a function of viewing aspect angle

Table I-3 — Number of Lines or Half Cycles Required per Minimum Object Dimension for Recognition

Object	Length-to-Width Aspect Ratio	Lines or Half Cycles/Minimum Object Dimension
Battleship	16/1	5.6
Destroyer	12/1	9.0
Aircraft Carrier	15/1	9.0
P.T. Boat	12/1	6.0
Passenger Ship	12/1	6.0
Fighter	6/1	6.0
Jet Transport	9/1	5.0
Tank	2/1	7.0
Armored Personnel Carrier	2/1	7.0

NRL REPORT 8311

As can be seen in Fig. I-12, the number of lines needed for recognition of a tank is about 7 in the side aspect and 8 head-on while identification requires about 13 on the side and 20 head-on. The results for the MIG 21 are similar to the aircraft carrier except for nose on recognition. The destroyer is characterized by a generally greater discrimination difficulty. In Table I-3, the resolution required for side aspect recognition, as measured in the same manner as for the above results, is given.

No single, unique number can be associated with any given level of visual discrimination. The analyst must therefore exercise judgment. It is clear that generally higher levels of visual discrimination will require generally higher levels of sensor resolution but that overlap in resolution requirement between levels will exist. For example 21 lines are required to recognize a destroyer in the frontal aspect while only 8 lines are needed to identify an aircraft carrier in the beam aspect.

INDEX

A

Aerosols, 25, 31
 urban, 25
 rural, 25
 maritime, 26
 continental, 26
 Anderson, A.E., 205
 Aperiodic object, 65
 Aperture, aperture response, 51, 64, 206
 Atmospheric transmission, 30
 Tables, 32

B

Backgrounds, 8
 Sea, 10
 Bandwidth, reference, 59, 78.
 Bar pattern, 66
 Barnard, 162
 Barnes, R&M., 50, 181
 Blur circle, 69

C

Carbon dioxide, 23
 Carbon monoxide, 24
 Channel, detector, 49
 Channel, SNR, 49, 79
 Characterization of scene, 119
 CIE, 143
 Clear line of sight, 119
 Cold shield, 61
 Conversions, 33
 Relative humidity, 33, 43
 Absolute humidity, 33, 43
 Dew point, 33
 Torr, 33
 Colman, J.W., 212
 Coordinate systems, 113
 Czerny, Z., 50, 181

D

D*, detectivity, 61, 210
 deVries, Hessel, 83, 181
 Diffraction limit, 69
 Display search, 127
 Display SNR, 49, 79
 Dwell time, 61
 Dynamic model, 111

E

Equivalent Temperature Difference, 18
 Extinction coefficient, 30

F

Flaherty, R., 246
 FLIR, 55
 Fourier methods, 62, 64, 162

G

Glimpse, definition, 122
 Grafenwhör field measurements, 26

H

Hudson, R.D., Jr., 167

I

J

Jacobs, Q.M., 162
 Jamieson, J.A., 160
 Johnson, J., 237

K

Koschmieder relation, 31
 Keller, R.B., 125

INDEX

L

Lamar, E.S., 126
Lavin, H.P., 53
LED, 55
Leqault, R., 91
LIDAR, 27
Line pairs, 63
Line spread function, 64
LOWTRAN code, 21, 31

M

Marsam II model, 128
Matched filter concept, 181
Methane, 24
Mie scattering, 26, 31
Minimum Detectable Temperature
(MDT), 90, 160, 175
Minimum Resolvable Temperature
(MRT), 50, 88, 94, 160, 175, 178, 179
Mixed gases, 31
Molecular absorption, 29

N

NEAT, 49, 61, 79, 160, 163
Nitrogen, 24
Nitrous Oxide, 24
Noise equivalent bandwidth, 69, 81
Noise equivalent power (NEP), 210, 213
Noise filtering factor, 69, 82
Noise increase function, 81
Nomenclature, 149
Nomogram, atmospheric transmittance, 34, 40
Nyquist frequency, 215

O

Observer threshold, 90
O'Neill, G., 104, 243
Oxygen, 24
Ozone, 24

P

Parallel scan, 56
Pearson, G.E., 128
Perceived SNR, 49
Periodic bar pattern, 65, 87, 199
Photoconductive, 212
Photovoltaic, 212

Photopic, 143
Physical target acquisition, 113
Pixel, 102
Point spread function, 64
Probability functions, 112
Probability of visual discrimination, 107
Psychophysical experiment, 191, 232

Q

R

Range interpolation table, 42, 44
Range prediction, 102
Reference bandwidth, 59
Responsivity, 210
Retinal fluctuation, 232
Rose, Albert, 53
Rosell, F.A., 159

S

Saccade, 122
Scene characteristics, 7
Schade, Otto Sr., 156
Scotopic, 143
Search field, 114
Sendall, R., 125, 159, 181
Serial scan, 56
Shade, Dr. Otto, Sr., 50
Shumaker, D.L., 125
SI units, 143
Sky
 overcast, 12, 14
SNR, Channel, 49, 58, 78, 210
 display, 49, 76, 77, 80, 81, 209
 Image, 52
 video, 50, 54, 79, 209
 perceived, 3
Spatial frequency, 71, 72, 73, 74, 76, 80
Symbols, 149
Synchronous integrator, 65
Synchronous integrator, 189

T

Thermal Images, 7
Tomasi and Tampieri, 27
Trucks as targets, 13

U

NRL REPORT 8311

V

Vapor pressure of water, 39
Visual-lobe models, 124
Visual range, 31
Visual search, 119

Willson, 125
Worthy, N., 125
Wozencraft, J.W., 162

X

W

Water vapor, 22
continuum, 31
Williams, L.E., 122

Yarbus, A.L., 122

Y

Z



DEPARTMENT OF THE NAVY
NAVAL MATERIAL COMMAND
ELECTRO-OPTICAL TECHNOLOGY PROGRAM OFFICE
NAVAL RESEARCH LABORATORY
WASHINGTON, D.C. 20375

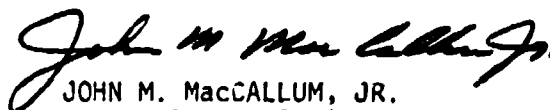
IN REPLY REFER TO
1409-197:RAS:cr
6 August 1979

From: Electro-Optical Technology Program Office
To: Distribution List

Subj: "The Fundamentals of Thermal Imaging"

1. The Electro-Optical Technology Program Office (EOTPO) has received numerous requests for multiple copies of "The Fundamentals of Thermal Imaging Systems", F. Rosell and G. Harvey, editors. Due to the limited size of the first printing and the large initial distribution we are unable to honor all such requests at this time.

2. Individuals and organizations desiring additional copies of the Rosell/Harvey report are requested to indicate their requirements in writing to the EOTPO. The written requests will be used to justify a second printing and to reserve copies from the second printing for the requestors.



JOHN M. MacCALLUM, JR.
Head, Electro-Optical
Technology Program Office

August, 1979

REVISED MAILING LIST

NRL REPORT 8311

"THE FUNDAMENTALS OF THERMAL IMAGING SYSTEMS"

Commander
Naval Air Development Center
(Steve Campana, Code 3011)
Warminster, PA 18974

Commander
Naval Air Systems Command
(AIR-03)
Washington, D.C. 20361

Commanding Officer
US Army Missile R&D Command
DRDMI-TEI
(Tracey Jackson)
Redstone Arsenal
Huntsville, AL 25809

Chief of Naval Operations
Navy Department (OP-98)
Washington, D.C. 20350

Director
Night Vision & E-O Laboratory
AMSEL-NV-VI
(Russell Moulton)
Fort Belvoir, VA 22060

Commander
Naval Sea Systems Command
Naval Sea Systems Command Hdqtrs
(CAPT L.R. Patterson, PMS405)
Washington, D.C. 20362

Commander
Naval Electronic System Command
Naval Electronic Command Hdqtrs
(Albert Ritter, PME107-52)
Washington, D.C. 20361

Grunman Aerospace Corporation
Research Department
(J. L. Selby, 3h/4000)
Bethpage, NY 11714

Revised Mailing List, NRL Report 8311, p. 2

Commanding Officer
US Army Aviation Research & Dev. Command
(Steven Smith)
DRCPM-ASE-TM
PO Box 209
St. Louis, MO 63166

Commanding Officer
Naval Material Command
Naval Material Command Hdqtrs
(Clinton Spindler, MAT 08T2211)
Washington, D.C. 20350

MRJ, Inc.
(Mel Watkins)
7929 Westpark Drive
McLean, VA 20901

Def. Adv. Research Projects Agency
(Steve Zakanyasz, STO)
1400 Wilson Blvd.
Arlington, VA 22209

Commanding Officer
AFAL
(Bill Lloyd, AFAL/WRE-3)
Wright Patterson AFB
Dayton, OH 45433

Commanding Officer
AFAL
(Roger Cranos, AFAL/NVN-1)
Wright Patterson AFB
Dayton, OH 45433

Commanding Officer
Eustace Directorate
USA Air Mobility R&D Laboratory
(J. P. Ladd, SAUDL-EV-MOS)
Ft. Eustace, VA 23604

Mr. Earl J. McCartney
2 Winding Road
Rockville Center, NY 11570

Mailing List, NRL Report 8311, p. 3

Commanding Officer
Office of Naval Research
(CDR Stanley E. Sokol)
223 Old Marylebone Rd.
London, NW1 5th England

Commander
Naval Air Systems Command Hdqtrs
(E. Beggs, AIR 360)
Washington, D.C. 20361

Commander
Naval Air Systems Command Hdqtrs
(Webb Whiting, 633365C)
Washington, D.C. 20361

Commander
Naval Air Systems Command Hdqtrs.
(E.V. Cosgrove, 533351)
Washington, D.C. 20361

Institute for Defense Analysis
(V. Corcoran)
400 Army Navy Drive
Arlington, VA 22202

Superintendent
Naval Post Graduate School
(Dr. Allen E. Fuhs, Code 57FU)
Monterey, CA 92940

Commander
Naval Air Development Center
(Nancy MacMeekin, Code 3011)
Warminster, PA 18974

Officer in Charge
Naval Surface Weapons Center
(L. J. Fontenot, N-54)
Dahlgren Laboratory
Dahlgren, VA 22448

Director
Night Vision & EO Laboratory
(R. J. Bergemann)
Fort Belvoir, VA 22060

Mailing List, NRL Report 8311, p.4

Chief of Naval Operations
Navy Department (OP-03)
Washington, D.C. 20350

Chief of Naval Material
Naval Material Command Hdqtrs
(R. E. Gaylord, 08TE)
Washington, D.C. 20360

Commander
Naval Weapons Center
(Sterling Haaland, 39012)
China Lake, CA 93555

Commander
Naval Ocean Systems Center
(Dr. J. Richter, 532)
San Diego, CA 92152

Commander
Naval Weapons Center
(S. T. Smith, 39403)
China Lake, CA 93555

Commander
Naval Sea Systems Command
Naval Sea Systems Command Hdqtrs
(Toshio Tasaka, 03415)
Washington, D.C. 20362

Defense Advanced Research Projects Agency
(CDR Thomas Wiener)
1400 Wilson Blvd.
Arlington, VA 22209

Hughes Aircraft Co.
(Ken Powers, Rm. 9208, Bldg. 369)
PO Box 92426
Los Angeles, CA 90009

Commanding Officer
Air Force Avionics Laboratory
(Louis Meuser)
AFAL/RWP
Wright Patterson AFB
Dayton, Ohio 45433

Superintendent
Naval Post Graduate School
(LT John Nute, Code 32)
Monterey, CA 92940

Mailing List, NRL Report 8311, p. 5

Defense Intelligence Agency
(Seymour Berler, DTIA)
Washington, D.C. 20301

Chief of Naval Operations
Navy Department (OP-05)
Washington, D.C. 20350

Commanding Officer
Commander Operational Test Forces
(LCDR C. L. Sale, Code 63)
Norfolk, VA 23511

Commanding Officer
AFAL-RWI-3
Air Force Systems Laboratory
(CAPT James D. Pryce)
Wright Patterson AFB
Dayton, OH 45433

Chief of Naval Operations
Navy Department
(CAPT J. H. Eckhart, OP506G)
Washington, D.C. 20350

Commander
Naval Electronic Systems Command
(CAPT L. E. Pellock, PME-107-5R)
Washington, D.C. 20360

Chief of Naval Operations
Navy Department
(B. R. Petrie, OP 987P4)
Washington, D.C. 20350

Commander
Naval Air Systems Command Hdqtrs
(V. A. Tarulis, 360E)
Washington, D.C. 20361

Commander
Naval Sea Systems Command
(CAPT A. Skolnick, PMS-405)
Washington, D.C. 20362

Commanding Officer
National Naval Medical Center
(Elliot Postow, 43)
Bethesda, MD 20014

Mailing List, NRL Report 8311, p. 6

Commanding Officer
Naval Weapons Support Center
(D. E. Douda, 50421)
Crane, IN 47522

Commanding Officer
Naval Avionics Center
(Ronald Wesolowski, 813)
21st & Arlington Avenue
Indianapolis, IN 46218

Commander
Naval Air Test Center
(Lynn C. Krouse, SA83)
Patuxent River, MD 20670

Commanding Officer
Naval Coastal Systems Laboratory
(H. Larrimore, 751)
Panama City, FL 32401

Commanding Officer
Naval Intelligence Support Center
(C. E. Field, 53)
Washington, D.C. 20390

Commander
Pacific Missile Test Center
(Milton R. Marson, 1230)
Point Mugu, CA 92042

Commander
Naval Surface Weapons Center
White Oak Laboratory
(Paul R. Wessel, Code R40)
Silver Spring, MD 20910

Commander
Naval Surface Weapons Center
White Oak Laboratory
(O. Dengel, CR-22)
Silver Spring, MD 20910

Superintendent
Naval Postgraduate School
(E. C. Crittenden, 61Ct)
Monterey, CA 93940

Officer in Charge
Naval Ship R&D Center
(J. W. Dickey, 2732)
Annapolis, MD 21402

REPRODUCED FROM
BEST AVAILABLE COPY

Mailing List, NRL Report 8311, p. 7

Commanding Officer
Naval Training Equipment Center
(George Derderian, 73)
Orlando, FL 32813

Commanding Officer
Naval Ocean Systems Center
(Gary Gilbert, 6514)
San Diego, CA 92132

Commanding Officer
Naval Ocean R&D Activity
(R. R. Goodman, 110)
NSTL Station, MI 39529

Commander
Naval Weapons Center
(E. E. Benton, 39401)
China Lake, CA 93555

Chief of Naval Research
(W. J. Condell, 421)
800 N. Quincy Street
Arlington, VA 22217

Director
Strategic Systems Project Office
(D. A. Rogers, SP-2025)
Department of the Navy
Washington, D.C. 20376

REPRODUCED FROM
BEST AVAILABLE COPY